J-PARC

ANNUAL REPORT 2014

Vol.2: Materials and Life Science Experimental Facility

MLF ANNUAL REPORT

J-PARC/MLF
Materials and Life Science Division
J-PARC Center
http://j-parc.jp/MatLife/en/index.html

J-PARC was jointly constructed and is now operated by the High Energy Accelerator Research Organization (KEK) and the Japan Atomic Energy Agency (JAEA).

CROSS
Comprehensive Research Organization for Science and Society
http://www.cross-tokai.jp/

J-PARC 16-01
KEK Progress Report 2015-5

Preface

Toshiji Kanaya
Division Head of Materials and Life Science Division, MLF

After the incident at the Hadron Facility on May 23rd, 2013, J-PARC/MLF resumed the beam operation for the user program on February 17th, 2014. In JFY2014, MLF kept 300 kW steady operation with gas micro-bubbles injection in the neutron target. The scheduled beam time in JFY2014 was 166 days and the availability was 69%. There were 895 unique users in that period and they presented 780 proposals.

In JFY2014, 18 instruments were under operation for neutron science. The construction of BL06 (VIN ROSE), BL22 (RADEN) and BL23 (POLANO) at the neutron facility advanced, and VIN ROSE and RADEN proceeded to the commissioning phase (see Figure 1). As for the muon beam lines, the D1 and D2 instruments were dedicated to the user programs and the U-line and the S-line were under commissioning (see Figure 2).

We had a fire accident in the muon area on January 16th, 2015, and the beam stopped until February 25th, 2015. We decided to carry the user experiments canceled due to the accident over to 2015A. After the accident, we reconsidered our protocols related to safety issues. The operation manuals have been reviewed. We also introduced a new working standard protocol. According to the new protocol, all activities done in MLF will be checked by each section. Any suspicious activities found by each section will be reviewed by the MLF safety reviewing, which will be held during regular MLF meetings.

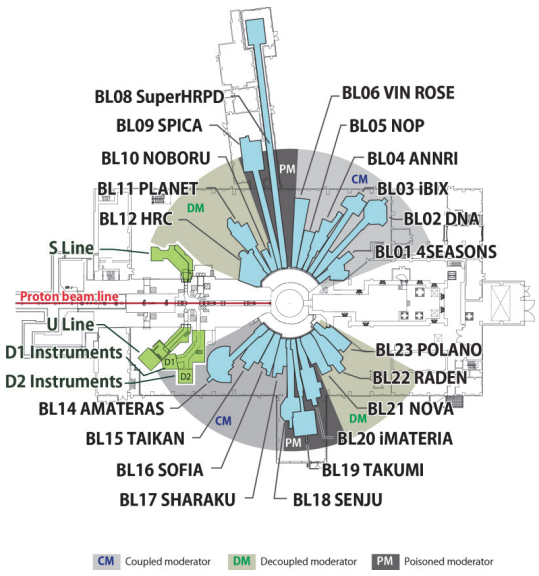

Figure 1. Layout of the neutron beam lines in MLF.

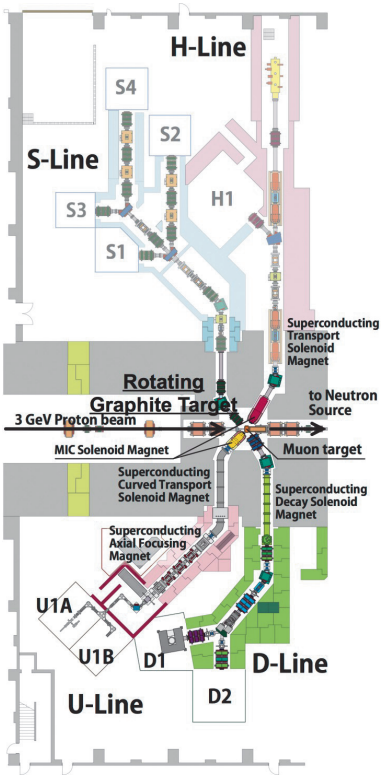

Figure 2. Layout of the muon beam lines in MLF.

Preface

Hideaki Yokomizo
Director, CROSS-Tokai

Four years have passed since CROSS-Tokai commenced operations in support of the user program at the Public Beamlines at the Materials and Life Science Experimental Facility of J-PARC (J-PARC MLF).

As required by the "*Promotion of Public Utilization of Specific Advanced Large-Scale Research Facilities*" legislation, under which CROSS was appointed and now operates, we are fully engaged in facility promotion activities, such as operating a fair and open proposal selection system for the MLF Public Beamlines, providing high-quality user support and promoting facility utilization by both academic and industrial researchers.

During 2014, CROSS-Tokai supported the user program on six fully-operational Public Beamlines: BL01 *4SEASONS*, BL02 *DNA*, BL11 *PLANET*, BL15 *TAIKAN*, BL17 *SHARAKU* and BL18 *SENJU*. In addition, the construction work and commissioning continued on the seventh Public Beamline, BL22 *RADEN*, which will be available to users in 2015. Unfortunately, the user operations during the year were affected by the Muon Facility incident and its aftereffects and the beamtime was suspended from mid-January to the end of March, 2015.

Special programs to promote facility utilization continued to operate successfully during 2014, such as Trial Use and Elementary Strategy Initiative. Trial Use is a program that promotes the use of neutrons by first-time or novice users from both the industrial and academic sectors, and Elementary Strategy Initiative is an integrated strategic research program of the Japanese Government that aims to promote the development of innovative materials and alternative technologies in the target areas of permanent magnets, catalysis and batteries, and electronic and structural materials. Moreover, Complementary Use is a program recommended to encourage and facilitate the complementary and collaborative use of pulsed neutrons (J-PARC MLF), synchrotron radiation (SPring-8), and supercomputer (K computer), which was added to this program in 2014.

I hope this Annual Report would serve as a useful resource for anyone wishing to know more about the current status of the MLF, its recent scientific achievements, the technical R&D projects that support the science program, and the operational details of our facility.

On behalf of the team at CROSS-Tokai, I extend a warm welcome to all researchers who wish to make use of the Public Beamlines at J-PARC MLF.

Research Center for Neutron Science and Technology, Comprehensive Research Organization for Science and Society
www.cross-tokai.jp

Contents

Neutron Science

Muon Scinece

MLF Safety

MLF Operations in 2014

Organization Chart

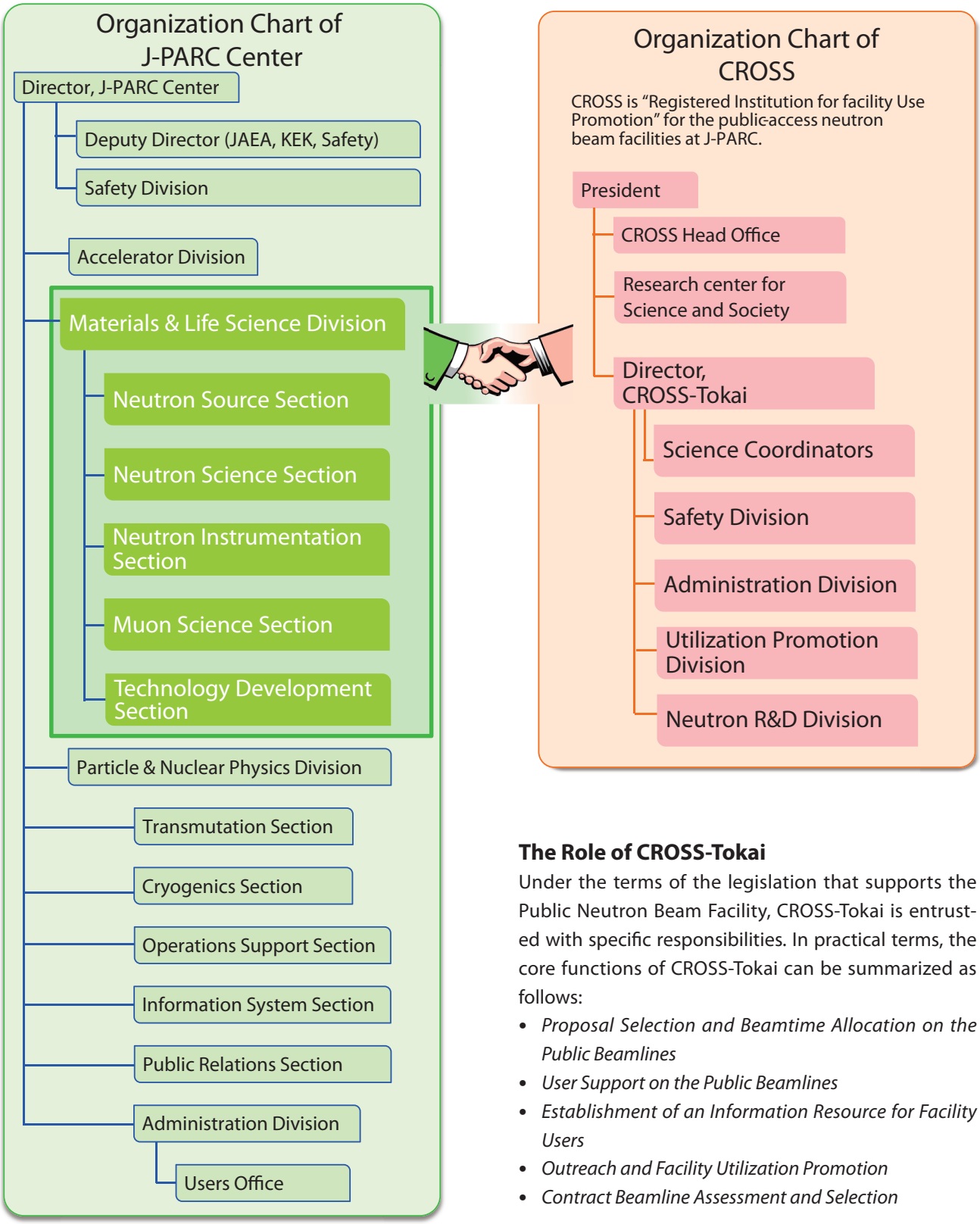

The Role of CROSS-Tokai

Under the terms of the legislation that supports the Public Neutron Beam Facility, CROSS-Tokai is entrusted with specific responsibilities. In practical terms, the core functions of CROSS-Tokai can be summarized as follows:

- *Proposal Selection and Beamtime Allocation on the Public Beamlines*
- *User Support on the Public Beamlines*
- *Establishment of an Information Resource for Facility Users*
- *Outreach and Facility Utilization Promotion*
- *Contract Beamline Assessment and Selection*

J-PARC Map


CROSS – Tokai
(Ibaraki Quantum Beam Research Center)
J-PARC Center Users Office
R245
N
KEK Tokai Campus
Main Gate
R245
Linac
HENDEL R&D Building
3 GeV Synchrotron
MLF
50 GeV Synchrotron

Muon and Neutron Instruments

Muon Source

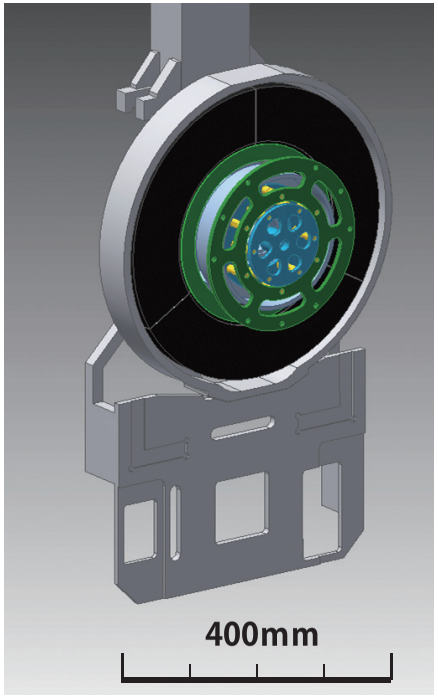

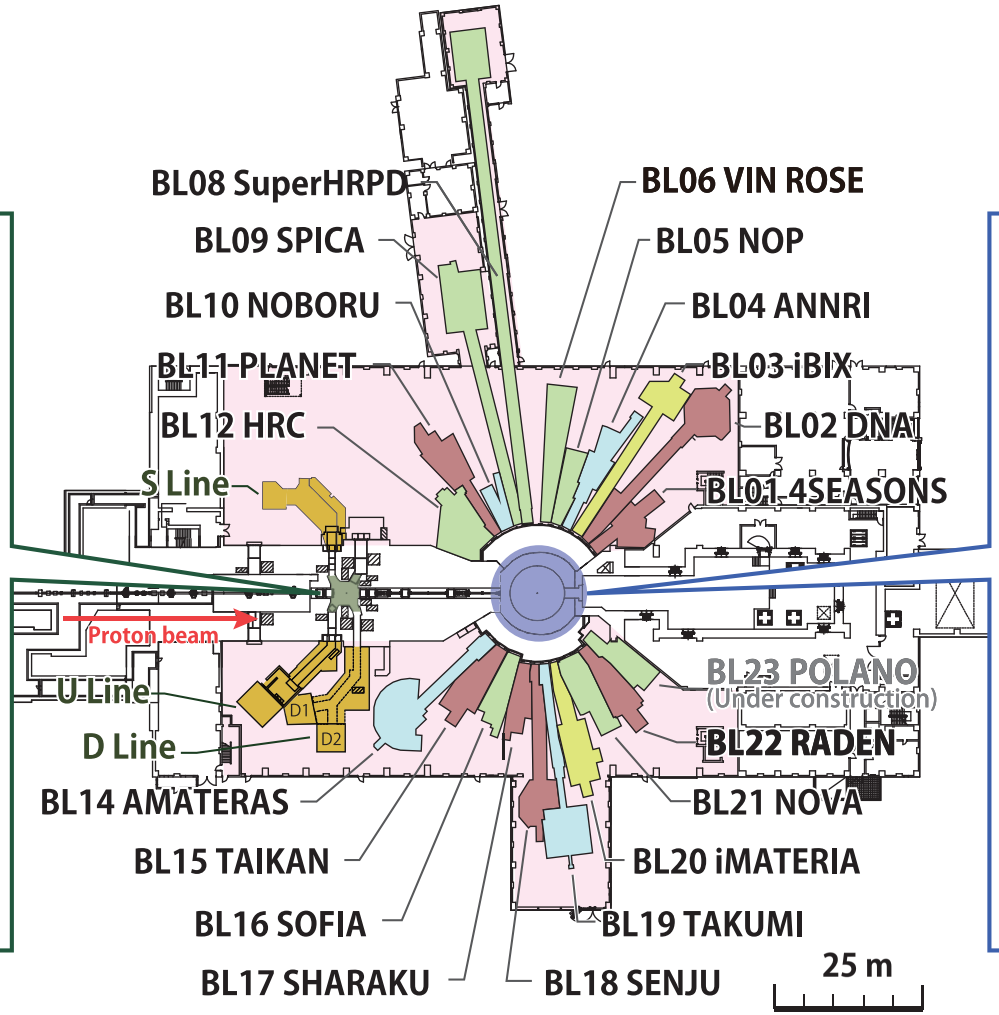

Neutron Source

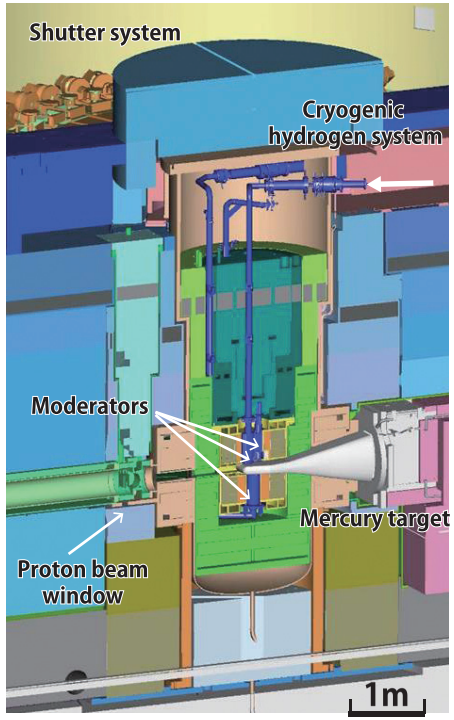

Muon Instruments

Neutron Instruments

JAEA

KEK

Public beam lines

Ibaraki Pref.

Type of moderators

Research and Development Highlights

Site Occupancy of Interstitial Deuterium Atoms in Face-Centered Cubic Iron

1. Introduction

The iron (Fe) – hydrogen (H) system has attracted interest from both scientific and technological point of view. The H concentration and occupancy in Fe metal lattice provides important information concerning some properties of the Fe–H system, such as phase stability. At ambient conditions, a relatively small number of H atoms dissolve in Fe metal, while under high H_2 pressure above several GPa, a hydride, FeH_x, is formed. The in-situ X-ray diffraction measurements were employed to investigate the hydrogenation process of Fe under high H_2 pressure and high temperature. The phase diagram of the Fe–H system is established at temperatures up to 2000 K and pressures up to 20 GPa [1, 2]. In those conditions three different phases are exhibited: body-centered cubic (bcc), double hexagonal close-packed (dhcp), and face-centered cubic (fcc). The fcc-FeH_x appeared as a high temperature phase and the H concentration x was estimated to be in the range from 0 to 1. In the fcc metal lattice there are two interstitial sites capable of accommodating H atoms: octahedral (O) and tetrahedral (T). In the fcc Fe metal, it is considered that dissolved H atoms would most likely occupy the O site rather than the T site, like in the case of other fcc transition metal hydrides [3]. However, the H occupation sites and occupancies of the fcc-FeH_x still remain unknown. Because the fcc-FeH_x is thermodynamically stable only under high H_2 pressure and high temperature, the attempts to quench it at ambient pressure so far have not been successful. Therefore it has been quite difficult to determine the H occupation states experimentally at the above mentioned high pressure and high temperature conditions. In this study, we have investigated the deuterium (D)-occupation state of fcc iron deuteride (FeD_x) using in-situ neutron diffraction measurement.

2. Experimental

The in-situ neutron diffraction experiment at high pressure up to about 7 GPa and high temperature below 1000 K was performed using the high pressure neutron diffractometer (PLANET) [4]. The PLANET enables us to perform in-situ neutron diffraction experiments at high pressure and high temperature conditions. The most important feature of PLANET is that it has a 6-axis multi-anvil press (ATSUHIME) that is good at generating condition of simultaneous high pressure and high temperature. A high pressure cell for the in-situ neutron diffraction was designed based on that for the in-situ X-ray diffraction [5]. We used an Fe rod with 3 mmφ × 2.5 mm in size for the measurement sample. The Fe rod was placed at the center of a deuterium-sealing capsule made of NaCl with internal D_2 sources of AlD_3 pellets above and below. The NaCl capsule was in a cylindrical graphite heater embedded in a pressure-transmitting medium made of ZrO_2 (17 mm-edge cube). The high pressure cell was compressed at room temperature up to 7.4 GPa and then heated to 988 K at a rate of about 40 K per min.

The neutron diffraction profile at 988 K and 6.3 GPa for the structural refinement of fcc-FeD_x was accumulated for about 1 hour. We refined the structural parameters by Rietveld analysis using the Z-Rietveld software (version 0.9.42.2) [6] and succeeded in determining the site occupancies of dissolved D atoms in the fcc-Fe lattice.

3. Results and discussion

Figure 1 shows the results of the Rietveld refinements of the neutron diffraction profile for the FeD_x at 6.3 GPa and 988 K. We first analyzed the results by using the conventional structural model, which is the fcc structure with D atoms only at O sites (Fig. 2(a)). The profile seems to be reproduced by this model (Fig. 1(a)). However, we found a misfit for the 220 reflection peak (inset of Fig. 1(a)). We reconsidered the structural model; based on the structure factor of the fcc-FeD_x, the T site occupation of the D atom provided additional intensity to the $h + k + l = 4m$ reflection peaks.

Using the new model with the D atoms occupying both the O and T sites (Fig. 2(b)), the profile was well reproduced and the refined occupancies of the O and T sites were determined to be 0.532(9) and 0.056(5), respectively (Fig. 1(b)). This unexpected occupation of the D atoms was interpreted in terms of thermally activated movement of D atoms by quantum mechanical calculations. Assuming the Boltzmann distribution, the site occupancy ratio obtained at 988 K yielded an energy difference between the two sites of 0.19 eV, which was in agreement with the calculated value of 0.22 eV.

Furthermore, the obtained in situ neutron diffraction data provide a volume expansion rate of the fcc-Fe due to dissolved D atoms. The volume expansion rate at 6.3 GPa and 988 K can be estimated to be 2.21(4) $Å^3$ per

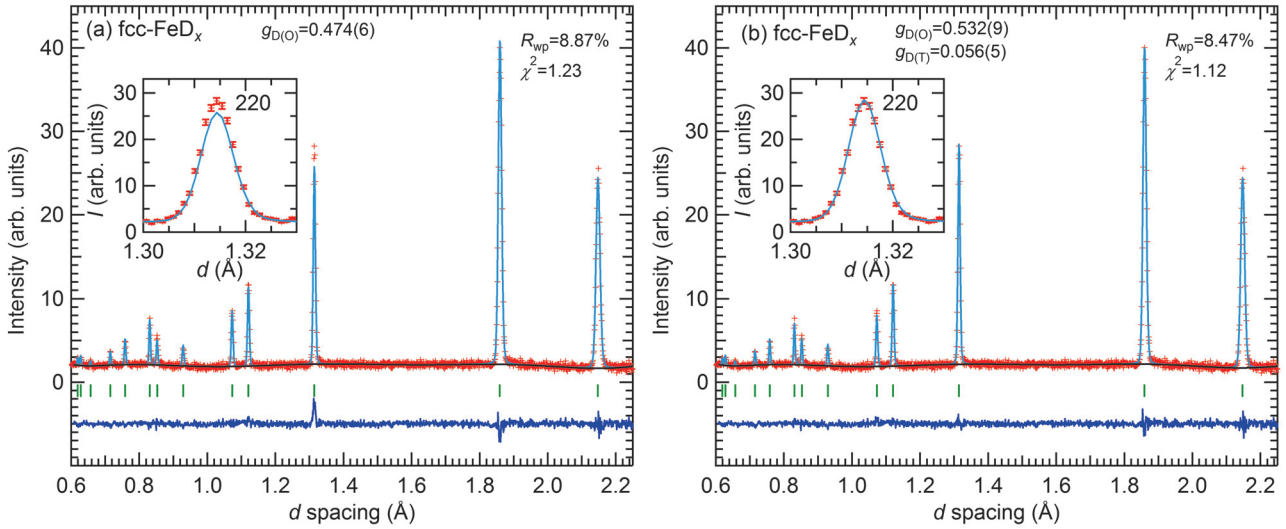

Figure 1. Results of Rietveld refinements for diffraction profiles of fcc-FeD$_x$ at 988 K and 6.3 GPa. $g_{D(O)}$ and $g_{D(T)}$ stand for the site occupancies of the O and T sites, respectively. Reliable values for the parameters R_{wp} and χ^2 are given in the panels. Inset for each panel shows the magnification of diffraction profile around 220 reflection.

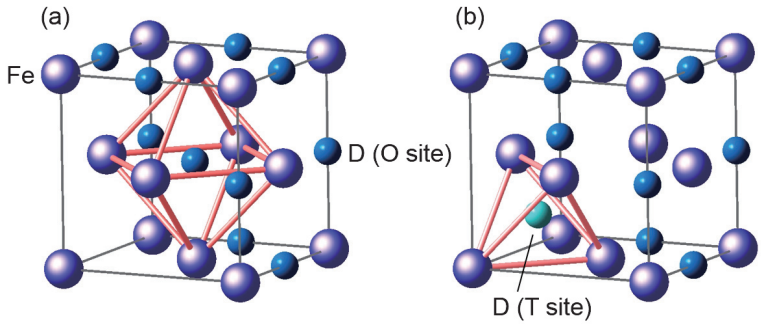

Figure 2. Structural models of the fcc-FeD$_x$. The D atoms are accommodated in (a) the only O site and (b) both the O and T sites. Frames colored in red show typical T and O sites.

D atom, which is larger than the value of 1.9 Å^3 per D atom conventionally used for the fcc-FeH$_x$. The volume expansion rate for the T site occupation is larger than that for the O site occupation, hence the larger volume expansion rate would be interpreted in terms of the slight T site occupation.

References

[1] Y. Fukai, Nature **308** (1984) 174.

[2] K. Sakamaki *et al.*, Phys. Earth Planet In. **174** (2009) 192.

[3] Y. Fukai, The Metal–Hydrogen System 2nd ed. (Springer-Verlag, 2005).

[4] T. Hattori *et al.*, Nucl. Instrum. Methods Phys. Res., Sect. A **780** (2015) 55.

[5] A. Machida *et al.*, Nat. Commun. **5** (2014) 5063.

[6] R. Oishi *et al.*, Nucl. Instrum. Methods Phys. Res. Sect. A **600** (2009) 94.

A. Machida[1], H. Saitoh[1], H. Sugimoto[2], T. Hattori[3], A. Sano-Furukawa[3], N. Endo[1], Y. Katayama[1], R. Iizuka[4], T. Sato[5], M. Matsuo[5], S. Orimo[5,6], and K. Aoki[5]

[1]Quantum Beam Science Center, JAEA; [2]Department of Physics, Chuo University; [3]Neutron Science Section, Materials and Life Science Division, J-PARC Center; [4]Geodynamics Research Center, Ehime University; [5]Institute for Materials Research, Tohoku University; [6]WPI-Advanced Institute for Materials Research, Tohoku University

Simultaneous Characterization of Small-Angle Neutron Scattering and Bragg-Edge Transmission in Steel

1. Introduction

Steel is one of the most important materials that support the infrastructure of modern societies. Since microstructures, such as grain structure, precipitates, and dislocations, play a key role in mechanical properties of steels, the precise characterization of the microstructures in steels is crucial. For example, practical steels utilize various strengthening phenomena such as solid solution hardening, precipitation hardening, work hardening, and grain refinement. The development of advanced steels requires precise control of solvent atoms, precipitates, dislocation, and grain size.

Neutron scattering is a powerful tool to quantitatively characterize the microstructures because neutrons can penetrate thick steel plates and measure large sample volumes. In addition, the new-generation pulsed neutron sources like MLF enable a new characterization technique, i.e., simultaneous analysis of small-angle neutron scattering and Bragg-edge transmission spectra [1]. This technique provides simultaneously crystallographic information of the grains from Bragg-edge and nanostructural information of the precipitates from SANS. In this study, this technique was applied to model alloys of precipitation-strengthened steels.

2. Experimental

The chosen steel samples containing Cu and vanadium carbide (VC), which are known as typical precipitates in steels. To form nano-sized precipitates, the steels were aged at 823 K. The matrices were ferrite in the Cu steel and partially pearlite in the VC steel.

The SANS experiments were conducted using the time-of-flight (TOF) SANS instrument BL15 TAIKAN [2]. Each sample was cut into a plate with thickness of about 1 mm. To separate nuclear and magnetic scattering contributions, a magnetic field of 1 T was applied to the samples perpendicular to the incident neutron. In this condition, since the magnetization is saturated, the scattering profiles parallel to the magnetic field (//**H**) contain only the nuclear scattering contribution, whereas the scattering profiles perpendicular to the magnetic field (⊥**H**) are composed of both the nuclear and magnetic scattering contributions. The scattering intensities were converted into absolute units using the glass carbon standard [3]. The neutron transmission spectra were converted into attenuation coefficient spectra to normalize the sample volumes. For the Bragg-edge transmission analysis, incident neutrons with wavelength between 0.2 and 0.4 nm were used, while the scattering intensity between 0.45 and 0.76 nm was analyzed for SANS. To avoid a possible multiple Bragg scattering, SANS intensity with wavelength below 0.45 nm was not used.

3. Results and discussion

Figure 1 shows the SANS profiles of the Cu and VC steels. The SANS profiles of the Cu steel have a shoulder at $q < 1$ nm^{-1}, where q is the modulus of the scattering vector. The shoulder is the onset of the so-called Guinier region, which reflects the size of scatterers. Hence, the results indicate that the Cu precipitates are formed in the Cu steels. The difference in the intensity between //**H** and ⊥**H** is attributed to the magnetic scattering contribution. Since Cu is nonmagnetic, the Cu precipitates have high magnetic scattering contrast with the ferromagnetic ferrite matrix.

On the other hand, the VC steel has no shoulder in the SANS profiles. This indicates that almost no nano-sized precipitates are formed in the VC steels. Observation conducted with an electron microscope showed that VC precipitates were not effectively formed, most likely because cementite consumed carbon. The slope at $q < 0.6$ nm^{-1} is probably the scattering of the large cementite grains.

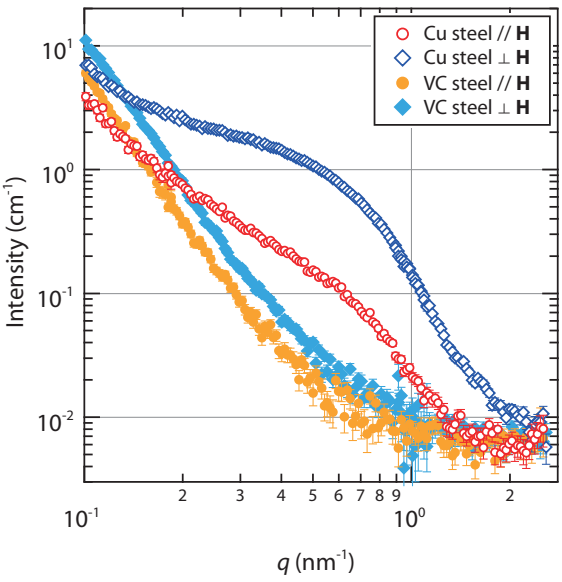

Figure 1. SANS profiles of Cu and VC steels.

Figure 2 shows the attenuation coefficient spectra simultaneously measured with SANS. The vertical dotted lines in Figure 2 show the wavelengths of the Bragg-edges calculated for bcc Fe. A clear jump of the attenuation coefficient is observed at a wavelength of about 0.4 nm. This result agrees well with the Bragg-edge of the bcc Fe {110}. Therefore, we successfully measured the SANS and Bragg-edge at the same time using TOF-SANS. Small jumps are also found at the wavelengths of bcc Fe {200} and {211}.

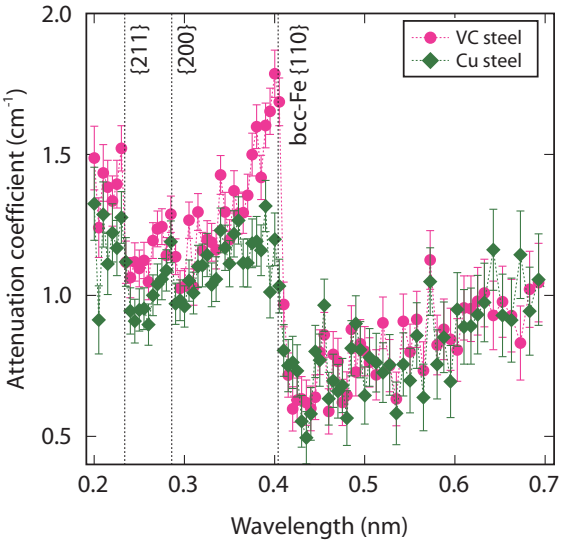

Figure 2. Attenuation coefficient spectra of Cu and VC steels. Dotted lines indicate the wavelength of Bragg-edges of bcc Fe.

The height of the Bragg-edge is different between the Cu and VC steels. This indicates the difference in crystallite size. Since larger crystallite generates higher multiple Bragg scattering, the height of the Bragg-edge becomes lower [1,4-6]. Hence, the crystallite size of the Cu steel is larger than that of the VC steel. Vanadium probably delays recrystallization via the solute drag effect in the VC steel.

References

[1] Y. Oba, S. Morooka, H. Sato, N. Sato, K. Ohishi, J. Suzuki, and M. Sugiyama, ISIJ Int. 55, 2618 (2015).
[2] S. Takata, J. Suzuki, T. Shinohara, T. Oku, T. Tominaga, K. Ohishi, H. Iwase, T. Nakatani, Y. Inamura, T. Ito, K. Suzuya, K. Aizawa, M. Arai, T. Otomo, and M. Sugiyama, JPS Conf. Proc. 8, 036020 (2015).
[3] F. Zhang, J. Ilavsky, G. Long, J. Quintana, A. Allen, and P. Jemian, Metall. Mater. Trans. A 41A, 1151 (2010).
[4] H. Sato, T. Kamiyama, and Y. Kiyanagi, Mater. Trans. 52, 1294 (2011).
[5] T. M. Sabine, Acta Cryst. A44, 368 (1988).
[6] T. M. Sabine, R. B. V. Dreele, and J. E. Jørgensen, Acta Cryst. A44, 374 (1988).

Y. Oba[1], S. Morooka[2], H. Sato[3], N. Sato[1], K. Ohishi[4], J. Suzuki[4], and M. Sugiyama[1]
[1]Research Reactor Institute, Kyoto University; [2]Department of Aerospace Engineering, Tokyo Metropolitan University; [3]Faculty of Engineering, Hokkaido University; [4]Neutron R&D Division, Comprehensive Research Organization for Science and Society

Relation between Vickers Hardness and Bragg-edge Broadening in Quenched Steel Rods

1. Introduction

Bragg-edge transmission imaging is a new material analysis tool that makes it possible to map non-destructively crystalline microstructural information of bulk material with spatial resolution around 100 μm over a large area (about 10 cm × 10 cm) [1]. In this report, we explain the recent result [2] that indicated the relation between material hardness and width of d-spacing distribution in a quenched ferritic steel (martensite), obtained by using this method.

Quenching is a popular method to harden steel surface. In the quenched region, martensite is produced, which has fine microstructure due to carbon solid solution in the crystal structure. We conducted experiments in order to visualize the quenched region in the thick steel rods. Real-space distributions of d-spacing (macrostrain) in quenched ferritic steel rods (Fe-0.45%C; 2.6 cm diameter and 2 cm height) were evaluated [3, 4] by mapping the areas of larger d-spacing of martensite, and successfully identified the quenched spaces as a longer d-spacing area.

However, the deduced {110} d-spacing (0.2042 nm) in the quenched region was much larger than the normal value (0.2032 nm) of martensite with a composition of Fe-0.45%C. Furthermore, the Bragg-edge is gentler in the quenched region than in the ferrite region. To obtain more accurate evaluation and avoid overestimation, the Bragg-edge broadening caused by microstrain and crystallite-size effects due to fine microstructure of martensite, which is equivalent to diffraction peak broadening, should be considered in the analysis.

Thus, a single-Bragg-edge analysis function of the RITS code [1, 3] was revised so that the Bragg-edge broadening was reflected in the analysis, then we extracted the information about the width of the d-spacing distribution. Furthermore, the Bragg-edge width was compared with the Vickers hardness in ferrite and martensite, and it was indicated that the width is proportional to the Vickers hardness. The result suggests that the Bragg-edge transmission imaging can be used as a non-destructive method to investigate quenched steels.

2. Development of the Bragg-edge broadening analysis method

For d-spacing/macrostrain analysis, the profile fitting analysis method was used. In the RITS code, the Jorgensen-type edge-profile function was adopted [3]. This function is derived from the convolution of the Heaviside step function and a Gaussian function with two back-to-back exponentials.

So far, the edge-profile function was constant and independent of the pixel position. This is because the instrumental resolution, which is expressed by the Jorgensen-type edge-profile function, is usually not changed. Therefore, the analysis is correct if the shape of d-spacing distribution remains the same. However, for a ferritic steel containing martensite, the distribution of d-spacing changes with the content of martensite. The width of d-spacing distribution (the Bragg-edge broadening) of martensite is larger than that of ferrite. In other words, for analysis of a ferritic steel containing martensite, another broadening parameter for this phenomenon should be implemented into the edge-profile function.

In the new analysis procedure, it is assumed that the distribution of d-spacing depending on microstrain and crystallite-size follows a Gaussian function. Then, the whole Jorgensen-type edge-profile function consists of two functions. One is the Jorgensen-type instrumental resolution function, and the other is the Gaussian d-spacing distribution function. In the actual analysis, firstly, we analyze the sharp Bragg-edge data of the region which consists mainly of ferrite to determine the Jorgensen-type instrumental resolution function. Secondly, we evaluate the average (macrostrain) and the width (microstrain) of the Gaussian d-spacing distribution function by using the Jorgensen-type instrumental resolution function obtained in the first-stage analysis.

3. Experimental

The specimens were three sections of ferritic steel rod (Fe-0.45%C; 2.6 cm diameter and 2 cm height) quenched from each rim surface by axial-symmetric induction hardening. The quenched depth from the surface was expected to be 3 mm, 5 mm and 7 mm, respectively. Neutrons were transmitted along the axial direction of the sample cylinder (2 cm thickness).

The pulsed neutron transmission imaging experiment was carried out at J-PARC MLF BL10 "NOBORU" [5]. The beam angular divergence was ± 3 mrad in this experiment. The neutron TOF imaging detector used was

a neutron ^{10}B-MCP (Micro Channel Plate) detector [6]. The pixel size was 55 μm, and the detection area was 1.4 cm × 1.4 cm.

4. Results and discussion

Fig. 1 shows Bragg-edge transmission spectra of the center (ferrite) region and the rim (martensite) region of the 7 mm-depth quenched rod. This figure shows that both {110} Bragg-edge data can be reproduced by the developed data analysis procedure. Additionally, it was found that the extracted d-spacings were reasonable (0.2026 nm for ferrite and 0.2032 nm for martensite). An overestimation on d-spacing of martensite (0.2042 nm), evaluated in the previous work [3, 4], was corrected by this analysis method. Furthermore, an FWHM of the Gaussian d-spacing distribution due to microstrain and crystallite-size was estimated in a value of the order of 10^{-3} nm from the data in the martensite region.

Fig. 2 shows results of the FWHM mapping of the d-spacing distribution of 7 mm, 5 mm and 3 mm quenched steel rods. It is clear from the first sight at the images that the areas with value of the order of 10^{-3} nm almost correspond to the expected quenched area depth (7 mm, 5 mm or 3 mm) from the rim surface.

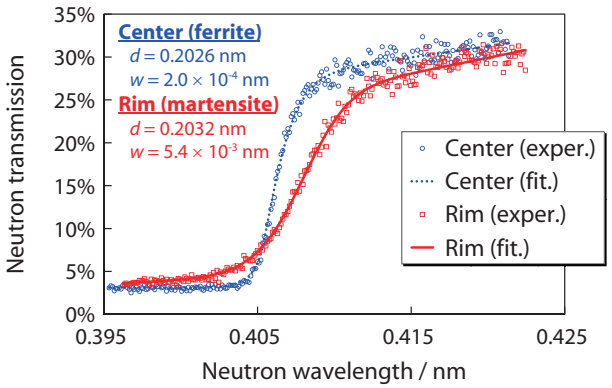

Figure 1. {110} Bragg-edge transmission spectra with the fitting curves of ferrite (center) region and martensite (rim) region in the 7 mm-depth quenched rod.

The significance of the obtained parameter is discussed in terms of the quantity of martensite by using the Vickers hardness data. At first, we calculated the radially dependent data of the width of d_{110}-spacing, w_{110}, of each rod from Fig. 2. Figure 3 (a) shows radial changes of w_{110} of 7 mm-, 5 mm- and 3 mm-depth quenched rods. Continuously, we fitted the sigmoid functions to the radial dependences (curves in Fig. 3 (a)), and derived the inflection point of each curve (vertical dashed lines in Fig. 3 (a)). As a result, the inflection points are 6.5 mm, 5.2 mm and 3.3 mm for 7, 5 and 3 mm-depth quenched rods. These seem to correspond to the actual depths of quenching.

To verify this estimation, Fig. 3 (a) was compared with the radial dependence of the Vickers hardness, which correlates to the ratio of ferrite/martensite. In particular, the Vickers hardness of 450 (Hv 450) is well known as the hardness boundary between ferrite and martensite. Figure 3 (b) shows the radial dependence of the Vickers hardness of each quenched rod. From this figure, it was found that the shape of radial dependence of w_{110} was quite close to those of the Vickers hardness for each quenched rod. Additionally, the points of Hv 450 also correspond to the inflection points of radial dependence of w_{110}. Therefore, these results indicate that w_{110} depicts the ferrite/martensite concentration ratio in a ferritic steel.

Finally, we deduced the relation between the Vickers hardness and w_{110} by comparing both values at the same position. Figure 4 shows plots of the Vickers hardness as a function of w_{110}, with the fitting lines. This figure shows that the Vickers hardness and the ferrite/martensite quantity are proportional to w_{110}.

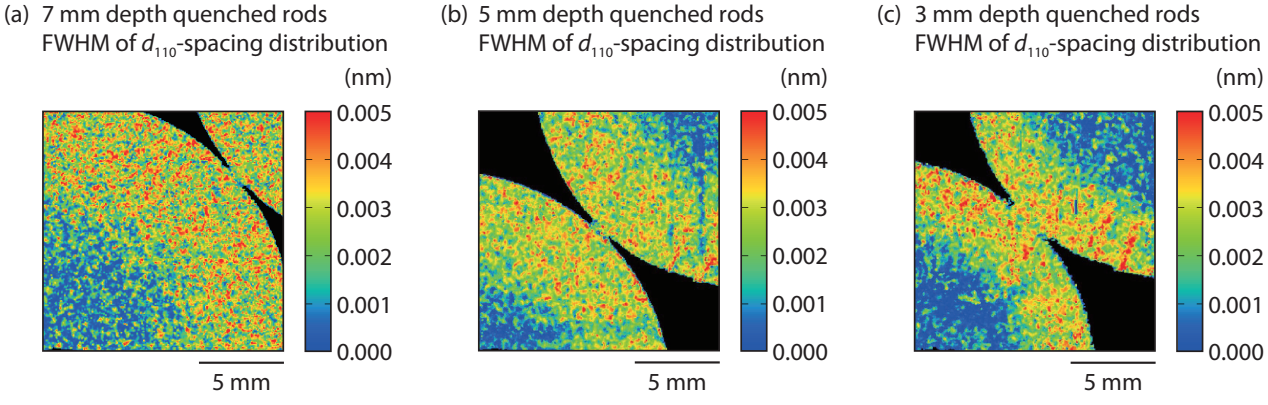

Figure 2. Real-space map (55 μm pixel size) of FWHM of the d-spacing distribution in quenched steel rods. The quenched (martensite) regions exist near the rim surface.

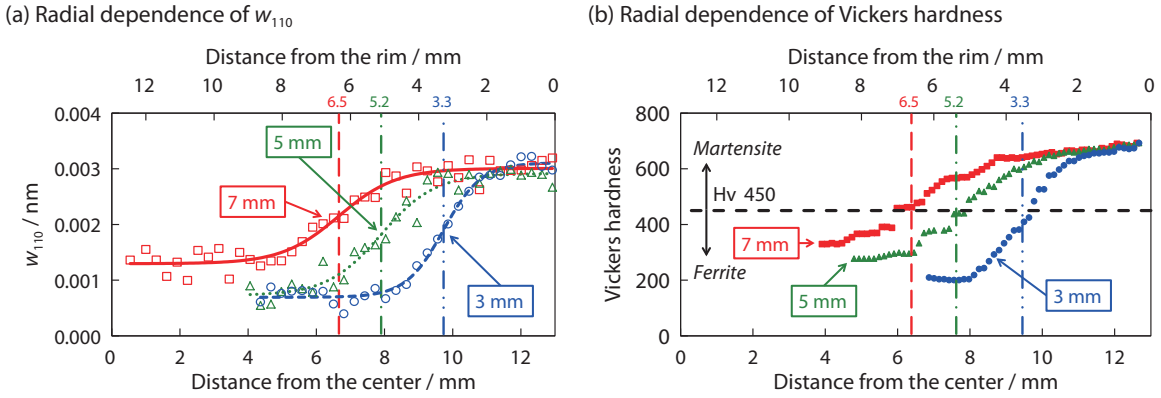

Figure 3. (a) Radial dependences of FWHM of d_{110}-spacing distribution, and (b) radial dependences of the Vickers hardness, of 7 mm-, 5 mm- and 3 mm-depth quenched steel rods.

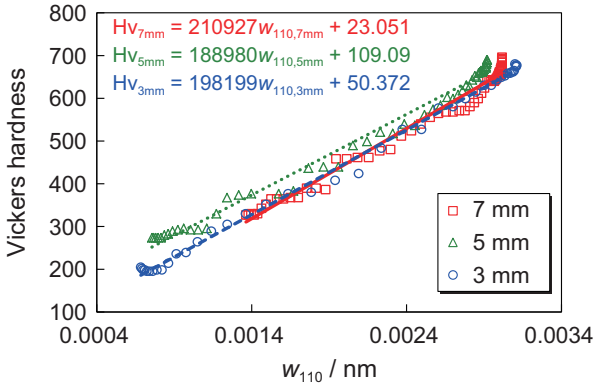

Figure 4. Relation between the Vickers hardness and FWHM of d_{110}-spacing distribution in quenched steel rods.

5. Conclusion

By using the pulsed neutron transmission imaging combined with the revised RITS code, the Bragg-edge broadening due to martensite in a bulk ferritic steel was analyzed over a large area with high spatial resolution. As a result, the width of d-spacing distribution related to hardness, ferrite/martensite quantity, microstrain and crystallite-size could be successfully evaluated. Furthermore, it was found that the Vickers hardness was linearly proportional to the width of d-spacing distribution.

The use of this method is viable because it is non-destructive. The condition for this is that the width should not depend on the measuring direction, namely the scalar value. It is expected to be scalar since the martensite texture is not strong. Therefore, in the future, non-destructive measurements of the material hardness in a ferrite/martensite steel may be carried out by using this method. Furthermore, it is expected that the information about dislocation density and crystallite size can be evaluated by further improvement of the Bragg-edge profile analysis.

Acknowledgments

The authors are greatly thankful to Dr. Anton S. Tremsin of University of California at Berkeley for using the MCP detector, and the NOBORU instrument scientists for their experimental assistance. This work was supported by Grant-in-Aid for Scientific Research (S) No. 23226018 from JSPS.

References

[1] H. Sato, T. Kamiyama and Y. Kiyanagi, Mater. Trans. 52, 1294-1302 (2011).
[2] H. Sato, T. Sato, Y. Shiota, T. Kamiyama, A. S. Tremsin, M. Ohnuma and Y. Kiyanagi, Mater. Trans. 56, 1147-1152 (2015).
[3] Y. Kiyanagi, H. Sato, T. Kamiyama and T. Shinohara, J. Phys. Conf. Ser. 340, 012010 (2012).
[4] T. Kamiyama, H. Sato, R. Takamori, N. Ayukawa, Y. Iwasaki, A. S. Tremsin and Y. Kiyanagi, MLF Annual Report 2010, 115-117 (2011).
[5] F. Maekawa, K. Oikawa, M. Harada, T. Kai, S. Meigo, Y. Kasugai, M. Ooi, K. Sakai, M. Teshigawara, S. Hasegawa, Y. Ikeda and N. Watanabe, Nucl. Instrum. Methods A 600, 335-337 (2009).
[6] A. S. Tremsin, J. B. McPhate, A. Steuwer, W. Kockelmann, A. M. Paradowska, J. F. Kelleher, J. V. Vallerga, O. H. W. Siegmund and W. B. Feller, Strain 48, 296-305 (2012).

H. Sato[1], T. Sato[1,2], Y. Shiota[1,3], T. Kamiyama[1], M. Ohnuma[1], and Y. Kiyanagi[1,3]
[1]Graduate School of Engineering, Hokkaido University; [2]Present affiliation: Muroran Plant, The Japan Steel Works, Ltd.; [3]Present affiliation: Graduate School of Engineering, Nagoya University

Study of the Structural Change in the Human Stratum Corneum Induced by the Treatment of Surfactant Solutions

1. Introduction

The outermost layer of the skin, stratum corneum (SC), consists of corneocytes and intercellular lipid matrix, as shown schematically in Figure 1. The structure of the SC plays an important role in the barrier function [1, 2]. The surfactant used in skin cleansers sometimes induces swellings of SC. They are accompanied by structural changes in the keratin fibers in the corneocytes, as well as in the intercellular lipids lamellar structure around the corneocytes. The aim of this research is to study the conformation change of human SC, particularly the soft keratin conformation, induced by the treatment of surfactant solutions using scattering analysis.

A problem emerged while conducting small-angle X-ray scattering (SAXS) measurements – the scattering of the surfactant micelles disturbed the observation of keratin fibers, particularly microfibril structures. To resolve this problem, the influence of the scattering of surfactant micelles was eliminated by using deuterated surfactant solutions in the small-angle neutron scattering (SANS) measurements, and observing only keratin fibers in the heel SC powder (without the intercellular lipids lamellar structures) became possible [3]. Using this technique, this year, we analyzed the swelling of the keratin fiber in SC powder soaked with the surfactant solution of various conditions.

On the other hand, since the SANS measurement required long time, several hours per one scan, it was difficult to pursue SC structural change in a short time (from several minutes to 1 hour) after surfactant solution soak. Therefore, the SC internal structure change was measured by SAXS for a short time using the structural orientation in the stacked SC sheets. And the SAXS measurement results after prolonged progress were compared with the SANS measurement results.

2. Experimental

The SANS experiments were performed using the TAIKAN instrument installed on the BL15 beamline at the MLF, J-PARC (Tokai, Japan). The SAXS experiments were performed using the SAXS spectrometer installed on the BL19B2 beamline at the SPring-8 (Sayo, Japan).

The human heel SC powder was obtained from the healthy volunteer from Kao Corporation. We confirmed that the powder samples had no peaks of the intercellular lipids lamellar structure by SAXS and WAXS. The human abdominal SC sheets were supplied by Biopredic International (Rennes, France). As a surfactant solution for soaking, the 3% and pH 7 sodium dodecyl sulfate (SDS) solution was prepared. Deuterated SDS (d-SDS) solution in heavy water and heavy water were used for the SANS experiments instead of the usual SDS solution and water, respectively.

The SANS experiments were conducted at 30, 40, or 50°C using the heater of the automatic sample changer. All SAXS experiments were conducted at RT (26-27°C) without the heater.

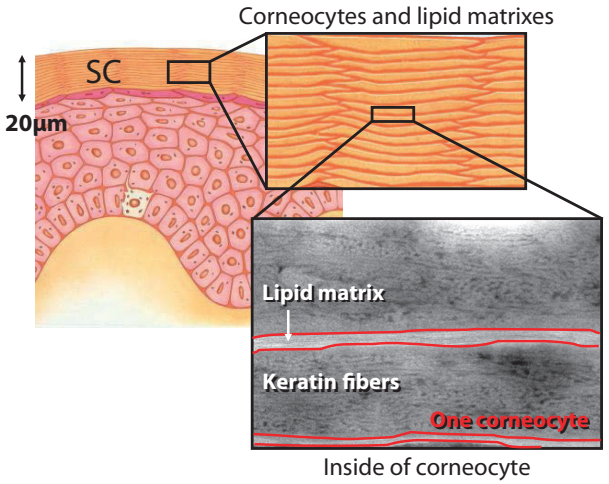

Figure 1. Schematic diagram of the stratum corneum (SC) structure.

3. Results and discussions

Figure 2 shows the result of the SANS measurements of SC powder soaked with the d-SDS solution or the heavy water. The contrast-matching technique using deuterated surfactant solutions enabled comparison of the swelling of keratin fibers. The peak position shifted toward lower q and the peak width became broader, by soak of d-SDS solution than heavy water. Furthermore, systematic peak shift toward a lower q and broadening took place by increasing the temperature. These were considered to be the results in which the keratin fiber swelled more.

Figure 3 shows the results of SAXS and SANS measurements of SC sheets. We analyzed the scattering profiles of the vertical and parallel direction separately since the scattering profiles of measurements using the stacked SC sheets have anisotropy. Since the keratin

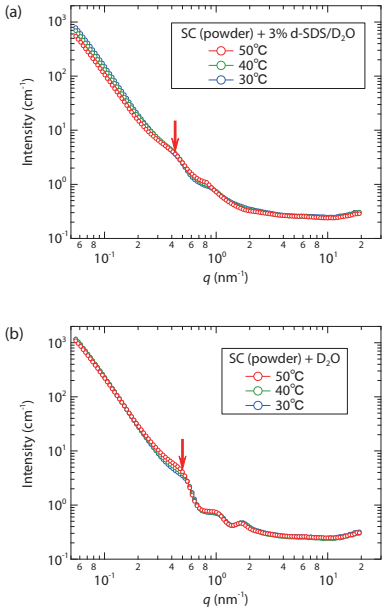

Figure 2. SANS profiles of SC powder soaked with (a) surfactant solutions (SC + 3% d-SDS/D_2O) and (b) heavy water (SC + D_2O) at pH 7. Arrows indicate the 1st interference peak position of spacing of swollen keratin fibers at 50°C.

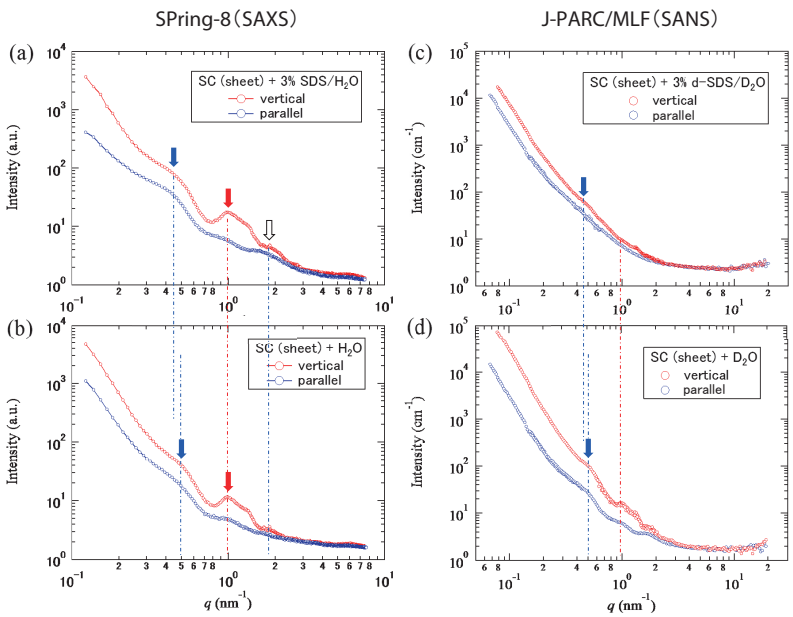

Figure 3. SAXS (a,b) and SANS (c,d) profiles of stacked SC sheets. (a,c) soaked with surfactant solutions, (b,d) soaked with (heavy) water. Blue filled-in arrows indicate the 1st interference peak position of spacing of swollen keratin fibers. Red filled-in arrows indicate the peak position of the intercellular lipids lamellar structure. Black outlined arrows indicate the peak position of the SDS micelles.

fibers and the intercellular lipids lamellar structure exist in parallel with the SC sheet, their perpendicular scattering peaks became stronger. By comparing the results of the SAXS and SANS measurements, a significant difference emerged in the peak of the intercellular lipids lamellar structure. The peak of the intercellular lipids lamella structure was not so prominent in the SANS measurement. Moreover, the peaks of the intercellular lipids lamella structure were almost the same after soaking in both SDS solution and water in the SAXS measurement. These results suggested that wetting of surface of the skin by the surfactant solution of several percent or the water did not change intercellular lipids lamella structure mostly. Furthermore, the SANS result indicated that (deuterated) water outside of the skin did not penetrate the water layers in the intercellular lipids lamella structure.

It became clear that the keratin fiber swelled more quickly and largely by soaking the SDS solution rather than water, according to the short-term SAXS measurement of the SC internal structure change using the stacked SC sheets (data not shown) [4]. Consequently, the usefulness of the method of analyzing SC structural change using the stacked SC sheets was suggested.

References

[1] S. H. White *et al.*, *Biochemistry* **27** (1988) 3725.
[2] J. A. Bouwstra *et al.*, *Biochim. Biophys. Acta* **1212** (1994) 183.
[3] T. Kume *et al.*, *Hamon* **24** (2014) 15.
[4] T. Kume *et al.*, *SPring-8/SACLA Research Reports Early edition* (2015) 2014A1516.

T. Kume[1], M. Onoo[1], and I. Hatta[2]
[1]*Analytical Science Research Labs. Kao Corporation;* [2]*Nagoya Industrial Science Research Institute*

Understanding the Mechanism of Gene Expression by Flexibility of the DNA Structure - Observation of Base-sequence Dependent DNA Dynamics by Quasi-elastic Neutron Scattering

1. Introduction

The genomes (DNA sequences) of many organisms have been obtained, and a research base for analyzing and predicting the biological function from a genome has been established. However, during the process of gene expression, amino acids and bases interact with each other to form a complex tertiary structure of protein and DNA, and a clear match between gene sequence and biological function cannot necessarily be seen.

Recent studies have shown that the direct interaction between protein and DNA (known as "direct recognition") is not the only important factor in passing the information contained within a genome, but so is the "indirect recognition," which is an easy transformation of the sequence-dependent DNA structure (Fig. 1). Because the analysis of the fluctuations in the sequence-dependent DNA structure under indirect recognition is important, it is necessary to experimentally demonstrate that the dynamics of DNA can be observed directly by experiment [1].

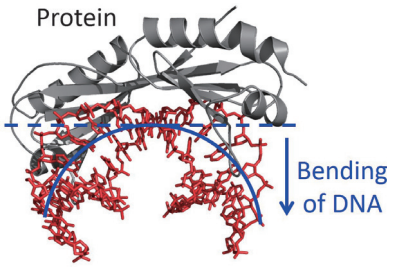

Figure 1. Bending of DNA by protein binding. Dotted line indicates the stable DNA conformation, but the conformation accommodates the bending depending on base sequence.

2. Results & Discussions

In this study, we performed quasi-elastic neutron scattering experiments using the AMATERAS instrument at J-PARC/MLF to study the dynamics of two kinds of DNA sequences: 5'CGCGAATTCGCG3' (AATT) and 5'CGCGTTAACGCG3' (TTAA). These sequences were predicted to be rigid and flexible, respectively, by analysis of a systematic molecular dynamics simulation. We successfully acquired neutron spectrum with the required precision (Fig. 2).

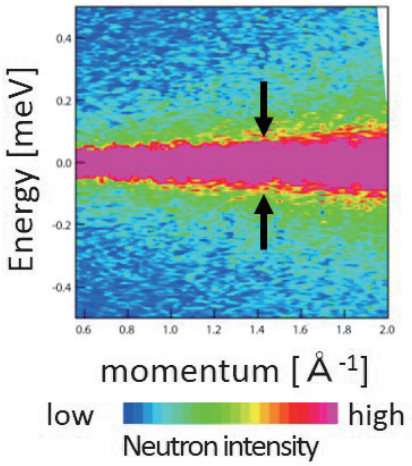

Figure 2. Neutron quasi-elastic scattering spectrum have the signal which an energy change spread through for 0 elastic scattering symmetrically.

Examining the half-width at half maximum (HWHM) of the spectrum as a function of Q provides information on the relaxation time of the DNA dynamics. HWHM increases with Q^2 at the lower Q region, and asymptotically approaches a constant value at large Q for both sequences. The constant value of TTAA was larger than that of AATT in the high Q region, although they were similar to each other in the low Q region. This indicates that the diffusive motion is dominant with similar frequency for both sequences at longer length scales, whereas at shorter length scales, the frequency of motion of TTAA is larger than that of AATT. The plateau of HWHM at higher Q region indicates that the correlation times are independent of the length scale, suggesting that the jump motion dominates toward smaller length scales. These behaviors can be well explained by the jump diffusion model [2], as follows

$$\Gamma(Q) = \frac{DQ^2}{1 + DQ^2\tau_0}$$

The fitting curves to the data are shown in Fig. 3. The diffusion coefficients, 6.0±0.8 $nm^{2*}s^{-1}$ and 5.5±0.5 $nm^{2*}s^{-1}$ for AATT and TTAA, respectively, are the same within the error range. The residence time of a hydrogen atom on one site is calculated as $\tau = 1/\Gamma(Q\rightarrow\infty)$, where $\Gamma(Q\rightarrow\infty)$ is HWHM obtained from the asymptotic behavior at higher Q. The resulting residence times are

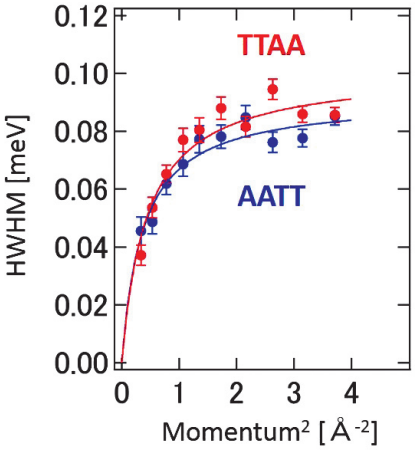

Figure 3. HWHM of QENS spectrum of AATT and TTAA dodecamers.

$\tau = 45.2 \pm 1.5$ ps and $\tau = 40.9 \pm 1.1$ ps for AATT and TTAA, respectively. The residence time of AATT is longer than that of TTAA.

This result demonstrates agreement with the molecular dynamics simulation [3] and supports the importance of the indirect interaction of DNA flexibility in the recognition of DNA, as has been proposed based on simulations and statistical analyses of crystal structures.

This result demonstrates that DNA sequences should include not only the string of bases but also information about the DNA flexibility. We expect that the discovered structural property of DNA in this study will contribute to elucidation of the mechanism controlling the "on–off switch" of gene-expression.

3. Acknowledgments

This study was partially subsidized with scientific research funds from the Ministry of Education, Culture, Sports, Science and Technology (No. 18031042).

References

[1] H. Nakagawa *et al.*, Phys. Rev. E., 90 022723 (2014).
[2] Y. Yonetani *et al.*, Biophys. Chem. 160 54 (2012).
[3] M. Bee, *Quasielastic Neutron Scattering: Principles and Applications in Solids State Chemistry, Biology and Materials Science* (Adam Hilger, Bristol, UK, 1988).

H. Nakagawa[1,2], Y. Yonetani[1], K. Nakajima[2], S. Ohira-Kawamura[2], T. Kikuchi[2], Y. Inamura[2], M. Kataoka[3], and H. Kono[1]
[1]Quentum Beam Science Center, Japan Atomic Energy Agency; [2]J-PARC Center, Japan Atomic Energy Agency; [3]Graduate School of Materials Science, Nara Institute of Science and Technolog

QENS Study of Protein Dynamics in Glycerol and Water Mixture Measured on DNA

1. Introduction

Protein in solution has a dynamical hierarchy from diffusion to structural dynamics (internal motions). The protein diffusion contributes to the transportation of the protein as a colloidal particle in solution and subsequently it improves the efficiency of the encounter of an enzyme with substrate. The structural dynamics is closely related to the protein function, such as the substrate binding of the enzyme. The protein dynamics are affected by the physicochemical propitiates of the solvent, such as viscosity and solute concentration (crowding). In vivo, the intracellular environment displays high viscosity and it is also crowded. Glycerol is used as a low-molecular weight-crowding agent. Furthermore, glycerol is accumulated inside the bodies of some insects as bioprotectant [1]. Therefore, it is important to examine the effect of glycerol on protein dynamics.

In this study, the global diffusion and structural dynamics of hen egg white lysozyme in glycerol-water mixtures between 0 and 50% glycerol (v/v) were examined by quasi-elastic neutron scattering experiment at BL02 in J-PARC/MLF.

2. Results & Discussions

Figure 1 shows the quasi-elastic neutron scattering spectrum of lysozyme in D_2O solution at Q = 0.625 [Å^{-1}]. To characterize the global diffusion and structural dynamics of the protein, the experimental data were analyzed by the following function, which includes the contributions of the global diffusion and internal motions,

$$\begin{aligned} S_p(Q,\omega) &= S_{dif}(Q,\omega)\otimes S_{in}(Q,\omega) \\ &= L_{dif}(\Gamma_{dif},\omega)\otimes[EISF\cdot\delta(\omega) + (1-EISF)\cdot L_{in}(\Gamma_{in},\omega)] \\ &= [EISF\cdot L_{dif}(\Gamma_{dif},\omega) + (1-EISF)\cdot L_{tot}(\Gamma_{tot},\omega)] \end{aligned}$$

$L(\Gamma,\omega)$ is a Lorentzian function. And $L_{tot}(\Gamma_{tot},\omega)$ represents the convolution of global diffusion and internal motions, where $L_{tot} = \Gamma_{dif} + \Gamma_{in}$. The scattering profile was adequately described by the above fitting function, as shown in Fig. 1.

Inset of Fig. 2 is the Half-Width at half-Maximum (HWHM = Γ_{dif}) of QENS from the global diffusion. The HWHM is proportional to Q^2, and the diffusion constants are obtained by the following equation:

$$\Gamma = DQ^2$$

The diffusion constant decreases as the glycerol concentration increases due to the viscosity.

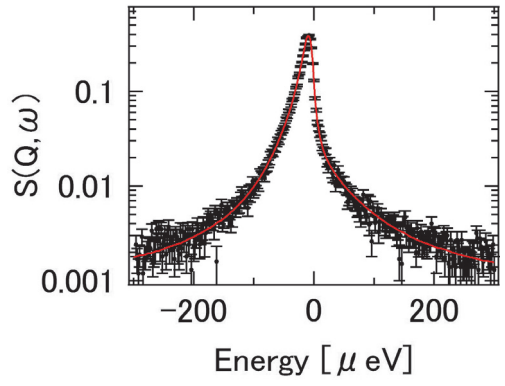

Figure 1. Quasi-elastic neutron scattering spectrum of lysozyme in D_2O solution at Q = 0.625 [Å^{-1}]. The red curve is the fitting curve of double Lorentzian.

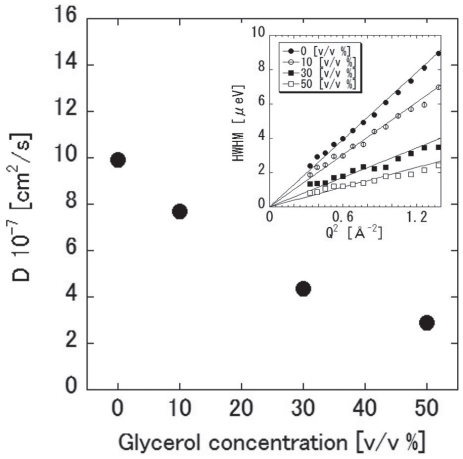

Figure 2. Protein diffusion constant as a function of glycerol concentration. The inset shows the HWHM (= Γ_{dif}) from protein global diffusion contribution.

Next, in order to examine the internal motions, EISF were analyzed. EISF data provide information on the conformational space geometries of protein dynamics. Here, we analyze the EISF with the continuous diffusion model within a restricted spherical volume (DSV). In DSV model, EISF is described as the following equation [2]:

$$EISF = p + (1-p)\cdot[3\cdot J_1(qr)/(qr)]^2$$

Here, $J_1(x)$ is the first-order Bessel function. The p accounts for the fraction of H atoms that do not undergo DSV motions on the measured time scale, and r is the radius of a hard-walled restricted sphere. Fig. 3a shows

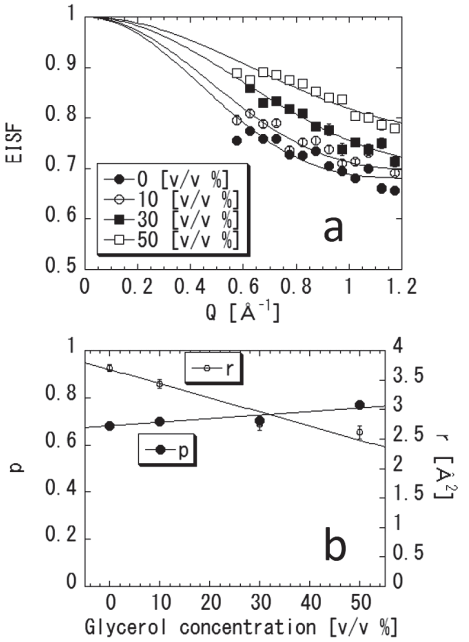

Figure 3. (a) EISF and fitting curves with the DSV model. (b) Immobile fraction *p* on the measured time scale, and the radius r of a hard-walled restricted sphere.

EISF and the fitting curves with the DSV model.

In Fig. 3b, p increases and r decreases as the glycerol concentration increases. These results indicate that the protein's internal motions are slowed down and the amplitude of the structural fluctuations is restricted by glycerol.

In conclusion, glycerol affects both the global diffusions and internal structural motions of protein, and reduces the protein dynamics in both time- and space-scale. This would lead to the reduction of enzymatic activity in the presence of glycerol. These effects of glycerol on bio-materials may be related to insects' resistance to low temperatures.

References

[1] C. Plolge *et al.*, Nature, 164 666 (1949).

[2] M. Bee, *Quasielastic Neutron Scattering: Principles and Applications in Solids State Chemistry, Biology and Materials Science* (Adam Hilger, Bristol, UK, 1988).

H. Nakagawa[1,2], K. Shibata[2], and T. Yamada[3]

[1]*Quentum Beam Science Center, Japan Atomic Energy Agency;* [2]*J-PARC Center, Japan Atomic Energy Agency;* [3]*CROSS-Tokai*

Neutron Crystallography Reveals Two Protonation States of PcyA, a Bilin Reductase

1. Introduction

Phycocyanobilin: ferredoxin oxidoreductase (PcyA), which is a major member of the ferredoxin-dependent bilin reductase (FDBR) family, catalyzes two steps of the two-proton-coupled two-electron reduction of biliverdin IXα (BV) to phycocyanobilin (PCB), one of the phytobilins [1]. Phytobilins, light harvesting and photoreceptor pigments in higher plants, algae and cyanobacteria, are synthesized from BV by FDBRs. PCB comprises the chromophore of algal phytochromes and the core phycobiliprotein antennae of cyanobacteria and red algae.

In the catalysis, PcyA strictly controls the regiospecificity and reaction sequence of the BV reduction; reduction of the BV D-ring exo-vinyl group to generate the reaction intermediate, 18^1,18^2-dihydrobiliverdin IXα (18EtBV) precedes the A-ring endo-vinyl reduction. Moreover, PcyA is unique not only because of its ability to catalyze the sequential reduction of two vinyl groups, but also because it is the only enzyme that catalyzes the BV D-ring reduction among FDBRs (Figure 1) [2].

Several unique features of PcyA catalysis have been revealed. First, the existence of two types of positively charged BV (BVH^+) states has been proposed when BV is bound to PcyA. One is an N-protonated structure in which four pyrrole N atoms of BV are fully protonated and the bis-lactam state is preserved [3]. The other is an O-protonated structure in which one or two lactim (C-OH) group(s) is (are) formed [4]. It has been also indicated that His88 and Asp105 are essential residues, both of which are located near the substrate BV and thought to be proton donors [5-8]. The side chain of Asp105 showed dual conformations in the structures of the PcyA-BV and PcyA-18EtBV complexes. It was proposed that a water molecule ("axial" water) in the active site, which was ejected upon one electron reduction, was essential for catalysis [4]. A proton-coupled electron transfer mechanism including the axial water molecule was proposed for its catalysis. However, this proposed mechanism has to be reassessed due to two issues. The first issue is that we could not identify the axial water molecule in the structure of the previous "cryo" wild-type PcyA-BV complex [6]. The second one is the uncertainty of the protonation states of the PcyA-BV complex. Knowing the protonation states of the substrate BV and of these essential residues is critical for understanding the catalytic mechanism of the PcyA reaction involving proton transfer.

It is difficult to determine the protonation state of the PcyA-BV complex. X-rays are known to generate electrons or harmful charged by-products when interacting with solvent molecules in protein crystals. The charged products might cause enzymatic and/or accidental side reactions and concomitant structural changes, thus resulting in incorrect structural information in studies of redox enzymes [9-11]. Furthermore, as some residues, including Asp105, have dual conformations in the PcyA-BV complex [6], the occupancies of hydrogens on such residues must be lower, making it much more difficult to determine their locations.

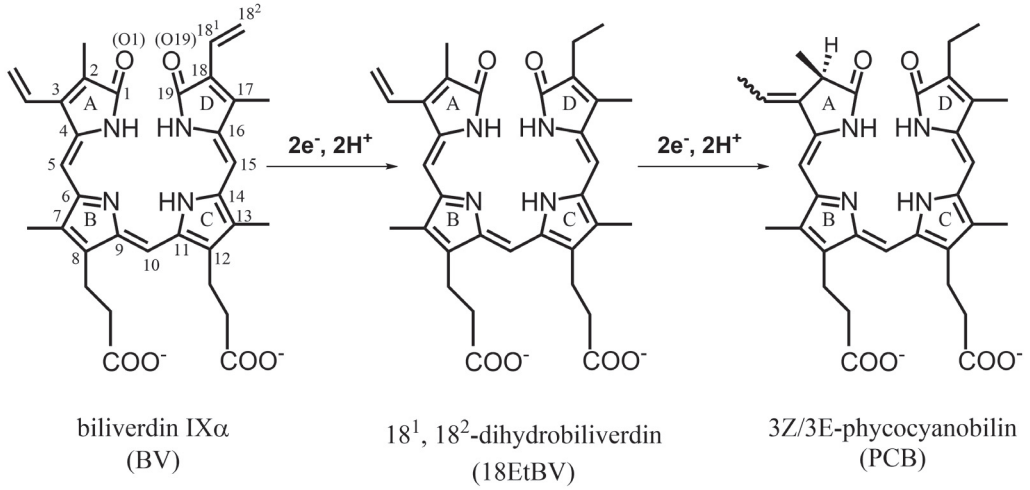

Figure 1. The PCB biosynthesis catalyzed by PcyA.

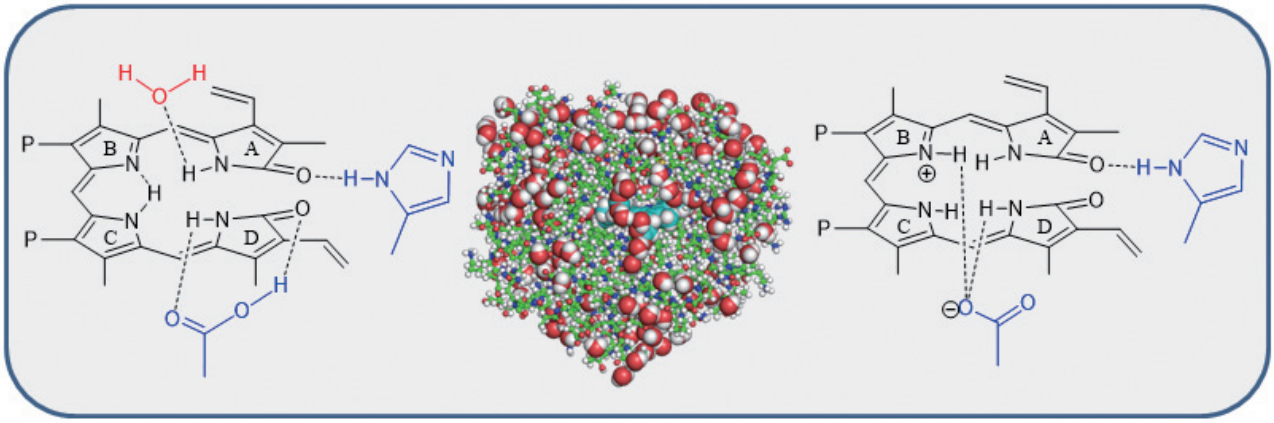

Figure 2. Chemical structures for two protonation states of the PcyA active site and BV (both sides) and the overall structure of the PcyA-BV complex (red; oxygen, green; carbon, blue; nitrogens).

To understand the unique reaction mechanism of PcyA, we used neutron crystallography to determine the structure of PcyA from *Synechocystis* sp. PCC 6803 complexed with BV, revealing the exact location of the hydrogen atoms involved in the catalytic reaction of PcyA [12].

2. Results and Discussions

This was the first study of the neutron structure of a FDBR family member that revealed the protonation state of BV and the surrounding residues. The resolution was 1.95 Å, and 1.50 Å resolution of the neutron and X-ray data, respectively [12]. Notably, approximately half of the BV bound to PcyA was BVH^+, a state in which all four pyrrole nitrogen atoms were protonated. The protonation states of BV (neutral BV and BVH^+) were in concert with the protonation of the adjacent Asp105, and two Asp105 conformations were involved in the catalytic activity of PcyA. Protonated Asp105 formed hydrogen bonds with both lactam oxygen and pyrrole nitrogen atoms in the D-pyrrole ring, whereas deprotonated Asp105 formed hydrogen bonds with the pyrrole nitrogen atoms of the B- and D-pyrrole rings (Figure 2). We also succeeded in identifying the "axial" water molecule that interacts with the neutral pyrrole nitrogen of the A-ring, which is believed to be essential for the A-ring reduction. The elucidated protonation states of the substrate BV and the surrounding residues determined by the present neutron crystallography imply that Asp105 and the axial water molecule are likely to contribute to the proton transfer in PcyA catalysis. Additionally, we found a hydronium ion between the essential His88 and the nearby His74. This hydronium ion is also likely to facilitate proton-transfer to the active site. This discovery of a hydronium ion in protein structure was the third such case worldwide [13, 14].

3. Acknowledgment

We thank the members of IBARAKI Biological Crystal Diffractometer in J-PARC for the neutron diffraction data collection. The neutron diffraction experiment was conducted under proposal 2012PX0011 (Ibaraki Prefecture Project). We thank Dr. Yusuke Yamada and the other members of the Structural Biology beamlines of PF and members of BL41XU of SPring-8 for X-ray diffraction data collection, including the preliminary experiments. The X-ray diffraction experiments in PF were conducted under proposals 2011G519 and 2013G504. Crystallization under microgravity was attempted in the "Kibo" project of the Japan Aerospace Exploration Agency (JAXA). We are grateful to Professor Takamitsu Kohzuma of Ibaraki University for his support and fruitful discussion regarding crystallization. We also thank Professor Masao Ikeda-Saito's laboratory at Tohoku University for use of the microspectrophotometer. This work was partly supported by JSPS KAKENHIs numbers 24570122, 22770096 (to M.U.) and 23370052 (to K.F., K.W., and M.U.).

References

[1] N. Frankenberg, J. C. Lagarias, *J. Biol. Chem.,* 278, 9219-9226 (2003).

[2] M. Unno, M. Sugishima, K. Wada, K. Fukuyama, Integrating Approach Photofunctional Hybrid Materials for Energy and the Environment, Akitsu, T. (ed), Nova Publishers, N.Y., 47-67 (2013).

[3] S. L. Tu, A. Gunn, M. D. Toney, R. D. Britt, J. C. Lagarias, J. Am. Chem. Soc. 126, 8682-8693 (2004).

[4] A. C. Kohler, D. D. Gae, M. A. Richley, S. Stoll, A. Gunn, S. Lim, S. S. Martin, T. I. Doukov, R. D. Britt, J. B. Ames, J. C. Lagarias, A. J. Fisher, A. J., Biochemistry, 49, 6206-6218 (2010).

[5] Y. Hagiwara, M. Sugishima, H. Khawn, H. Kinoshita, K. Inomata, L. Shang, J. C. Lagarias, Y. Takahashi, K. Fukuyama, *J. Biol. Chem.,* 285, 1000-1007 (2010).
[6] Y. Hagiwara, M. Sugishima, Y. Takahashi, K. Fukuyama, Proc. Natl. Ac. Sci. U.S.A., 103, 27-32 (2006).
[7] Y. Hagiwara, M. Sugishima, Y. Takahashi, K. Fukuyama, FEBS lett. 580, 3823-3828 (2006).
[8] S. L. Tu, W. Sughrue, R. D. Britt, J. C. Lagarias, *J. Biol. Chem.,* 281, 3127-3136 (2006).
[9] B. Chance, P. Angiolillo, E. K. Yang, L. Powers, FEBS lett. 112, 178-182 (1980).
[10] G. I. Berglund, G. H. Carlsson, A. T. Smith, H. Szoke, A. Henriksen, J. Hajdu, Nature 417, 463-468 (2002).
[11] J. Wuerges, J. W. Lee, Y. I. Yim, H. S. Yim, S. O. Kang, K. Djinovic Carugo, Proc. Natl. Ac. Sci. U. S. Am. 101, 8569-8574 (2004).
[12] M. Unno *et al.*, J. Am. Chem. Soc. 137, 5452-5460 (2015).
[13] M. G. Cuypers, S. A. Mason, M. P. Blakeley, E. P. Mitchell, M. Haertlein, V. T. Forsyth, Angew. Chem. Int. Ed. Engl. 52, 1022-1025 (2013).
[14] A. Y. Kovalevsky, B. L. Hanson, S. A. Mason, T. Yoshida, S. Z. Fisher, M. Mustyakimov, V. T. Forsyth, M. P. Blakeley, D. A. Keen, P. Langan, Angew. Chem. Int. Ed. Engl. 50, 7520-7523 (2011).

M. Unno[1,2], K. Ishikawa-Suto[1,2,3], K. Kusaka[2], T. Tamada[3], Y. Hagiwara[4], M. Sugishima[5], K. Wada[6], M. Ishihara[2], and K. Fukuyama[7]
[1]Graduate School of Science and Engineering, Ibaraki University; [2]Frontier Research Center for Applied Atomic Sciences, Ibaraki University; [3]Quantum Beam Science Center, Japan Atomic Energy Agency; [4]Department of Biochemistry and Applied Chemistry, Kurume National College of Technology; [5]Department of Medical Biochemistry, Kurume University School of Medicine; [6]Organization for Promotion of Tenure Track, University of Miyazaki; [7]Graduate School of Engineering, Osaka University

Phonon Anomaly in $La_{1.5}Sr_{0.5}NiO_4$

1. Introduction

$La_{2-x}Sr_xNiO_4$ is isostructural to one of the typical cuprate superconductors $La_{2-x}Sr_xCuO_4$. Similarly to the cuprates, one hole per Ni ion is introduced in the NiO_2 planes by the substitution of a La^{3+} ion with a Sr^{2+} ion. In the course of exploring the origin of the superconductivity in cuprates, the role of phonons has been extensively studied, and it was revealed that the hole doping induces a strong anomaly in the Cu-O bond stretching mode [1]. The phonon anomaly was seen as a result of the electron-lattice coupling associated with charge inhomogeneity in the CuO_2 planes [2]. In the nickelates, the electron-lattice coupling is considered to be larger than in the cuprates, as the charge inhomogeneity appears in the more obvious form of static charge stripes along the direction diagonal to the Ni square lattice. Then, phonons in the nickelates have been studied by inelastic neutron scattering (INS) to investigate whether the doped holes or charge stripes affect particularly the bond-stretching modes, which are the highest-energy longitudinal optical (LO) modes in this system. It was revealed that the LO modes are susceptible to the non-stoichiometry [3, 4] and hole-doping [5, 6], showing similar softening as in cuprates, but the anomalies in the phonons are independent of the charge stripe wave vector [6].

In the present study, we performed an INS study of the high-energy phonons in a single crystal of $La_{1.5}Sr_{0.5}NiO_4$ [7]. In this composition, the charge ordering results in a nearly checkerboard ordering of Ni^{2+} and Ni^{3+} sites: the checkerboard charge ordering with $\boldsymbol{q}_{CO}$ = (1/2, 1/2, 0) is formed below ~480 K, and is taken over by incommensurate charge order with $\boldsymbol{q}_{CO}$ ~ (0.44, 0.44, 0) below ~180 K.

2. Experimental details

Single crystals of $La_{1.5}Sr_{0.5}NiO_4$ were grown by the floating-zone method. Four crystal rods, each of which is ~5 mm in diameter and ~30 mm in length, were assembled for the present work. The crystal structure is tetragonal with the space group *I4/mmm*. The INS measurement was performed on the chopper spectrometer 4SEASONS. The incident energy was E_i = 111 meV with energy resolution of 10 meV at the elastic scattering condition. We aligned the crystals so that the [001] axis was parallel to the incident beam and the [110] axis was in the horizontal plane.

3. Results and discussion

Figure 1 shows the intensity maps at 5 K as functions of Q (momentum transfer) and $\hbar\omega$ (energy transfer) for several directions in the two-dimensional reciprocal lattice. Clear excitations by phonons were observed in the energy region between ~70 meV and ~90 meV, where the in-plane modes of phonons were observed in previous studies [1–6]. Figures 1(a) and 1(b) reflect scattering from the longitudinal optical (LO) modes along [100] and [110], while Figs. 1(c) and 2(d) reflect that from the transverse optical (TO) modes along [100] and [110], respectively. We also indicate the energies of phonons observed in La_2NiO_4 along the equivalent directions (circles) [3]. The energies of the LO modes in La_2NiO_4 show weak Q dependences both along [100] and [110] [Figs. 1(a) and 2(b)]. In contrast, the scattering spectra of $La_{1.5}Sr_{0.5}NiO_4$ show quite different dispersions from La_2NiO_4. There are large Q dependences with minimum energies of ~73 meV at H = 0.5 in both directions. On the other hand, for the TO modes in Figs. 1(c) and 1(d), the observed dispersions are almost similar to La_2NiO_4, though the energies are slightly higher. The hole doping and charge ordering do not affect the energies of the TO modes except for slight hardenings.

The observed anomalies in the LO modes as well as their minimum energies at ~73 meV are apparently similar to those observed in x = 0.31 [6]. The similarities support the idea proposed by Tranquada et al. for x = 0.31 [6] that the doped holes cause local effects on the bond-stretching phonons independent on the hole concentration. However, there is some difference between the two compounds. In x = 0.5, the dispersion of the LO mode along [110] shows a clear softening with its minimum at (0.5, 0.5) [Fig. 1(b)], while a splitting into two modes was observed in x = 0.31. The difference between the present x = 0.5 sample and x = 0.31 may be related to the difference in types of the charge ordering. In the case of the checkerboard charge ordering in x = 0.5, the holes enter every two Ni sites, and Ni^{2+} sites and Ni^{3+} sites always share the in-plane O ions. Therefore, the vibrations of the shared in-plane O ions may become more coherent along the direction of the charge-ordering wave vector, [110], resulting in the softening of the dispersion.

4. Summary

We performed an INS study on $La_{1.5}Sr_{0.5}NiO_4$ to investigate the effects of hole doping on the high-energy phonon modes. We found that the longitudinal modes

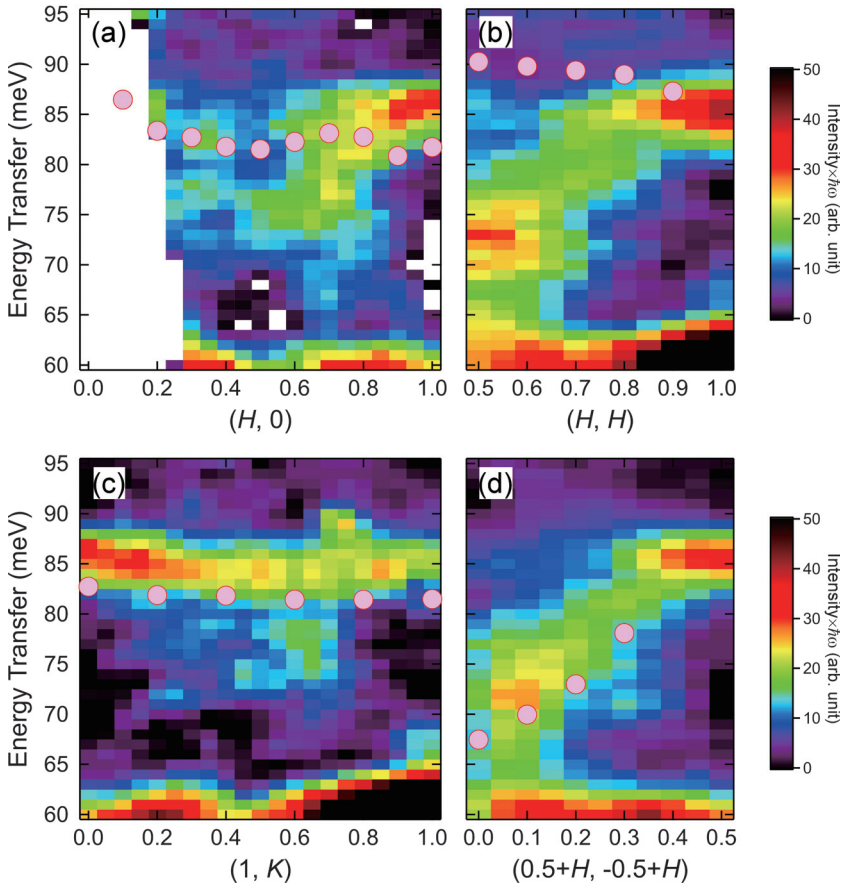

Figure 1. Intensity map of the high-energy excitations in $La_{1.5}Sr_{0.5}NiO_4$ at 5 K on the Q-$\hbar\omega$ planes. The intensity is multiplied by $\hbar\omega$ for clarity in a high $\hbar\omega$ region. The background of the intensity was estimated from the intensity in the region of $0.9 < H < 1.1$ and $-0.1 < K < 0.1$, and then was subtracted from the data [7].

show clearly different dispersions compared with La_2NiO_4. In particular, the longitudinal mode along the direction diagonal to the Ni square lattice shows a clear softening, in contrast to $x = 0.31$ where the mode shows a splitting [6]. We interpret the difference in the phonon anomalies between $x = 0.5$ and $x = 0.31$ as the difference in the type of charge ordering.

References

[1] D. Reznik, Advances in Condensed Matter Physics **2010**, 523549 (2010).

[2] D. Reznik, L. Pintschovius, M. Ito, S. Iikubo, M. Sato, H. Goka, M. Fujita, K. Yamada, G. D. Gu, and J. M. Tranquada, Nature **440**, 1170 (2006).

[3] L. Pintschovius, W. Reichardt, M. Braden, G. Dhalenne, and A. Revcolevschi, Phys. Rev. B **64**, 094510 (2001).

[4] L. Pintschovius, J. M. Bassat, P. Odier, F. Gervais, G. Chevrier, W. Reichardt, and F. Gompf, Phys. Rev. B **40**, 2229 (1989).

[5] R. J. McQueeney, J. L. Sarrao, and R. Osborn, Phys. Rev. B **60**, 80 (1998).

[6] J. M. Tranquada, K. Nakajima, M. Braden, L. Pintschovius, and R. J. McQueeney, Phys. Rev. Lett. **88**, 075505 (2002).

[7] R. Kajimoto, M. Fujita, K. Nakajima, K. Ikeuchi, Y. Inamura, M. Nakamura, and T. Imasato, J. Phys.: Conf. Ser. **502**, 012056 (2014).

R. Kajimoto[1], M. Fujita[2], K. Nakajima[1], K. Ikeuchi[3], Y. Inamura[1], M. Nakamura[1], and T. Imasato[4]

[1]Neutron Science Section, Materials and Life Science Division, J-PARC Center; [2]Institute for Materials Research, Tohoku University; [3]Neutron R&D Division, CROSS-Tokai; [4]Department of Physics, Tohoku University

Special Spin Density Distribution in *T'*-sturctured Cuprate Oxides Studied by μSR

1. Introduction

For the emergence of superconductivity in the electron-doped cuprate oxide, both substitution of cations such as Ce^{4+} at a rear-earth site and annealing procedure under the oxygen reduction condition are required [1]. Although magnetism is recognized to play a key role in the mechanism of superconductivity, the effects of Ce-doping and oxygenreduction on the spin correlation are not fully understood. In order to clarify these effects on magnetism, we studied the static spin correlations in as-sintered and annealed $Pr_{1.40-x}La_{0.60}Ce_xCuO_{4-y}$ (PLCCO) by means of the muon spin rotation/relaxation (μSR) technique. We confirmed the existence of two rotation components in both as-sintered and annealed $x = 0$ samples, while only a single rotation component remains in the as-sintered $x = 0.16$ sample. These results strongly suggest a distinct effect between annealing and Ce-doping on magnetism. From these observations and the numerical analysis of the internal magnetic field at muon stopping sites (See Fig. 1), we concluded that at low temperatures both Cu and Pr spins form order in the as-sintered and annealed $Pr_{1.40}La_{0.60}CuO_{4-y}$ through the Cu-Pr spin interaction, although the magnetic moment is reduced by annealing. In contrast, because of the suppression of Cu-Pr interaction by electrondoping, only the Cu spins on CuO_2 planes possess the magnetic transition in the highly electron-doped and as-sintered $Pr_{1.40}La_{0.60}CuO_{4-y}$ at a low temperature. These results are consistent with the previous neutron diffraction measurement [2], meaning that the numerical analysis works quite well for evaluation of magnetism and will be a powerful tool to determine the precise magnetism such as the spin density distribution. To further confirm the origin of the two components in the PLCCO and to expand our study based on the numerical analysis, we performed zero-field μSR measurement on the as-sintered Eu_2CuO_4 and the transversemagnetic- field μSR measurements on PLCCO ($x = 0$ and 0.16).

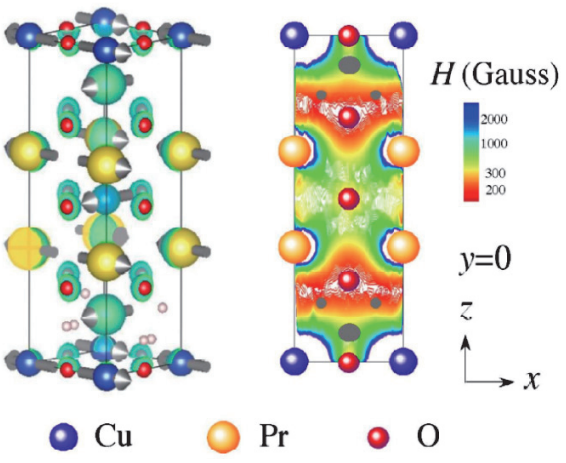

Figure 1. Magnetic structure of Pr_2CuO_4 (left) and the calculated internal magnetic field (right). The gray circles represent the possible muon stopping area evaluated from Hartree potential derived from density functional theory (DFT) calculation. The experimentally determined magnetic field is consistent with the calculated one for these positions.

2. Experiment

All powder samples were prepared by a conventional solid-state reaction method. We checked the phase purity by X-ray diffraction measurement. Zero-field μSR measurement was performed on the D1 instrument installed at the Materials and Life Science Experimental Facility (MLF) in J-PARC. For all samples, the temperature was lowered down to 12 K and a transverse magnetic field up to 1000 Oe was applied for PLCCO.

3. Results and discussion

Figure 2 shows the muon polarization rate along the field direction (P_z) as a function of the magnetic field (B_{ext}) for the as-sintered $x = 0$ and 0.16 samples, which was evaluated after the analysis of μSR time spectrum at each magnetic field. The result for $x = 0$ cannot be reproduced by a simple model with a single value for the magnetic field. This suggests the existence of plural muon stopping sites with different magnetic fields. In fact, the field dependence of P_z is well reproduced by taking the two values for the magnetic field into account. On the other hand, in the $x = 0.16$ sample, B_{ext}-dependence of P_z is reasonably fitted by a model with a single magnetic field at muon site(s). Figure 3 shows the amplitude of rotation frequency obtained from a Fourier transform of muon time spectrum, which corresponds to the density of state for the internal magnetic field. The field distribution in $Pr_{1.40}La_{0.60}CuO_4$ shows two well-defined peaks, while that in $Pr_{1.24}La_{0.60}Ce_{0.16}CuO_4$ has a broad single peak, consistent with the analysis of B_{ext}-dependence of P_z. Interestingly, the field distribution in the as-sintered Eu_2CuO_4 shows a sharp single peak, which is a stark contrast to the spectrum

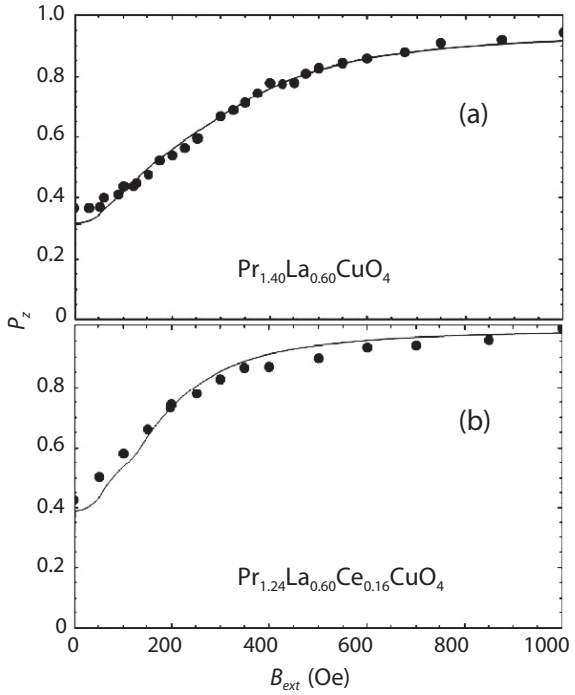

Figure 2. Field-dependence of muon polarization rate for the as-sintered (a) $Pr_{1.40}La_{0.60}CuO_4$ and (b) $Pr_{1.24}La_{0.60}Ce_{0.16}CuO_4$ samples.

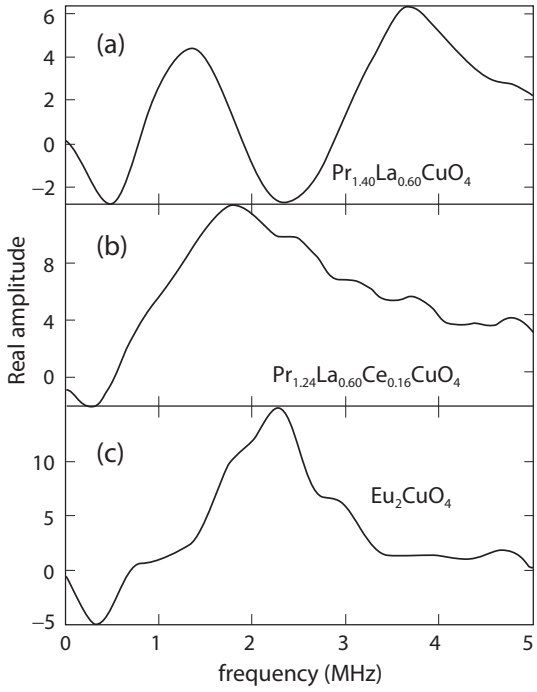

Figure 3. Real part of Fourier transform of muon time spectrum for the sintered (a) $Pr_{1.40}La_{0.60}CuO_4$, (b) $Pr_{1.24}La_{0.60}Ce_{0.16}CuO_4$ and (c) Eu_2CuO_4 measured at 12 K.

in $Pr_{1.40}La_{0.60}CuO_4$. The different field distribution in the two undoped compounds indicates that its origin is attributed to the size of the rare earth moment. Then, we calculated the internal magnetic fields at the two dominant muon stopping sites and confirmed that the comparable magnetic fields are indeed induced at the muon sites in the *T'*-structured cuprate with non-magnetic rear earth ion. With increasing the size of the rear earth moment, the difference in the magnetic field at the two muon sites increases substantially. The evaluated internal magnetic field from the magnetic structure shown in Fig. 1(a) with the ordered moment of 0.40 μ_B and 0.08 μ_B for Cu and Pr moments [2] can consistently reproduce both B_{ext}-dependence of P_z and the μSR time spectrum in the as-sintered $Pr_{1.40}La_{0.60}CuO_4$. This evaluation of the internal field at the muon sites further suggests the negligible contribution from the Pr moment in $Pr_{1.24}La_{0.60}Ce_{0.16}CuO_4$. Since the electron carrier is doped by Ce substitution, the mobile carriers degrade the magnetic interaction between Pr and Cu spins, possibly resulting into the paramagnetic fluctuation of the Pr moment.

So far, the magnetic properties are analyzed with the assumption that the spins are located on the atomic positions. However, the present result suggests that the combination between the precise μSR measurement and the numerical analysis based on the density functional theory (DFT) calculation potentially provide a new way to study the spin density distribution, which represents the hybridized orbitals, in a real compound. Although we could not carry out the measurement on annealed Eu_2CuO_4 and as-sintered $Eu_{2-x}Ce_xCuO_4$ within the limited beam-time, the observation of precise μSR time spectrum in these compounds without the effect from the rare earth moment could give conclusive information about annealing and Ce-doping effects on the intrinsic spin correlations on CuO_2 planes.

The DFT calculation was performed under the Large Scale Simulation Program No.14/15-13 (FY2014-2015) of High Energy Accelerator Research Organization (KEK).

References

[1] Y. Tokura *et al.*, Nature **337** (1989) 345-347, H. Takagi *et al.*, Phys. Rev. Lett. **62** (1989) 1197-1200.
[2] M. Matsuda *et al.*, Phys. Rev. B **42** (1990) 10098.

M. Fujita[1], K. Tsutsumi[2], K. Sato[2], M. Miyazaki[3], K. M. Kojima[3], and R. Kadono[3]
[1]Institute for Materials Research, Tohoku University; [2]Depertment of Physics, Tohoku University; [3]Muon Science Laboratory, High Energy Accelerator Research Organization (KEK)

Magnetic Model in Multiferroics $NdFe_3(BO_3)_4$ Investigated by Inelastic Neutron Scattering

1. Introduction

For over a decade, the coexistence of magnetic and dielectric orders, *multiferroics*, has attracted significant interest in the field of condensed matter physics. Rare-earth ferroborates $RFe_3(BO_3)_4$ (R = Y, and rare-earth metal) are a series of new multiferroic compounds containing R^{3+} ($4f^n$) and Fe^{3+} ($3d^5$ $S = 5/2$) as magnetic ions. They exhibit a diverse magnetoelectric (ME) effect as a function of the R^{3+} ions due to the variety of the magnetic anisotropy of the R^{3+} moments that are combined into Fe^{3+} framework through the interaction between the Fe^{3+} and R^{3+} moments (*f-d* coupling) [1]. Recent studies revealed that the mechanism of magnetoelecricity in these compounds was explained by the spin-dependence metal-ligand hybridization model [2,3].

We focus on $NdFe_3(BO_3)_4$, where the Nd^{3+} ions ($4f^3$) carry a magnetic moment with $J = 9/2$. Figure 1 shows the crystal structure with the trigonal symmetry $R32$. Studies in the heat capacity, magnetic susceptibility [4] and ME effect [1] revealed that an easy-plane type antiferromagnetic (AF) order and a spontaneous electric polarization simultaneously appear at $T_N = 30$ K and a huge electric polarization was induced by a magnetic field. A neutron diffraction study exhibited the collinear magnetic structure with propagation vector $k = (0, 0, 3/2)$ [5] as shown in Fig. 1.

In the present study, inelastic neutron scattering (INS) was performed to explore the magnetic excitations and to identify the magnetic model in $NdFe_3(BO_3)_4$. The identification of the magnetic model is essential to understand the mechanism of multiferroicity in $NdFe_3(BO_3)_4$.

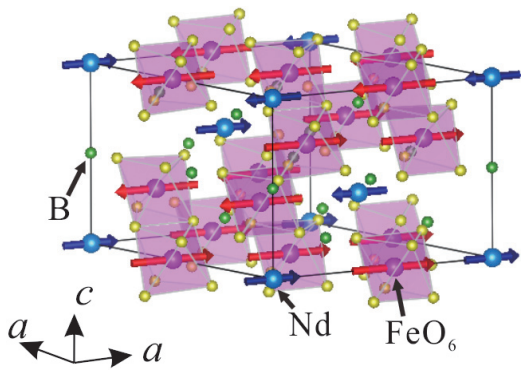

Figure 1. The crystal structure and magnetic structure of $NdFe_3(BO_3)_4$ (trigonal, space-group $R32$) [6]. Copyright 2015 by American Physical Society.

2. Experimental details

Single crystals of $NdFe_3(^{11}BO_3)_4$ were grown by a flux method. 22 pieces of the single crystals were coaligned so that the crystallographic a^*–c^* plane was horizontal. The alignment was performed by transmission Laue method using a high energy x-ray Laue camera. We placed the crystals on an aluminum holder.

The INS experiment was performed at the High Resolution Chopper Spectrometer (HRC) installed at MLF/J-PARC. We used a closed cycle cryostat to achieve $T = 15$ K. The energy of the incident neutron beam was $E_i = 11.46$ meV yielding an energy resolution of $\Delta E = 0.3$ meV at the elastic position. Initially we set an incident neutron beam with k_i // a^* at 15 K. In order to cover a wide q-range, INS spectra were collected by rotating the crystal by 70 degrees in 2-degree steps.

3. Experimental results

Figures 2(a) and 2(b) show the INS spectra at 15 K projected onto the $\hbar\omega$-(0, 0, l) and $\hbar\omega$-(h, 0, −1.5) planes, respectively. We clearly observed spin waves of the Fe^{3+} moments around $\boldsymbol{q}$ = (0, 0, −1.5) with an energy gap of 0.57 meV, indicating the existence of an in-plane magnetic anisotropy. In addition, we observed a flat excitation at 0.98 meV, which is the transition between the lifted states of Kramers doublet of the Nd^{3+} ion. The spin waves of the Fe^{3+} moments were more dispersive along the c^* direction than that along the a^* direction, meaning that the intrachain interaction along the c-axis was stronger than the interchain interaction. The peak energies, which were obtained by fitting using Gaussian functions, are plotted as open circles in Figs. 2(a) and 2(b). The white circles around $\boldsymbol{q}$ = (0, 0, −1.5) exhibit an anti-crossing between the spin wave of the Fe^{3+} moments and the flat mode of the Nd^{3+} moments, implying that the Fe^{3+} moments interact with the Nd^{3+} moments.

4. Analysis and discussion

In order to identify the magnetic model, we consider the following Hamiltonian [6]:

$$H = -\sum_{\text{n.n.}} J_1 \boldsymbol{S}_i \cdot \boldsymbol{S}_j - \sum_{\text{n.n.n.}} J_2 \boldsymbol{S}_i \cdot \boldsymbol{S}_j - \sum_{\text{n.n.}} J_3 \boldsymbol{S}_i \cdot \boldsymbol{S}_k + \sum_k H_{\text{CF}}(\boldsymbol{J}_k) \qquad (1)$$

where the x-axis is parallel to the crystallographic a-axis and the z-axis is parallel to the c-axis. J_1 and J_2 are the

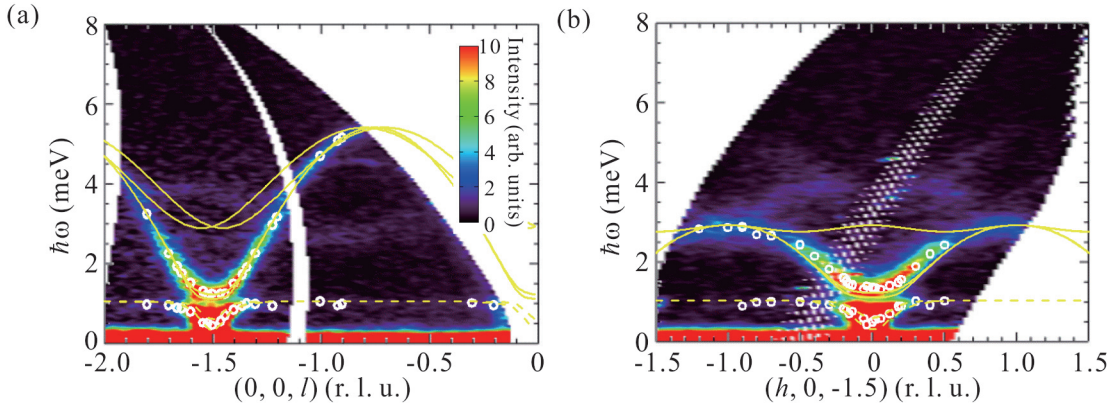

Figure 2. Color maps of the inelastic neutron scattering spectra obtained at HRC, along the (a) *l* and (b) *h* directions at 15 K. The open circles are the peak positions extracted Gaussian fits and the curves are the calculated spin wave dispersions. Fitting curves reasonably reproduce the experimental data [6]. Copyright 2015 by the American Physical Society.

exchange interactions in the nearest and 2nd neighbor paths of the Fe^{3+} ions. These terms mainly determine the dispersion along the *c**-axis and *a**-axis, respectively. J_3 is the nearest neighbor exchange interaction between the Fe^{3+} and Nd^{3+} moments, which induces the anti-crossing between the Fe^{3+} and Nd^{3+} modes. H_{CF} is the crystal field Hamiltonian of the Nd^{3+} ion, which leads to the anisotropy gap. We calculated the dispersions by a method described in Ref. [6]. The calculated dispersions are indicated by the solid curves in Figs. 2(a) and 2(b). The fit to the data provides excellent agreement with the overall spectrum.

In $NdFe_3(BO_3)_4$, the in-plane magnetic anisotropy plays a key role in the emergence of the multiferroicity [2]. Thus, we discussed the origin of the in-plane anisotropy in this system as far as the crystal symmetry is preserved. We considered possible magnetic anisotropies in the *ab*-plane of the Fe^{3+} moments, the magnetic-dipole interaction, single-ion anisotropy, and the polarization interaction. The discussion demonstrated that none of these anisotropies leads to the in-plane anisotropy. The direction of the Fe^{3+} moment, therefore, is determined by the anisotropy of the Nd^{3+} moment through the *f-d* coupling. It is interpreted from this discussion that the magnetic anisotropy of the Nd^{3+} moments by the crystal field drives the multiferroicity in $NdFe_3(BO_3)_4$.

5. Conclusion

INS measurements on the single crystals $NdFe_3(^{11}BO_3)_4$ were performed to explore the magnetic excitations. The obtained spectra were successfully analyzed by spin-wave calculation. We identified the magnetic model, where the Fe^{3+} moments form strongly coupled chains along the *c* direction and the chains are weakly coupled in the *ab*–plane, the Fe^{3+} and Nd^{3+} moments are strongly coupled, and the crystal electric field of the Nd^{3+} ion leads the anisotropy gap. The discussion of the origin of the in-plane magnetic anisotropy reveals that the crystal filed of the Nd^{3+} ion is a driving force in the induction of multiferroicity in $NdFe_3(^{11}BO_3)_4$.

References

[1] A. M. Kadomtseva *et al.*, Low Temp. Phys. **36**, 511 (2010).
[2] A. I. Popov *et al.*, Phys. Rev. B **87**, 024413 (2013).
[3] T. Kurumaji *et al.*, Phys. Rev. B **89**, 195126 (2014).
[4] N. Tristan *et al.*, J. Magn. Magn. Mater. **316**, 621 (2007).
[5] M. Janoschek *et al.*, Phys. Rev. B **81**, 094429 (2010).
[6] S. Hayashida *et al.*, Phys. Rev. B **92**, 054402 (2015).

S. Hayashida[1], M. Soda[1], S. Itoh[2], T. Yokoo[2], K. Ohgushi[3], D. Kawana[1], H. M. Rønnow[1,4], and T. Masuda[1]
[1]*The Institute for Solid State Physics, The University of Tokyo;* [2]*Neutron Science Section, Materials and Life Science Division, J-PARC center Institute of Materials Structure Science;* [3]*KEK, Department of Physics, Tohoku University;* [4]*Laboratory for Quantum Magnetism, École Polytechnique Fédéral Lausanne*

Crystal Field Excitations in Breathing Pyrochlore $Ba_3Yb_2Zn_5O_{11}$

1. Introduction

Geometrical frustration in magnetic materials disturbs the development of long-range order and induces novel states at low temperatures [1, 2]. A three-dimensional network of corner- sharing tetrahedra, i.e., the pyrochlore lattice, is one of the most interesting systems. The geometrical configuration prohibits the arrangement of the spins that satisfies the lowest energy of all spin bonds, leading to the ground state sensitive to perturbations including single-ion anisotropy, two-ion anisotropy, and lattice distortion. Indeed the variety of the magnetic phases have been reported in rare-earth pyrochlore compounds in $R_2Ti_2O_7$ [3]. In case of R = Dy and Ho spin- ice states emerge[4] due to the geometrical frustration induced by ferromagnetic interaction and the Ising anisotropy [5-8]. In contrast in $Yb_2Ti_2O_7$ the easy-plane type anisotropy of Yb ion enhances quantum effect, leading to quantum spin liquid state.

In a series of pyrochlore titanates $R_2Ti_2O_7$ rare earth ions carry magnetic moment. The J multiplets of the ions are lifted by crystalline electric field (CEF) from octahedral ligands with the point symmetry D_{3d}. In case of R = Dy, Ho, and Yb, the ground state is doublet and the first excited energies are larger than 20 meV [4], meaning that the degree of freedom of the magnetic moments are approximately two in the temperature range of T << 200 K. The magnetic moments are, thus, regarded as pseudospins S = 1/2 with anisotropies determined by the wave functions of the ground state. In most cases the localized orbitals of f-electrons give small magnetic interactions, and, therefore, insulating rare-earth mag- nets are regarded as interacting spin systems at low temperatures. Since the spin anisotropy is one of key features for the emerged magnetic state, experimental study on CEF is crucial particularly for the initial stage of the research on rare-earth magnets.

Breathing pyrochlore lattice, i.e., alternating arrays of corner-sharing large and small tetrahedra, is interesting in terms of realization of the perturbative expansion method in theoretical calculation [5]. The original model compounds were reported in 3d-transition metal spinels $LiInCr_4O_8$ and $LiGaCr_4O_8$ [6]. Recently rare-earth-based compound was found in $Ba_3Yb_2Zn_5O_{11}$ where Kramers ion Yb 3+ carries pseudospin S = 1/2 [7]. Fig. 1(a) shows the breathing pyrochlore network of Yb 3+ ions. Distances between Yb 3+ ions of small and large tetrahedra are 3.3 A and 6.2 A, respectively. The space group is *F-43m* with cubic symmetry. The local structure of YbO_6 is a distorted octahedron with the C_{3v} point group symmetry as shown in Fig. 1(b). No phase transition were observed in the specific heat and magnetic measurement in 0.4 K < T < 300 K. A temperature dependence of the magnetic susceptibility was reasonably reproduced using cubic symmetry for the CEF Hamiltonian down to 30 K, even though YbO_6 originally exhibited lower symmetry. This indicated that local distortion of aYbO_6 octahedron is small enough to be approximated as a structure with cubic symmetry. It has been reported that the ground state of CEF Hamiltonian was a Kramers doublet, and that the first excited state was a quartet state having an excitation energy of 45.1 meV [7]. Up to room temperature, the excitation energy was sufficiently high so that Yb^{3+} moment was regarded as an isotropic pseudospin S = 1/2. The bulk magnetic properties in the low temperatures were explained by the presumed isotropic Heisenberg S = 1/2 model having non- magnetic ground state. For the further understanding of the ground state, however, the information of the spin anisotropy is important and, therefore, the investigation on the CEF is indispensable. In the present study, we performed inelastic neutron (INS) scattering measurement to observe the CEF excitations.

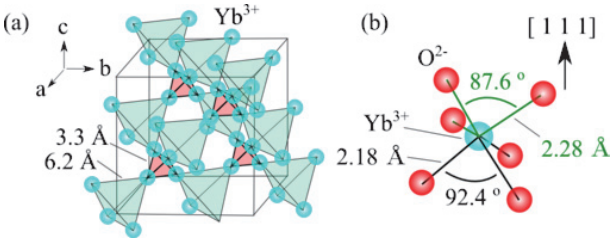

Figure 1. Crystal structure of $Ba_3Yb_2Zn_5O_{11}$. (a) Breathing pyrochlore network of Yb^{3+} ions. (b) Local structure of YbO_6, which has C_{3v} symmetry. The symmetry axis is [1 1 1].

2. Experimental details

The inelastic neutron scattering measurement (INS) was performed by using high resolution chopper spectrometer (HRC) installed in J-PARC/MLF. We used 17.7 g powder sample synthesized by a solid state reaction method. The sample was set in an Al-can filled with exchange He gas. Measurements were performed at T = 3, 200 and 300 K using an 4 He-type closed-cycle refrigerator. The T_0 chopper for the elimination of fast neutrons was set at 50 Hz. The initial neutrons were

monochromated by type "S" Fermi chopper with the frequency of 600 Hz to obtain the neutron energy of E_i = 154.4 meV with the instrumental resolution (full width at half maximum, FHWM) of 5.5 meV at the elastic position.

3. Results and discussion

Figure 2(a), (b), and (c) show contour maps of the INS spectrum at T = 3, 200, and 300 K, respectively. The arrows indicate three dispersionless excitations at 38.2, 55.0 and 68.3 meV. The intensities of these excitations decrease with the increase of *Q*, and they decrease with the increase of the temperature. None of the excitation-energy values changes in the observed temperature range. These behaviors are consistent with that of excitations of a magnetic cluster. At $\hbar\omega$ < 30 meV we observed broad excitation of which the intensity increases with the *Q*, and it increases with the temperature. The excitation is, thus, regarded as phonons. At $\hbar\omega$ = 100 meV flat stripe is observed in Fig. 2(a). Since no intensity was observed at 100 meV in preliminary measurement at MARI (not shown), the stripe is regarded as artifact. The intensities decrease with the increase of Q, and they follow the magnetic form factor of the Yb 3+ ion indicated by the solid curves [8]. These excitations, thus, derive from the CEF of the Yb^{3+} ion. Contour maps of INS spectra measured at at (a) T = 3, (b) T = 200, and (c) T = 300 K. The arrows indicate dispersionless excitations at $\hbar\omega$ = 38.2, 55.0 and 68.3 meV. ground state decreases with the increase of the temperature and the occupancy is one of coefficients in magnetic neutron cross section, all of the excitations derive from the transitions between the ground state and excited states. This means that the Yb^{3+} ion is the four-level system as described by solid bars in the first row in Fig. 3. The result is in contrast with the three level system assumed in the previous study [7] as described by dotted bars in the second row. The first excited energy of the present study is, however, close to that of previous one.

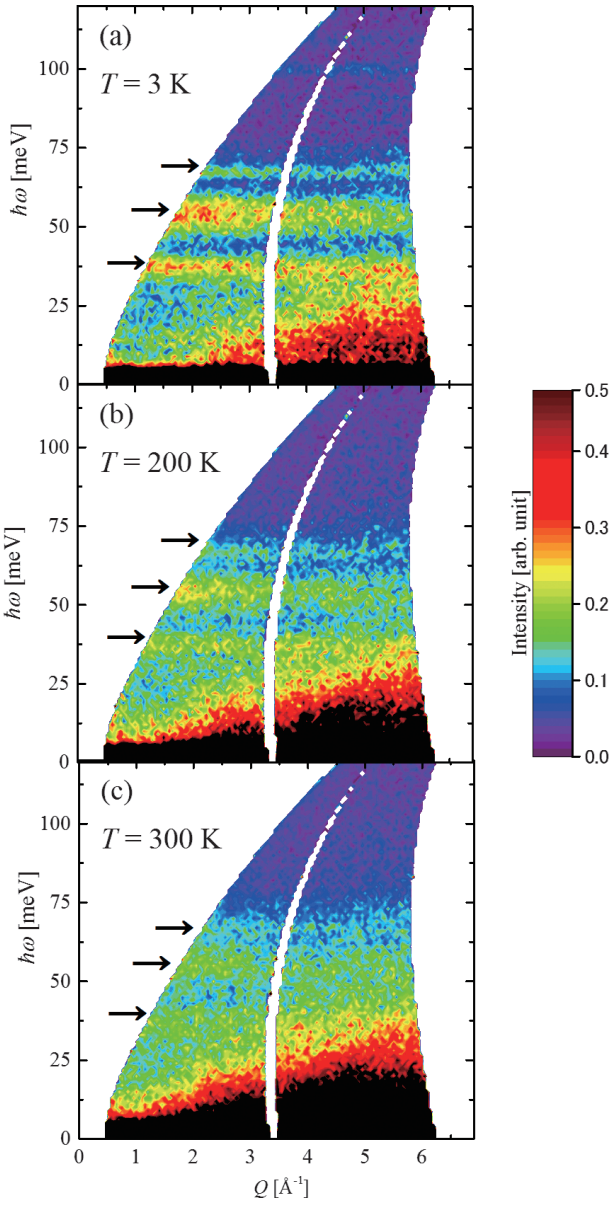

Figure 2. Contour maps of INS spectra measured at at (a) T = 3, (b) T = 200, and (c) T = 300 K. The arrows indicate dispersionless excitations at $\hbar\omega$ = 38.2, 55.0 and 68.3 meV.

4. CONCLUSION

We performed a neutron scattering experiment on a powder sample of $Ba_3Yb_2Zn_5O_{11}$ in order to identify the CEF Hamiltonian. The neutron spectrum was explained by four Kramers doublets of Yb^{3+} ion.

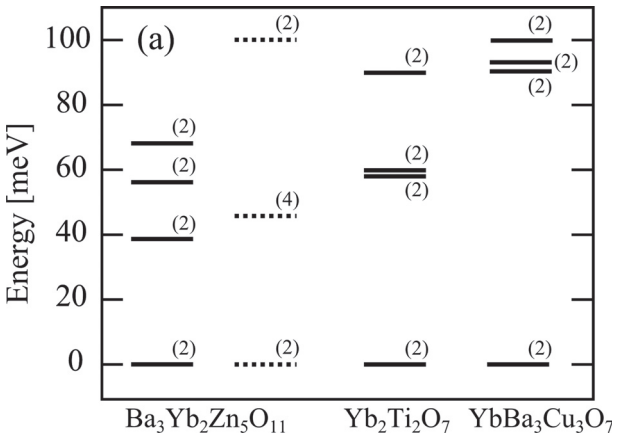

Figure 3. Energy diagrams of Yb^{3+} compounds, $Ba_3Yb_2Zn_5O_{11}$ 12), $Yb_2Ti_2O_7$ 4) and $YbBa_2Cu_3O_7$ 15). The solid and dotted lines indicate the levels obtained by neutron scattering studies and bulk measurement, respectively.

References

[1] A. P. Ramirez, Annu. Rev. Mater. Sci. **24**, 453 (1994).
[2] L. Balents, Nature **464**, 199 (2010).
[3] J. S. Gardner, M. J. P. Gingras, and J. E. Greedan, Rev. Mod. Phys. **82**, 53 (2010).
[4] A. Bertin, Y. Chapuis, P. D. Reothier, and A. Yaouane, J. Phys.: Condens. Matter **24**, 256003 (2012).
[5] H. Tsunetsugu, Phys. Rev. B **65**, 024415 (2001).
[6] Y. Okamoto, G. J. Nilsen, J. P. Attfield, and Z. Hiroi, Phys. Rev. Lett. **110**, 097203 (2012).
[7] K. Kimura, S. Nakatsuji, and T. Kimura, Phys. Rev. B **90**, 060414 (2014).
[8] P. J. Brown, International tables for crystallography (John Wiley and Sons, Inc, 2006) 1st online ed., Vol. C, p. 454.
[9] M. Guillaume, P. Allenspach, J. Mesot, *et al*., Solid State Commun.**81,** 999 (1992).

T. Haku[1], M. Soda[1], M. Sera[2], K. Kimura[2], S. Itoh[3], T. Yokoo[3], and T. Masuda[1]

[1]Institute for Solid State Physics, The University of Tokyo, Kashiwa, Chiba 277-8581, Japan; [2]Division of Materials Physics, Graduate School of Engineering Science, Osaka University, Toyonaka, Osaka, 560-8531, Japan; [3]Institute of Materials Structure Science, High Energy Accelerator Research Organization, Tsukuba, Ibaraki, 305-0801, Japan

Magnetic Excitations in the γ-FeMn Itinerant Electron Antiferromagnet

1. Introduction

There is a theoretical assumption that the magnetic excitations in itinerant electron magnets consist mainly of spin-wave excitation and Stoner excitation. The former is a collective excitation and the latter is a single-particle excitation. The spin-wave excitation localizes in the momentum $\boldsymbol{Q}$ space, and has dispersion relation between $\boldsymbol{Q}$ and the excitation energy $\hbar\omega$. On the other hand, the excitation spectrum of the Stoner excitation forms continuum. The dispersion curve of the spin-wave excitation enters into the continuum of Stoner excitation at a $\boldsymbol{Q}$ point, and is strongly damped by the coupling with the Stoner excitation. Inelastic neutron scattering is a powerful tool for exploring magnetic excitations, because it can observe the imaginary part of the dynamical magnetic susceptibility Imχ in $\boldsymbol{Q}$ and the $\hbar\omega$ space. In one of the itinerant electron ferromagnets, MnSi, the magnetic excitations, as described above, were observed experimentally by neutron scattering [1]. On the other hand, in itinerant electron antiferromagnets, a full picture of the magnetic excitations has yet to be revealed. One of the typical itinerant electron antiferromagnets is Cr metal. A recent calculation based on a multiband Hubbard model has predicted that the spin-wave excitation damps up to ~ 0.6 eV [2]. Experimentally, the magnetic excitations in Cr have been revealed only up to $\hbar\omega = 0.25$ eV [3], because it is difficult to measure excitations of sub-eV energy region. By the low-energy ($\hbar\omega < 0.1$ eV) excitation studies, it has been established to date that the spin-wave dispersion in itinerant electron antiferromagnets has steep and isotropic character. However, the spin-wave dispersion near the magnetic zone boundary is unknown, and it can be anisotropic like that in the Heisenberg spin system. In addition, it remains unclear whether the strong damping of the spin-wave excitation occurs. This limitation is due to the steep character of the spin-wave excitation. Therefore, we focused another typical itinerant electron antiferromagnet, γ-FeMn. The steepness of the spin-wave dispersion was determined to be moderate (160-250 meVÅ) [4] compared to that of Cr. Additionally, it was reported that the scattering intensity became weak at $\hbar\omega = 54$ meV [5], suggesting that the spin-wave damping may be observed at excitation energy lower than that of Cr. γ-FeMn has a face-centered cubic structure. The Fe ions, which are located at the face-centered position, have magnetic moments, and form non-coplanar magnetic structure under the transition temperature between 400 and 500 K [6]. In this study, we performed inelastic neutron scattering measurement in γ-FeMn.

2. Experiments

A single crystal of $Fe_{0.7}Mn_{0.3}$ was aligned in the *hkk* zone. The volume of the sample was about 5 cc. The sample was sealed in an aluminum can in He gas atmosphere. Inelastic neutron scattering experiments were performed at the High Resolution Chopper Spectrometer installed at BL12 beamline, J-PARC/MLF. The incident neutron energy E_i was selected as 33, 82 and 206 meV. The energy resolution at the elastic scattering position was 1.2, 4 and 15 meV, respectively. A closed cycle ^{4}He refrigerator was used to cool down the sample to temperature $T = 14$ K.

3. Results and discussion

The $\hbar\omega$ dependence of Imχ at a magnetic zone center $\boldsymbol{Q} = (0, -1, -1)$ measured with $E_i = 33$ meV is shown in Fig. 1. The energy gap of $E_g = 10.2(7)$ meV was confirmed, a result which was consistent with the previous report [4]. The $\hbar\omega$ dependence of Imχ monotonically increased, which was different from the Heisenberg spin system. The scattering intensity map along $[0, -k, k]$ and $[h, 0, 0]$ around at $\boldsymbol{Q} = (0, -1, -1)$ and $\hbar\omega = 75$ meV with $E_i = 206$ meV is shown in Fig. 2, indicating the isotropic nature of the magnetic excitation. The data analysis along [001], [011] and [111] directions revealed that the excitation was isotropic in all three directions. The measurement performed around at $\hbar\omega = 48$ meV with $E_i = 82$ meV indicated a similar result (not shown). Strong damping or

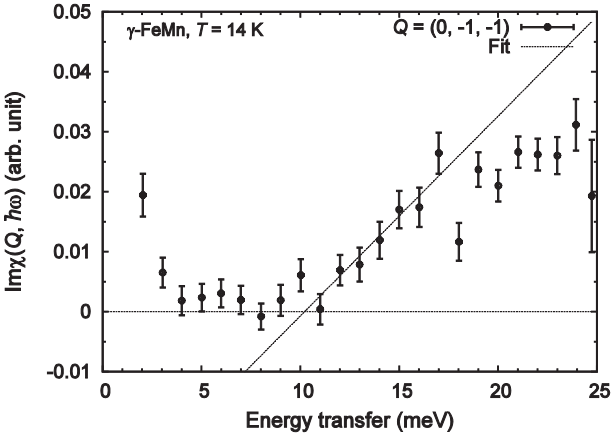

Figure 1. $\hbar\omega$ dependence of Imχ at $Q = (0, -1, -1)$.

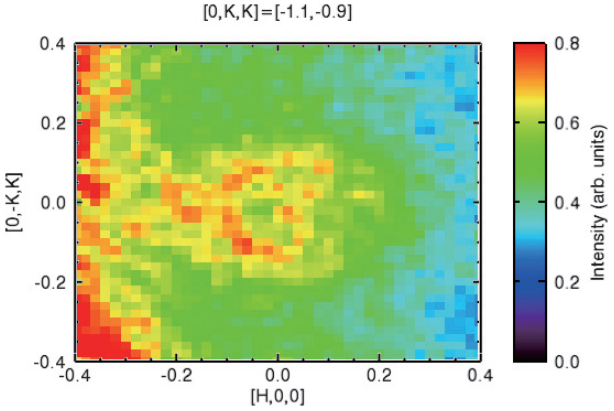

Figure 2. The scattering intensity map around at $Q = (0, -1, -1)$ and $\hbar\omega = 75$ meV.

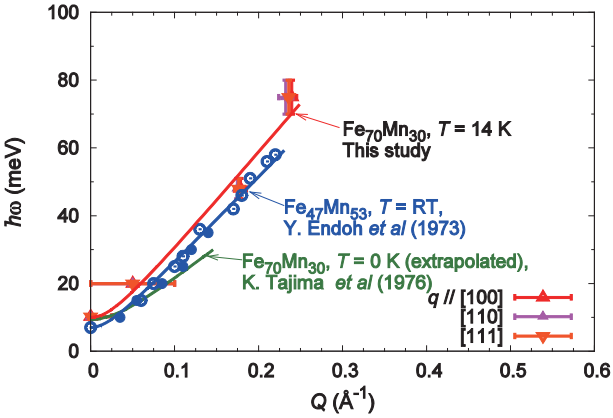

Figure 3. The spin-wave dispersion of γ-FeMn.

broadening of the dispersion curve was not found up to $\hbar\omega = 75$ meV. The spin-wave dispersion is summarized in Fig. 3. The dispersion was found to be steeper than the one previously reported [4], and similar to that of $Fe_{0.47}Mn_{0.53}$ [5]. The dispersion at $\hbar\omega = 75$ meV was $Q = 0.24$ Å^{-1}, which is still far from the zone boundary of about 0.9 Å^{-1}.

4. Summary

Magnetic excitations in γ-FeMn itinerant electron antiferromagnet were investigated by the neutron scattering technique. The spin-wave dispersion was isotropic and did not show strong damping up to $\hbar\omega = 75$ meV. To reveal a full picture of the magnetic excitations, measurements at a higher excitation energy are required.

References

[1] Y. Ishikawa, J. Appl. Phys. **49** (1978) 2125.
[2] K. Sugimoto, Z. Li, E. Kaneshita, K. Tsutsui and T. Tohyama, Phys. Rev. B **87** (2013) 134418.
[3] S. Itoh, H. Hiraka *et al*, KENS REPORT **19** (2012) 17.
[4] K. Tajima, Y. Ishikawa, Y. Endoh and Y. Noda, J. Phys. Soc. Jpn., **41** (1976) 1195.
[5] Y. Endoh, G. Shirane, Y. Ishikawa and K. Tajima, Solid State Comm. **13** (1973) 1179.
[6] Y. Endoh and Y. Ishikawa, J. Phys. Soc. Jpn. **30** (1971) 1614.

S. Ibuka[1,2], T. Yokoo[1,2], S. Itoh[1,2], and Y. Endoh[2,3]
[1]Neutron Science Section, Materials and Life Science Division, J-PARC Center; [2]Institute of Materials Structure Science, KEK; [3]Tohoku University

Anomalous Magnetic Response in the Overdoped Checkerboard Ordered Phase of Layered Nickel Oxides $Nd_{2-x}Sr_xNiO_4$

1. Introduction

The stripe-type charge spin ordering, which emerges in the layered transition-metal oxides resulting from carrier doping, has attracted wide attention because of its close relationship with the high-T_c superconductivity in $La_{2-x}Sr_xCuO_4$ [1]. In particular, it is of great importance to understand the spin dynamics of the layered transition-metal oxides through wide hole concentrations from an antiferromagnetic Mott-insulating region to a fully metallic overdoped region. In this regard, the layered nickel oxide $RE_{2-x}Sr_xNiO_4$ (RE: rare earth) is one of the most noteworthy systems, where the diagonal stripe ordering appears in a wide insulating hole concentration range (~1/3 ≤ x ≤ ~1/2), as observed in previous systematic neutron scattering studies [2, 3]. For nickel oxides, the stripe ordering is characterized by diagonally segregated hole stripes (Ni^{3+}: S = 1/2) separating the antiferromagnetic spin order (Ni^{2+}: S = 1) as a domain boundary (see Fig. 1(a)). Above x ~ 0.5, the doped holes are still highly correlated, and then they are alternately localized on the nickel sites at low temperatures and form a static checkerboard (CB)-type charge (spin) pattern, as shown in Fig. 1(b). Such CB-type charge spin ordering in $Nd_{2-x}Sr_xNiO_4$ persists up to the insulator-to-metal transition x ~ 1.0 [2, 3], although the electronic conductance gradually increases with hole doping [3, 4].

As already known, the magnetic excitation spectra in the Mott-insulating antiferromagnetic region (La_2NiO_4; x = 0) can be explained by the 2D linear spin wave (LSW) theory [5]. Similarly, the qualitative features of the spin dynamics in the stripe ordered region (x ~ 1/3) can also be well reproduced by the 2D LSW theory [6]. Meanwhile, Freeman et al. observed broad magnetic excitation spectra for the CB ordered x = 1/2 sample ($La_{3/2}Sr_{1/2}NiO_4$). Although they argued that the observed excitations can be approximately explained within the frame work of the LSW theory [7], the existence of any differences in the spin dynamics between the stripe and the overdoped CB ordered regions still remains questionable. When examining further the spin dynamics in the overdoped CB region, it becomes clear that a major bottleneck obstructs the growth of large single crystal samples of the $La_{2-x}Sr_xNiO_4$ system. As an alternative strategy, we focused on the Nd-based $Nd_{2-x}Sr_xNiO_4$ system and

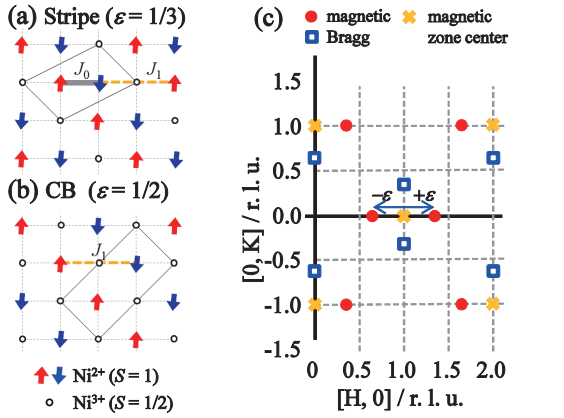

Figure 1. A schematic illustration of (a) stripe and (b) checkerboard type charge-spin ordering in the NiO_2 planes where the doped holes (open circles) enter into the Ni^{3+} sites. The arrows indicate the spins of S = 1 on the Ni^{2+} sites. The parallelogram in (a) and rectangle in (b) correspond to the superstructures of the stripe and CB ordering, respectively. (c) A diagram of the 2D reciprocal space showing the Bragg points for the stripe and CB spin ordering characterized by the incommensurability ε. The circles and squared symbols represent two equivalent sets of the Bragg points from orthogonal domains in the (H, K) plane. The cross symbols indicate the antiferromagnetic zone center.

carried out inelastic neutron scattering experiments on that system through a wide hole concentration range. The advantage of the Nd-based system is the possibility of growing a single-crystal for the overdoped region (x > 0.5). Furthermore, it is also convenient that magnetic properties derived from Ni spins are fully identical between the Nd- and La-based systems, as confirmed in our previous studies of the Nd-based system [2, 3, 8]. In this column, we report our recent observation of the anomalous spin response in the overdoped CB ordered phase.

2. Experimental Procedure

Single crystalline samples of $Nd_{2-x}Sr_xNiO_4$ (x = 0.33, 0.60, and 0.70) were grown by a floating zone method in a four-elliptical mirror furnace [8]. The mass of each single crystal samples of x = 0.33, 0.60 and 0.70 is 18.5, 53.1 and 17.2 g, respectively. These single crystal rods were coaligned within 0.5° by utilizing the high-energy transmission Laue instrument installed at ISSP. Inelastic neutron scattering experiments were performed with the

High Resolution Chopper spectrometer installed at BL12 in MLF of J-PARC in Tokai. The T0 chopper was used to reduce the background noise, which originates from high-energy neutrons emitted during neutron production. An incident collimation with 1.5° and an iron squared collimator with an aperture of 50*50 mm were used to improve incident beam collimation. The samples were enclosed in the standard Al cell with 4He gas and cooled below 10 K (2.5 K for x = 0.33) by utilizing the closed-cycle 4He refrigerator (PASCAL, Sumitomo). Following previous works, we denoted the reciprocal space by the orthorhombic notation (F4/mmm). In all measurements, the [001] direction was set parallel to the incident neutron beam (ki // c), and the measured neutron intensity was projected in the (h, k) plane as a function of the energy transfer.

3. Results and Discussion

Figures 2(a)-2(c) exhibit the constant energy slices of the stripe ordered x = 0.33 sample at various energy transfers. At lower energy transfers, reflected in panel 2(a), clear magnetic excitations were observed at around the magnetic Bragg points characterized by incommensurability ε ~ 0.36. As the energy transfer increases, the circle-like spectrum in Fig. 2(a) changes to a ring-shaped excitation spectrum, as seen in Figs. 2(b) and 2(c). The peak position of the observed excitations for the x = 0.33 sample was examined by fitting the data to the Gaussian function and the results are plotted in Fig. 3(a). Here, one can recognize that the magnetic excitation splits into two counterpropagating peaks above ~40 meV, indicating the existence of the clear "V-shaped" dispersion relation for the x = 0.33 sample. The energy of the magnetic zone boundary for the x = 0.33 sample is estimated to be about 80-100 meV. In Fig. 3(a), the calculated spin wave dispersion relation is also displayed by the solid and dashed lines using the same exchange parameters (J_0 = $2J_1$ = 14 meV: see also Fig. 1(a)) as those of the La-based x = 1/3 sample [6]. As seen in Fig. 3(a), these features of the excitation spectra in the Nd-based x = 0.33 sample are qualitatively identical to those of the La-based samples [6]. These results clearly indicate that the influence of the Nd ion on the spin wave excitations of the Ni spins is practically negligible. Consequently, these findings ensure that the study of the $Nd_{2-x}Sr_xNiO_4$ system yields results that are qualitatively identical with those obtained from the study of the La-based system.

Next we focused on the magnetic excitation spectra for the overdoped x = 0.60 sample in the CB ordered region. Figures 2(d)-2(f) show the constant energy slices of the Nd-based x = 0.60 sample at various energy transfers.

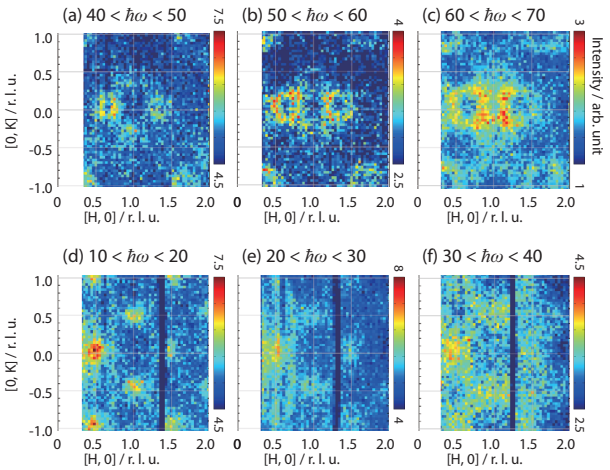

Figure 2. Constant energy contour plots of (a-c) the x = 0.33 sample (E_i ~ 165 meV, resolution ~ 15 meV, T ~ 2.5 K) in the stripe ordered region, and (d-f) the x = 0.60 sample (E_i ~ 124 meV, resolution ~ 10 meV, T < 10 K) in the CB ordered region.

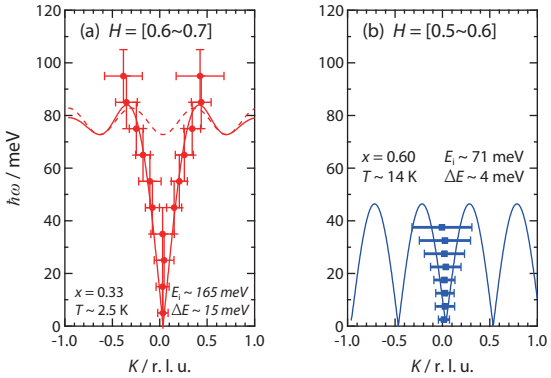

Figure 3. Dispersion relation of the observed magnetic excitation spectra for (a) the x = 0.33 sample (E_i ~ 165 meV, resolution ~ 15 meV) and for (b) the x = 0.60 sample (E_i ~ 71 meV, resolution ~ 4 meV). The solid and dashed lines in the panel (a) shows a calculation of the spin wave dispersion for the stripe-type spin order model with $J_0 = 2J_1 = 14$ meV. The solid line in the panel (b) is also a calculation for the CB-type spin order model with $J_1 = J_0/2$. The definition of the exchange constants is described in Fig. 1(a) for the stripe order and 1(b) for the CB order.

As seen in Fig. 2(d), clear spots were observed at around (H, K) = (0.44, 0) and its equivalent positions in the Q space, suggesting that the CB-type charge-spin ordering in the x = 0.60 sample. When the energy transfer increased, the observed magnetic excitations became broader in the Q space in the energy range of Fig. 2(e), and began to overlap at higher energy transfers, as shown in Fig. 2(f). Above 60 meV, no significant magnetic excitations were observed in the x = 0.60 sample. Note that qualitatively similar magnetic excitations were observed for the further overdoped x = 0.70 sample. The peak position of the

observed excitations for the x = 0.60 sample is shown in Fig. 3(b). In marked contrast to the well-defined dispersing excitation spectra observed in the x = 0.33 sample, the magnetic excitations of the x = 0.60 sample are broader than those of the x = 0.33 sample, and they remain centered at the magnetic Bragg point up to the energy of the magnetic zone boundary (J ~ 40-60 meV). Namely, no significant split of the magnetic excitation spectra was observed for the CB-ordered samples within the experimental resolution. We could summarize several marked features in the observed magnetic excitations in the CB-ordered region as follows: (i) the energy scale of the magnetic zone boundary (J ~ 40-60 meV) is roughly half of that of the stripe ordered region, (ii) there is no significant split (dispersion relation) of the magnetic excitation in the CB region, (iii) features (i) and (ii) are qualitatively unchanged in the CB region, at least up to x = 0.70.

As for feature (i), we consider that such a reduction of the energy scale can be attributed to the lack of J_0 in the CB region, as shown in Fig. 1(b). For feature (ii), the origin still remains to be determined. To clarify the unusual feature of (ii) in the magnetic excitation spectra in the CB region, further experimental and theoretical studies would be indispensable. In order to reveal the origin of feature (iii), we should refer to a pioneering investigation of the orbital state of the Ni ions [4]: here, Uchida et al. suggested that the doped holes first enter into $d(x^2–y^2)$ orbital for $x < 0.5$ and subsequently into $d(3z^2–r^2)$ for $x > 0.5$. Furthermore, they indicated that the site occupancy of $d(x^2–y^2)$ is kept at 50% for the CB region up to x ~ 1.0. In Fig. 4, we visualized a possible structural model of the arrangement pattern of the orbitals for the stripe and overdoped CB-ordered regions [10] on the basis of Uchida's results [4] and previous neutron scattering experiments [2, 3, 9]. This structural model can explain the robustness of the CB-type pattern and the independence of several features in the observed magnetic excitations from the hole concentration above $x > 0.5$. We believe that the orbital degrees of freedom of the Ni ions and their arrangement pattern would be crucial to understanding the observed unusual magnetic excitations in the overdoped CB regions in the layered nickel oxides.

4. Concluding Remarks

We investigated the magnetic excitations of the stripe ordered and the overdoped CB-ordered layered nickel oxide $Nd_{2-x}Sr_xNiO_4$. The magnetic excitations of the stripe ordered x = 0.33 sample can be described by the LSW theory and they are qualitatively identical to those of $La_{5/3}Sr_{1/3}NiO_4$. In marked contrast to the clear spin wave excitations in the stripe ordered sample, the CB-ordered sample shows unusually non-dispersive broad magnetic excitation spectra. No significant hole concentration dependence in the features of the magnetic excitation spectra was observed in the CB-ordered region. We investigated the origin of the robustness of the CB order above $x > 0.5$ by taking into account the orbital degrees of freedom of the Ni ions. These experimental results appeared in the Journal of the Physical Society of Japan [10].

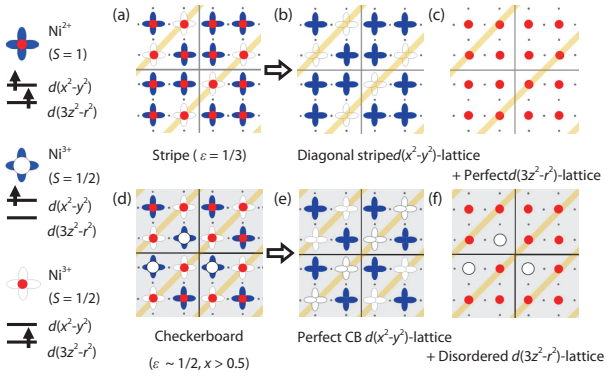

Figure 4. (Cited from ref. [10]) A simplified structural model of (a-c) the x = 1/3 stripe and (d-f) the overdoped CB order in the layered nickel oxides. Orbital and spin degrees of freedom of the Ni ions are illustrated in the left side of the figure, here, $d(x^2-y^2)$ and $d(3z^2-r^2)$ orbitals are individually drown in (b, e) and (c, f), respectively.

References

[1] J. M. Tranquada *et al.*, Nature 375, 561 (1995).
[2] H. Yoshizawa *et al.*, Phys. Rev. B 61, R854 (2000).
[3] K. Ishizaka *et al.*, Phys. Rev. B 67, 184418 (2003).
[4] M. Uchida *et al.*, Phys. Rev. B 86, 165126 (2012).
[5] S. Itoh *et al.*, J. Phys. Soc. Jpn. 63, 4542 (1994), and references therein.
[6] A. T. Boothroyd *et al.*, Phys. Rev. B 67, 100407(R) (2003); H. Woo *et al.*, Phys. Rev. B 72, 064437 (2005).
[7] P. G. Freeman *et al.*, Phys. Rev. B 71, 174412 (2005).
[8] Y. Ikeda *et al.*, J. Phys. Soc. Jpn. 84, 023706 (2015).
[9] R. Kobayashi *et al.*, J. Phys. Soc. Jpn. 84, 064711 (2015).
[10] Y. Ikeda *et al.*, J. Phys. Soc. Jpn. 85, 023701 (2016).

Y. Ikeda[1], S. Suzuki[1], T. Nakabayashi[1], H. Yoshizawa[1], T. Yokoo[2], and S. Itoh[2]
[1]Neutron Science Laboratory, Institute for Solid State Physics, The University of Tokyo; [2]Neutron Science Division, Institute of Materials Structure Science, High Energy Accelerator Research Organization, KEK

Nd-Substitution Effect on Metal–Nonmetal Transition in $PrRu_4P_{12}$

1. Introduction

The metal–nonmetal transition at $T_{M\text{-}I}$ = 63 K of $PrRu_4P_{12}$ has been studied extensively [1]. The nonmetallic phase below $T_{M\text{-}I}$ is characterized by the wave vector $\boldsymbol{q}_0$ = (1, 0, 0), which indicates the structural transition from body-centered cubic to simple cubic [2]. Inelastic neutron scattering (INS) studies have proven that the nonmetallic phase is associated also with the $\boldsymbol{q}_0$ alignment of two inequivalent crystal-field (CF) level schemes of the Pr-ion $4f^2$ state: a singlet at Pr1 and a triplet at Pr2 at the lowest temperature [3]. This phase transition was interpreted as charge-density-wave (CDW) formation, which is accompanied by the antiferro-type ordering of an *f*-electron totally symmetric multipole [4, 5]. It is worth noting that a reentrant-type phase transition is induced by substituting Ce to Pr [6]. The ordered state appears once at $T_{M\text{-}I} \sim 45$ K, and disappears below approximately 10 K. The atomic substitution, which corresponds to carrier doping, destabilizes the multipole-ordered nonmetallic phase [7]. On the other hand, the triplet state at Pr2 in the nonmetallic ordered phase is considered controversial because of its finite entropy owing to the degeneracy. This fact raises the question of magnetic perturbation's influence on the ordered state.

In order to investigate the magnetic-impurity effect on the order of $PrRu_4P_{12}$, we studied the CF scheme and the superlattice of $Pr_{1-x}Nd_xRu_4P_{12}$. The result is to be published elsewhere [8].

2. Experimental Procedure

Samples of $Pr_{1-x}R_xRu_4P_{12}$ (R = La, Ce, and Nd) were synthesized by the Sn-flux method. We measured the CF level schemes by using the high-resolution chopper neutron spectrometer HRC at BL12, MLF. X-ray diffraction was performed on a four-circle diffractometer at Tohoku University.

3. Results

We measured temperature dependences of the X-ray superlattice reflection intensities of $Pr_{1-x}Nd_xRu_4P_{12}$ with x = 0.05, 0.15, and 0.20. Figure 1 shows the data for x = 0.15, in which the superlattice peak at (9, 6, 0) emerges at low temperature. The $T_{M\text{-}I}$ of x = 0.05, 0.15, and 0.20 are determined to be 61.5, 58.0, and 57.1 K, respectively. It is worth noting that $T_{M\text{-}I}$ of the Nd-substituted material with x = 0.20 is higher than 52.6 and 36.0 K of $Pr_{0.8}La_{0.2}Ru_4P_{12}$ and $Pr_{0.8}Ce_{0.2}Ru_4P_{12}$, respectively [6, 7].

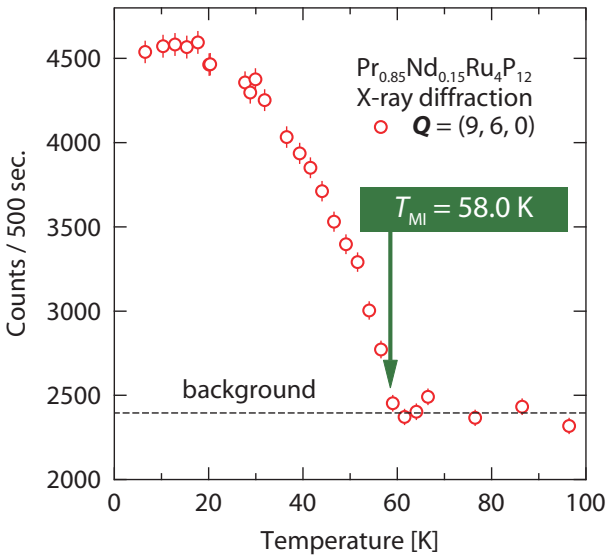

Figure 1. Temperature dependence of X-ray superlattice peak intensity of $Pr_{0.85}Nd_{0.15}Ru_4P_{12}$ [8].

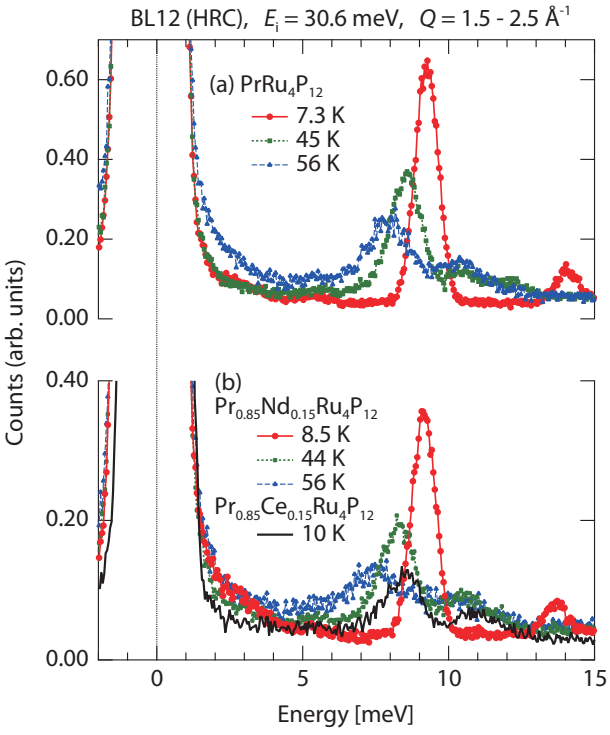

Figure 2. Temperature dependences of INS spectra of (a) the pure system $PrRu_4P_{12}$ and (b) $Pr_{1-x}R_xRu_4P_{12}$ (R = Ce and Nd) [8].

Figure 2 shows the INS spectra of (a) $PrRu_4P_{12}$ at 7.3, 45, 56 K, (b) $Pr_{0.85}Nd_{0.15}Ru_4P_{12}$ at 8.4, 44, 56 K, together with $Pr_{0.85}Ce_{0.15}Ru_4P_{12}$ at 10 K. The spectra in the whole temperature range below $T_{M\text{-}I}$ are almost identical between $PrRu_4P_{12}$ and $Pr_{0.85}Nd_{0.15}Ru_4P_{12}$. Therefore, the multipole order parameter at the Pr-ion sites is robust against the Nd-ion substitution. On the other hand, the lower-temperature spectrum of $Pr_{0.85}Ce_{0.15}Ru_4P_{12}$ is much broader than the pure and Nd-substituted compounds. This experimental result indicates that carriers do not vanish because of the imperfect Fermi-surface nesting caused by the carrier doping effect.

4. Discussion

$NdRu_4P_{12}$ undergoes a ferromagnetic transition at 1.6 K with an ordered magnetic moment of 1.8 μ_B/Nd [8]. This supports the hypothesis that magnetic moments are introduced into $PrRu_4P_{12}$ by the Nd substitution. The present INS result indicates that the ordered state is not destroyed by the introduced Nd-ion magnetic moments. On the contrary, the Nd substitution seems to assist the multipole ordering because the reduction in $T_{M\text{-}I}$ is less than that of the La-substituted system: $T_{M\text{-}I}$ = 52.6 K for La 20%. It is indicative that a site-dilution effect on the ordered state is overcome by the Nd substitution. A magnetic interaction between Nd and Pr is expected to stabilize the Pr2 triplet ground state, which should be located at the neighbors of the introduced Nd ion. Because the CF ground state of the Nd ions in $NdRu_4P_{12}$ is a quartet, multipole degrees of freedom of Nd ion may also contribute to the stabilization of the Pr2 triplet. Therefore, we conclude that the multipole-ordered CDW state is compatible with the magnetic impurity.

The findings raise another question concerning the *f*-electron state: how the robust multipole ordered phase in the lower Nd-concentration region crosses over or transforms into the ferromagnetic ordered state of the pure $NdRu_4P_{12}$. We are continuing the investigation of the series of $Pr_{1-x}Nd_xRu_4P_{12}$ in a wide range of *x*.

References

[1] C. Sekine, T. Uchiumi, I. Shirotani, and T. Yagi, Phys. Rev. Lett. 79, 3218 (1997).

[2] C. H. Lee, H. Matsuhata, H. Yamaguchi, C. Sekine, K. Kihou, T. Suzuki, T. Noro, and I. Shirotani, Phys. Rev. B 70, 153105 (2004).

[3] K. Iwasa, L. Hao, K. Kuwahara, M. Kohgi, S. R. Saha, H. Sugawara, Y. Aoki, H. Sato, T. Tayama, and T. Sakakibara, Phys. Rev. B 72, 024414 (2005).

[4] Y. Kuramoto, J. Otsuki, A. Kiss, and H. Kusunose, Proc. Theo. Phys. Suppl. 160, 134 (2005).

[5] T. Takimoto, J. Phys. Soc. Jpn. 75, 034714 (2006).

[6] C. Sekine, M. Takusari, and T. Yagi, J. Phys. Soc. Jpn. 80, SA024 (2011).

[7] K. Saito, C. Laulhé, T. Sato, L. Hao, J.-M. Mignot, and K. Iwasa, Phys Rev B 89, 075131 (2014).

[8] K. Iwasa, A. Yonemoto, S. Takagi, S. Itoh, T. Yokoo, S. Ibuka, C. Sekine, and H. Sugawara, accepted by Physics Procedia.

K. Iwasa[1], A. Yonemoto[1], S. Takagi[1], S. Itoh[2], T. Yokoo[2], S. Ibuka[2], C. Sekine[3], and H. Sugawara[4]

[1]Department of Physics, Tohoku University; [2]Condensed Matter Research Center and Neutron Science Division, Institute of Materials Structure Science, KEK; [3]Department of Electrical and Electronic Engineering, Muroran Institute of Technology; [4]Department of Physics, Kobe University

Spin and Hole Dynamics in Carrier Doped Quantum Haldane Chain

1. Introduction

In a low-dimensional system, the quantum nature of spins appears in macroscopic phenomena. A Haldane gap is one of those unconventional properties of the one-dimensional (1D) integer spin systems in which a spin gap exists between the ground state and the first excited state [1, 2]. Inorganic nickelate Y_2BaNiO_5 was found to be a good candidate for a Haldane system with a spin gap of 10 meV at the magnetic zone center (MZC) [3, 4]. In R_2BaNiO_5 (R = Nd, Pr), the observed excitation energy is quite similar to the Haldane gap in Y_2BaNiO_5 and shows a structure factor reflecting a 1D Ni chain correlation even though it displays 3D antiferromagnetic order at low temperature [5-9]. Thus, it was found that Nd_2BaNiO_5 was not a simple Haldane system.

Another topic of interest regarding the transition metal chain oxides is carrier doping, which yields phenomena ranging from strongly renormalized Fermi liquid behavior to high-temperature superconductivity. In view of the enhanced quantum fluctuations in 1D systems, doping of transition metal chains could well lead to equally surprising discoveries. R_2BaNiO_5 is a charge-transfer insulator [10, 11], and some quantity of hole carriers has been successfully introduced primarily into oxygen sites by replacing part of the off-chain R^{3+} with Ca^{2+} [4]. The spin dynamics of the hole-doped Ni 1D chains have also been addressed using a theoretical approach [12, 13] and through neutron experiments [14, 15].

In this article, we present the spin and hole dynamics of hole-doped Nd_2BaNiO_5 measured by means of a pulsed neutron scattering technique to survey the entire area of the Brillouin zone in momentum and energy space.

2. Experimental

The carrier content can be controlled by replacing a portion of the Nd^{3+} ions with Ca^{2+}. Lightly doped (x = 0.1) $Nd_{2-x}Ca_xBaNiO_5$ was chosen for the neutron experiments. T_N was evaluated as 30 K. Two cylindrical single crystals with a total mass of 13 g were assembled in an aluminum can. Three pieces of specimens with dimensions of 5 mm in diameter, and 31 to 35 mm in length were co-aligned. A closed-cycle refrigerator was used to cool the sample down to low enough temperature. Inelastic neutron scattering experiments were conducted at the High-Resolution Chopper spectrometer (HRC) installed at the Materials and Life Science Experimental Facility in J-PARC [16, 17]. The measurement temperatures were 4, 20, 30, 40, and 150 K, which are above and below T_N. Incident neutron energy Ei of 102.0 meV was chosen to measure a wide Q-E space.

3. Results

In the neutron scattering experiment, the [H 0 L] zone was into the horizontal scattering plane, where H corresponds to the chain direction (crystallographic a-axis). Figure 1 shows the obtained dynamical structures S(Q,E) at T = 4.0 K (well below T_N = 30 K) and T = 40 K (above T_N). Both spectra are normalized by the measurement time. Intense crystal electric field (CEF) excitations of Nd^{3+} ions lie at E = 24 and 38 meV. The site symmetry of Nd^{3+} in Nd_2BaNiO_5 is sufficiently low to split the tenfold degenerate J = 9/2 multiplet into five Kramers doublets. In addition to the CEF excitations, excellent dispersion relations for the Ni 1D chain are observed at both temperatures for the entire first and second Brillouin zones. The minima of the dispersion observed at the MZC, H = 0.5, 1.5, and even 2.5, occur where the magnetic scattering intensity becomes weak because of the magnetic form factor, and the phonon scattering is dominant in this high-Q region. On the other hand, at H = 1.0 and 2.0, the weight of the magnon dispersion is known to be zero at the zone boundary. At low temperature [Fig. 1(a)], the magnon bandwidth reaches 60 meV, with somewhat large gap energy of $\Delta = 20$ meV, compared to the bare (unperturbed) 1D Haldane gap. In addition, a flat band lying at E = 65 meV and corresponding to a phonon or magnon optical branch was observed.

At T = 40 K, the Haldane gap is lowered, and the spectral weight is slightly shifted with respect to the MZC. The boundary energy is almost the same at both temperatures.

To survey the spectra near the gap, constant-Q cuts are shown in Fig. 2 for both temperatures. Because the transfer energy in Figs. 1 and 2 is strongly related to the wave vector parallel to the incoming neutron beam ki (crystallographic c-axis in our experiment), the 1D spectra are also a function of L. However, in the 1D system, only the chain direction can be varied,

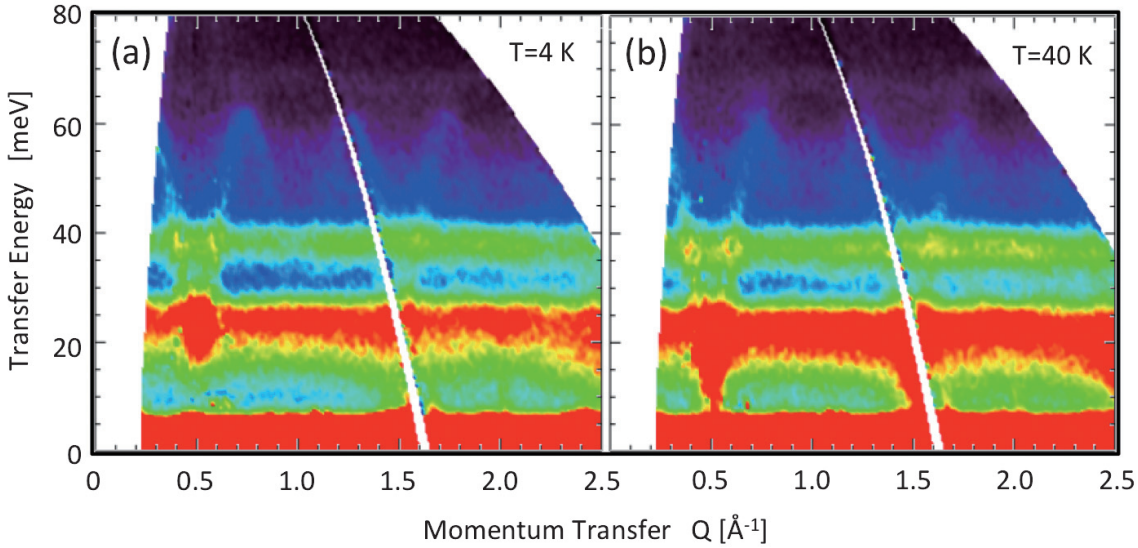

Figure 1. Observed dispersion relation of x = 0.1 at (a) T = 4.0 K (< T_N) and (b) T = 40 K (> T_N). Flat bands at E = 24 and 38 meV are contributions from crystal field excitation of Nd^{3+} ions. Oscillating signals showing minima at magnetic zone center (H = 0.5 and 1.5) are from 1D chain. (from Ref. [18])

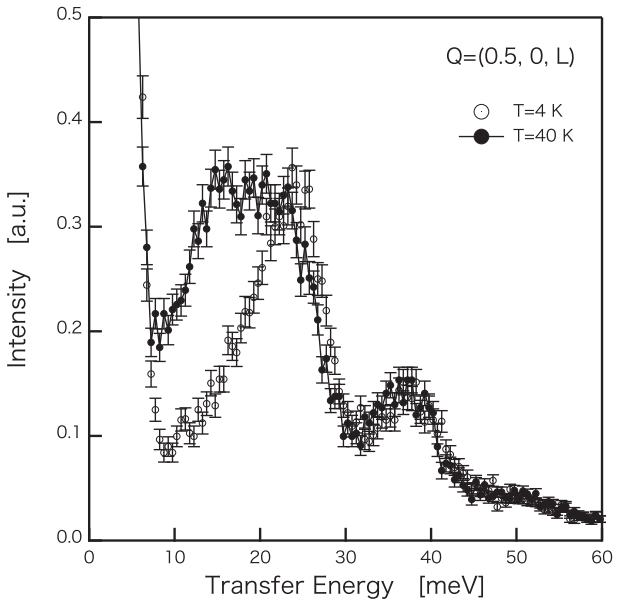

Figure 2. Energy spectra at Q = (0.5, 0, L). Open symbol is the measurement at T = 4 K, which is well below T_N. Solid symbol is at T = 40 K (above T_N). The gap value was evaluated at Δ = 14 meV from 1D profiles. (from Ref. [18])

and the wave numbers in the other direction are totally unchanged. Thus, we can safely accumulate the spectra with a finite index L. The spectra at T = 40 K, where the 1D Ni chain can be bare without any magnetic perturbation, shows the original gap value of 14 meV. In contrast, the gap peak merged into the CEF peaks at 24 meV, which shows a much narrower profile. Although the energy resolution is not sufficient to show the detailed structure below the Haldane gap, considerable weight was observed, indicating a hole dynamical structure as an in-gap state. By analogy with the slightly doped (x = 0.035) compound [19], the weight at the MZC (H = 0.5) appeared as a result of hole doping. We now plan to perform further experiments at a high-energy resolution to observe the dynamical structure below the gap.

Thus, the entire dynamical set of properties of a hole-doped 1D Ni chain was successfully measured by pulsed neutron inelastic scattering. At T_N, the dynamical structure changes dramatically, presenting new features - a local excitation at E = 10 meV and doped hole dynamics below the gap energy - in addition to a view of the entire 1D chain dispersion.

References

[1] Haldane F D M 1983 Phys. Lett. **93** 464.
[2] Haldane F D M 1983 Phys. Rev. Lett. **50** 1153.
[3] Darriet J and Regnault L P 1993 Solid State Commun. **86** 409.
[4] DiTusa J F, Cheong S W, Park J H, Aeppli G, Broholm C and Chen C T 1994 Phys. Rev. Lett. **73** 1857.
[5] Sachan V, Buttrey D J, Tranquada J M and Shirane G 1994 Phys. Rev. B **49** 9658.
[6] Zheludev A, Tranquada J M, Vogt T and Buttrey D J 1996 Phys. Rev. B **54** 7210.
[7] Zheludev A, Tranquada J M, Vogt T and Buttrey D J 1996 Phys. Rev. B **54** 6437.
[8] Yokoo T, Zheludev A, Nakamura M and Akimitsu J

1997 Phys. Rev. B **55** 11516.
[9] Yokoo T, Raymond S, Zheludev A, Maslov S, Ressouche E, Zaliznyak I, Erwin R, Nakamura M and Akimitsu J 1998 Phys. Rev. B **58** 14424.
[10] Mattheiss L F 1993 Phys. Rev. B **48** 4532.
[11] Eisaki H and Uchida S 1995 J. Phys. Chem. Solids **56** 1811.
[12] Dagotto E, Riera J, Sandvik A and Moreo A 1996 Phys. Rev. Lett. **76** 1731.
[13] Penc K and Shiba H 1995 Phys. Rev. B **52** R715.
[14] Xu G, Aeppli G, Bisher M E, Broholm C, DiTusa J F, Frost C D, Ito T, Oka K, Paul R L, Takagi H and Treacy M M J 2000 Science **289** 419.
[15] Sasaki T, Yokoo T, Katano S and Akimitsu J 2005 J. Phys. Soc. Jpn. **74** 267.
[16] Itoh S, Yokoo T, Satoh S, Yano S, Kawana D, Suzuki J and Sato T J 2011 Nucl. Instrum. Methods A **631** 90.
[17] Itoh S, Ueno K and Yokoo T 2012 Nucl. Instrum. Methods A **661** 58.
[18] Yokoo T, Itoh S, Ibuka S, Yoshizawa H, Akimitsu J, Journal of Physics Conf. Ser. **568** (2014) 042035.
[19] Yokoo T, Itoh S, Kawana D, Yoshizawa H and Akimitsu J 2014 J. Phys. Conf. Ser. **502** 012045.

T. Yokoo[1,2], S. Itoh[1,2], S. Ibuka[1,2], Y. Ikeda[3], H. Yoshizawa[3], and J. Akimitsu[4]
[1]Neutron Science Section, Materials and Life Science Division, J-PARC center; [2]Institute of Materials Structure Science, KEK; [3]The Institute for Solid State Physics, The University of Tokyo; [4]Physics Deparment, Aoyama-Gakuin University

Intermultiplet Transitions in $SmFe_4P_{12}$

1. Introduction

Filled skutterudites RT_4X_{12} (R = rare-earth, T = transition metal, X = pnictogen) have been intensively studied because they exhibit unusual low temperature properties, such as heavy fermion (HF) behavior, multipolar ordering and unconventional superconductivity [1]. Among them, $SmFe_4P_{12}$ is reported to be the first Sm-based ferromagnetic Kondo-lattice compound exhibiting a ferromagnetic transition at the Curie temperature 1.6 K [2]. It shows the unconventional HF state with the large electronic specific-heat coefficient γ = 370 mJ/mol K^2, which is the second heaviest in Sm-based compounds next to $SmOs_4Sb_{12}$ [3, 4]. As is in the case with $SmOs_4Sb_{12}$, the γ–value of $SmFe_4P_{12}$ also seems to be robust against magnetic fields.

In general, the energy from the ground J multiplet to the first excited J multiplet in Sm and Eu compounds is known to be not large compared to k_BT at room temperature [5]. Therefore, it is necessary to consider the influence of the excited J multiplet for these compounds. Although it is reported that the local environment surrounding rare-earth ions has little effect on the energy between the J multiplets split by the spin-orbit interaction [6], it may be important to examine the energy splitting in the Sm-based HF compounds for understanding the unusual electronic states of these materials.

2. Experimental

Single crystals of $SmFe_4P_{12}$ were grown by the tin-flux method using raw materials of 99.9% (3N)-pure naturally occurring Sm, 3N-Fe, 6N-P and 5N-Sn. The dimensions of most crystals were less than 1 mm. Many small single crystals of $SmFe_4P_{12}$ were combined for a total mass of 2.38 g. Inelastic neutron scattering (INS) experiments were conducted by using the time-of-flight high resolution chopper spectrometer HRC at J-PARC.

Usually it is difficult to do INS experiments on Sm containing materials because of the huge thermal-neutron absorption by natural Sm, but, it is possible to reduce the effects of the neutron absorption by using higher energy neutrons. As shown in Fig. 1, there is a transmission window between the strong ^{149}Sm nuclear resonances which peak at 100 meV and 900 meV. Therefore, we chose high incident neutron energy of E_i = 514.1 meV and a chopper frequency of 600 Hz, where the scattered neutrons also have low absorption

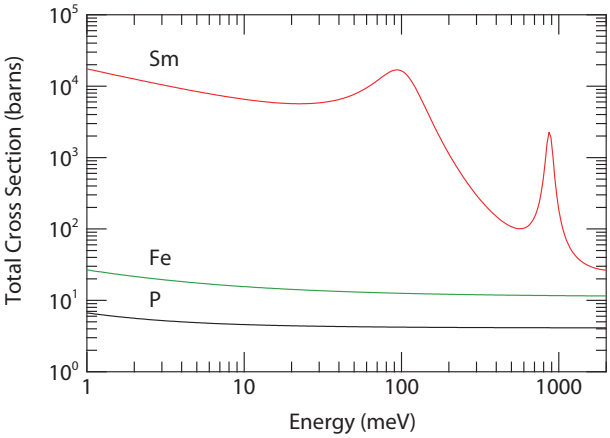

Figure 1. Energy dependence of the neutron cross sections of natural Sm, Fe and P.

cross sections. In this experimental set up, the instrument resolution at zero energy transfer was a full width at half maximum of 19 meV.

3. Results

Figure 2 shows the INS energy spectra of $SmFe_4P_{12}$ at temperatures of 6.5 K and 280 K [6]. At the low Q region, one small inelastic peak was observed around 80 meV at 6.5 K as denoted by the arrow in Fig. 2(a). The peak almost disappears at the high Q region, indicating its magnetic origin. Except for this small peak around 80 meV, no clear difference between the data at 6.5 K and 280 K was seen. If the small peak corresponds to the intermultiplet transition between the ground J = 5/2 multiplet and the excited J = 7/2 multiplet in Sm^{3+} ion, interestingly, the energy level is much lower than the free Sm^{3+} ion value ~130 meV and the reported values in usual trivalent Sm compounds, for example, 131.5 meV in Sm^{3+} ion doped in LaF_3 and 129 meV in $SmPd_3$. The low energy is comparable with the energy gap estimated by the bulk magnetic susceptibility of $SmFe_4P_{12}$. We also confirmed the existence of small excitation below 100 meV and the absence of excitation around 130 meV at low Q and low temperatures by a tentative INS experiment with the incident energy E_i = 300 meV. Furthermore, the observed rapid decrease of the intensity of the small peak in Fig. 2 with increasing Q agrees with the theoretical inelastic structure factor of Sm^{3+} [8].

The intermultiplet transitions in many Sm-based compounds have been studied by INS experiments. Specifically, significant changes of INS spectra are

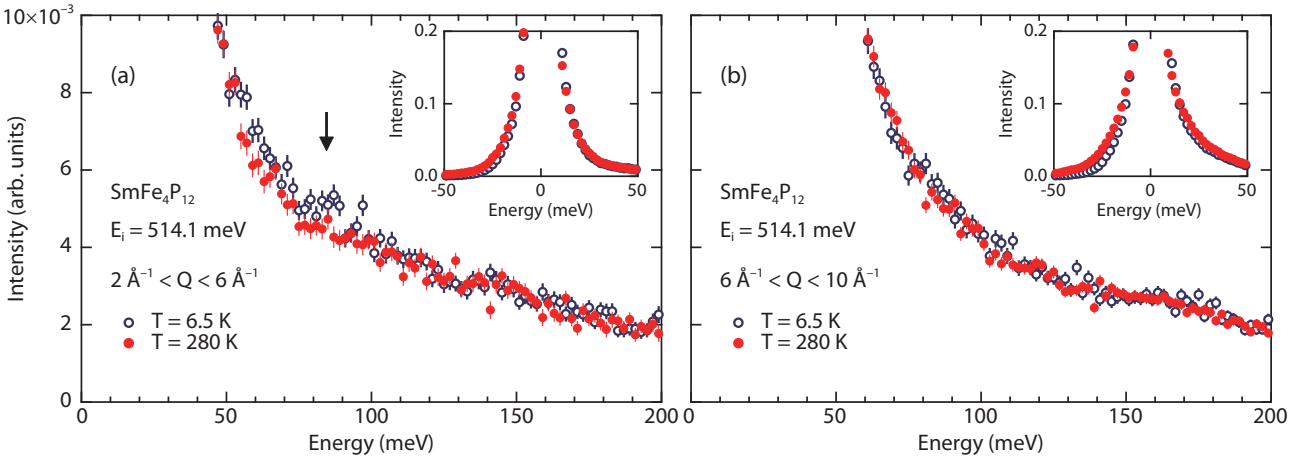

Figure 2. Energy spectra of neutrons scattered from $SmFe_4P_{12}$ measured with $E_i = 514.1$ meV at 6.5 K and 280 K for (a) 2 Å^{-1} < Q < 6 Å^{-1} and (b) 6 Å^{-1} < Q < 10 Å^{-1}, where Q is the magnitude of the scattering vector. The arrow denotes the small inelastic peak at 6.5 K. The insets show the data below 50 meV.

reported in intermediate valence compounds such as $Sm_{1-x}Y_xS$ [6, 9]. If the valence of Sm ions in $SmFe_4P_{12}$ deviates slightly from trivalent, the J = 0 to J = 1 excitation around 36 meV for Sm^{2+}, which has the largest inelastic structure factor in the rare-earth ions, may be expected. However, no significant difference between the data at 6.5 K and 280 K around 36 meV was observed as shown in the inset of Fig. 2. This is consistent with the results of the magnetic susceptibility and the X-ray absorption spectra [10].

The strong mixing between 4f electrons and conduction electrons, resulting from the characteristic cage structure in filled skutterudites, might renormalize the spin-orbit transition between the J multiplets in $SmFe_4P_{12}$. The present study suggests that the contribution of the excited J = 7/2 multiplet should be taken into account to understand the electronic states in the Sm-based filled skutterudites.

References

[1] H. Sato, H. Sugawara, Y. Aoki and H. Harima, Handbook of Magnetic Materials, Vol. 18, ed. K. H. J. Buschow (Elsevier, 2009).
[2] N. Takeda and M. Ishikawa, J. Phys. Condens. Matter 15 L229-L233 (2003).
[3] S. Sanada *et al.*, J. Phys. Soc. Jpn. 74 246-249 (2005).
[4] W. M. Yuhasz *et al.*, Phys. Rev. B 71 104402-1-9 (2005).
[5] J. H. Van Vleck, The Theory of Electric and Magnetic Susceptibilities (Oxford University Press, 1932).
[6] R. Osborn, S. W. Lovesey, A. D. Taylor and E. Balkar, Handbook of Physics and Chemistry of Rare Earths, Vol. 19, ed. K. A. Gschneider Jr. and L. Eyring (Elsevier, 1991).
[7] S. Konno *et al.*, J. Phys. Conf. Ser. 592 012029-1-6 (2015).
[8] E. Balcar and S. W. Lovesey, Theory of Magnetic Neutron and Photon Scattering (Clarendon Press, 1989).
[9] P. A. Alekseev *et al.*, Phys. Rev. B 74 035114 -1-13 (2006).
[10] M. Mizumaki *et al.*, J. Phys. Soc. Jpn. 76 053706-1-4 (2007).

S. Konno[1], A. Suzuki[1], K. Nihei[1], K. Kuwahara[1], D. Kawana[2], T. Yokoo[3], and S. Itoh[3]
[1]*Institute of Applied Beam Science, Ibaraki University;* [2]*The Institute for Solid State Physics, The University of Tokyo;* [3]*Neutron Science Section, Materials and Life Science Division, J-PARC Center*

Observation of the Inside of a Lithium-ion Battery by Muonic X-ray

The measurement principle of an elemental analysis technique with muonic x-ray has been known for over 30 years [1]. Since sufficient flux of negative muons (μ^-) with low energy can now be obtained due to the recent development of the intense pulsed muon source at J-PARC, several experiments with muonic x-ray have been reported since 2008 [2-5]. These experiments are non-destructive elemental analyses of cultural property [3] or a small amount of rare meteorites [5] with the great advantage of high penetrating power and high resolution in depth.

We have applied this non-destructive analysis to lithium-ion batteries, for which it is urgently required to improve their safety and durability. The key technique is to keep the Li-distribution homogeneous in electrodes and electrolyte under working conditions; when the distribution becomes inhomogeneous, the segregated Li ions change into a needle-shape crystal (dendrite), leading to short circuit of the battery.

As a first step of the Li elemental analysis on the battery structure, we measured the LiF crystals sandwiched by two sheets of Al foils, in order to make sure that a signal from Li can be obtained through multi-layers. As a result, we observed the Li-Kα signal at 18.7 keV [Fig. 1]. This is, to our knowledge, the first data for detecting the Li-Kα signal by muonic x-ray – Li has such a small atomic number that the muon K-α signal detection requires high resolution in low energy.

We have initiated an elemental analysis on a model sample consisting of stacked sheets of an uncharged anode and cathode, separator, which are designed for a commercial lithium-ion battery, and Al laminated films [Fig. 2], instead of a commercial lithium-ion battery itself with a thick Al outer case. Figure 2 shows an estimation of the range of μ^- in the multi-layered model sample by a Monte Carlo simulation with SRIM [6].

We have obtained profiles of muonic x-ray with the momentum of μ^- (M_μ) at 21.2 MeV/c and 15.7 MeV/c, respectively [Figs. 3 and Figs. 4]. The profile of the cathode [Fig. 3(a)] includes a clear peak of the Al-Lα signal, while such a peak in the anode is weak [Fig. 4(a)]. The former is naturally caused by the Al current collector in the cathode sheet, and the latter is thought to be a background signal from the sample chamber made of Al. It should

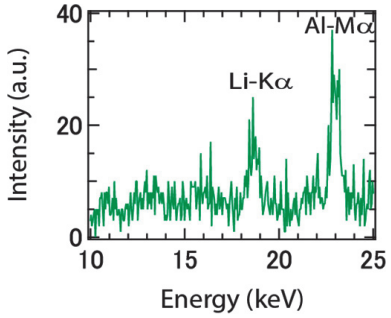

Figure 1. The profile obtained for LiF crystals sandwiched by two sheets of Al foils.

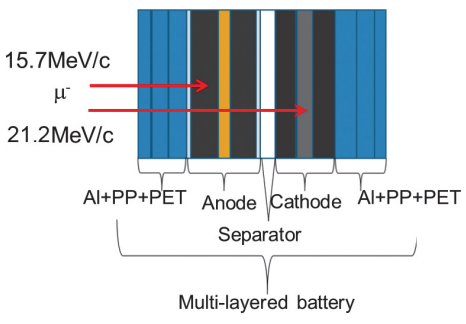

Figure 2. Illustration of the multi-layered sample. The arrows indicate the range of μ^- in the sample.

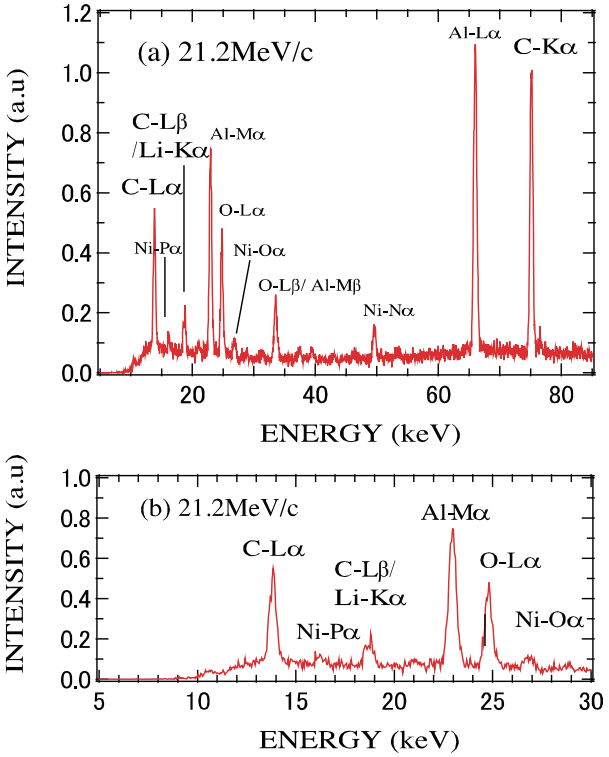

Figure 3. (a) Muonic x-ray profile with M_μ= 21.2 MeV/c. (b) Enlarged view in the low-energy region below 30 keV.

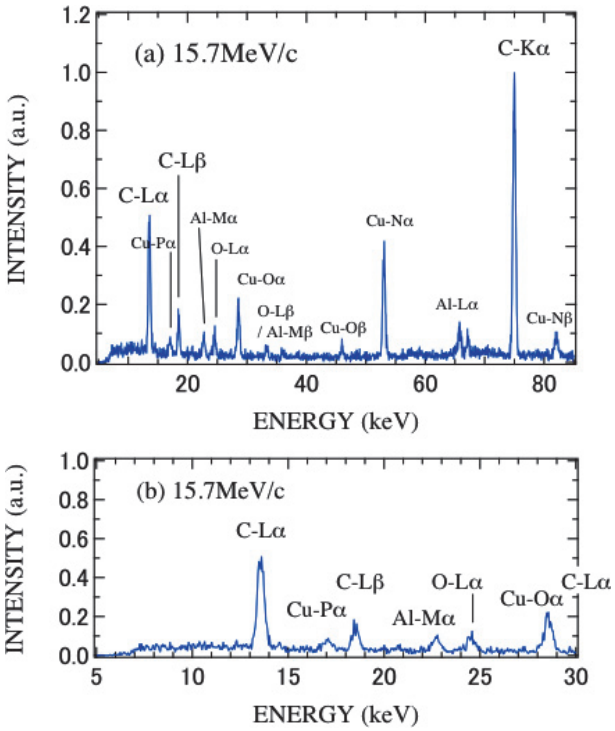

Figure 4. (a) Muonic x-ray profile with M_μ = 15.7 MeV/c. (b) Enlarged view in the low-energy region below 30 keV.

be noted that both C-Lα and C-Lβ signals are clearly observed in the both profiles at $E_{L\alpha}$ = 13.95 keV and $E_{L\beta}$ = 18.83 keV. Since the anode consists of graphite and Cu, the observed result is very reasonable. The cathode, on the other hand, also includes ~ 5 wt% carbon in order to increase the electric conductivity. This is the reason why the signals from C are detected for the cathode sheet.

Since the energy of the C-Lβ (= 18.83 keV) signal is only 0.13 keV lower than that of the Li-Kα (= 18.70 keV), we could not separate the two signals in the profile of the cathode by the Ge semiconductor detectors with energy resolution 0.4 keV.

We have obtained muonic x-ray profile on a plate of graphite to confirm that the intensity ratio of the C-Lα signal to that of C-Lβ is intrinsic, that is, 1 : 0.28. In fact,

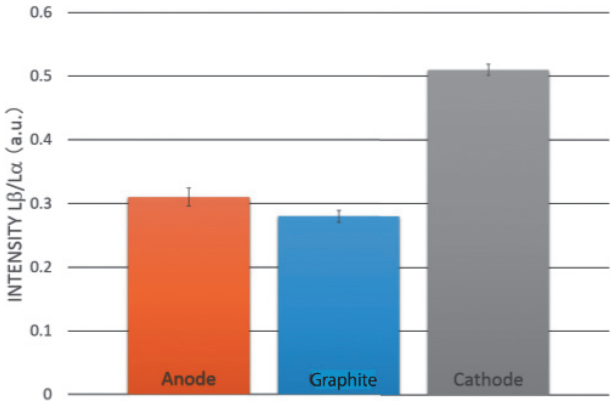

Figure 5. The ratio of the intensity of signals of μC-Lβ and μC-Lα for the anode and the cathode in the multi-layered sample and a graphite.

the ratio in the profile of the anode was found to be 1 : 0.31. However, we determined the ratio as 1 : 0.51 in the cathode profile [Fig. 5]. If we assume that the ratio of the intensity of the C-Lα signal to that of C-Lβ does not depend on conditions, where other elements, including Li, exist together with C, we could estimate the contribution of the Li-Kα signal to the peak at E ~ 18.8 keV in the profile for the cathode [Fig. 3(b)].

References

[1] H. Daniel *et al.*, Nucl. Instr. Meth. **B3** (1984) 65.
[2] M. K. Kubo, K. Ninomiya, *et al.*, J. Radioanal. Nucl. Chem. **278** (2008) 777.
[3] K. Ninomiya *et al.*, J. Phys. Conf. Ser. **225** (2010) 012040.
[4] K. Ninomiya *et al.*, Bull. Chem. Soc. Jpn. **85** (2012) 228.
[5] K. Terada *et al.*, Nature Scienti_c Reports **4** (2014) 5072.
[6] SRIM is a software package for calculating the range of ions in solids and available here; http://www.srim.org/

I. Umegaki[1], H. Nozaki[1], K. Ninomiya[2], M. K. Kubo[3], M. Tampo[4], K. Hamada[4], N. Kawamura[4], Y. Miyake[4], H. Yamashige[5], and J. Sugiyama[1]

[1]Toyota Central Research and Development Laboratories, Inc.; [2]Osaka University; [3]International Christian University; [4]Muon Science Laboratory, High Energy Accelerator Research Organization (KEK); [5]Toyota Motor Corporation

Systematic Studies on Muonium Production in Vacuum from Structured Silica Aerogel

1. Introduction

The goal of this experiment is to systematically study muonium emission to vacuum from newly developed silica aerogel with laser-ablated holes. The development of muonium emitting material with high efficiency from surface muon beams is required for the introduction of an ultra-slow muon source in the muon *g*-2/EDM experiment at MUSE H-line [1]. Such a material would also be desired in other applications that utilize the ultra-slow muon beam.

In the past, two measurements of muonium emissions from silica aerogel were done at TRIUMF before this experiment [3, 4]. The second measurement at TRIUMF in 2013 tested the laser-ablated samples and gave an order of magnitude enhancement of the muonium yield. In this study, we tested the newly developed laser-ablated silica aerogel samples by using the track-back system for decay positrons at the J-PARC D-line.

2. Aerogel samples

The silica aerogel samples were developed in Chiba university [5]. The laser-ablation processing was done at the laser-processing facility in RIKEN. In this study, we developed three new samples with holes. The diameter of holes was about 55 μm. The chosen hole pitch was 285 μm, 185 μm, and 115 μm, respectively. As a reference, we took data with the same sample that was used in Ref. [2, 4]. Figure 1 shows a schematic representation of the newly developed silica aerogel samples with laser-ablated holes.

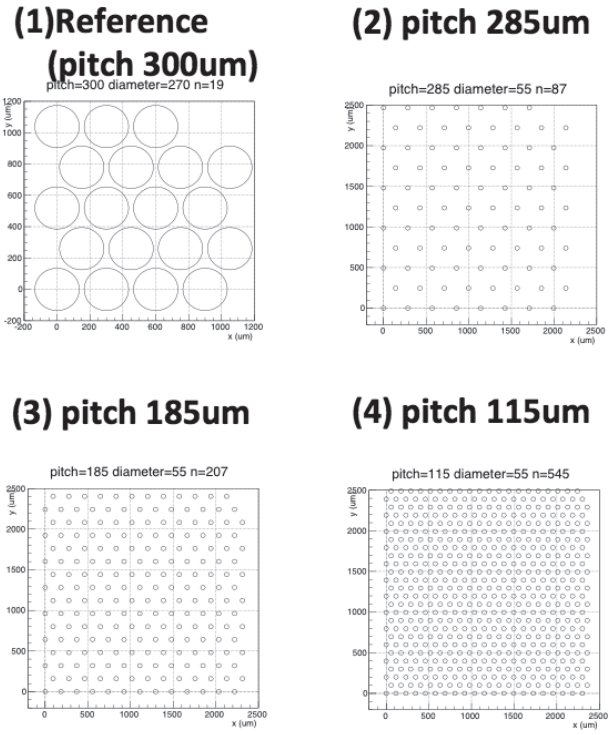

Figure 1. Schematic representation of the laser-ablated aerogel sample.

3. Experimental method

The experiment used the surface muon beam at the MUSE D2 area. Sub-surface muons with momentum 23.7 MeV/*c* were used. The beam momentum is tuned so that half of the muons are stopped in the target to maximize muon stopping density at the rear surface of the target. A description of the experimental apparatus is given in Ref. [2].

4. Results

The time distribution of positrons for the three *z* regions are shown in Fig. 2. Signal from muonium in vacuum observed as event excess over the silica plate data in the vacuum regions are clearly seen in the time region $t > 2$ μs.

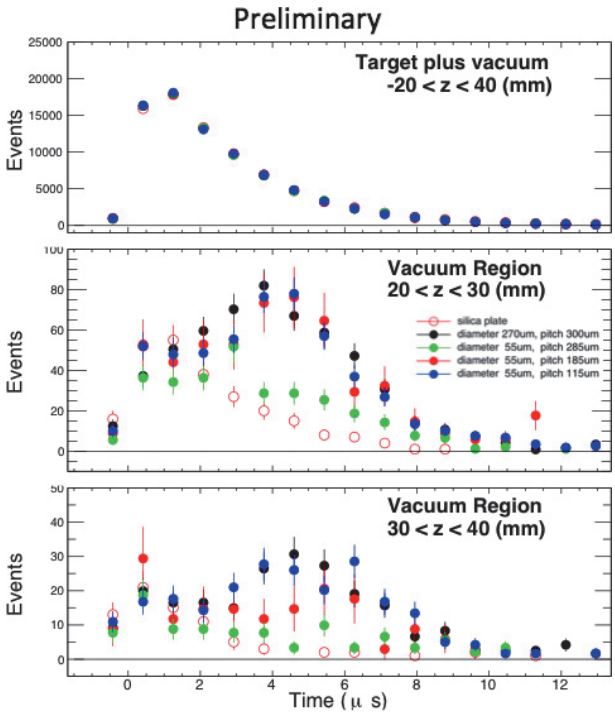

Figure 2. Time distribution of positrons from three *z* regions for the Laser-ablated aerogel sample (preliminary results).

By combining the results from the previous study [2], we confirmed that introducing laser-ablated holes in silica aerogel increases the muonium yield with independently-processed samples. The muonium yield in vacuum for the 115 μm-pitch sample is similar to the reference sample with a lager pitch (300 μm) and hole diameter (270 μm). We noticed that the deformation of the sample was much lower for these samples than of the reference sample. Flat surface is preferred for better match to the muonium ionization laser. Therefore, the new sample would be better suited for the muonium production target at the ultra-slow muon source.

5. Acknowledgment

The authors are pleased to acknowledge the support from the J-PARC MUSE facility by providing a stable beam during the experiment. We would like to thank Dr. K. Sugioka and his group for their assistance in laser processing at RIKEN. Our research was supported in part by the MEXT KAKENHI Grant Number 2318005 (Japan), NSERC Discovery Grant (Canada), and the Center for Korean J-PARC Users No. NRF-2013K1A3A7A06056592 (Korea).

References

[1] J-PARC E34 conceptual design report, (2011).
[2] G. Beer *et al*., KEK-MSL progress report 2013, pp 57 (2013).
[3] P. Bakule *et al*., Prog. Theor. Exp. Phys., 103C01 (2013).
[4] G. Beer *et al*., Prog. Theor. Exp. Phys. 091C01 (2014).
[5] M. Tabata *et al*., Nucl. Instrum. Meth. A **668**, 64 (2012).

G. A. Beer[1], Y. Fukao[6], H. Fujimori[7], Y. Ikedo[7], K. Ishida[8], M. Iwasaki[8], S. Kanda[8,5],H. Kawai[2], N. Kawamura[7], R. Kitamura[8,5], K. M. Kojima[7], S. Lee[3], W. Lee[3], J. Nakamura[7], S. Nishimura[5], S. Makimura[7], G. M. Marshall[10], T. Mibe[6], Y. Miyake[7],T. Nagatomo[9], Y. Nagashima[4], K. Nagumo[4], S. Okada[8], A. Olin[10,1], Y. Oishi[8], M. Otani[6], N. Saito[6,5], K. Shimomura[7], P. Strasser[7], T. Suzuki[4], M. Tabata[2], K. Ueno[6], and E. Won[3]

[1]Department of Physics and Astronomy, University of Victoria; [2]Department of Physics, Chiba University; [3]Department of Physics, Korea University; [4]Department of Physics, Tokyo University of Science; [5]Department of Physics, The University of Tokyo; [6]Institute of Particle and Nuclear Studies, High Energy Accelerator Research Organization (KEK-IPNS); [7]Muon Science Laboratory, High Energy Accelerator Research Organization (KEK-IMSS); [8]Advanced Meson Science Laboratory, Nishina Center for Accelerator-Based Science, RIKEN; [9]Accelerator Group, Nishina Center for Accelerator-Based Science, RIKEN; [10]TRIUMF

Neutron Activation Analysis using Pulsed Neutrons at J-PARC ANNRI

1. Introduction

Many different analytical methods for multi-elemental analysis have been developed and improved during the recent decades due to its importance in fundamental research and applied technology. In many cases, a nondestructive method is preferred because the specimen can be reused, as it is, after the measurement. Prompt gamma-ray analysis (PGA) [1] and time-of-flight elemental analysis (TOF), formally known as neutron resonance capture analysis (NRCA) [2], are nondestructive and multi-element analytical techniques. Both methods use neutron beams, and measure the gamma rays produced by neutron capture reactions. The characteristic energies of the gamma rays emitted in neutron capture reactions are used as fingerprints for nuclei identification in PGA. By contrast, TOF enables us to determine the nuclei contained in the sample by the measuring the energy of the neutron capture resonance. PGA and TOF are similar methods. Then, these could be replaced by a single measurement. However, PGA and TOF have never been simultaneously applied for elemental analyses since the gamma-ray detector used is different. We have developed a new analytical technique that combines PGA and TOF by using an intense pulsed neutron beam at the Japan Proton Accelerator Research Complex (J-PARC) [3].

Most pure metal samples provide clear peaks on the PGA and TOF spectra. Thus, these elements are typically easy to measure by PGA and TOF for a single element sample. In contrast, severe peak overlaps in both PGA and TOF spectra will occur when a mixed sample is measured. Therefore, the analysis of the mixed samples provides a clear and simple demonstration of the advantage of the TOF-PGA method. Here, we demonstrate how the TOF-PGA method enables us to extract reliable information from unresolved peaks in both PGA and TOF spectra.

2. Experimental

The Accurate Neutron-Nucleus Reaction Measurement Instrument (ANNRI) has been designed and developed for PGA, nuclear data measurement, and nuclear astrophysics [4, 5]. ANNRI is located at beamline No. 04 at the Materials and Life Science Experimental Facility (MLF) of J-PARC. MLF is high intensive pulsed neutron facility, which operates at approximately 500 kW proton beam power that will be increased up to 1 MW in the near future. The germanium detector-array, which is a combination of two cluster-Ge detectors, eight large coaxial-Ge detectors and BGO anti-Compton shields surrounding cluster-Ge and coaxial Ge detectors, is being installed at the flight path length of 21.5 m in ANNRI. Each cluster-Ge detector consists of seven individually encapsulated coaxial-Ge detectors. The absolute photo peak efficiency of the array for 1.3 MeV of a gamma ray is approximately 3.6%.

3. Results and Discussion

Ag, Au, Cd, Co, and Ta are commonly used as standard samples. In this study, we have measured a mixed sample that includes these elements. The sample weights are approximately 13, 5, 23, 1 and 41 mg for Ag, Au, Co, Cd and Ta, respectively. Figure 1 shows the PGA and TOF spectra of the mixed sample. All intense gamma rays from Co overlap ones from other elements in the sample and the background. The neutron

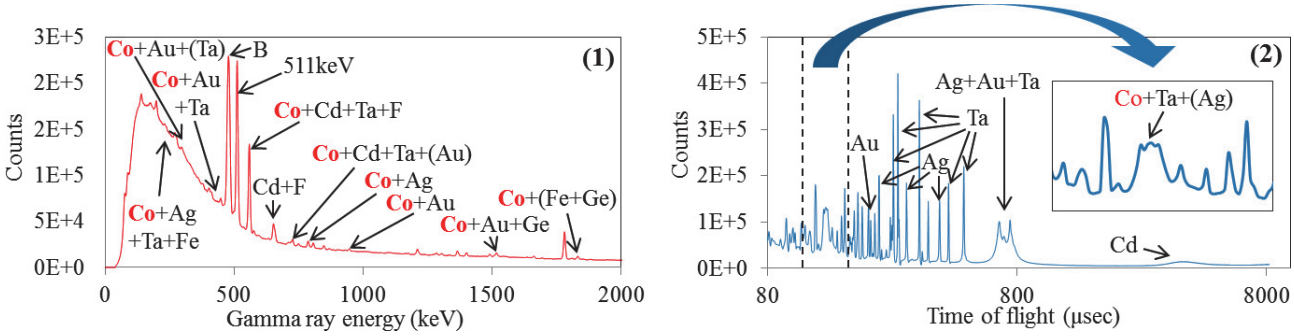

Figure 1. Prompt gamma-ray and time-of-flight spectra. Intense gamma-ray peaks (1) and some of resonance peaks (2) are labeled with chemical symbols.

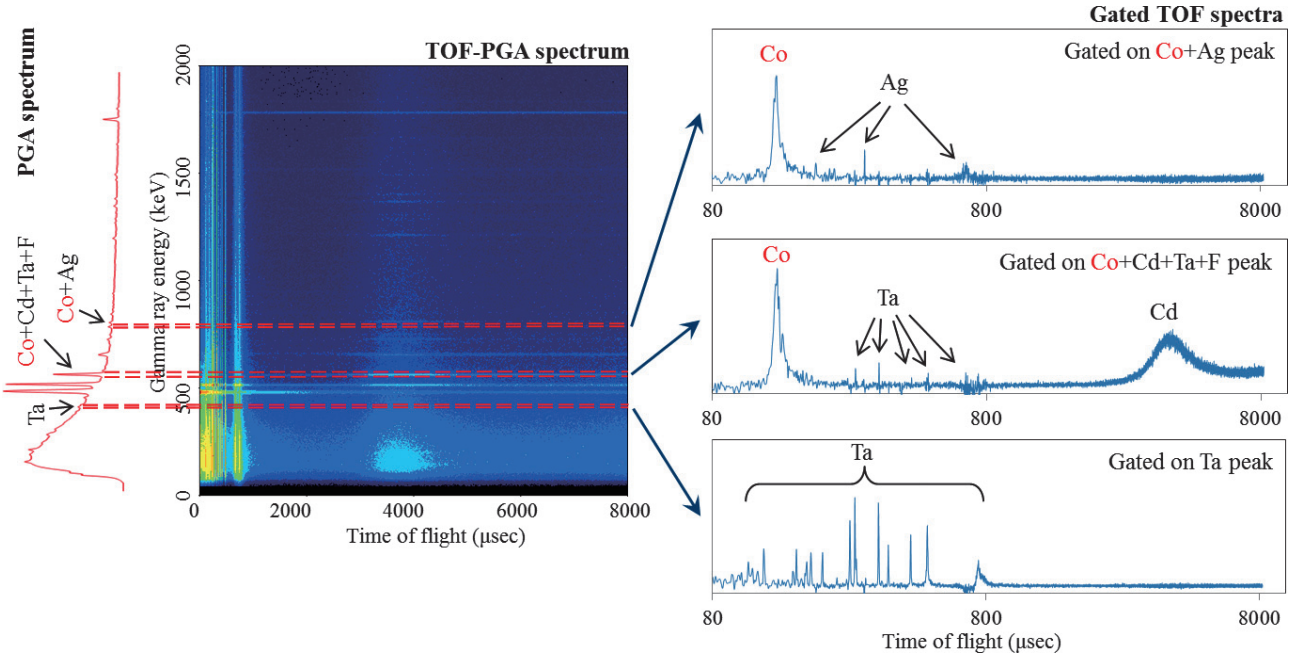

Figure 2. TOF-PGA spectrum analysis by gating on the PGA peaks.

resonance peak of approximately 130 eV of Co has serious overlap with that of Ta (and Ag) because the width of the Co peak is broad. Consequently, time-consuming and very careful peak shape analysis for unresolved peaks is required to obtain accurate results for Co by either PGA or TOF in the present experiment. It is quite likely that neither PGA nor TOF can obtain accurate results in some cases, especially if a sample contains a number of elements.

Figure 2 shows the TOF-PGA spectrum analysis of the mixed sample by gating on the TOF peaks. The gamma-ray peaks that are used for making the gated spectra seen in Figure 2 contain the γ rays not only from Co but also from the other elements. Most of overlapping gamma-ray events appear in different points on the gated TOF spectrum because the resonance peak energies of Co are different from most of these of Cd, Ta etc. As a result, the TOF-PGA method allows us to eliminate or at least greatly suppress the contributions of the other elements and the background in the Co peak, and can accurately quantify Co even with the presence of these elements.

TOF-PGA method will be an irreplaceable tool for research in many fields because it makes it possible to obtain reliable and valid results.

4. Acknowledgement

This work was supported in part by Grants-in-Aid for Scientific Research (25246038)

References

[1] M. P. Failey, D. L. Anderson, W. H. Zoller, G. E. Gordon, R. M. Lindstrom, Anal. Chem. 1979, 51, 2209-2221.
[2] H. Postma, M. Blaauw, P. Bode, P. Mutti, F. Corvi, P. J. Siegler, Radioanal. Nucl. Chem. 2001, 248, 115-120.
[3] Y. Toh, M. Ebihara, A. Kimura, S. Nakamura, H. Harada, K. Y. Hara, M. Koizumi, F. Kitatani, K. Furutaka, Anal. Chem. 2014, 86, 12030-12036.
[4] M. Igashira, Y. Kiyanagi, M. Oshima, Nucl. Instrum. Methods Phys. Res., Sect. A 2009, 600, 332-334.
[5] H. Harada *et al.*, J. Korean Phys. Soc. 2011, 59, 1547-1552.

Y. Toh[1], M. Ebihara[2], M. Huang[1], A. Kimura[1], and S. Nakamura[1] on behalf of the ANNRI collaboration
[1]*Nuclear Science and Engineering Center, Japan Atomic Energy Agency;* [2]*Graduate School of Science and Engineering, Tokyo Metropolitan University*

Neutron Reflectivity Measurement for Study of Water Permeability of Anticorrosive Ultrathin Film

1. Introduction

Maintaining and repairing the structural integrity, appearance, and functional properties of metals, alloys or other structural materials is a matter of immense concern in our daily lives. Corrosion of metals and alloys is often regarded as a major factor in these issues. Therefore, various technologies, including chromate passivation, electrochemical plating, anodizing, and coating/painting, have been used to resolve those problems [1]. However, with the rapid advance of (nano) science and technology and serious concerns over pollution caused by heavy metals used in major existing technologies, it is becoming of paramount importance to find alternative ways to protect modern (nano)devices from corrosive hazards. Within this context, we have been exploring a biomimetic anticorrosion ultrathin polymer coating produced through a versatile, eco-friendly and easy process. Specifically, poly(dopamine methacrylamide-*co*-alkyl methacrylate), poly(DOMA-*co*-AMA) (Fig. 1) exhibited a great potential as a high-performance anticorrosive coating. Here dopamine, which is a key component of the adhesive secretion of the blue mussel, was utilized as an adhesive moiety towards a variety of substrates. As expected, the obtained poly(DOMA-*co*-AMA) demonstrated excellent anticorrosion property on variety of metals and alloys (Fig. 2). Most importantly, thermal treatment of the as-spun ultrathin film drastically improved anticorrosion property for longer duration in sharp contrast with the film without thermal treatment that gets damaged by corrosion just after several days. To address the question about how thermal treatment affects preventive ability of the polymer film, we evaluated water penetration into the polymer thin film using neutron reflectivity (NR, SOFIA@BL-16), which is one of the most depth-sensitive techniques [2, 3].

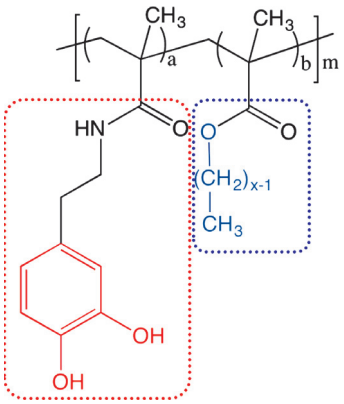

Figure 1. Chemical structure of poly(dopamine methacrylamide-*co*-alkyl methacrylate), poly(DOMA-*co*-AMA).

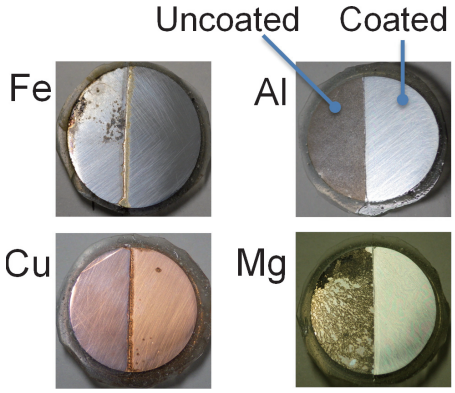

Figure 2. Images of half-coated metal/alloy plates embedded in resin after immersion in corrosive salt-water solution (3.5 wt.% in water) for several days. Left and right side shows uncoated and coated area, respectively.

2. Experimental

Tetrahydrofuran (THF) solution of poly(DOMA-*co*-AMA) was spun on a silicon block. If the density profile of thin-film is examined along normal direction to the surface only in air, the X-ray reflectivity should be good enough. However, we focused on density profiles of the coating layer in contact with liquids. The density profiles of the film in air and in contact with water were examined by NR measurements using horizontal type neutron reflectometer SOFIA at the Materials and Life Science Experimental Facility (MLF). A glass reservoir filled with liquid was mounted onto the film. The measurements were conducted in air, and then in purified and degassed deuterated water (D_2O). Prior to the measurements in D_2O, the film was aged in D_2O for 2 h, which was apparently enough to cause a structural change in the film. A beam of neutrons with a wavelength (λ) that ranged from 0.25 to 0.88 nm at a resolution of 3% was guided into the specimen from the silicon side. Details of our experimental setup were described elsewhere [4, 5]. The reflectivity was calculated on the basis of the model (*b*/*V*) profile along the depth direction by means of Parratt 32 software, a freeware program from the Hahn-Meitner Institute.

3. Discussion

Figures 3a and 3c show the reflectivity curves as a function of the scattering vector ($q = (4\pi/\lambda)\sin\theta$, where λ and θ are the wave length and the incident angles of the neutron beams, respectively) for as-spun and annealed poly(DOMA-*co*-AMA) films under air and deuterated water (D_2O). For clarity, the data set for the film in D_2O is offset by three orders of magnitude. The open symbols denote the experimental data, and the solid curves were fit curves calculated from the scattering length density (*b*/*V*) profiles in Fig. 3b and 3d. To understand the role of thermal treatment and the importance of the catechol units for high anticorrosion efficiency, only interfacial regions are shown. Since the solid curves in Fig. 3a and 3c are in good agreement with the experimental data, it is most likely that the model (*b*/*V*) profiles depicted in Fig. 3b and 3d would reflect the density profiles of the films. The (*b*/*V*) values for silicon (Si), native oxide layer (SiO_x) and D_2O used in these calculations were 2.21×10^{-4}, 4.18×10^{-4}, and 6.62×10^{-4} nm^{-2}, respectively. In both cases, when measured under air, the (*b*/*V*) values were constant over the entire region of the film thickness with *ca*. 150 nm, except for the interface with the Si substrate. This indicates that a slightly dense layer formed with *ca*. 5 nm in thickness adjacent to the substrate, although the density of the upper region was identical to the polymer bulk. Since this phenomenon was not observed for spin-coated poly(methyl methacrylate) (PMMA) film, [4] it is more likely that the catechol moiety stimulated anchoring of the polymer chains to the substrate and resulted in a slightly dense layer at the interface. In the case of measurement under water for non-annealed film, the (*b*/*V*) value was drastically changed (Fig. 3b). The magnitude was slightly higher than that in air, and increased substantially at the substrate interface. This indicates that the adsorbed D_2O molecules (with high (*b*/*V*) value) reached the substrate and enriched it. Similar behavior has been reported for PMMA spin-coated film, in which tiny channels were generated during solvent evaporation, and within several hours the thin film was swelled by the penetrated water molecules [5]. Surprisingly, the annealing process overcame this shortcoming and significantly improved the barrier ability against foreign molecules. Thus in the case of annealed film, D_2O could not penetrate the substrate even after 2 hours of immersion in D_2O, which otherwise would be enough time to cause swelling by the water molecules (Fig. 3d). These results suggest that the annealing aids the closing of the tiny channels and makes the polymer chain arrangements more uniform, leading to prevention of foreign molecules. Therefore, we conclude that a combination of formation of a *ca*. 5 nm dense layer adjacent to the substrate and thermally cured sub-micron layer above this dense layer completely inhibits the penetration of foreign molecules and exhibits high anticorrosion property (Fig. 4).

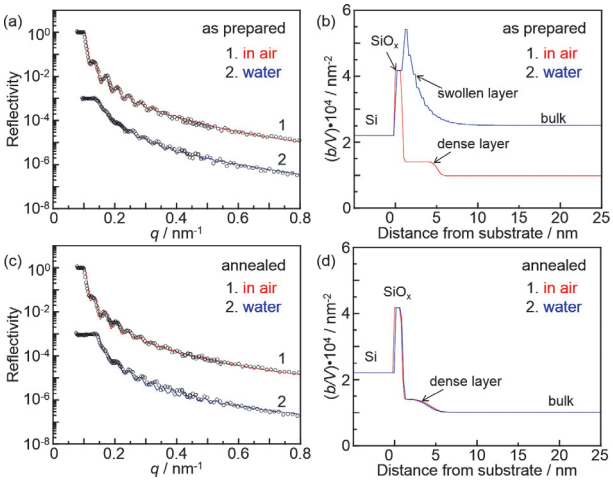

Figure 3. Neutron reflectivity for (a) as-spun and (c) annealed films in air and water. Open symbols depict experimental data, and solid lines represent the reflectivity calculated on the basis of the scattering length density (*b*/*V*) profiles shown in (b, d). For clarity, the values in panel (a, c) are offset from one another.

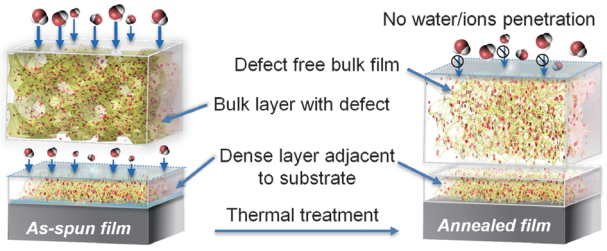

Figure 4. Schematic illustration of difference between as-spun and annealed film determined by neutron reflectivity measurement.

In conclusion, we have developed a simple and practical coating method for anti-corrosion of versatile metals and alloys inspired by an underwater bio-adhesion [1]. On the basis of NR technique, we observed that spin-coated copolymers enabled the formation of a dense nanolayer adjacent to the metal surface, which normally does not occur with conventional poly(alkyl methacrylate)s. This happened by strong binding affinity of the catechol unit towards metal/alloy substrates, resulting in a spontaneous condensation of the polymer chains at the metal interface. Additionally, the

annealing process was found to be essential to improve the protecting ability against corrosive molecules, due to the formation of defect-free coating.

References

[1] D. Payra, M. Naito, Y. Fujii, N. L. Yamada, S. Hiromoto, A. Singh, RSC Adv., **5**, 15977 (2015).

[2] N. L. Yamada, N. Torikai, K. Mitamura, H. Sagehashi, S. Sato, H. Seto, T. Sugita, S. Goko, M. Furusaka, T. Oda, M. Hino, T. Fujiwara, H. Takahashi, A. Takahara, Eur. Phys. J. Plus, **126**, 108 (2011).

[3] K. Mitamura, N. L. Yamada, H. Sagehashi, N. Torikai, H. Arita, M. Terada, M. Kobayashi, S. Sato, H. Seto, S. Goko, M. Furusaka, T. Oda, M. Hino, H. Jinnai, A. Takahara, Polym. J., **45**, 100. (2013).

[4] K. Tanaka, Y. Fujii, H. Atarashi, K. Akabori, M. Hino, T. Nagamura, Langmuir, **24**, 296 (2008).

[5] H. Atarashi, T. Hirai, K. Hori, M. Hino, H. Morita, T. Serizawa, K. Tanaka, RSC Adv., **3**, 3516 (2013).

M. Naito[1], Y. Fujii[2], D. Payra[1], and N. L. Yamada[3]

[1]Research Center for Strategic Materials, Structural Materials Unit, National Institute for Materials Science (NIMS); [2]Advanced Key Technologies Division, Polymer Materials Unit, National Institute for Materials Science; [3]Neutron Science Division, Institute of Materials Structure Science, High Energy Acceleration Research Organization

Measurement of Neutron Spatial Brightness from Coupled and Decoupled Para-hydrogen Moderators

Introduction

A moderator's neutron spatial brightness is one of the most important pieces of data needed for its proper design.

Especially, after it was reported that a liquid para-hydrogen moderator had an eccentric spatial brightness in the simulation [1]. The measurement of the spatial brightness is necessary for the Japanese Spallation Neutron Source (JSNS) Group to validate the neutronic design of JSNS at J-PARC. On the other hand, because the European Spallation Source (ESS) Group proposes a flat liquid hydrogen coupled moderator in the ESS design, they require the special brightness data from the coupled liquid hydrogen needed for the coupled spatial distribution. Therefore, the JSNS Group and the ESS Group collaborated to measure the neutron spatial brightness for the moderators at J-PARC.

Measurements and Results

The nGEM detector [2], which was a gaseous ionization chamber using boron files, prepared for the neutron imaging experiment at BL22, was used for the measurement. Two measurements were done at BL10 for the decoupled moderator and at BL04 for the coupled moderator. At BL10, the detector was located at 13 m and a tiny collimator (3.1 × 3.1 mm) in the rotary collimator at 8.0 m was used. At BL04, the detector was located at 28.5 m and a pinhole Cd plate with a hole of 3 mm in diameter was placed at 21.5 m.

Figure 1 shows the neutron spatial brightness around 5 meV from the decoupled moderator (BL10). The figure on the left shows the measurement result and the one on the right depicts the simulation. The simulation was done by PHITS [3] calculation with the engineering model of JSNS [4]. It was found that the distributions of the two sets of data were very similar with the largest intensities at the center. Also, an aluminum tube in the moderator was observed (the two vertical lines near the center).

Figure 2 shows the neutron spatial brightness around 5 meV from the coupled moderator (BL04). In the same way as in Fig. 1, the figure on the left shows the measurement result and the one on the right depicts the simulation. It was found that the distributions of the two sets of data were very similar and the largest intensities were observed near the target (upper side) and far from it (lower side).

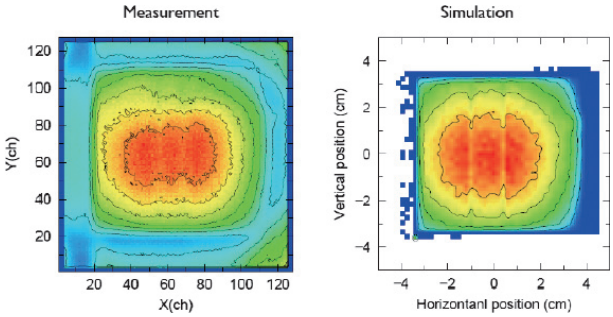

Figure 1. Neutron spatial distribution from the decoupled moderator (BL10) Left: measurement; right: simulation.

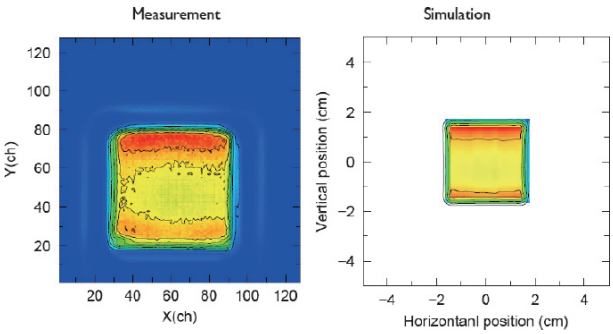

Figure 2. Neutron spatial distribution from the decoupled moderator (BL04) Left: measurement; right: simulation.

Summary

The particular spatial brightness from the coupled moderator is of great interest to us and it is very important to measure these data for the moderator in a high-power spallation neutron source. These results validated the JSNS neutronic design. And they would be also very helpful for the ESS design.

References

[1] T. Kai *et al.*, Nucl. Instr. Meth. A, 523 398 (2004).
[2] S. Uno *et al.*, Physica Procedia, **26**, 142 (2012).
[3] T. Sato, J. Nucl. Sci. Technol., **50**, 913 (2013).
[4] M. Harada *et al.*, Prog. Nucl. Sci. Technol., **2**, 872 (2011).

M. Harada[1], M. Teshigawara[1], M. Ooi[1], K. Esben[2], and L. Zanini[2]
[1]Neutron Source Section, Materials and Life Science Division, J-PARC Center JAEA; [2]European Spallatin Source ESS AB

Dynamic Structures of Superionic Conductors of MAg_4I_5 (M = K, Rb) by Inelastic Neutron Scattering

1. Introduction

$RbAg_4I_5$ and KAg_4I_5 are well known as superionic conductors [1, 2]. In particular, $RbAg_4I_5$ has a superionic phase in a wide temperature range from −155 to 228°C [1] and remains a solid electrolyte even at ambient temperature. In the superionic phase of $RbAg_4I_5$ and KAg_4I_5, the Ag ions migrate through the sublattice formed by the I and Rb (or K) ions, as shown in Fig. 1 [3]. The ionic conductivity of $RbAg_4I_5$ (σ = 0.21(6) $\Omega^{-1}cm^{-1}$) is approximately three times higher than that of KAg_4I_5 (σ = 0.08(5) $\Omega^{-1}cm^{-1}$) at ambient temperature [2]. It was proposed that the Rb ion, whose radius is larger than that of the K ion, causes a lattice expansion, which contributes to easier Ag diffusion in $RbAg_4I_5$ [2]. Shapiro et al. reported the energy dependence of inelastic neutron scattering for single crystalline $RbAg_4I_5$ at $\mathbf{Q}$ = (0, 5.7, 5.7), and the low-energy excitation peak was found at around E = 2.5 meV [4], which is consistent with the results of polarized Raman scattering [5]. This low-energy excitation is presumed to be caused by local vibrations of Ag ions within an immobile cage formed by I ions [4, 5]. On the other hand, KAg_4I_5 has not been studied using inelastic neutron scattering and even Raman scattering.

In the present study, inelastic neutron scattering measurements were carried out for $RbAg_4I_5$ and KAg_4I_5 at the BL14 beamline (AMATERAS: Cold–Neutron Disc–Chopper Spectrometer) to investigate the difference in the low-energy excitations in the two materials.

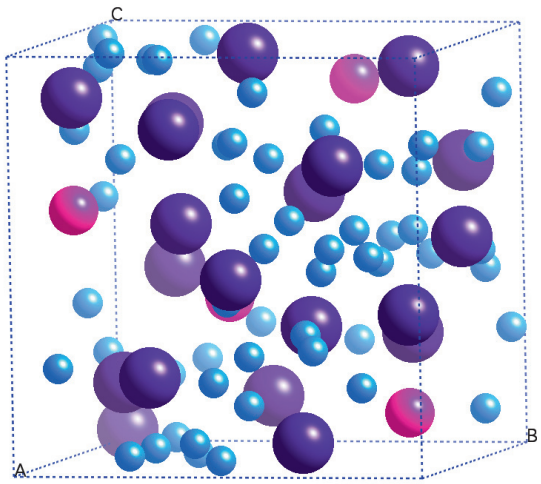

Figure 1. Crystal structure of superionic phase of $RbAg_4I_5$ and KAg_4I_5. Blue, pink, and purple spheres exhibit Ag, Rb (or K), and I ions, respectively.

2. Inelastic Neutron Scattering

The sample of $RbAg_4I_5$ was prepared from powder samples of pure RbI and AgI by mixing them in a quartz tube under vacuum at 1073 K above their melting points, and then cooling to solidify the mix into a bulk sample. After this process, the sample was annealed at 510 K for 48 hours and powdered at room temperature, just before the experiments. Although the sample of KAg_4I_5 was prepared in the same manner as $RbAg_4I_5$, the anneal temperature for KAg_4I_5 was 500 K which was the same temperature applied in the experiment in reference [2]. Each sample was placed in an Al-foil cell, which weighed 20 g. This Al-foil cell was set in the Al standard cell which was architected for the inelastic neutron scattering measurements. The inside of the Al standard cell was filled with He gas. The inelastic neutron scattering measurements were carried out with time-of-flight technique [6]. AMATERAS covers a scattering angle of 5° ~ 112° horizontally and −16° ~ 22° vertically. For an easy access to the dynamics in different time scales, multi-E_i technique [7] was applied, where the monochromating chopper operating at 150 Hz, 6 times faster than the neutron pulse emerging at 25 Hz, and the band chopper at 25 Hz yielded incident energies (E_i's) of 94.3, 23.7, 10.5 and 5.9 meV simultaneously with energy resolutions of 8.4, 1.1, 0.4 and 0.15 meV for elastic scattering, respectively. In the case of $RbAg_4I_5$, the sample temperature was controlled by using a cryo-furnace within a wide temperature range from 10 K to 348 K. Since KAg_4I_5 decomposes to AgI and K_2AgI_3 below 311 K [8], the sample temperature was kept at around 348 K during the sample setup and the measurement for KAg_4I_5 was carried out only at 348 K. We confirmed that the sample was not decomposed by confirming that the profile of the elastic spectrum was maintained in the measurement process.

3. Results and Discussion

The energy dependence of the dynamic structure factor $S(Q,E)$ for $RbAg_4I_5$ at T = 135 K and several Q points are shown in Fig. 2. Although no characteristic peak is observed at small Q (= 1.35 $Å^{-1}$), a single low-energy excitation peak is observed at around E = 1.5 meV and Q = 1.73 $Å^{-1}$. In the middle Q region (> 2 $Å^{-1}$), an additional low-energy excitation peak is clearly observed at around E = 2.2 meV.

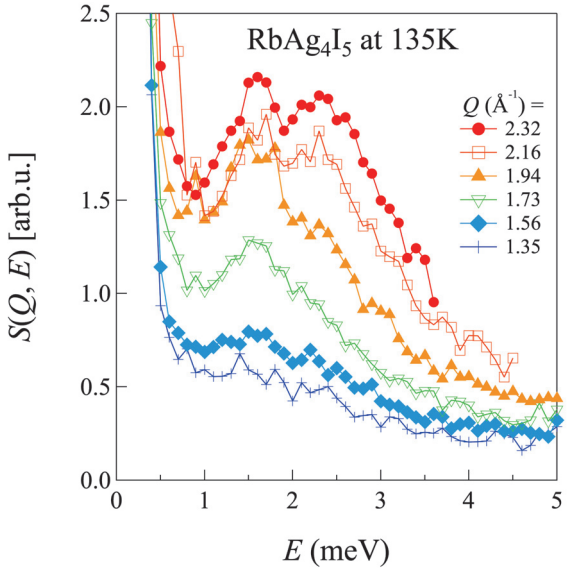

Figure 2. Energy dependence of dynamic structure factors, $S(Q, E)$, sliced at several Q points for $RbAg_4I_5$ at T = 135 K with E_i = 5.9 meV.

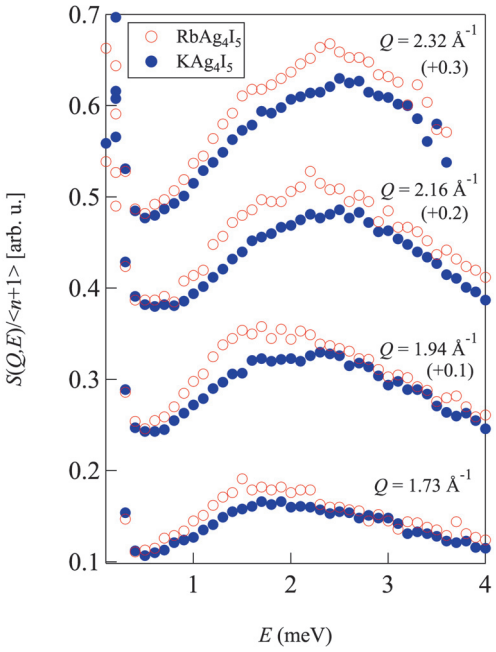

Figure 3. Energy dependence of normalized dynamic structure factors for $RbAg_4I_5$ and KAg_4I_5 at 348 K. These data are corrected by Bose factor, $<n+1> = \exp(\hbar\omega/k_BT) / (\exp(\hbar\omega/k_BT) - 1)$ and are offset in vertical direction for clarify.

Figure 3 shows the energy dependence of normalized $S(Q,E)$ for the superionic phases of $RbAg_4I_5$ and KAg_4I_5 at T = 348 K. Å^{-1}. $S(Q,E)$ for KAg_4I_5 has a single peak at around E = 1.7 meV and Q = 1.73, and the peak height is lower than that for $RbAg_4I_5$. An additional peak is observed in the vicinity of E = 2.4 meV and Q = 1.94 Å^{-1} for KAg_4I_5 which grows with increasing Q. Although the peak positions are the same for the two materials, the peak intensities for $RbAg_4I_5$ are larger than those for KAg_4I_5 at all Q, indicating that the local vibrational modes of Ag ions are easily excited in $RbAg_4I_5$ in comparison with KAg_4I_5, which would relate to the difference in ionic conductivity between the two materials.

References

[1] B. B. Owens and G. R. Argue, Science, 157 308 (1967).

[2] S. Hull, D. A. Keen, D. S. Sivia and P. Berastegui, J. Solid State Chem., 165 363 (2002).

[3] S. Geller, Science, 157 310 (1967).

[4] S. M. Shapiro, D. Semmingsen and M. B. Salamon, Proc. Int. Conf. on Lattice Dynamics, 538 (1977).

[5] D. Gallagher and M. V. Klein, J. Phys. C: Solid State Phys., 9 L687 (1976).

[6] K. Nakajima, S. Ohira-Kawamura, T. Kikuchi, M. Nakamura, R. Kajimoto, Y. Inamura, N. Takahashi, K. Aizawa, K. Suzuya, K. Shibata, T. Nakatani, K. Soyama, R. Maruyama, H. Tanaka, W. Kambara, T. Iwahashi, Y. Itoh, T. Osakabe, S. Wakimoto, K. Kakurai, F. Maekawa, M. Harada, K. Oikawa, R. E. Lechner, F. Mezei and M. Arai, J. Phys. Soc. Jpn., 80 SB028 (2011).

[7] M. Nakamura, R. Kajimoto, Y. Inamura, F. Mizuno, M. Fujita, T. Yokoo and M. Arai, J. Phys. Soc. Jpn., 78 093002 (2009).

[8] J. N. Bradley and P. D. Greene, Trans. Faraday Soc., 63 424 (1967).

[9] K. Shibata and S. Hoshino, J. Phys. Soc. Jpn., 54 3671 (1985).

S. Tahara[1,2], Y. Kawakita[3], M. Nakamura[3], H. Shimakura[4], T. Kikuchi[3], Y. Inamura[3], K. Nakajima[3], S. Ohira-Kawamura[3], T. Sunakawa[1], and T. Fukami[1]

[1]*Department of Physics and Earth Sciences, Faculty of Science, University of the Ryukyus;* [2]*Research and Utilization Division, Japan Synchrotron Radiation Research Institution (JASRI/SPring-8);* [3]*Neutron Science Section, Materials and Life Science Division, J-PARC Center;* [4]*Faculty of Pharmacy, Niigata University of Pharmacy and Applied Life Sciences*

Progress in the Dynamic Nuclear Polarization on POLANO

1. Introduction

Polarized neutron scattering is a useful method for conducting studies in materials science. One of the ways to polarize neutrons is by using a polarized proton target (PPT). As neutron-proton scattering length of the triplet channel is much smaller than that of the singlet channel [1], the neutron beam transmitted through a PPT gets polarized.

A brute-force way to polarize sufficient number of protons in the target is by applying a strong external magnetic field to it and cooling it down to a low temperature. However, even if we cool it down to 1 K and apply an external magnetic field of 5 T to it, the thermal equilibrium Boltzmann polarization of the protons is still less than 1% and the target cannot be used as a practical neutron polarizer.

To highly polarize proton spins, we can use the dynamic nuclear polarization (DNP) method. In the above mentioned situation, although the polarization of protons is less than 1%, that of unpaired-electrons is nearly equal to unity since the magnetic moment of the electron is much larger than that of the proton. The DNP method exploits the microwave-irradiation-driven transfer of polarization from unpaired-electrons to protons. To test the enhancement of the proton polarization by this method for several target materials that contain protons and unpaired-electrons and estimate their performance as neutron polarizers for POLANO, we are preparing instruments for DNP of proton spins.

2. Instruments

To cool down a target and apply an external magnetic field to it, we use the cryostat that was used by Crabb and coworkers [2]. The ^{4}He evaporation refrigerator can cool the target down to 1 K and the split coil superconducting magnet can apply the magnetic field of 5 T to it.

To measure the proton polarization, we prepared instruments, which are used in studies of continuous wave nuclear magnetic resonance (CW NMR) spectroscopy. As reported in the MLF Annual Report 2013 [3], we measured successfully the signal of a Teflon sheet, which contains fluorine nucleus whose magnetic moment is 6% smaller than that of a proton.

To irradiate microwave to a target, we prepared an extended interaction oscillator (Communication & Power Industries, VKT 2438P). The output frequency can be controlled from 138.5 GHz to 141.5 GHz by using a mechanical tuner. The output power is typically 20 W and depends on the output frequency. To control the output power, we prepared a variable attenuator (Keycom, AT-8-20). Most of the microwave power through the attenuator was directed at the cryostat using standard F-band rectangular waveguides. A small part of it was coupled off by a directional coupler (Keycom, DC-8-10) to estimate the power and measure the frequency fed to the cryostat. The spectrum of the microwave that was coupled off by the coupler was measured using a spectrum analyzer (Agilent, EXA N9010A) and a harmonic mixer (OML, M06HWD). Figure 1 depicts the measured spectrum, which clearly shows that a microwave with a frequency of 140 GHz had been generated.

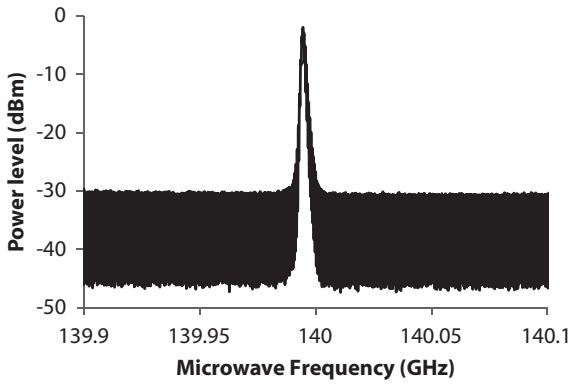

Figure 1. A spectrum of microwave through a variable attenuator and a directional coupler.

3. Test Sample

To test the system, we prepared a TEMPO (2,2,6,6-tetra-methyl-piperidine-1-oxyl), which contains unpaired-electrons, doped low-density polyethylene film, which contains protons.

First, we heated the polyethylene film using a drying oven (Sanyo, MOV-202). 1.888 g of polyethylene film (Sanipak Company of Japan, L-43) was placed on a plate made of soda-lime glass and inserted into the oven. The temperature was kept at 100 °C for 1 hour. We then set the setting temperature to a room level and waited for 2 hours.

Next, we took the film out of the oven and put it into a vacuum chamber (As One, VCP-15L) for 1 day. The pressure inside the chamber was 0.4 atm.

Finally, we doped TEMPO (Sigma-Aldrich, 214000) into the film. We took the film out of the vacuum chamber and put it together with 10 mg of TEMPO powder

into a sealed bottle made of soda-lime glass. We placed the bottle into the drying oven and kept the inside temperature at 80 °C for 1 day. We then set the setting temperature to a room level and waited for 2 hours. To prevent TEMPO from sublimating from the film, we took it out of the sealed bottle and put it into a cryopreserving container (Cryo One, SR-31).

If all the amount of TEMPO had been uniformly absorbed into the film, the spin density would be 2×10^{19} spins / cc. To estimate how much amount of TEMPO was doped into the film, we measured its electron spin resonance (ESR) spectrum. We cut off a small piece of the film and put it into the microwave cavity of an ESR spectrometer (JEOL, TE200). By scanning the external magnetic field applied to the cavity, we observed a clear ESR spectrum shown in Figure 2. Using calibration data and this spectrum, we estimated that about half of the TEMPO was absorbed into the film.

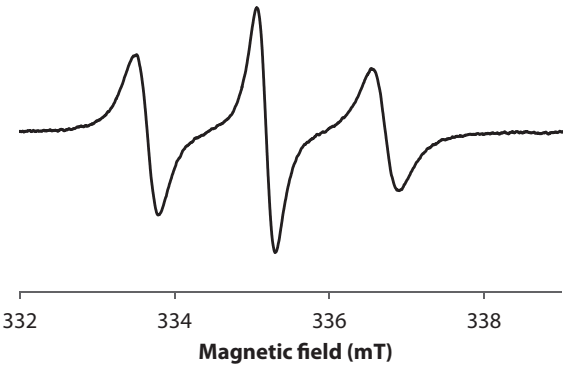

Figure 2. The ESR spectrum of the prepared test sample. The applied microwave frequency was 9.43408 GHz.

4. Plan

We can now irradiate a frequency and power tunable microwave to the target, apply 5 T external magnetic field and cool it down to 1 K. By comparing the CW NMR spectrums with and without microwave irradiation, we are going to estimate the proton polarization enhanced by the DNP method.

Acknowledgement

We thank Takayuki Kumada (JAEA) for the cooperation in measuring the electron spin resonance spectrum of the sample.

References

[1] H. A. Bethe and P. Morrison, *Elementary Nuclear Theory* (Wiley, 1956).

[2] D. G. Crabb, C. B. Higley, A. D. Krisch, R. S. Raymond, T. Roser, J. A. Stewart, and G. R. Court, Phys. Rev. Lett. 64, 2627 (1990).

[3] K. Taketani, S. Ishimoto, S. Itoh, K. Iwasa, K. Ohoyama, S. Suzuki and T. Yokoo, MLF Annual Report 2013.

K. Taketani[1,2], T. Yokoo[1,2], Y. Nambu[3], S. Itoh[1,2], S. Ishimoto[4], S. Suzuki[4], and T. Otomo[1,2]

[1]Neutron Science Section, Materials and Life Science Division, J-PARC center; [2]Institute of Materials Structure Science, KEK; [3]Institute for Materials Research, Tohoku University; [4]Institute of Particle and Nuclear Studies, KEK

^{3}He Neutron Spin Filter for POLANO

1. Introduction

A ^{3}He neutron spin filter (NSF) is one of the essential devices in POLANO for polarization of the incident neutron beam. It is required to be operated *in-situ* to provide a stable neutron polarization, and the spin-exchange optical pumping (SEOP) method is employed to polarize the ^{3}He nuclei. Since there is limited space to accommodate the ^{3}He NSF, we designed a compact system that fits well between the disk choppers and the sample chamber [1]. It is now under development and will be installed as soon as POLANO gets the first neutron beam in 2016. The first ^{3}He NSF in POLANO will cover a neutron beam diameter of 50 mm with neutron energy up to 100 meV.

2. R&D on ^{3}He NSF for POLANO

A schematic view of the ^{3}He NSF in POLANO is shown in Fig. 1. The necessary elements for *in-situ* polarized ^{3}He neutron spin filters are (1) a ^{3}He cell, (2) a homogeneous magnetic field with neutron guide fields, (3) a high-power laser with optical components for the optical pumping of Rb, (4) a heater to achieve the appropriate number densities of K and Rb, and (5) adiabatic fast passage (AFP) spin flipping of polarized ^{3}He.

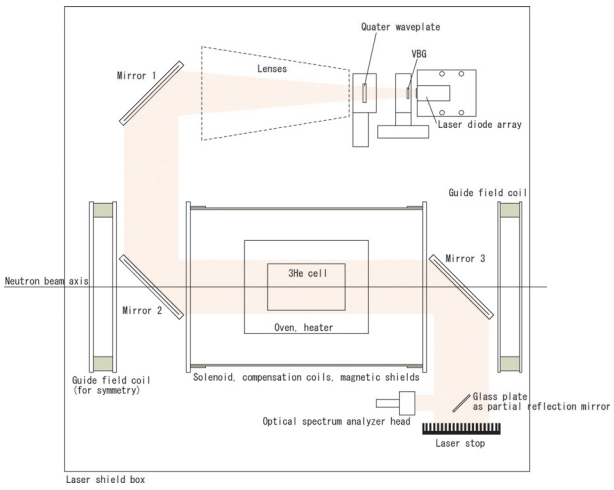

Figure 1. A schematic view of the ^{3}He NSF in POLANO. All the essential elements are packed in a laser shield box with a size of 60 cm by 60 cm by 25 cm.

(1) ^{3}He cell

We will prepare cylindrical cells made of GE180 aluminosilicate glass with a dimeter of 60 mm and a length of 60 to 100 mm. The cells will be filled with ^{3}He at 2.0 to 3.5 atm, and the effective ^{3}He thickness will range from 12 to 35 atm-cm for various measurements.

(2) Homogeneous magnetic field

A solenoid and compensation coils at both solenoid edges with Permalloy magnetic shield were designed, and a prototype magnet was constructed (Fig. 2). The neutrons are polarized in the axial direction in the ^{3}He NSF, and the spins are rotated adiabatically in the transverse direction by the magnetic guide field [2]. The compensation coils will be optimized in accordance with the guide field.

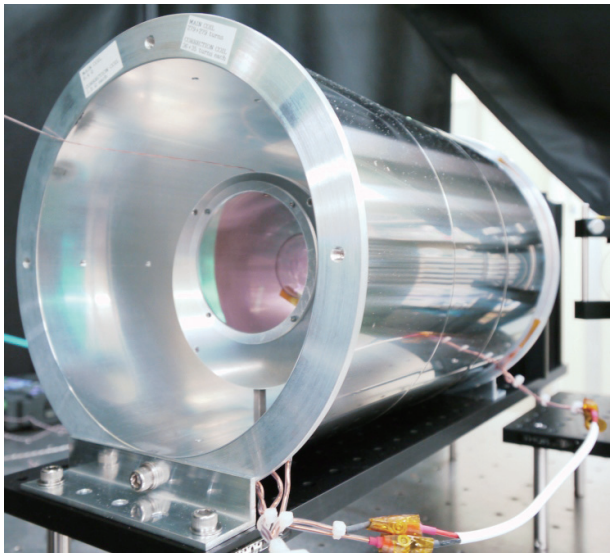

Figure 2. Magnetically shielded solenoid to produce a homogeneous field for ^{3}He NSF. The diameter of the solenoid is 20 cm and the length - 30 cm. Additional magnetic shields will be added to the both ends of the solenoid.

(3) Laser and optical components

A laser diode array with an output power of 100 W with a chirped volume Bragg (holographic) grating (VBG or VHG) emits a spectrally narrowed 795 nm light (Rb D_1 line) for the optical pumping of Rb (Fig. 3). A quarter waveplate converts the linear polarization into circular polarization. The waveplate can be remotely rotated by +/–90 degrees to change the left and right states depending on the AFP spin flipping of ^{3}He. The laser optical apparatus is shown in Fig. 4.

(4) Heater

In SEOP, hot air blowers (compressed air blowers) are commonly used to keep ^{3}He cells at an elevated

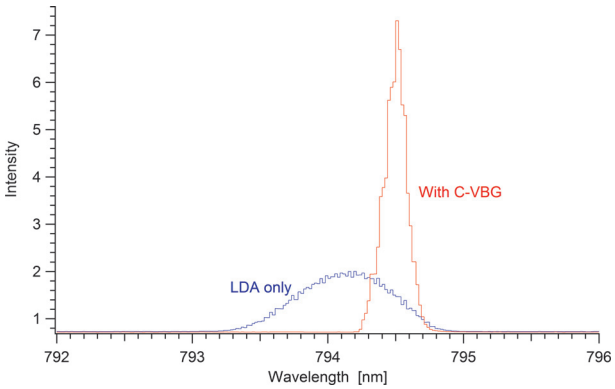

Figure 3. Laser spectra from the 100 W laser diode array (LDA) with and without the chirped volume Bragg grating (C-VBG). Not only is the spectrum narrowed, but the peak intensity is also much higher with the use of the C-VBG.

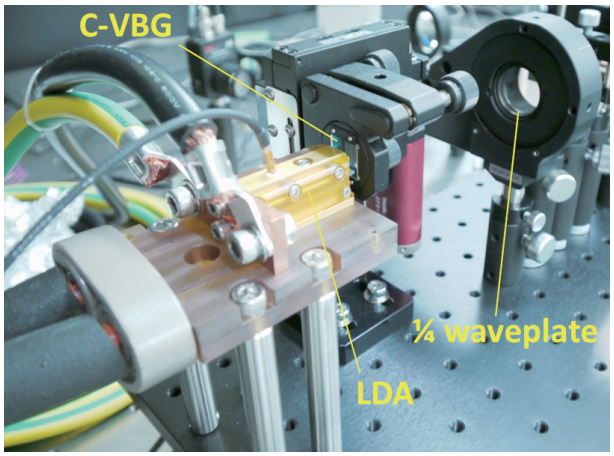

Figure 4. A picture showing the laser optical apparatus, a laser diode array (LDA), a chirped volume Bragg grating (C-VBG), and a quarter waveplate.

temperature because they do not interfere with the homogeneous magnetic field while conventional electric heaters produce unnecessary magnetic fields. However, a hot air blower occupies a fair amount of space and requires heat insulation around itself for safety. Due to the limited available space, we have decided not to use a hot air blower but a thin electric heater made of polyimide films and NiCr strips, which is attached to the outer surface of an aluminum oven for a ^{3}He cell. The NiCr strips will be specially designed in order to minimize the magnetic field interference.

(5) AFP ^{3}He spin flipper

In almost all measurements with polarized neutrons, neutron spin flipping is a must for cancelling out any systematic uncertainties. We demonstrated successfully a compact AFP spin flipper for polarized ^{3}He with an RF coil positioned inside an aluminum oven [3]. The ^{3}He spins can be flipped within a half second, and the polarization loss was less than 4×10^{-4} in one spin flip. Such an AFP spin flipper will be redesigned to fit the ^{3}He cells described in (1).

3. Safety and future upgrading

The controllers for the in-situ polarized ^{3}He NSF system are equipped with various safety mechanisms such as interlocks for the laser and the heater to meet the J-PARC safety standards. The ^{3}He NSF system will be ready for operation by the first day of POLANO's operation and the goal is to upgrade it continuously to widen the beam diameter and improve the ^{3}He polarization.

References

[1] T. Yokoo *et. al.*, "BL23 Polarized Neutron Scattering Spectrometer POLANO," in this report.

[2] K. Ohoyama *et. al.*, "Estimation of Magnetic Field Distribution for Polarized Neutron Experiments," in this report.

[3] T. Ino *et al.*, "A compact SEOP ^{3}He neutron spin filter with AFP NMR," J. Phys.: Conf. Ser. **340**, 012006 (2012).

T. Ino[1,2], M. Ohkawara[3], K. Ohoyama[4], T. Yokoo[1,2], S. Itoh[1,2], H. Kira[5], H. Hayashida[5], K. Sakai[6,7], T. Oku[6], and K. Kakurai[8]

[1]Institute of Materials Structure Science, KEK; [2]Neutron Science Section, Materials and Life Science Division, J-PARC Center; [3]Institute for Materials Research, Tohoku University; [4]Ibaraki University; [5]CROSS-Tokai; [6]Technology Development Science Section, Materials and Life Science Division, J-PARC Center; [7]Neutron Source Section, Materials and Life Science Division, J-PARC Center; [8]Quantum Beam Science Directorate, JAEA

Estimation of Magnetic Field Distribution for Polarized Neutron Experiments

1. Introduction

A polarization analysis neutron spectrometer, POLANO, has been constructed at beam line 23 (BL23) in the second experimental hall of the Materials and Life Science Experimental Facility (MLF) at the Japan Proton Accelerator Research Complex (J-PARC) [1, 2].

Since the careful control of the magnetic fields around the beam is very important for performing precise polarized neutron experiments, magnetic devices, such as guide magnets, Helmholtz coils, and so on, will be used. However, the optimization of magnetic devices during beam-times is almost impossible in pulsed neutron spectrometers. Thus, the optimization of magnetic fields by calculations and off-beam tests is required. Based on the estimation of magnetic field distributions by the finite element method, we succeeded in finding alignments of magnetic devices which can provide satisfactory high neutron polarization in the energy range of up to 100 meV. This report explains the calculation method of transportation of the polarization and its results.

2. Calculation of polarization

To optimize magnetic field distributions, we estimate the change of neutron polarization between the polarizer and the supermirror analyzer. For BL23, a cylindrical ^{3}He spin filter polarized by the on-beam spin exchange optical pumping (SEOP) technique will be used as a polarizer. When neutrons with finite velocity enter a magnetic field, the neutron spin rotates by Larmor precession. The final spin wave function ψ_f by Larmor precession can be represented using the initial spin wave function ψ_i as,

$$\psi_f = \exp\left(-i\frac{\vec{S}\cdot\vec{n}}{\hbar}\frac{2\omega l}{\upsilon}\right)\psi_i \qquad (1)$$

Here, ω, l, and υ are Larmor frequency, the length of the flight path under the magnetic field, and neutron velocity, respectively. $\vec{S}$ is the neutron spin and $\vec{n}$ is the unit vector of the magnetic field, $\vec{B}$. The average value of each spin component for ψ_f is obtained as

$$\langle S_\alpha \rangle = \frac{\hbar}{2}\psi_f^* \sigma_\alpha \psi_f \quad (\alpha = x, y, z) \qquad (2)$$

where σ_α is the Pauli matrix for α-component. From the average spin components, the neutron polarization, P_n, of the final state can be defined as

$$P_n = \frac{\langle S_x \rangle B_x + \langle S_y \rangle B_y + \langle S_z \rangle B_z}{|\vec{S}||\vec{B}|} \qquad (3)$$

Thus, when the magnetic field distribution with an interval of l is provided, the value of P_n at each point can be estimated.

The calculations of the magnetic field distribution were done using the finite element method program ANSYS in SR16000 supercomputing resources at the Center for Computational Materials Science of the Institute for Materials Research, Tohoku University. For these calculations, the z-axis is defined to be parallel to the beam direction, the y-axis is in the vertical direction, and the x-axis is perpendicular to the y-and z-axes. Since the magnetic field at the ^{3}He spin filter is parallel to the beam direction, the initial neutron spin is parallel to the z-axis. We assumed the initial neutron polarization at the spin filter to be $P_n = 1$.

3. Basic alignment of magnetic devices for BL23

Figure 1 shows the basic alignment of the magnetic field devices for BL23. Shown from left to right, are a solenoid coil, a guide coil with a width of 3 cm, square shape vertical guide magnet with pillars of permanent ferrite magnets, a Helmholtz coil with additional three coils which generate horizontal magnetic fields, a guide magnet with fan-shape with neodymium magnets, and a supermirror analyzer. The magnetic housing for the supermirror analyzer generates strong magnetic fields to the mirror; the magnetic field at the center of the housing is set to about 400 G, when the magnetic mirror is not installed.

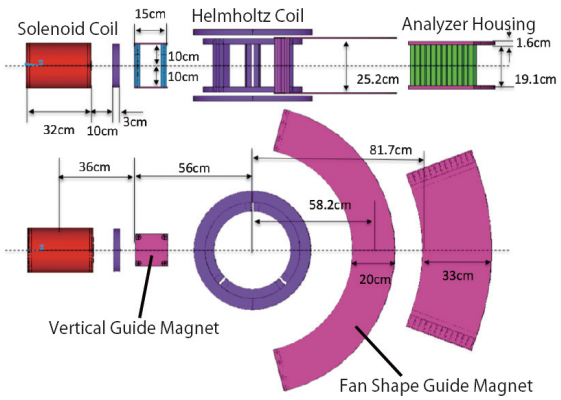

Figure 1. A typical alignment of the magnetic field devices for BL23. The beam goes through from left to right.

4. Results of the calculations of polarization

We estimate the change of polarization along the beam route to optimize the alignment of the magnetic devices in a way which minimizes the depolarization. Figure 2 shows typical results of the calculated polarization based on the found optimized alignment. The position of each device is indicated with arrows in Fig. 2(a). The calculations were done on the line at the beam center (Y = 0 cm: Fig. 2(b)), and at the 3 cm above (Y = +3 cm: Fig. 2(a)) and below (Y = −3 cm: Fig. 2(c)) the beam center. The red and blue lines indicate the angle, θ_B, between the spin and the magnetic field and the neutron polarization, P_n, respectively. For this calculation, the neutron energy was 60 meV. θ_B becomes slightly worse at z~15 cm because the direction of the magnetic field changes from horizontal to vertical in the area between the solenoid coil and the vertical guide magnet (z = 0.15~0.25 m). However, this does not affect significantly the polarization. P_n is almost constant at Y = 0 cm and +3 cm along the beam route. The polarizations at the entrance of the analyzer housing are indicated at the right-top of the figures. Even for Y = −3 cm (Fig. 2(c)), P_n = 0.96 is obtained. These values are satisfactory for practical polarization experiments. Moreover, we have found a criterion from the calculations that depolarization can be avoided if the amplitude of the magnetic field is larger than 20 G. We also confirmed the alignment ensures satisfactory polarization in the energy region between 5 meV and 100 meV, which is the target region of BL23. The results mean that we can construct the magnetic field circumstance in BL23, which gives minimized depolarization for white neutrons using the obtained alignment.

5. Measurements of magnetic field distribution

To confirm the reliability of the calculations of the magnetic field distributions in Sec.4, we measured magnetic fields using a real size test-bench of the magnetic devices whose alignment is the same as the optimized one in Sec.4. Figure 3 shows a picture of the test-bench, which consists of guide magnets, and a Helmholtz coil. The test bench does not include the supermirror housing. The magnetic fields were measured with a 3D gaussmeter.

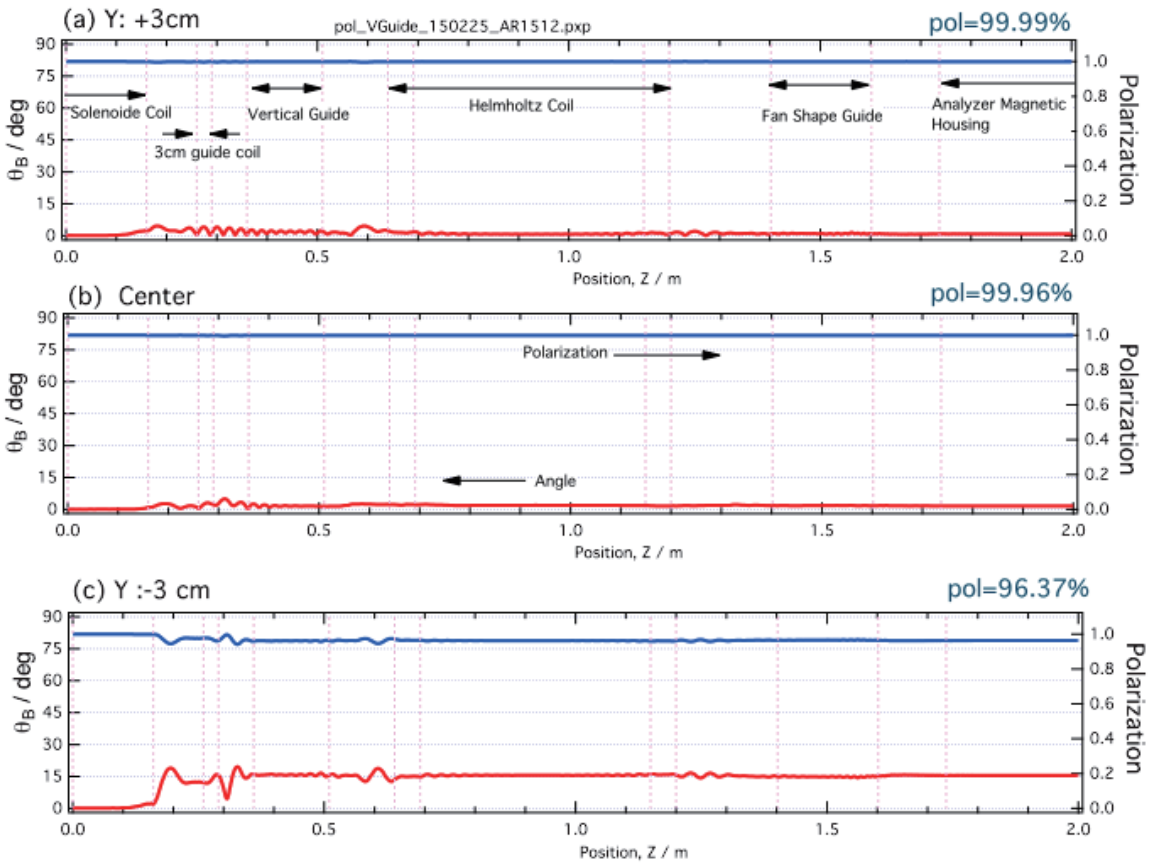

Figure 2. Position dependence of neutron polarization (blue: right axis) and the angle, q_B, between neutron spin and magnetic field (red: left axis) obtained by the calculations. The neutron energy is 60 meV. (a), (b) and (c) are the results at the beam center, the line at 3 cm below and above the center, respectively.

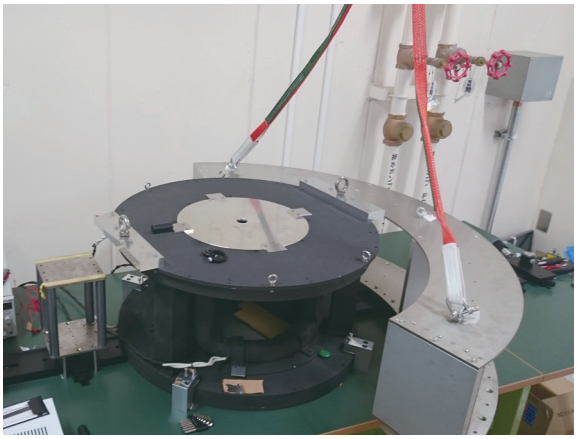

Figure 3. A picture of the test bench for magnetic field measurements.

Figure 4 shows an amplitude of the magnetic field perpendicular to the beam route obtained by the calculation with ANSYS (red line) and by measurements using the test-bench. The Helmhortz coil generated a vertical magnetic field at the sample position. For the measurements, the solenoid coil and the 3 cm guide coil in Fig. 1 were not used. The observed magnetic fields after the Helmholtz coil is lower than the calculations because the test-bench does not include the analyzer housing, which generates a strong magnetic field. Excluding this region, roughly speaking, the agreement is satisfactory. Note that the observed magnetic fields between the Helmholtz coil and the fan shaped-vertical magnet (z~80 cm) is about 20 G, which is not smaller than the criterion value (~20 G) shown in Sec.4. Since the effect of the analyzer housing increases the amplitude of the magnetic field as shown in Fig. 4, the depolarization around z~80 cm can be decreased. Though the observed magnetic field between vertical guide magnet and the Helmholtz coil (z~15 cm) is not consistent with the calculation, the observed magnetic field at the minimum point at z~10 cm is about 35 G, which is larger than the criterion value (~20 G). Based on these results, it is expected that the optimized device alignment obtained in the calculations in Sec.4 could provide satisfactory polarization in BL23 of up to 100 meV.

This work is partly supported by the S-type project of KEK (2009S09, 2014S09). The calculations were performed under the inter-university cooperative research program of the Center for Computational Materials Science, Institute for Materials Research, Tohoku University (Proposal No.: 13S0416, 14S0413)

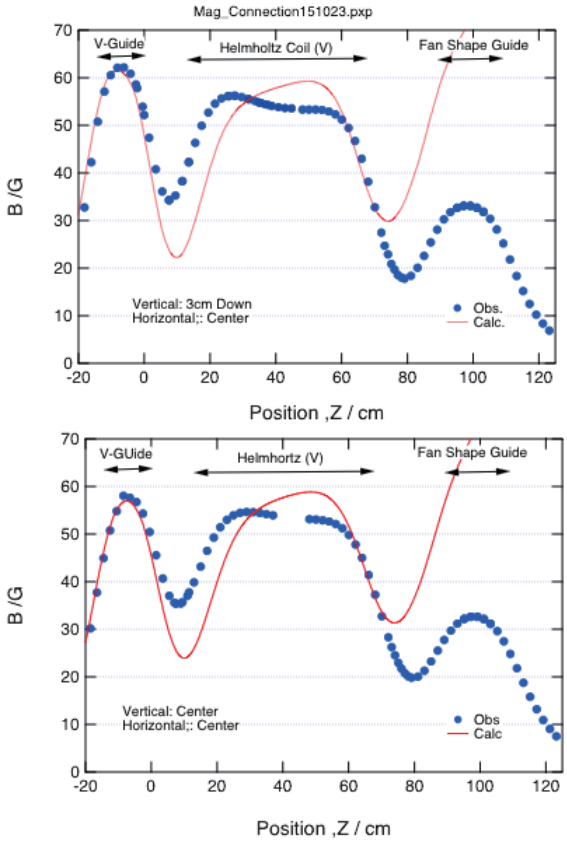

Figure 4. Amplitude of the magnetic fields perpendicular to the beam obtained by calculations (red lines) and observations (blue points). The origin of the horizontal axis is the right edge of the square-shaped vertical guide magnet. The upper and lower panels are results of the magnetic field distribution at the beam center and that along the line at 3 cm below the beam center.

References

[1] K. Ohoyama, T. Yokoo, S. Itoh, J. Suzuki, K. Iwasa, T.J. Sato, H. Kira, Y. Sakaguchi, T. Ino, T. Oku, K. Tomiyasu, M. Matsuura, H. Hiraka, M.Fujita, H. Kimura, T. Sato, J. Suzuki, H.M. Shimizu, T. Arima, M. Takeda, K. Kaneko, M. Hino, S. Muto, H. Nojiri, C.H. Lee, J.G. Park, and S. Choi, J. Phys. Soc. Jpn. 82 (2013) SA035.

[2] T. Yokoo, K. Ohoyama, S. Itoh, J. Suzuki, K. Iwasa, T. J. Sato, H. Kimura, N. Kaneko, and M. Ohkawara, J. Phys.: Conf. Ser. 502 (2014) 012046.

K. Ohoyama[1], T. Yokoo[2,3], S. Itoh[2,3], M. Sakaguchi[2,3], M. Ohkawara[4], Y. Nambu[4], T. Ino[2,3], and N. Kaneko[2,3]

[1]Ibaraki University; [2]Neutron Science Section, Materials and Life Science Division, J-PARC Center; [3]Institute of Materials Structure Science, KEK; [4]Institute for Materials Research, Tohoku University

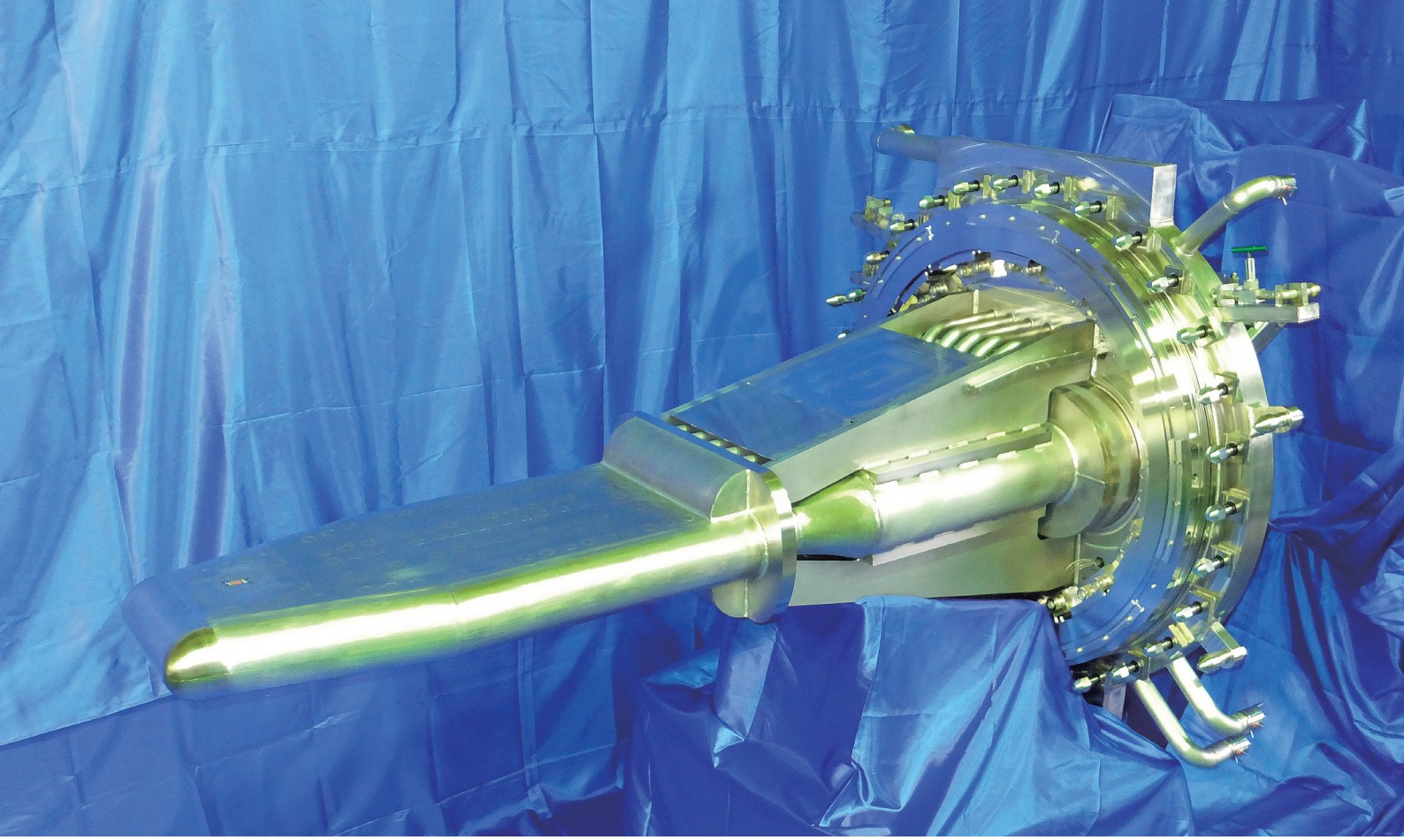

Neutron Source

Progress of the Neutron Source Section

1. 3-GeV proton beam transport facility

In fiscal year 2014, the 3-GeV Proton Beam Transport Facility (3NBT) steadily delivered proton beam with a power of 300 kW extracted from the 3-GeV Rapid Cycling Synchrotron (RCS) to the neutron production mercury target until the summer shutdown period. After the mercury target vessel was replaced in the summer shutdown period, the 3NBT delivered a 300-kW beam to the new mercury target until March, 2015, and a 400-kW proton beam since then.

On January 12, 2015, for the first time proton beam pulses were accelerated to a power equivalent of 1 MW in the 3-GeV RCS and successfully delivered to the neutron production mercury target through the 3NBT facility. It was a memorable moment for the Materials and Life Science Experimental Facility as an important milestone towards steady operation with a 1-MW beam.

Furthermore, we made efforts to reduce the beam loss through the beam transport line, especially from the muon target to the neutron production target. For example, a beam tuning tool was developed with the Strategic Accelerator Design (SAD) system to optimize the operational parameters of the magnets so that the beam loss could be minimized. An automatic beam orbit adjustment system was developed to compensate for the change of the magnetic field on the primary beam line at the muon target when the solenoid magnet of the ultra-slow muon beam line is turned on.

2. Mercury target system

The neutron production mercury target has been operated steadily at a beam power of 300 kW with mitigating pressure waves induced in it successfully thanks to the gas micro-bubbles injection. The accumulated beam power on the target reached 2050 MWh at the end of June, 2015.

The mercury vessel was replaced with an advanced type. As shown in Fig. 1, the new target vessel has a double-wall structure with a narrow mercury flow channel with 2 mm width at the target front. Part of the mercury flow is led into the narrow channel with a flow velocity of 4 m/s without passing through the bubbler, a gas micro-bubbles generator. The rest of the flow passes through the bubbler and advances to the inner wall with micro-bubbles. This structure enhances the cooling performance of the inner wall, making it possible to increase the wall thickness from 3 to 5 mm. This prolongs the life time of the target front preventing cavitation damage from operations with higher beam power.

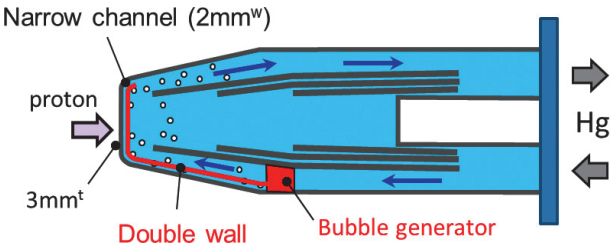

Figure 1. Illustration of cross sectional plane view of the mercury target vessel with double-walled target front.

We cut out a disk-shaped specimen from the target vessel front with a remote-handling cutting device. Unfortunately, the specimen fell inside the target vessel, as shown in Fig. 2. However, we could observe the mercury flow facing surface of the specimen, and did not observe damages there. This was a proof of the pressure wave mitigation with the gas micro-bubbles injection. Based on this promising result, we upgraded the operational proton beam power from 300 kW to 400 kW in March, 2015.

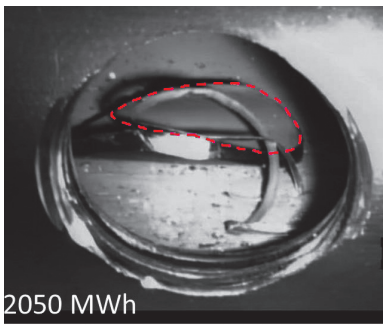

Figure 2. Photograph of the disk-shaped specimen in the target vessel. The dotted line indicates the outline of the specimen.

3. Effort to suppress tritium release during the mercury target vessel replacement operation

During the first target vessel replacement operation in 2011, a certain amount of tritium was released when surrounding air penetrated the target vessel while operations such as specimen cut-out from the target front and target vessel removal from the target trolley were performed. Major mechanism of the tritium release is the isotope exchange reaction between

the air moisture and tritium stuck in the target vessel. The accumulated beam power on the first target was 450 MWh. Considering that it was 2050 MWh on the current target vessel and the allowable radioactivity at the stack, it was needed to reduce the tritium release as much as possible.

To meet the requirement, we introduced a process to evacuate the target system by an off-gas processing system when surrounding air penetrated the target vessel (see Fig. 3). We also put plugs in the mercury pipes of the target vessel after it was removed from the target trolley. As a result, the amount of tritium released through the stack was suppressed remarkably to as low as about 12.5 GBq. This was only about 5.4% of the estimated value. It was a promising progress for us because the target is planned to be irradiated to reach an accumulated power of 5000 MWh or more in the future.

4. Progress of the spare components fabrication

2014 was the second year of a 6-year project to prepare moderators and a reflector. We continued the fabrication of a coupled moderator and a reflector. We employed new material of Au-In-Cd alloy with a composition of 74.9 : 0.5 : 24.6 in at% for the de-coupler to get neutron pulse with narrow shape. We made the Au-In-Cd alloy with a crucible and processed it to a plate configuration. And then we contacted it with aluminum alloy, the structural material of the reflector, by means of the Hot Isostatic Pressing method. It is estimated that the residual radioactivity of the used moderator and reflector assembly could be reduced to one-thousandth of that induced in the current assembly in which the Ag-In-Cd alloy was installed as the de-coupler.

We also started the fabrication of a new de-coupled moderator in which the Au-In-Cd alloy is used. Call for bids on the poisoned moderator was opened in the end of 2014.

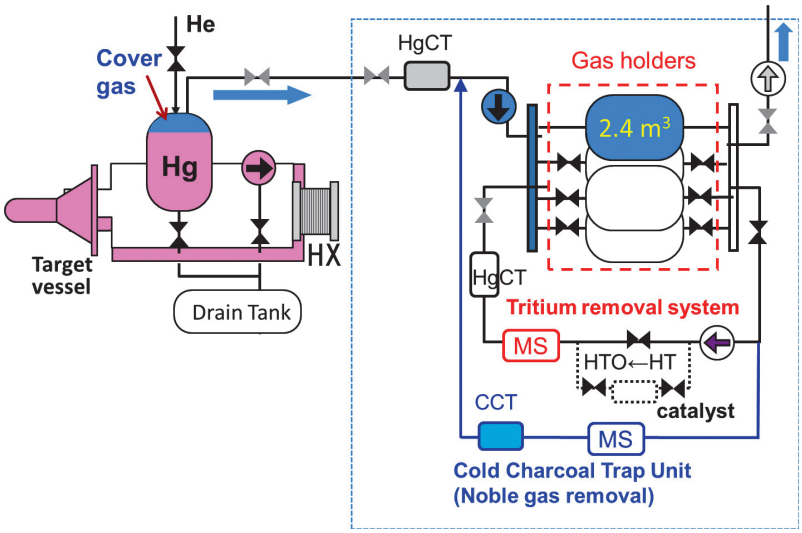

Figure 3. Conceptual drawing of the off-gas process system and the mercury target system.

H. Takada
Neutron Source Section, Materials and Life Science Division, J-PARC Center

Status of Proton Beam Commissioning at MLF

1. Beam commissioning status

In Japanese Fiscal Year (JFY) 2014, a beam for neutron and muon production with power of 300 kW had been steadily delivered. During the summer shutdown period, the LINAC's front end such as the ion source and RFQ was replaced to accelerate a beam with peak current of 50 mA to achieve the designed beam power of 1 MW. After the replacement at the LINAC, some shots of the beam were extracted from the 3-GeV rapid cycling synchrotron (RCS) to the beam dump and successfully delivered to the mercury target placed at the MLF during the beam study. In the end of JFY2014, a steady beam delivery has started with power of 400 kW.

As topics of the beam commissioning, two subjects are described below: 1) Examination of the purification of the cooling water for the muon production target and magnets placed at the M2. 2) To mitigate the damage at the mercury target vessel, beam flattening system based on octupole magnets was used to reduce the peak current density at the target.

2. Examination of cooling water purification

To isolate electrically the magnet coils from the earth, ceramic insulators were placed at the inlet and the outlet of the cooling channel. At the magnet, copper was employed as a hollow conductor of the coil. Last year, it was found that copper adheres to the inside wall of the magnet insulator at the upstream section, which may lead the short circuit of the coil. To avoid the adherence, we concluded that the water should be frequently replaced. For the cooling of the muon production target and the magnets in the vicinities, a cooling water loop, called 20 system, was installed at the MLF. Although the system is dedicated to serve the muon source, 3NBT is responsible for it for historical reason. Due to the interaction at the muon target, 8% of the beam is lost. As a result of the radiation caused by the beam loss, the cooling water is high activated, which was thought to be proportional to the beam power. About 5% of the total water flow introduced into the ion exchange resin to decrease the impurities caused by erosion at the cooling channel of the magnet has high activation. After the beam operation, high dense tritium and Be-7 was observed in the water by the measurement performed by radiation safety group with liquid scintillator and gamma spectrometer. The tritium production rate normalized by the integration of the beam power was constantly observed as 0.2 Bq/cm^3/MWh, which showed good agreement with the result from the PHITS code. On the contrary, the production rate of Be-7 was scattered from 1×10^{-4} to 0.1 Bq/cm^3/MWh. Even though the density of Be-7 at the discharge line for the 20 system was much lower than the value prescribed by the Japanese law, the local government required us to decrease the radiation to an undetectable level at the transfer line discharging the water into the ocean so that decrease of the Be is required.

To match this condition, we decided to install an additional purification system employed with the ion exchange resin. To estimate the capture rate of Be at the ion resin, the Be-7 density was measured by using actual waste water and test loop. In the examination, Be-7 density was measured at the initial condition. After 1 h flow of the loop, the density was measured again. It was found that the ion exchanger resign reduced 99.9% of Be-7, which indicated 1/1000 of the density. In JFY 2014, the system will be fabricated and will be installed during the summer of 2015.

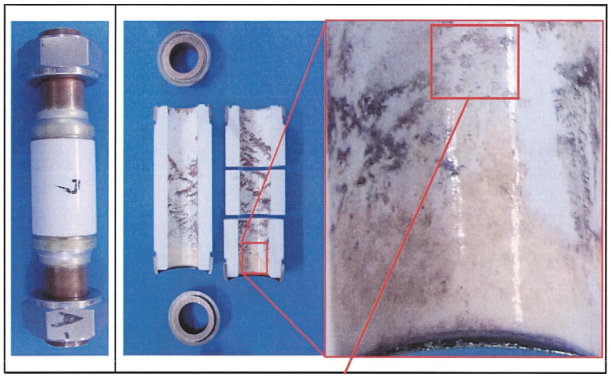

Figure 1. Status of magnet insulator adherences of copper at inside.

3. Development of beam flattening system

Since pitting damaged at the mercury target vessel is known to be proportional to the 4th power of peak intensity of the proton beam, it is required to decrease the peak intensity so a beam flattening system was developed for that purpose. The 3-GeV proton beam extracted from the RCS is well described by a simple Gaussian. With ordinary beam optics, the beam shape remains a Gaussian at all positions. Using nonlinear optics with octupole magnets, the beam particles located at the beam periphery are deflected toward the beam center, which flattens the beam distribution. To obtain a flat distribution in both the horizontal and

vertical directions, two octupole magnets are required. In FY2013, octupole magnets were installed at the beam line shown in Fig. 2. After replacement of the muon production target from fixed type to rotating one, octupole magnets can be fully utilized for user beam operation.

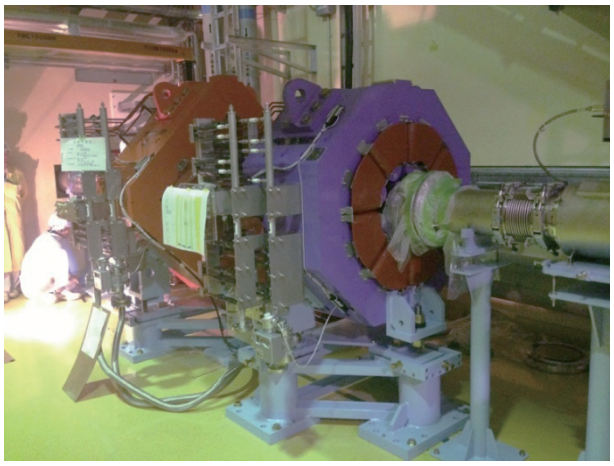

Figure 2. Octupole magnet installed at the beam transport.

In order to obtain a flat beam distribution with an octupole magnet, the beam width at the octupole magnet is expanded to a large β amplitude, which is proportional to the square root of the beam width. The physical aperture of the quadrupole magnets was fixed at 300 mm; therefore, we set the physical aperture of the octupole magnets to 300 mm. For linear beam optics, the admittance of the beam is designed to be 324 π mm mrad, which is given by the beam collimator placed at the RCS. A recent study of the RCS shows that the transverse emittance will be reduced to as little as 250 π mm mrad. Therefore, the beam admittance at the octupole magnet must be 250 π mm mrad and β is set to 200 m at the octupole magnets.

In January, 2015, the beam profile was measured by a profile monitor placed at 1.8 m upstream of the mercury target for the case of with and without octupole magnets. The obtained beam profile is shown in Fig. 3. Although some disagreement existed between experiment and calculation, the beam shapes were found to be controlled as predicted in the design calculation. By excitation of the octupole magnet, the beam halo was converged to the target center. It was also found that the heat and the dose of neutron produced at the target vicinity such as shielding and reflectors decrease. The calculations indicate that, by introducing octupole magnets, the peak current density can be reduced by 30%. Note that the present nonlinear optics system represents the first attempt to install such a system in a MW-class hadron accelerator.

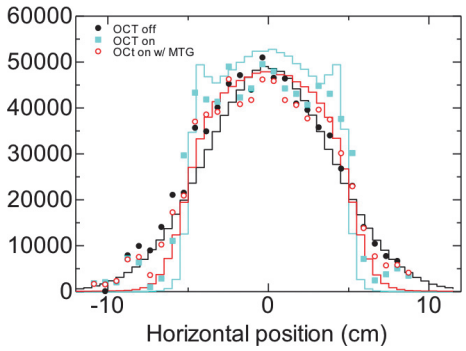

Figure 3. Beam profile in horizontal direction obtained by beam monitor placed at the entrance of the neutron target compared with calculation with (cyan) and without octupole magnets (black) and muon production target (red).

S. Meigo[1], M. Ooi[1], A. Akutsu[1], T. Kawasaki[1], M. Nishikawa[1], and H. Fujimori[2]
[1]*Neutron Source Section J-PARC Center, JAEA;* [2]*Muon Section J-PARC Center, KEK*

Operation Experience for Mercury Target in 2014

1. Introduction

In the summer of 2014, the mercury target vessel was exchanged to #5 from #3. The target #3 had been operated since January, 2012, and the injection of gas-microbubbles into mercury was started in October, 2013. The injection of helium gas microbubbles into mercury is one of the prospective technologies available to reduce pressure wave induced cavitation.

In the process of proton beam injection into the mercury target vessel, pressure waves are generated in mercury by rapid heat deposition due to proton beam incidence. Negative pressure waves were generated near the target vessel during the pressure wave propagation due to the difference in the sound impedance between mercury and the target vessel. This negative pressure generates cavitation, which causes severe erosion damage to the target vessel. This damage determines the service life of the target vessel. If gas microbubbles are injected into mercury, microbubbles absorb and attenuate the pressure waves and mitigate the damage due to cavitation erosion. A gas microbubble generator had been developed and installed in the mercury target vessel #3 [1].

Before exchanging the target vessel, the beam window portion of target vessel #3, where the severe damage was predicted, was sampled by using an annular cutter to evaluate the effect of the gas microbubble injection on cavitation damage formation, and to produce specimen for post-irradiation examination.

The operation of the newly installed target vessel #5 started in November with beam power of 300 kW. In March, 2015, the beam power was increased to 400 kW . Immediately after the operation with the new target vessel started, a wrong alarm from the mercury detector was raised.

2. Cutout and inspection of the target vessel

The cutting was performed in a hot-cell using a remotely controlled cutting machine with an annular cutter with outer diameter of 55 mm. The cutting was performed without any coolant. In the process, the innermost specimen fell inside the vessel. The fallen specimen was not retrieved from the target vessel because of concerns regarding the contamination control inside the hot-cell.

Video inspection with a CMOS camera was performed to observe the cavitation damage inside the interior surface of the beam window region. Since the equivalent dose rate of the beam window was approximately 320 Sv/h, signal noise was superimposed on the images obtained using the CMOS camera. The inspection did not obtain a clear image of the interior surface demonstrating cavitation damage mitigation by the gas microbubble injection. Two of the three cameras used herein were damaged during the inspection because of high doses of radiation.

Figure 1 shows the photographs of the inner surface of the beam window of target vessel #3 and a cross section of the cut hole obtained by the radiation proof camera. It can be seen that the large machining swarf that suggest the remaining of ductility on specimen. Furthermore, no obvious cavitation damage was noticed. In the cross section of the cut hole, the severe cavitation erosion and V-shape erosion that was observed at the SNS target vessel was not registered here. The conclusion is that the cavitation damage due to the proton beam-induced pressure waves was dramatically reduced by the gas microbubbles. Although it was impossible to quantitatively measure the damage depth, it seems that the depth was less than 0.25 mm of the depth obtained from target vessel #1, because it was observed that the concave surface of the inner wall was relatively smooth.

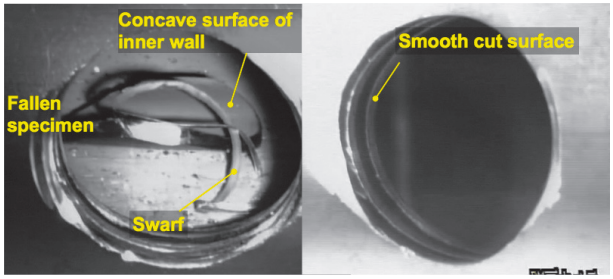

Figure 1. Captured images of the cut specimen and cut surface of target vessel #3.

3. Wrong alarm from the mercury detector and countermeasures

Immediately after the operation with target vessel #5, an alarm indicating that mercury leaked into the safety shroud surrounding the mercury vessel was raised. The leakage of mercury into the safety shroud was detected by the electric resistance between the target vessel and the wire set in the shroud. To reset the alarm, the mercury should be removed from the space between the vessel and the wire. However, the alarm

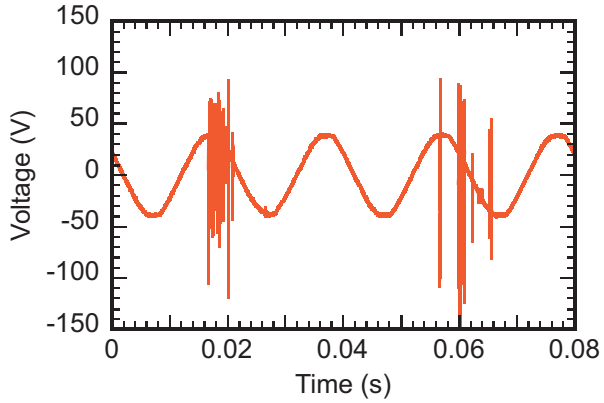

Figure 2. Time history of the voltage between the target vessel and the mercury detector when the false alarm was raised.

could be reset without removing it. We assumed that it was a false alarm and started an investigation. Figure 2 shows the history of the electrical voltage between the target vessel and the wire. Alternative voltage of 50 Hz was applied between the target vessel and the wire. Noises were observed every 40 ms (25 Hz), which have the same frequency as the beam injection. Hence noise-cut filter was installed between the target vessel and the wire. It was effective in killing the noise and the false alarm.

Reference

[1] H. Kogawa *et al.*, J. Nucl. Sci. Technol. **52** (2015) 1461.

H. Kogawa, T. Naoe, T. Wakui, and K. Haga
Neutron Source Section, Materials and Life Science Division, J-PARC Center

Development Status of the AuIC Decoupler

1. Introduction

Thermal neutron absorber, called "Decoupler" is used for producing neutron beams with sharp pulse shape. The new gold-indium-cadmium (AuIC) alloy as a decoupler is expected to have a better capability of reducing the residual radio-activity than the previous silver-indium-cadmium (AIC) one [1]. This AuIC will be installed to spare moderator-reflector assembly. In order to implement Au-In-Cd alloy as a decoupler, it is to be bonded with an aluminum alloy (A5083), which is a part of the structural material of moderator and reflector, to remove the high heat deposition by neutrons from the mercury target during high intensity proton operation. By adopting the hot isostatic pressing (HIP) method, an optimal HIPing condition was also found for a small size case with dimensions of 30 mm in diameter and 2 mm in height to assure a required bonding strength of more than 30 MPa [2]. However, there was still a critical engineering issue of the actual fabrication of moderator-reflector assembly with enlarged size. We report on the development status of AuIC decoupler, especially for reflector assembly.

2. Development status of AuIC decoupler for reflector assembly

In order to install AuIC alloy to the neutron beam hole of the actual reflector assembly, we produced the AuIC plates with dimensions of 2 or 3 × 130 × 130 mm from AuIC alloy ingots. These plates were cut to proper shape by using wire cutting (WEDM) to spread along the neutron beam hole and cover it. The thickness of the AuIC alloy plate was satisfactory within ±10% of the thickness requirements, however, it was noticeable that the plate had lumpy surface. HIPing without surface treatment would not provide the necessary bonding strength, which was observed in the previous study between AIC and aluminum alloys. We performed small sized HIPing tests with three different surface treatment conditions, such as no surface treatment, emery paper grinding up to 500 grift, and up to 1200 grift, to investigate the effect of bonding on the HIPing process. HIPing was performed under the condition of 535°C, 100 MPa and 1 hour holding time, which is optimal HIPing conditions for a small size case. Regardless of the surface treatment, the tensile strength gave over 90 MPa, which was 3 times higher than the required one. In the tensile test, fracture position was bonding area. The surface treatment with emery paper grinding up to 500 grift was applied for actual sized HIPing. Before actual sized HIPing, middle sized HIPing (100 × 100 mm) test was performed to confirm the effect of the enlarged size, such as the tensile strength and the bonding area. HIPing was performed under the same HIPing conditions, small sized, as mentioned above. Separation at the bonding area was not observed. Result of the tensile test also gave over 80 MPa, and the fractured position was bonding zone. We performed an actual sized HIPing of the reflector assembly based on the obtained results. After HIPing, the HIPed block was machined to parts of the reflector, which had neutron beam holes. AuIC plates were embedded in the neutron beam holes. No separation was found at the embedded area after ultrasonic inspection, as shown in Fig. 1. At present, we are continuing to the next step, fabricating a spare reflector.

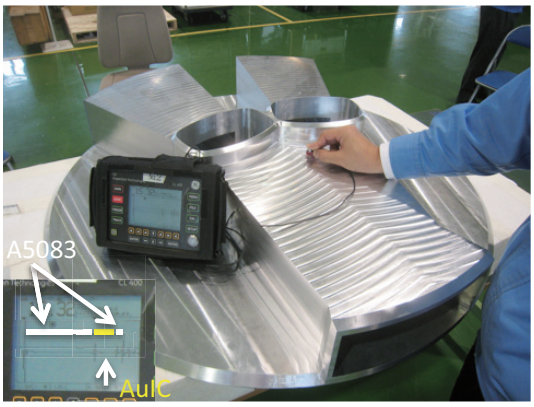

Figure 1. Ultrasonic inspection of the neutron beam hole of the reflector. The AuIC plates are embedded in the neutron beam holes. No separation was found by ultrasonic inspection.

Acknowledgment

We thank for the cooperation of Metal Technology Co. Ltd. to fabricate the spare reflector assembly. We also thank the NAT staff for their help.

References

[1] M. Harada *et al.*, Journal of Nucl. Mat. Vol. 398 (2010) pp.93-99.

[2] M. Ooi *et al.*, Journal of Nucl. Mat. Vol. 450 issue 1-3 (2014) pp.117-122.

M. Ooi, M. Teshigawara, M. harada, and G. Noguchi
Neutron Source Section, Materials and Life Science Division

Upgrade of the MLF Control Network System

1. Introduction

At the Materials and Life Science Experimental Facility (MLF), four LANs are supported. One of them, J-LAN, serves for the MLF users. The rest, which are used for facility control, are called 3NBT-Control-LAN, MLF-Control-LAN and MLF-Monitor-LAN. The 3NBT-Control-LAN is used for control of the 3 GeV proton beam transport line (3NBT), is located in the 3NBT building and the north side of the MLF building. The MLF-Monitor-LAN monitors MLF's network cameras, whose number exceeds 100. The network traffic of the cameras is normally high and that traffic is isolated from the MLF-Control-LAN. The MLF-Control-LAN is used for the MLF control system which controls many instruments for both the neutron source facility and the muon source facility in MLF.

2. Objective

The network hardware of the 3NBT and MLF was designed as a part of the J-PARC control LAN which was installed from 2005 to 2007. This network system is maintained and extended, but eventually it ages and needs gradual replacement. So, we have performed replacement and upgrade of the network system, including network speed enhancement. In the MLF, the system's replacement has been planned for the period between 2013 and 2015. Although it takes three years, the operation of the MLF must continue during this time. High reliability would be required even if old and new network systems are mixed.

3. Equipment

The concept of the redundant network system of J-PARC is shown in Fig. 1. Taking into account the fact that the future traffic load and network speed between the MLF and CCR would increase, we upgraded the 1st and 2nd edge switches of 20 Gbps network speed for the MLF and 10 Gbps for the 3NBT, and the terminal switches of 1000 MBps. In addition, the 2nd edge switches and the important terminal switches are duplicated based on the concept of the redundant system. Models of the previous and the new LAN switches are shown in Table 1.

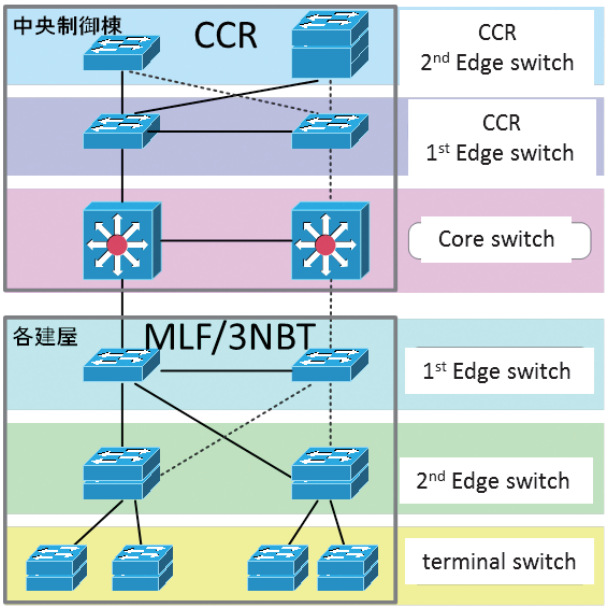

Figure 1. Concept of the redundant network system of J-PARC.

Table 1. list of the LAN switches.

	Previous	Replaced
1st Edge switch	BlackDiamond BD6804	Summit X650
2nd Edge switch	Alpine 3804 Summit48si	Summit X480
Terminal switch	Allied Telesis switch	Summit X440

4. Summary

The LAN switches have been replaced gradually from 2013 to 2015 in the following regions:

2013: 3NBT and 1st Edge switches of the MLF

2014: MLF Control-LAN

2015: MLF Monitor-LAN.

As the maintenance period in J-PARC is scheduled from July to September, our upgrade, including the system check after replacement, had been done in this period of every year. The replacement works will be completed by September, 2015.

Acknowledgement

We thank to Kikuzawa, Kawase and Yukawa for their help with this work.

M. Ooi, K. Sakai, and A. Watanabe
Neutron Source Section, Materials and Life Science Division

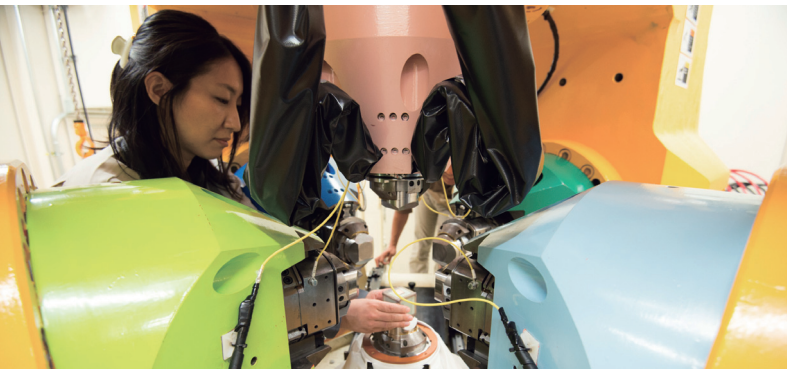

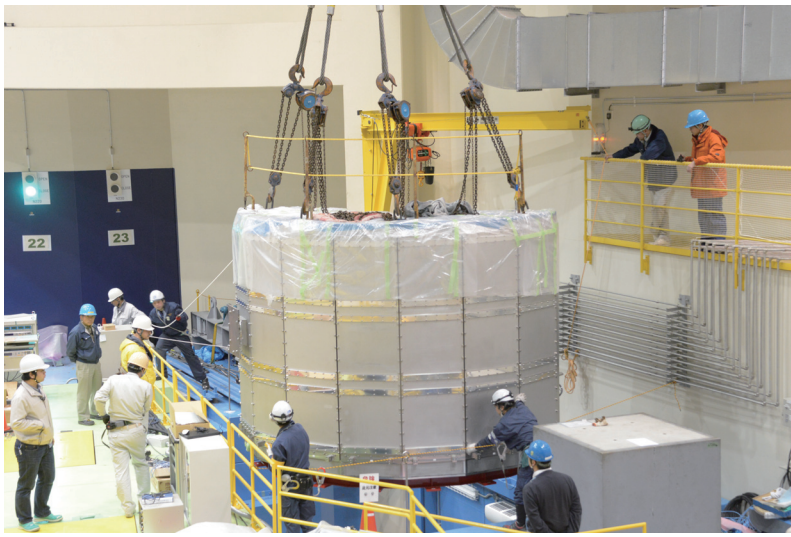

Neutron Science

Neutron Science Section

1. User Program

In the 2014A and 2014B proposal rounds, 17 neutron instruments were in operation for users and 603 proposals were applied to them. The number increased dramatically from 475 in 2013. 345 proposals or 57% of the proposal applications, were approved. The reserved ones were 81 and the rest were not approved. The beam operation scheduled from January 17 was highly affected by the fire accident in the muon area in MLF and the problems at RCS and the neutron source, so a total of 33.5 days of user beamtime was lost. The experiments, which could not be carried out in the term from January to March, were carried over into 2015 as exceptional measures.

2. Instruments development and construction

The layout of the neutron instruments at MLF as of the end of JFY 2014 is shown in Fig. 1.

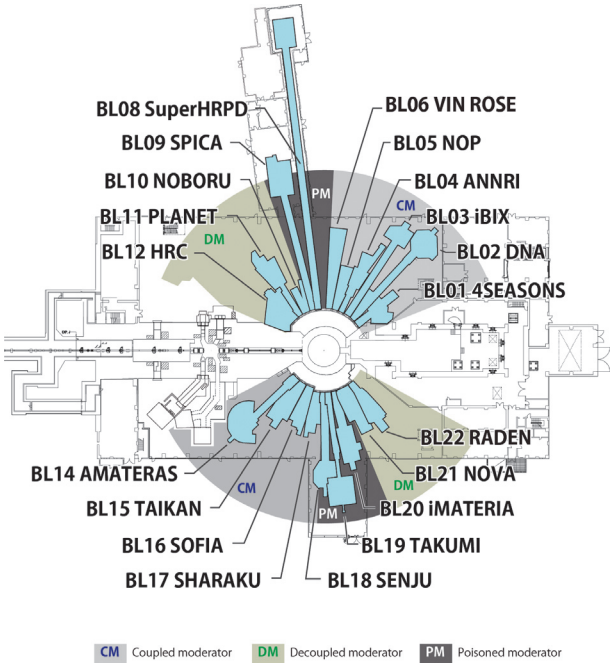

Figure 1. Layout of the neutron instruments at MLF as of JFY 2014. BL06 & 22 had proceeded to the commissioning phase in this fiscal year. BL23 remained under construction.

Kyoto University and KEK installed the VIN ROSE at BL06, which consists of a neutron resonance spin echo (NRSE) instrument and a modulated intensity by zero effort (MIEZE) instrument. The construction of the shielding and the interlock system was completed and the VIN ROSE received the first neutron beam on April 22, 2014 (Fig. 2). Since then, the VIN ROSE has been under commissioning. The performance of the beam transport system has been evaluated and the devices tuned.

Figure 2. First beam of the VIN ROSE.

At BL22, the energy-resolved neutron imaging system, RADEN, was installed by JAEA as a public beam line instrument. The RADEN received the first neutron beam on November 4, 2014. Test imaging measurements of several samples are in progress. An example is shown in Fig. 3.

Figure 3. First imaging on RADEN.

3. International Activities

MLF held the 2nd MLF School from December 16 to 19. 22 students (13 from Japan, 9 from foreign countries) participated and enjoyed lectures and actual experiments using muon and neutron beams (Fig. 4). The Neutron Science Section contributed to the neutron part of the school. 7 neutron instruments were provided for practical experiments.

The 14th Korea-Japan Meeting on Neutron Science was held from January 7 to 9 at the Ibraki Quantum Beam Research Center. 50 Japanese and 29 Korean

scientists participated and recent scientific and instrumental topics were presented in 59 oral and poster presentations. Also, the future plans for the Korea-Japan collaboration in neutron science was discussed. (Fig. 5)

Figure 4. MLF school students performing thier experiment at SIKI, BL01.

Figure 5. Participants of the 14th Korea-Japan Meeting on Neutron Science.

4. Resultant outcomes

The research activities in neutron science at MLF resulted in more than 110 papers. The number includes articles in influential journals such as Nature Physics, Nature Communications.

Two staff members, Dr. H. Nakagawa and Dr. N. L. Yamada won the Encouraging Prize of the Japanese Society for Neutron Science. Prof. M. Hino of Kyoto University received the Technology Prize from the Japanese Society for Neutron Science for his work in developing neutron optical devices for VIN-ROSE.

We distributed 6 press releases on scientific outcomes and technical development from our beam lines:

- Combination of neutron and X-ray inelastic measurement reveals the whole scheme of electron excitation states: Electron doping effect on high-energy magnetic excitations in high-Tc cuprate. (Apr. 25, 2014)
- How does water define the shape of DNA?: Local dynamics coupled to hydration water determines DNA-sequence-dependent deformability. (Aug. 29, 2014)
- Combination of neutron and X-ray inelastic measurement reveals the whole scheme of electron excitation states: Electron doping effect on high-energy magnetic excitations in high-Tc cuprate. (Apr. 25, 2014)
- Finding hydrogen in Iron dissolved under high-pressure: Determination of site occupancy of interstitial deuterium atoms in face-centred cubic iron. (Sep. 26, 2014)
- New elemental analysis realized with J-PARC: Development of Time-of-flight prompt gamma-ray analysis (TOF-PGA) for multi-elemental analysis. (Dec. 22, 2014)
- New hydride with Cr: Predicted by the first principle calculation and confirmed by neutron scattering. (Mar. 24, 2015)

K. Nakajima[1], Y. Kawakita[1], S. Itoh[1,2], and T. Otomo[1,2]

[1]Neutron Science Section, Materials and Life Science Division, J-PARC Center; [2]Institute of Materials Structure Science, High Energy Accelerator Research Organization, KEK

BL01: 4D-Space Access Neutron Spectrometer 4SEASONS

1. Introduction

4SEASONS is a thermal neutron Fermi-chopper spectrometer for inelastic scattering measurements, and one of the Public Beamlines in MLF [1]. It is operated by 6 instrumental scientists and 1 dedicated engineer. In fiscal year 2014, 37 General Use proposals, including 2 trial ones, were applied for, and 27 of them were approved. 8 proposals were submitted by international users. The major research field was strongly correlated electron system and magnetism, which dominated 70% of the General Use proposals in 2014. The high interest in these research fields seems to be natural considering that 4SEASONS was originally constructed for the research project of the copper oxide high-temperature superconductivity [2]. However, it should be noted that a sizeable number of proposals belong to other research fields such as thermoelectric materials and catalysts. In addition to the General Use proposals, one Strategic Use proposal for the Element-Strategy Project for electronic materials was submitted and approved. Unfortunately, a few of the approved proposals were postponed for 2015 because of an unexpected long-term shut-down of MLF.

2. Development in the Fermi chopper

The original Fermi chopper of 4SEASONS holds a slit package with 65 × 70 mm cross-section and 100 mm depth. Its designed maximum rotation frequency was 600 Hz [1]. However, in 2011, it was found that the rotation was unstable at high frequencies because of a secular change of the slit package, and we restricted the rotation frequency at 350 Hz and lower. This situation restricted severely the available energy resolutions, especially for high-energy experiments. Accordingly, we developed a new Fermi chopper, which was manufactured by MIRROTRON Ltd. and SKF Magnetic Bearings (Fig. 1). The new Fermi chopper has a more compact slit package whose cross-section and depth are 58 × 53.4 mm and 20 mm, respectively. The spacing of the slits is designed so that it gives the same energy resolution as the original chopper. Thanks to the compact design, it can rotate stably at up to 600 Hz. Another important benefit of the shallow depth slits is that the chopper provides much higher neutron transmission than that of the original chopper particularly for low energy neutrons and high rotation speeds [3]. A test measurement with the new chopper performed in the end of fiscal year 2014 showed that the ratio of available neutron flux between the new chopper and the original chopper is, for example, 1.9 for 43 meV neutrons and 250 Hz rotation. It reaches even 17 for 18 meV and 300 Hz. The new Fermi chopper will be available for the users program in 2015.

Figure 1. The Fermi chopper translation unit with the original and new Fermi choppers being installed on 4SEASONS by the technical support staffs.

Simultaneously, we are developing another Fermi chopper, called MAGIC chopper, which utilizes supermirror-coated slits [4]. In 2014, we operated the prototype of the MAGIC chopper on BL01. Although the available neutron flux was much lower than the expected values due to the low reflectivity of the utilized supermirrors, we verified successfully the basic performance of this type of chopper. Now we are developing a new slit package with higher-reflectivity supermirrors.

3. Increase of detectors

The vacuum scattering chamber of 4SEASONS is equipped with 11 detector banks. Each of the detector banks can hold 32 pieces of 2.5 m-long ^{3}He position sensitive detectors, and the whole set of detector banks can provide scattering angle in the range of −35.3° − +130.5° in the horizontal [1]. However, the detector banks are not fully occupied due to the recent shortage and the resulting higher price of ^{3}He gas, and it is desired to fill as much vacancies as possible. Following 2013, we installed 33 pieces of detectors in fiscal year 2014, which resulted in the maximum scattering angle in the horizontal of 84°. In addition, we have already purchased another 13 pieces of detectors. They will be available in fiscal year 2015.

4. Background originating from delayed neutrons

Suppressing background scattering is critical for high-quality inelastic neutron scattering experiments, and the background problem has been continuously investigated on 4SEASONS. Recently we found that a continuous background that oscillates in synch with the rotation of the Fermi chopper was observed even in the time region when neutrons should be suppressed (Fig. 2). The characteristics of the background strongly suggest that high-energy delayed neutrons continuously emitted from the mercury target are its cause [5]. A similar oscillating background was observed by a chopper spectrometer at the ISIS facility of the Rutherford Appleton Laboratory when the facility used uranium as the neutron target [6]. The observation on 4SEASONS demonstrated that the effect of the delayed neutrons is carefully considered even in facilities that do not use fissionable targets.

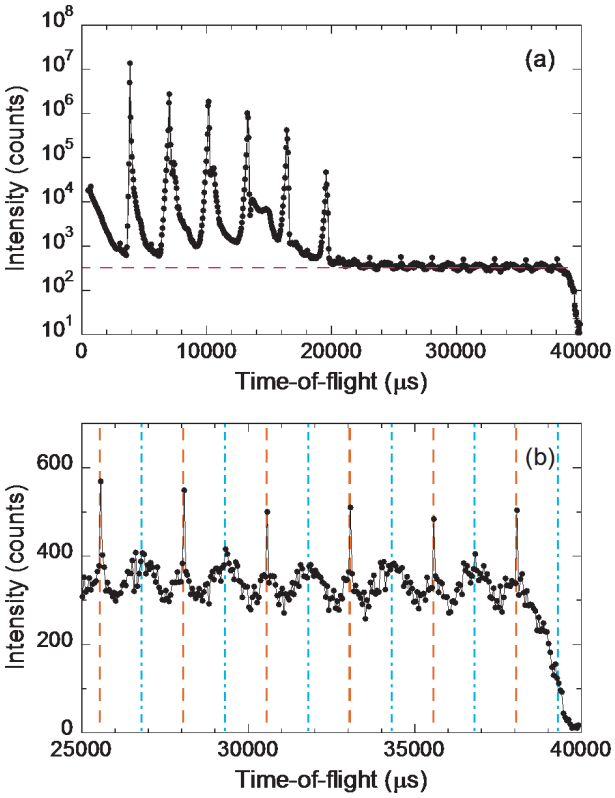

Figure 2. (a) A time spectrum acquired by 4SEASONS. The dashed line shows the background dominated by delayed neutrons. (b) Magnified view of the panel (a) in the time range between 25 000 μs and 40 000 μs. Dashed and dash-dotted lines show times when the Fermi chopper opens and rotates by π/2, respectively [5].

References

[1] R. Kajimoto, M. Nakamura, Y. Inamura, F. Mizuno, K. Nakajima, S. Ohira-Kawamura, T. Yokoo, T. Nakatani, R. Maruyama, K. Soyama, K. Shibata, K. Suzuya, S. Sato, K. Aizawa, M. Arai, S. Wakimoto, M. Ishikado, S. Shamoto, M. Fujita, H. Hiraka, K. Ohoyama, K. Yamada, and C. H. Lee, J. Phys. Soc. Jpn. **80**, SB025 (2011).

[2] M. Arai *et al.*, Grant-in-Aid for Specially Promoted Research from MEXT (17001001).

[3] M. Nakamura and R. Kajimoto, JPS Conf. Proc. **1**, 014018 (2014).

[4] M. Nakamura, M. Arai, R. Kajimoto, T. Yokoo, K. Nakajima, and Th. Krist, J. Neutron Res. **16**, 87 (2008).

[5] R. Kajimoto, M. Nakamura, Y. Inamura, K. Kamazawa, K. Ikeuchi, K. Iida, M. Ishikado, K. Nakajima, M. Harada, and M. Arai, JPS Conf. Proc. **8**, 036001 (2015).

[6] M. Arai, A. D. Taylor, S. M. Bennington, Z. A. Bowden, R. Osborn, M. Kohgi, K. Ohoyama, and T. Nakane, Proc. the 11th Meeting on Inter. Collaboration of Advanced Neutron Sources (KEK Report 90-25, 1991), p. 644.

R. Kajimoto[1], M. Nakamura[1], Y. Inamura[1], K. Kamazawa[2], K. Ikeuchi[2], K. Iida[2], and M. Ishikado[2]

[1]Neutron Science Section, Materials and Life Science Division, J-PARC Center; [2]Neutron R&D Division CROSS-Tokai

Oscillating Radial Collimators for the Chopper Spectrometers at MLF in J-PARC

1. Introduction

Inelastic neutron scattering (INS) measurement using chopper spectrometers has greatly contributed to the development of materials science. A chopper spectrometer is still a flagship instrument in high-power pulsed spallation neutron source facilities, such as the Materials and Life Science Experimental Facility (MLF) in the Japan Proton Accelerator Research Complex (J-PARC). Even though the MLF provides a high-intensity neutron beam, the countermeasure against the background is indispensable in the INS measurement due to the weak signal during the inelastic process. Recently, INS measurements under high temperature or high magnetic field have been frequently required [1]. Obviously, the sample environment apparatus causes unwanted scattering and affect the data quality. In order to overcome these background problems in the INS measurement under special sample environment, we developed oscillating radial collimators specifically for the chopper spectrometers at MLF in J-PARC. A radial collimator has been conventionally used to suppress the off-sample parasitic scattering without perturbing the sample scattering [2, 3]. The performances of newly-developed radial collimators will be described in this report.

2. Design and Operation of Radial Collimators

We have developed two types of oscillating radial collimators in-house based on the result of preliminary evaluation tests for many kinds of shielding blades [4]. One is made of Gd_2O_3 shielding blades and the other of Cd shielding blades. The total thickness of a Gd_2O_3 blade is 100 μm, that is 25 μm Gd_2O_3 + 50 μm Mylar + 25 μm Gd_2O_3. On the other hand, a Cd blade attached to a radial collimator has a total thickness of 150 μm (25 μm Cd-plating + 100 μm *5052* aluminum alloy + 25 μm Cd-plating). We have adopted the metal substrate for a Cd blade in order to improve the performance in relatively high-energy region. There is no difference in mechanical design between these collimators. A radial collimator can be attached on the conventional 800 mm flange based on the sample environment (SE) protocol of MLF. Also, a 400-mm flange can be prepared to allow the standard SE apparatuses, such as a cryostat, to be mounted. Our collimator has an inner radius r of 210 mm, an outer radius R of 400 mm, and an angular separation α of 2.5°. The shielding blades cover the range from –45° to +135° in horizontal direction. The blade length is given by $R–r$, which is 190 mm, and the blade height is 482 mm. Using these parameters, the diameter of visible sample d is calculated by

$$d = \alpha \cdot \frac{Rr}{R-r}$$

where d is identical to the 'maximum impact parameter' introduced in Ref. [2]. Substituting parameters r, R, and α, the value of d for our radial collimator is estimated to be 19.3 mm.

The oscillation of a radial collimator is driven by a stepping motor placed in vacuum, and a feedthrough electrical connection is used at the vacuum boundary. An aluminum plate is used to transfer the generated heat from the motor to the flange. The lubrications of the driving elements are done with commercial ultra-high vacuum grease. Linear motion produced by a ball screw coupled to the motor is converted to rotary motion by a crossed roller bearing. The oscillating speed is set to 0.04°/s. as default and the oscillation range is ±2.5°. Each shielding blade is tautened by using tension springs.

To evaluate the performance of each radial collimator, we performed neutron scattering measurement with and without a radial collimator on 4SEASONS installed at BL01 of MLF [5]. The sample for the evaluation measurement was vitreous silica (v-SiO_2) rod with 8.5 mm diameter which is much less than 19.3 mm. The sample was set into the top-loading cryostat conventionally used at 4SEASONS. The dynamical structure factors were obtained at room temperature with and without a Gd_2O_3 radial collimator. The Q dependences of the elastic structure factor are given in Fig. 1. The incident neutron energies were 37.0, 80.7, and 300.0 meV using the Multi-E_i method [6]. The unwanted scatterings from the cryostat are represented by arrows in Fig. 1. It was found that the Gd_2O_3 radial collimator could effectively shield the unwanted scattering from the cryostat window and provide us the high-quality data. The shielding property of Gd_2O_3 is getting worse in the high-energy region, the large incoherent scattering from a Mylar substrate significantly affects the data, as shown in Fig. 1(c). However, the Gd_2O_3 radial collimator provides enough performance for the experiments at

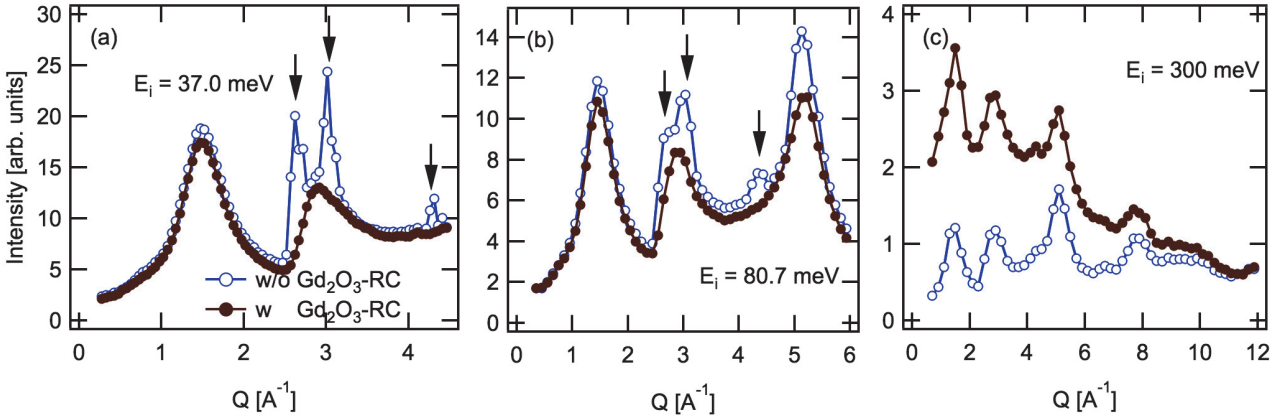

Figure 1. Q dependences of the elastic structure factor for *v*-SiO_2 with and without a Gd_2O_3 radial collimator. The diameter of *v*-SiO_2 is 8.5 mm. The sample is set into the cryostat and the measurements are performed at room temperature. Incident neutron energy is (a) 37.0 meV, (b) 80.7 meV, and (c) 300 meV.

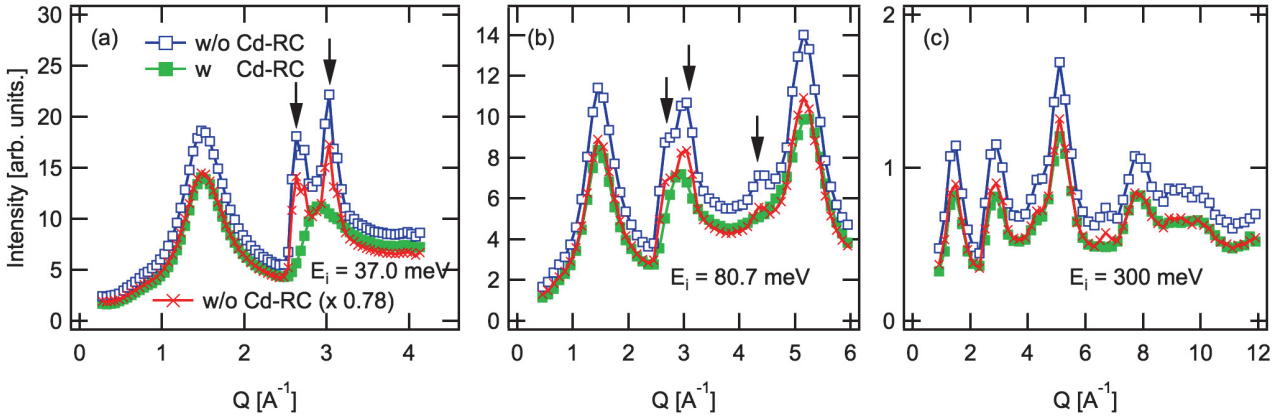

Figure 2. Same as in Fig. 1, but with and without a Cd radial collimator. Cross symbols show the reduced intensity for the data without a Cd radial collimator. The reduced factor is 0.78 for all incident energies.

the chopper spectrometer with curved guide system such as AMATERAS installed at BL14 of MLF [7]. The spectrometer with a curved-guide system can avoid the delivery of high-energy neutrons to the sample position. In fact, the best performance of AMATERAS can be achieved in the energy range from 1 to 20 meV, and sufficient performance can be realized up to 80 meV.

Next, we shall discuss the performance evaluation tests of the Cd radial collimator. Figure 2 represents the experimental results for Cd radial collimator, where the experimental conditions are the same as for Gd_2O_3 given in Fig. 1. The Cd radial collimator provides better quality data in the high-energy region as expected. The cross symbols in Fig. 2 represent the intensity without a Cd radial collimator reduced by the factor of 0.78. The reduced factor provides the same value for all incident energies. It was also confirmed that the reduced factor in the inelastic region was equal to 0.78. The diameter of the *v*-SiO_2 rod was much smaller than the maximum impact parameter 19.3 mm, and the experimental results for Gd_2O_3 shown in Fig. 1 have surely demonstrated the negligible intensity loss. The thickness of the respective shielding blades is certainly different, but geometrically it cannot make a significant difference in the intensity loss between the Gd_2O_3 radial collimator and the Cd one. Keeping tension when using metal substrate should be more difficult than in the case with Mylar substrate. It seems reasonable to suppose that the unexpected intensity loss in the Cd radial collimator is caused by this difficulty. In other words, there is room for improvement in the current Cd radial collimator.

3. Summary

We have developed two types of oscillating radial collimators for the chopper spectrometer at MLF in J-PARC based on the evaluation test of shielding materials as a blade for the radial collimator. One is made of commercially available Gd_2O_3 sheets designed for low-energy chopper spectrometers, and the other of Cd-plated aluminum sheets for relatively high-energy chopper spectrometers. The Cd radial collimator provides better performance in the high-energy region than the Gd_2O_3 radial collimator, but it has shown a loss with unexpected intensity. We are planning to investigate the causes and improve the performance of the Cd radial collimator.

References

[1] M. B. Stone *et al.*, Rev. Sci. Instrum. 85 (2014) 085101.
[2] J. R. D. Copley *et al.*, Nuclear Inst. and Meth. Phys. Res., A345 (1994) 313.
[3] A. F. Wright *et al.*, Nuclear Inst. and Meth. Phys. Res., A180 (1981) 655.
[4] M. Nakamura *et al.*, JPS Conf. Proc. 8 (2015) 036011.
[5] R. Kajimoto *et al.*, J. Phys. Soc. Jpn. 80 (2011) SB025.
[6] M. Nakamura *et al.*, J. Phys. Soc. Jpn. 78 (2009) 093002.
[7] K. Nakajima *et al.*, J. Phys. Soc. Jpn. 80 (2011) SB028.

M. Nakamura[1,2], Y. Kawakita[1], W. Kambara[1,2], K. Aoyama[1], R. Kajimoto[1], K. Nakajima[1], S. Ohira-Kawamura[1], K. Ikeuchi[3], T. Kikuchi[1], Y. Inamura[1,2], K. Iida[3], K. Kamazawa[3], and M. Ishikado[3]

[1]Neutron Science Section, Materials and Life Science Division, J-PARC Center; [2]Technology Development Section, Materials and Life Science Division, J-PARC Center; [3]Neutron R&D Division CROSS-Tokai

BL02: Current Status of the Broadband micro-eV Inelastic Neutron Spectrometer DNA

1. Introduction

The time-of-flight (TOF) near-backscattering spectrometer (n-BSS), DNA, was constructed and started operating in 2012 at the Materials and Life Science Experimental Facility (MLF) of the Japan Proton Accelerator Research Complex (J-PARC). It is an indirect geometry instrument with Si crystal analyzers and sees the coupled moderator of the pulsed spallation neutron source in MLF, which has the most intense but also the widest pulse among all three moderators in MLF. With the aim of a high energy resolution even with high intensity, DNA is the first n-BSS installed with a high-speed pulse-shaping disc-chopper in the world. The purpose of DNA is to research, in nanosecond timescale or with micro-eV resolution, the dynamical behaviors of atoms and spins in bio-molecules, functional-materials, strongly-correlated electron systems and so on [1, 2]. The instrumental overview and the present specifications of DNA are shown in Table 1 and Figure 1.

Table 1. Instrumental specifications of DNA.

Items	Specification
Neutron source (NS)	Coupled Liquid H2 Moderator
L1 (source-sample)	42 [m]
L2 (sample-analyzer)	~ 2.3 [m]
L3 (analyzer-detector)	~2.0 [m]
Pulse-sharpening chopper (PS-chopper)	
Max speed: 300 Hz at ~7.5 m from NS	
(Present Max speed: 225 Hz by 4 slits on one disc)	
Crystal Analyzer	
Crystal and reflection index	Si(111)
	Si(311) in test
Bragg angle of analyzers	~87.5 [deg.]
Energy resolution	
	~2.4 [μeV]: Si(111) with 10 mm Slit @225 Hz
	~3.5 [μeV]: Si(111) with 30 mm Slit @225 Hz
	~14 [μeV]: Si(111) without PS-chopper
	~12[μeV]: Si(311) with 10 mm Slit @225 Hz
Momentum range	0.08 < Q < 1.85 [A^{-1}]: Si(111)
	0.60 < Q < 3.80 [A^{-1}]: Si(311) in plan
Scan energy range:	
Si(111):	−40 < E/μeV < 100: Single pulse scan around Ef
	−400 < E/μeV < 600: Multi pulse scan around Ef
	−500 < E/μeV <1500:
	without PS-chopper in second frame
Si(311):	−150 < E/μeV <300: Single pulse scan around Ef
(Specifications as of the end of March. 2015)	

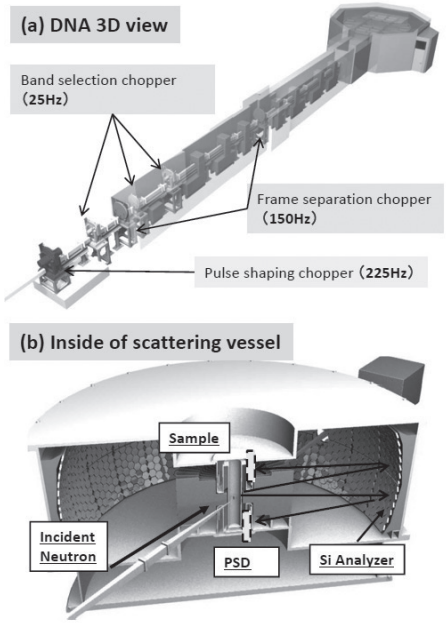

Figure 1. DNA 3D view (a) and inside of the scattering vessel (b).

2. Construction works and installation status until 2014

Almost all spectrometer components were installed before February, 2012, except the high-speed pulse-shaping disc chopper. At this time, the commissioning work have been carried out without the pulse-shaping chopper. The pulse-shaping chopper, which is designed as a counter-rotating double-disc chopper with a maximum rotational frequency of 300 Hz, was set up at a position of 7.75 m away from the moderator into the interstice of the super-mirror neutron guides and commissioned at 225 Hz rotational frequency in early April, 2013. After that, the measurement using the pulse-shaping chopper became the main measurement mode.

By the end of September, 2013, the coverage of the Si(111) crystal analyzers was extended to a scattering-angle range from -18 degrees to +138 degrees in the horizontal plane by adding some analyzer units. That in the vertical direction is in the range from +21 degrees to −14 degrees. Neutrons scattered by the sample are measured by position-sensitive 3He gas detectors arranged on the same circumference of the scattering center shifted upwards and downwards, after being energy-analyzed (back-scattered) by the upper and the lower parts of the Si crystal analyzer units, respectively.

These arrangements of the analyzer units and the detectors enable us to angle-resolve scattered neutrons not only in horizontal but also in vertical directions two-dimensionally, and therefore, DNA has a potential to carry out experiments even for single crystalline sample.

References

[1] K. Shibata, N. Takahashi, Y. Kawakita, M. Matsuura, T. Yamada, T. Tominaga, W. Kambara, M. Kobayashi, Y. Inamura, T. Nakatani, K. Nakajima, and M. Arai, JPS Conference Proceedings, 8, 036022 (2015).

[2] N. Takahashi *et al.*, Journal of the Physical Society of Japan, 80, SB007 (2011).

K. Shibata[1], Y. Kawakita[1], M. Matuura[2], T. Tominaga[2], T. Yamada[2], K. Nakajima[1], W. Kambara[1], M. Kobayashi[2], Y. Inamura[1], T. Nakatani[1], and S. Kasai[2]

[1]*Neutron Science Section, Materials and Life Science Division, J-PARC Center;* [2]*Neutron R&D Division CROSS-Tokai*

IBRAKI Biological Crystal Diffractometer iBIX

1. Introduction

Single crystal neutron diffraction is one of the powerful methods to obtain structure information including that of hydrogen atoms. The IBARAKI biological crystal diffractometer called iBIX is a high-performance time-of-flight single-crystal neutron diffractometer to elucidate the hydrogen, protonation and hydration structures of organic compounds and biological macromolecules in various life processes.

2. Current status of iBIX

Since the end of 2008, iBIX has been available for user experiments supported by Ibaraki University [1]. In FY 2012, we successfully upgraded the 14 existing detectors and installed the 16 new detectors for the diffractometer of iBIX [2]. The total measurement efficiency of the present diffractometer was higher by one order of magnitude than the previous one, coupled with increased accelerator power. In the end of FY 2012, the use of iBIX in user experiments for biological macromolecules started on a regular basis. In FY 2014, the accelerator power of J-PARC was 300 kW. We can collect a full data set of biological macromolecules for neutron structure analysis with around 2.0 Å resolution in 10 days by using iBIX. The size of the samples measured by iBIX is from 1 to 6 mm^3 in volume. If the accelerator power is increased to 1 MW, the total measurement time or the sample size will be reduced to onethird of the time needed before. In the beginning of FY 2014, we collected successfully the diffraction data sets of 6 biological macromolecules over a period of about 4 months. Some interesting results were obtained from these experiments which shows the benefits from the neutron diffraction experiment.

3. Developments

We started the process of improving the data reduction method and upgrading the diffractometer instruments in order to increase the data accuracy for the integrated intensities of Bragg reflections and make the system more user-friendly in the next phase of development of the instruments.

In order to carry out precisely the integration of Bragg intensities, we should be able to predict precisely the X, Y, TOF positions of Bragg reflections in the histogram data. In other words, the UB matrix should be determined precisely with the instrument parameters, such as detector positions and distance between the moderator and sample position L_1 and offset angle of goniometer. Therefore, we determined the instrument parameters by measurement of Bragg reflections of a standard sample. The L_1. detector parameters of 30 detectors and goniometer offset angle were obtained and then the accuracy of the indexing of Bragg reflections and the refinement of UB matrix could be successfully improved.

In order to improve the quality of the integrated intensity of weak reflections, we are aiming to implement the software component of profile fitting to data reduction software STARGazer. We are trying to seek functions representing asymmetry intensity distribution from the existing profile functions by using TOF powder diffraction method and verify the usefulness of these functions by the non-linear least square method. We discovered successfully the most suitable profile function, which is back-to-back exponentials convolved with a Gaussian. We will apply this function to profile fitting in order to obtain accurately the integrated intensity of the weak reflections.

To respond to users' various needs, we are developing new equipment of the sample environments. Figure 1 shows the heating system for the fiber sample. The attainable temperature is from room temperature to about 300°C. Figure 2 shows the tension applying device for the fiber sample. The specifications are as follows: stretching rate: 1~100 μm/sec, range of stretching: 90 mm, maximam load: 200 N. These parts of the equipment can be mounted on the multi-purpose stage, which was developed in FY 2013. In FY 2015, we will try to test measurement of sample environments with this equipment.

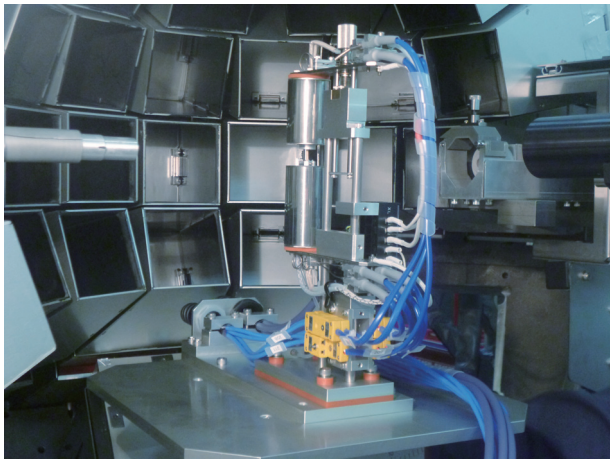

Figure 1. Heating system for the fiber sample.

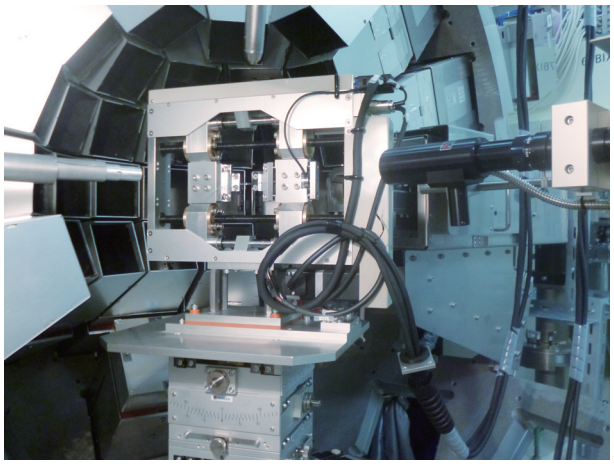

Figure 2. Tension applying device for the fiber sample.

4. Feature prospects

In FY 2015, we will continue the development of the data reduction software to make it more user-friendly and complete the work on the integration component with the profile fitting method for weak reflection. In the case of the diffraction data from larger unit cell crystals measured by iBIX, some neighboring Bragg spots will overlap partially each other because iBIX was installed on the coupled moderator with a wide pulse shape. It is necessary to de-convolute the overlapped spots in order to obtain their integrated intensity, we will start the development of the de-convolution component for overlapped Bragg spots to obtain the intensity of each one of them.

As of the hardware, we should carry out the commissioning of the utility equipment for sample environment that was developed in FY 2014 (e.g. heating and extension devices).

References

[1] I. Tanaka, K. Kusaka, T. Hosoya, N. Niimura, T. Ohhara, K. Kurihara, T. Yamada, Y. Ohnishi, K. Tomoyori and T. Yokoyama, Acta Cryst. **D**66 (2010) 1194-1197.

[2] K. Kusaka, T. Hosoya, T. Yamada, K. Tomoyori, T. Ohhara, M. Katagiri, K. Kurihara, I. Tanaka and N. Niimura J. Synchrotron Rad. **20** (2013) 994-998.

K. Kusaka[1], T. Yamada[1], N. Yano[1], T. Hosoya[1], I. Tanaka[1], T. Ohhara[2], and M. Katagiri[1]

[1]Frontier Research Center for Applied Atomic Sciences, Ibaraki University, Tokai; [2]J-PARC Center, JAEA

BL04: Developments of New Data Acquisition System and Total Cross-section Measurement Detectors at ANNRI

1. Introduction

A new data acquisition system (DAQ system) and a new total neutron cross-section measurement system are now being developed at the BL04 ANNRI facility (ANNRI) as a part of a research project entitled "Research and development for Accuracy Improvement of neutron nuclear data on Minor ACtinides (AIMAC)". In ANNRI, two different types of γ-ray detector systems are operated in order to measure neutron capturing cross-sections. One is a Ge detector system (Ge system), which has very fine γ-ray energy resolution, the other is an NaI detector system (NaI system) with wide neutron energy range measurement capability. Depending on the experimental purpose, only one system is selected in each experiment.

Now, in ANNRI, an Li-glass neutron detector system (Li-glass system) is being developed for total neutron cross-section measurement. In the case of a total neutron cross-section measurement, the setup of detectors can include a neutron capture cross-section measurement without any experimental conflict. Once the development of the total cross-section measurement system is completed, ANNRI will be able to measure the total and capture cross-sections simultaneously. In order to complete the project successfully, not only the Li-glass system but also the DAQ system itself must be developed because the current DAQ system cannot be applied to the Li-glass detector signal as-is. Moreover, it will be difficult to maintain the current DAQ for the Ge system due to its aging.

2. New DAQ system constitution

In order to measure the total cross-sections, both the upstream and downstream sides of the measuring sample must be collimated well to reduce the small angle scattering effects. In ANNRI, two collimator systems are prepared. One is the rotary collimator on the upstream side of the Ge system, the other is the intermediate collimator between the Ge and NaI systems. As there is no remaining space to set additional collimator on the downstream side of the NaI system, the measured sample must be located between the rotary collimator and the intermediate collimator in the case of a total cross-section measurement. As the Li-glass system must be located at more than 1 m downstream from the NaI system because of experimental limitations, simultaneous measuring mode is required to obtain detector data at two separate positions at the same time. In order to overcome this problem, a new DAQ system is being designed by the TCP/IP protocol based client-server model.

The role of the client-side application is to gather data from each ADC and send it to the server-side. The server-side receives data from each client, builds one event data block, and saves it to a disk. Each client is controlled by a common signal issued from the server-side application. Basically, client and server applications are designed to be operated on different PCs, but if the IP address of the server application is set as localhost, this DAQ system can be operated with only one standalone PC.

Inside the client-side application, the DAQ system backend makes a parallel routine for each ADC board automatically. Without any modifications in the user side code, this DAQ system runs with linear scalability to the ADC board number, up to the CPU core number minus one. (One core is used for the DAQ system except for the case of single core PC). The max data building rate is limited by the TCP/IP network speed limit. In local tests, the local area network speed in ANNRI was about 250 MB/s.

To digitize the detector signals, two different types of ADCs are used. CAEN v1724 [1] 14-bit 100-MHz peak hold ADC boards are characterized by fine pulse height digitizing resolution, which is suitable for Ge systems. For the Li-glass system, which has a fast response signal output, CAEN v1720 12-bit 250-MHz charge-sensitive ADCs are prepared. Optical link connections are used for data transfer from ADC boards to PC using CAEN A3818 PCI express board. The maximum data transfer rate was about 80 MB/s/fiber.

3. DAQ system performance

Test of the new DAQ system was performed using standard γ-sources and the ANNRI beamline. Figure 1 shows the Ge detector energy resolution dependency on the shaping time setting, as tested by using ^{60}Co standard γ-ray source. Keeping shaping time at 4 μs, a 2.7 keV FWHM for a 1332 keV γ-ray was achieved. Moreover, 5 keV FWHM was achieved even if the shaping time was only 1 μs. In the current DAQ system, the live time was about 60% for a 100 kcps event rate. With the new DAQ system, 90% live time for 100 kcps event rate was achieved. The integral nonlinearity was also checked by using ^{152}Eu standard γ-ray source and ^{27}Al(n,γ)^{28}Al reaction in ANNRI. When the energy dynamic range was set to 10 MeV, a nonlinearity in the order of 0.3 keV was achieved.

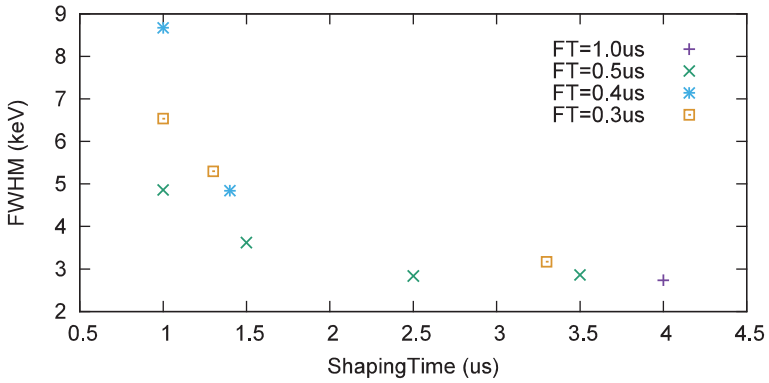

Figure 1. The shaping time dependency of the energy resolution at 1332 keV in ^{60}Co. Each point indicates the flat-top time of the trapezoidal pulse shaping.

4. Development of total cross-section measurement system

Measurements of capture cross sections of Minor Actinides (MAs) have been performed at ANNRI to improve the reliability of the cross section data for MAs. However, capture measurements are not sufficient to determine the resonance parameters accurately, and total neutron cross-section measurements are required. Therefore, we are promoting the development of a technique to obtain total neutron cross sections at ANNRI with Li-glass neutron detectors and the new DAQ system, which is still in progress. The purpose of the study is to obtain accurate resonance parameters of MAs.

The neutron total cross-section measurement for ^{197}Au was performed by the time-of-flight (TOF) method with the Li-glass neutron detectors and the new DAQ under development for the Li-glass detector. Two types of Li-glass detectors were utilized for total cross-section measurements. A GS20 ^{6}Li-glass detector manufactured by OKEN with dimensions of 10 cm x 10 cm and thickness of 1 cm using enriched ^{6}Li (^{6}Li>90%) was used to obtain transmission neutron TOF spectra. Neutrons are detected by the ^{6}Li-glass detector via the ^{6}Li(n,α)^{3}H reaction. Furthermore, we used a GS-30 ^{7}Li-glass detector manufactured by OKEN with dimensions of 10 cm × 10 cm and thickness of 1 cm depleted in ^{6}Li (^{7}Li>99.99%) in order to evaluate the background except for neutrons from neutron TOF spectra measured with the ^{6}Li-glass detector. The ^{6}Li-glass detectors were placed in a borated polyethylene shield to reduce the thermal neutrons moderated by the structural material in the experimental area. The distance between these Li-glass detectors and the neutron source was 29 m. Signals from the ^{6}Li-glass detector were amplified with the ORTEC 474 timing filter amplifier, and the TOF and the pulse height of each event were recorded event-by-event in a list-data format file with the DAQ.

Gold-197, which is a monoisotopic nuclide, has superior chemical stability, and the precise resonance parameters of ^{197}Au are well known, so that ^{197}Au is used to validate experimental setup and data analysis. The ^{197}Au sample (purity 99.99%) with diameter of 9.0 cm and thickness of 1.0 mm was placed at the middle collimator. The distance between the neutron source and the sample was about 15 m. The neutron beam was collimated by the X-stage and rotary collimators located at an upstream side of the experimental area of the ANNRI so that the size of the neutron beam becomes smaller than that of the Au sample. The transmitted neutrons were measured by the ^{6}Li-glass detector.

We repeated the measurements of the ^{197}Au sample (^{197}Au run) and with no sample (blank run) to obtain the neutron transmission ratio. A Pb filter with a thickness of 3.75 cm was used to reduce the dead time of the Li-glass detector caused by intense gamma flash from the spallation neutron source. Neutron notch filters of ^{nat}Mn, ^{nat}Co, ^{nat}In and ^{nat}Ag were utilized to estimate the backgrounds due to frame overlap neutrons and gamma-rays from the TOF spectra obtained by the ^{6}Li-glass detector by the black resonance technique. Moreover, we carried out the measurements of the background by using the ^{7}Li-glass detector.

In the beginning, dead time corrections were made for TOF spectra assuming that the DAQ has a fixed dead time of 750 ns for each signal. The backgrounds of the TOF spectra of ^{197}Au and blank runs were estimated and subtracted, and the net TOF spectra were obtained. Neutron beam intensity determined by the number of proton beam pulses and proton beam power were used for normalization of the background subtraction. Finally, total cross sections of ^{197}Au were derived

by using the net TOF spectra of ^{197}Au and blank runs. Figure 2 shows the preliminary results. In the thermal energy region, the results are in agreement with the evaluation of JENDL-4.0 [2]. At the 4.9 eV resonance of ^{197}Au, cross section data is not available because transmitted neutrons equaled 0.

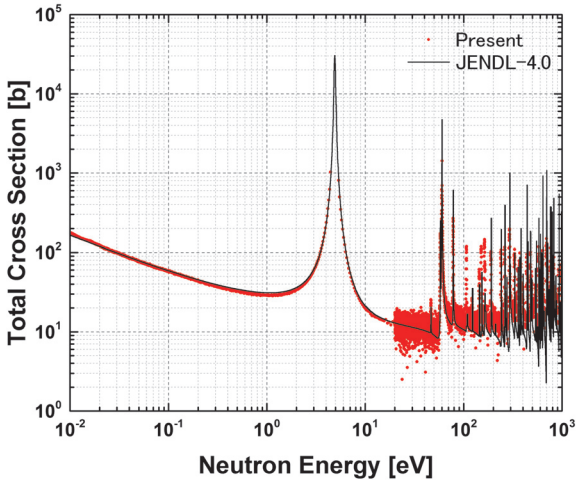

Figure 2. Neutron total cross sections of ^{197}Au in the neutron energy region from 10^{-2} to 10^{3} eV. The red points indicate present results. The black line indicates evaluated values of JENDL-4.0.

K. Terada and T. Nakao
Nuclear Data Center, Nuclear Science and Engineering Center, JAEA

5. Future Plans

A new DAQ system and new total neutron cross-section measurement system have been developed at ANNRI. The latter meets the demanded performance specifics that measurements of gamma-ray capture cross sections can be measured fine energy resolution by the Ge detectors and total neutron cross sections can also be obtained by the ^{6}Li-glass detector. Measurements of the neutron capture and total neutron cross-sections of ^{241,243}Am are planned.

The author would like to thank the accelerator and technical staff at J-PARC for operation of the accelerator and the neutron production target and for the other experimental supports. Present study includes the result of "Research and Development for accuracy improvement of neutron nuclear data on minor actinides" entrusted to the Japan Atomic Energy Agency by the Ministry of Education, Culture, Sports, Science and Technology of Japan (MEXT).

References

[1] http://www.caen.it/
[2] JENDL-4.0 data file for ^{197}Au (MAT = 7925), evaluated by Iwamoto N (2010).

Present Status of BL05 (NOP)

1. Introduction

BL05 (NOP) is a beamline designed to carry out fundamental physics experiments using neutrons. The beamline is divided upstream into three branches to conduct in parallel different experiments [1, 2]. The present status of the ongoing experiments at BL05 (NOP) will be reported.

2. Measurement of the neutron lifetime

A neutron decays into a proton, an electron, and an antineutrino. The lifetime is an important parameter for the unitarity of the CKM matrix or primordial big bang nucleosynthesis. However, the recently reported values for the neutron lifetime deviate significantly from the systematic errors claimed and require improvement. An experiment to measure the neutron lifetime with a pulsed beam is ongoing at BL05 (NOP). The lifetime is measured as the ratio of the electron events to the $^{3}He(n,p)^{3}H$ events caused by precisely doped ^{3}He gas using a time projection chamber (TPC) [3].

The TPC was improved in May, 2014. The inner surface of the TPC was lined by ^{6}LiF/PTFE tiles to capture scattered neutrons without gamma rays. The tiles were covered with a PTFE sheet to suppress the ions caused by neutron captures. In the commissioning run of 2012, contamination events due to $^{6}Li(n,t)^{4}He$ by leaks from gaps of PTFE sheet were observed. By improving the coverage of the PTFE sheet, we reduced successfully the contamination (see Figure 1, left). In 2012, the energy resolution of the TPC was getting worse with the elapsed time. We found it was due to charging up and solved the problem by setting electrodes to define voltages instead of the charging up material. As a result, the energy resolution of the X-ray from ^{55}Fe was improved from ~20% to 12%, and remained stable in time (see Figure 1 Right).

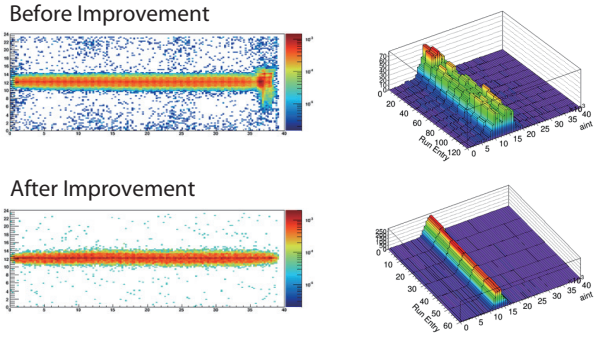

Figure 1. Figure 1: Before and after improvement of the TPC. Contamination due to $^{6}Li(n,t)^{4}He$ disappeared (left), and gained stability measured by ^{55}Fe (right), respectively.

Physics data were taken for about 2 weeks by the improved TPC. The data are under analysis by using Monte Carlo simulation. In Figure 2, the track length spectra of the beta decay candidates are shown with simulations. The simulation reproduced the signals well (χ^2/ndf < 2).

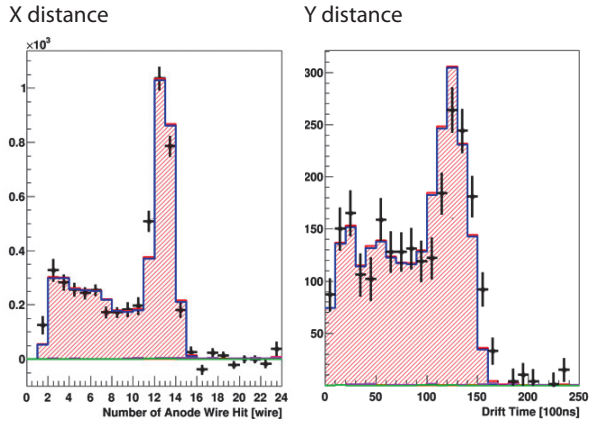

Figure 2. Spectra of the beta decay candidates with Monte Carlo simulation. The X distance was calculated by the number of hit wires. The Y distance was calculated by the drift time.

3. Ultracold neutron production by Doppler shifter

Ultracold neutrons (UCNs) with energy of less than ~250 neV (velocity of 6.8 m/s), are utilized for various precision measurements in fundamental physics. In order to develop and test UCN optical devices, a Doppler shifter was installed to provide UCNs on BL05 (NOP) beamline. The Doppler shifter reflects very cold neutrons (VCNs) with velocity of ~136 m/s by a moving mirror with 68 m/s and produces neutrons with less than 20 m/s.

The reflected neutron intensity at an extraction port on the top was 410 cps at the 1-MW equivalent beam power [4]. The reflected neutron flux was compared with a Monte Carlo simulation, which is shown in Figure 3. The measured and calculated spectra were in good agreement. The UCN intensity and peak UCN density are estimated as 160 cps and 1.4 /cm^3 according to the simulation [4].

An additional port was set up at the side of the Doppler shifter. A UCN storage vessel to study reflectivity of UCN on surfaces was installed (Figure 4). UCN storage experiment will be performed.

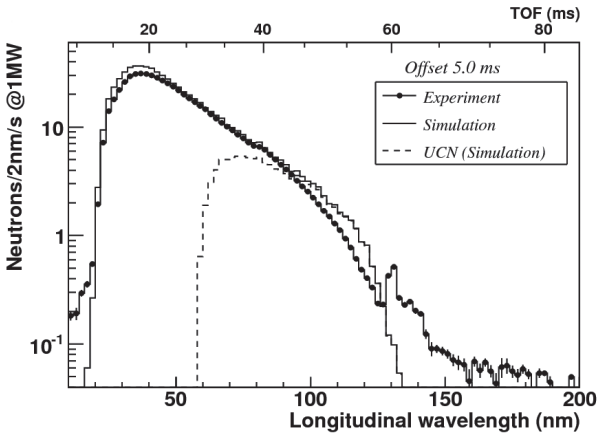

Figure 3. Measured (dotted) and calculated (solid) longitudinal UCN wavelength spectra of Doppler shifted neutrons. The dashed line shows that of UCN, whose total velocity is less than 6.8 m/s [4].

Figure 4. Additional side UCN port (left) and a UCN storage chamber assemble with the Doppler shifter (right).

References

[1] KENS Annual report 2014.

[2] K. Mishima, Neutron network news (Hamon), vol25, No2 (2015) 156-160.

[3] Y. Arimoto, N. Higashi, Y. Igarashi, Y. Iwashita, T. Ino, R. Katayama, R. Kitahara, M. Kitaguchi, H. Matsumura, K. Mishima, N. Nagakura, H. Oide, H. Otono, R. Sakakibara, T. Shima, H.M. Shimizu, T. Sugino, N. Sumi, H. Sumino, K. Taketani, G. Tanaka, M. Tanaka, K. Tauchi, A. Toyoda, T. Tomita, T. Yamada, S. Yamashita, H. Yokoyama, T. Yoshioka, Nuclear Instruments and Methods in Physics Research A, 799 (2015) 187-196.

[4] S. Imajo, K. Mishima, M. Kitaguchi, Y. Iwashia, N. L. Yamada, M. Hino, T. Oda, T. Ino, H. M. Shimizu, S. Yamashita, R. Katayama, Progress of Theoretical and Experimental Physics (PTEP),accepted. http://arxiv.org/abs/1507.07223v3.

K. Mishima[1,2] on behalf of NOP collaboration

[1]Neutron Science Section, Materials and Life Science Division, J-PARC Center; [2]Institute of Materials Structure Science, KEK

BL06: Commissioning Status of VIllage of Neutron ResOnance Spin Echo Spectrometers (VIN ROSE)

1. Introduction

The neutron spin echo (NSE) technique is an essential spectroscopic method, which at present time has achieved the highest neutron energy resolution. NSE with a pulsed neutron source makes it possible to scan very efficiently a wide spatiotemporal space. Kyoto University and KEK have been installing jointly two types of NSE spectrometers at BL06 since 2011, that is, a neutron resonance spin echo (NRSE) instrument and a modulated intensity by zero effort (MIEZE) instrument. One of the characteristics of the instruments is the use of resonance spin flippers that make it possible to install compact and multiple spectrometers in a limited space. The beam line has been named "VIN ROSE" (VIllage of Neutron ResOnance Spin Echo spectrometers), which will spawn a new field of spectroscopic methods [1]. Figure 1 shows the schematic top view and a recent photo of BL06.

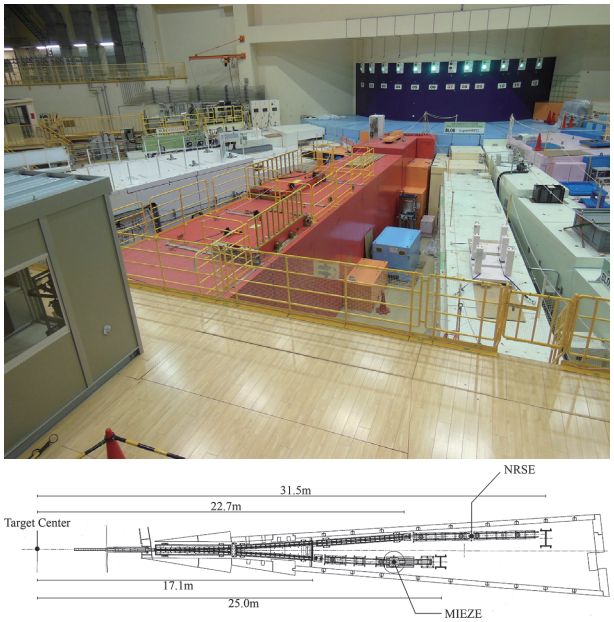

Figure 1. Top: a recent picture of BL06. Bottom: schematic top view of the MIEZE and NRSE beam lines at BL06.

2. Commissioning Status at BL06

BL06 has been allowed to accept neutron beams since April, 2014. After that, the performance of the installed neutron guides had been tested with several methods. All the supermirrors for the guides (Q_c = 2.5 and 3 for NRSE and MIEZE, respectively) were made at KURRI by using the ion beam sputtering machine [1, 2], which were held in the precise positions and covered by iron shields to reduce the dose level. The spectra at the guide-end positions were measured by a ^{3}He neutron beam monitor with a borosilicate glass plate as an attenuator. Figure 2 shows the measured and calculated neutron fluxes. Both the coefficient of attenuation for borosilicate glass and the wave-length dependent neutron detection efficiency for the monitor were corrected. In the case of NRSE, a very good agreement (95%) was achieved, on the other hand, the agreement for MIEZE was 56% due to the disagreement mainly in the shorter wavelength range. At this moment, we are carefully considering the reasons that may originate from the misalignment of the mirrors, their deflection, etc.

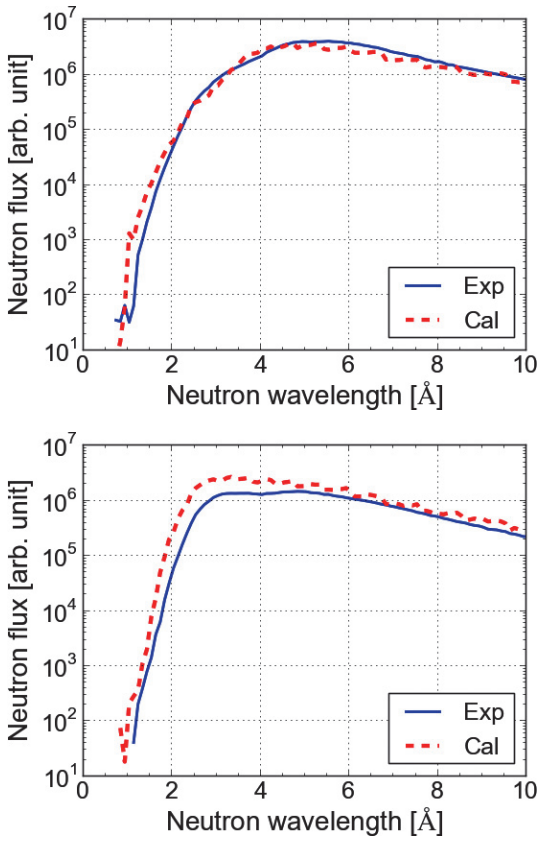

Figure 2. Measured (solid line) and calculated (dashed line) absolute neutron fluxes of NRSE (top) and MIEZE (bottom).

After the investigation of the neutron guide performance, we installed the components (a polarizer, two resonance spin flippers, and an analyzer) in MIEZE to observe the neutron spin echo signals. The combination

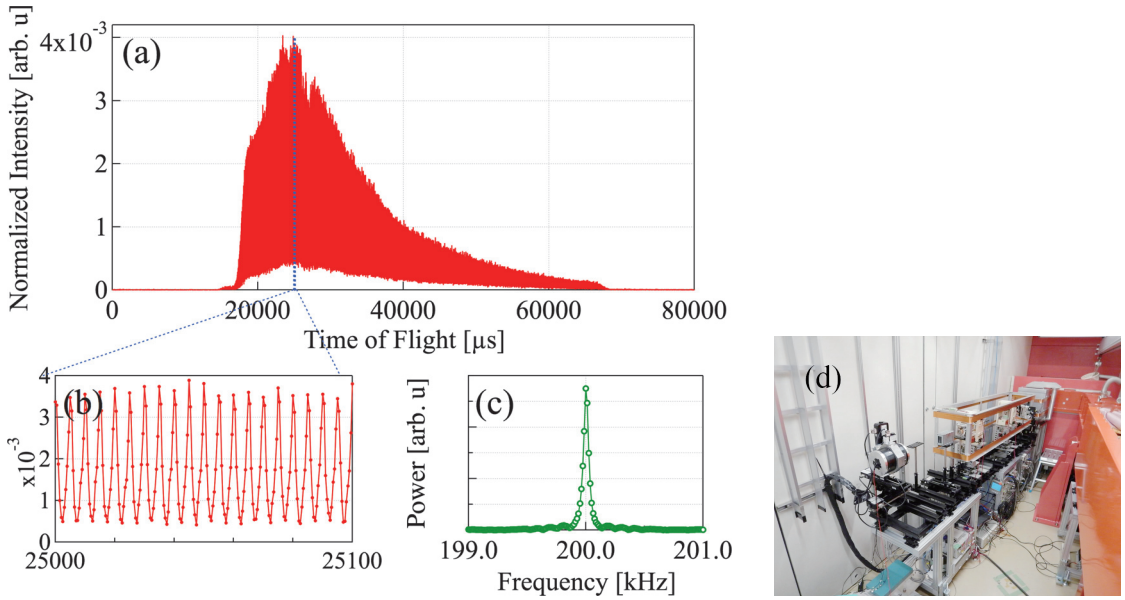

Figure 3. Left: (a) the measured TOF-MIEZE signal with an effective frequency of 200 kHz, (b) the TOF-MIEZE signal between 25 and 25.1 ms, (c) power spectrum of the TOF-MIEZE signal by Fourier transformation. Right: (d) picture of the MIEZE spectrometer at BL06 VIN ROSE.

of MIEZE and time-of-flight (TOF) is a quite new method, and the related previous studies were just tentative [3, 4]. Therefore, the quantitative verification of TOF-MIEZE was necessary and expected. We were able to measure successfully TOF-MIEZE signals with several different conditions. The measured TOF-MIEZE signal with an effective frequency of 200 kHz is shown in Figure 3. The time range of the TOF signal is between 0 and 80 ms due to the double frame (12.5 Hz) operation of the disk chopper. The acceptable neutron wavelength was limited by the opening section of the chopper. Very clear oscillation can be observed for the wide wavelength band (from 4 Å to 12 Å). Fourier analysis of the signal confirms an exact 200 kHz oscillation, see Figure 3c.

As a next step, now we are investigating the detailed characteristics of TOF-MIEZE.

3. Summary

After a brief introduction, the current status of BL06 VIN ROSE was described. In FY2014, we were able to observe the TOF-MIEZE signal successfully. Now we are proceeding with further commissioning for both MIEZE and NRSE. Some standard experiments with MIEZE may start in FY2015.

References

[1] M. Hino, T. Oda, M. Kitaguch, N. L. Yamada, H. Sagehashi, Y. Kawabata, and H. Seto, *Physics Procedia* **42**, (2013) 136.

[2] M. Hino, H. Sunohara, Y. Yoshimura, R. Maruyama, S. Tasaki, H. Yoshino, and Y. Kawabata, *Nucl. Inst. Meth. A* **529**, (2004) 54.

[3] M. Bleuel, M. Bröll, E. Lang, K. Littrell, R. Gähler, and J. Lal, *Physica B* **371**, (2006) 297.

[4] G. Brandl, J. Lal, J. Carpenter, L. Crow, L. Robertson, R. Georgii, P. Böni, and M. Bleuel, *Nucl. Inst. Meth. A* **667**, (20012) 1.

H. Endo[1,2], M. Hino[3], T. Oda[4], N. L. Yamada[1,2], H. Seto[1,2], and Y. Kawabata[3]

[1]Neutron Science Section, Materials and Life Science Division, J-PARC center; [2]Institute of Materials Structure Science, KEK; [3]Kyoto University Research Reactor Institute; [4]Departmente of Nuclear Engineering, Kyoto University Graduate School of Engineering

Status Report for BL08 SuperHRPD

1. Introduction

SuperHRPD is the world's highest resolution neutron powder diffractometer. SuperHRPD is expected to 1) detect tiny distortion never detected before in the field of strongly correlated systems, multiferroics, magnetic materials, etc., 2) attain high precision structure analysis in energy materials, and 3) develop the structure science of hybrid materials, supermolecules, pharmaceuticals, etc. [1-3]. In the S-type project in 2014, we continued to develop SuperHRPD as well as Z-Code, a powder diffraction data analysis suite, and worked on various scientific topics including the Elements Strategy Initiative of MEXT and the RISING project of NEDO (The New Energy and Industrial Technology Development Organization).

2. New detector system with an 8-mm diameter position sensitive detector

Initially, we installed 1/2-inch diameter position sensitive detectors (PSDs) that had been used at the KENS facility of KEK since the initial budget was limited and the development of the high spatial-resolution detector system was stopped. The imposed limit reduced the instrumental resolution compared with the original design. Then we developed a new detector system based on 8-mm diameter PSDs and managed to improve the resolution as shown below. The 16 PSDs of 8 mm in diameter were assembled together into one unit and an amplifier circuit was connected to each PSD. In the new detector system, 8 amplifier circuits were built into one application specific integrated circuit (ASIC) chip and this contributed to a more compact circuit (Fig. 1).

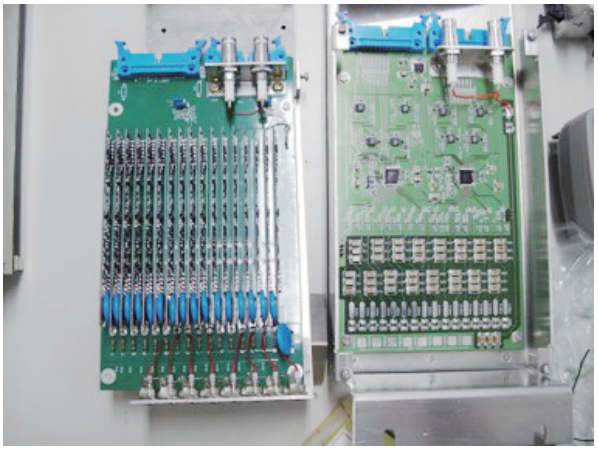

Figure 1. The conventional amplifier circuit (left) and the advanced one with an ASIC chip (right); the 16 amplifier circuits are implemented within two ASIC chips.

A new detector system installed at the backward banks in FY2013 has improved the overall resolution from $\Delta d/d$ = 0.1% to 0.08%. The best resolution of 0.04% was attained by using limited number of detectors located at high angle as well as narrowing down the width of the beam as shown in Fig. 2. All detectors of the backward bank were replaced with this new detector system, and have been routinely used to conduct all measurements in FY2014. The Rietveld analyses have already been successfully applied to data obtained from the new detector system.

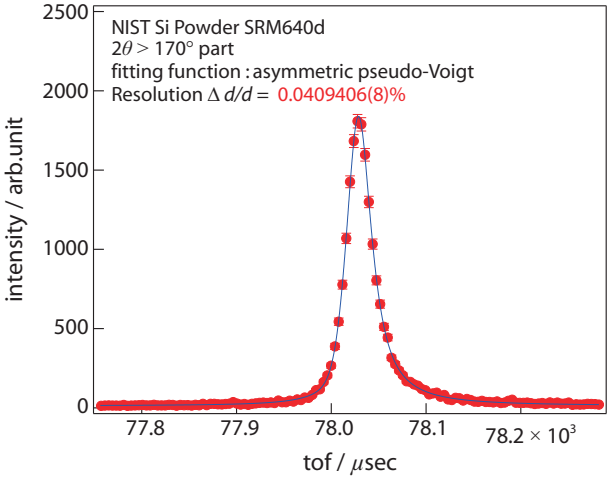

Figure 2. Neutron diffraction pattern of a NIST Silicon powder sample (6 mm diameter) with 8 mm PSD. The peak fitting result is obtained by an asymmetric pseudo-Voigt function.

3. Scientific topics

One of the scientific highlights was achieved by extracting precise structure factors using SuperHRPD [4]. Among the 4*d* transition metal oxides, $SrRuO_3$ is known to be a rare ferromagnet with *T*c = 165 K, while $CaRuO_3$ with the same structure shows nonmagnetic character in the whole temperature range. $SrRuO_3$ also has other peculiar and unexplained behaviors; one is a negative thermal expansion below *T*c, and the other is the failure of the Glazer structural description. In the Glazer description, which assumes a simple octahedron rotation, the *a* axis is always shorter than the *b* axis in a distorted ABO_3 perovskite with Pbnm ($a^-a^-c^+$; '–' and '+' represent the out-of-phase tilting and the in-phase tilting of neighboring octahedrons, respectively). This rule is found to hold for most orthorhombic perovskite compounds, with a few exceptions such as $SrRuO_3$, whose *a* axis is longer than its *b* axis.

Although tiny atomic structure changes below *T*c had not been detected in previous neutron diffraction experiments, SuperHRPD gave us precise in-plane deformation of the RuO_6 octahedra and structural evidences for a negative thermal expansion and non-Glazer like distortion.

Below *T*c, the average bond length <Ru–O> of $SrRuO_3$ obtained using SuperHRPD is 'increased' by as little as 0.0005 Å (such small distortion could not be detected previously). In contrast, <Ru–O> of $CaRuO_3$ shows 'decrease' by an ordinary thermal expansion behavior at a low temperature, and <Mn–O> of $La_{0.75}Ca_{0.25}MnO_3$ shows some 'decrease' by 0.005 Å (ten times of $SrRuO_3$) upon entering its ferromagnetic state.

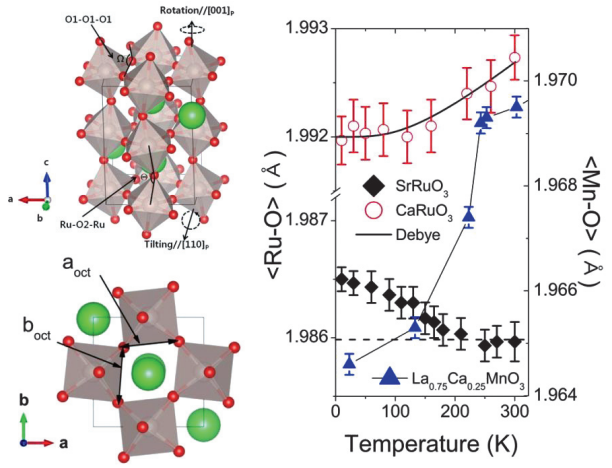

Figure 3. Glazer tilting description (Pbnm, $a^-a^-c^+$). Mean <Ru-O> and <Mn-O> bond of itinerant ferromagnetic $SrRuO_3$, paramagnetic $CaRuO_3$ and CMR $La_{0.75}Ca_{0.25}MnO_3$.

These differences in the behaviors of the bond lengths provide clear experimental evidence that a different mechanism of ferromagnetism is at work for $SrRuO_3$ as opposed to $La_{0.75}Ca_{0.25}MnO_3$. It is natural to think that an increase in <Ru–O> at low temperature could make 4*d* bands of Ru localized. In fact, the calculated bandwidth using an empirical formula shows temperature-induced narrowing of the Ru 4*d* bands for $SrRuO_3$, in contrast to $CaRuO_3$ and $La_{0.75}Ca_{0.25}MnO_3$. So it is speculated that the ferromagnetism in $SrRuO_3$ is induced by the localization of the Ru 4*d* bands.

References

[1] T. Kamiyama and K. Oikawa, Proc. of ICANS-XVI, Deusseldorf-Neuss, Germany, May 12-15 (2003) 309.

[2] S. Torii, M. Yonemura, Surya Panca Putra Y T, J. Zhang, P. Miao, T. Muroya, R. Tomiyasu, T. Morishima, S. Satoh, H. Sagehashi, Y. Noda and T. Kamiyama, J. Phys. Soc. Jpn. 80 (2011) SB020.

[3] S. Torii, M. Yonemura, Y. Ishikawa, P. Miao, R. Tomiyasu, S. Satoh, Y. Noda and T. Kamiyama, Journal of Physics: Conference Series 502 (2014) 012052.

[4] S. Lee, J. R. Zhang, S. Torii, S. Choi, Deok-Yong Cho, T. Kamiyama, Jaejun Yu, K. A. McEwen and Je-Geun Park, J. Phys.: Condens. Matter, 25 (2013) 465601.

[5] M. Hiraishi, S. Iimura, K. M. Kojima, J. Yamaura, H. Hiraka, K. Ikeda, P. Miao, Y. Ishikawa, S. Torii, M. Miyazaki, I. Yamauchi, A. Koda, K. Ishii, M. Yoshida, J. Mizuki, R. Kadono, R. Kumai, T. Kamiyama, T. Otomo, Y. Murakami, S. Matsuishi & H. Hosono, Nature Phys, 10 (2014) 303.

S. Torii[1,2], P. Miao[1,2], S. Lee[1,2], M. Yonemura[1,2], and T. Kamiyama[1,2]

[1]*Neutron Science Section, Materials and Life Science Division, J-PARC center;* [2]*Institute of Materials Structure Science, KEK*

Development of an Advanced Special Neutron Powder Diffractometer under Extreme Environment for Materials

1. Introduction

Batteries are a very important technology because compact and wearable devices such as laptop computers and mobile phones, which work in an environment that lacks power, need mobile energy storages. Additionally, high performance batteries are necessary for larger devices, such as hybrid vehicles (HV) and pure electronic vehicles (EV). Those vehicles are designed to reduce the consumption of fossil fuels and advance the transition to a low carbon society. The lithium-ion battery is one of the most promising battery systems as energy storage for both small and large cells. However, with the lithium-ion battery there are still challenges to be resolved regarding its cyclic life and high temperature use. The capacity of that type of battery is also limited and needs to be improved.

The lithium-ion battery works through the lithium ion transfer between cathode and anode. The reactions of both electrodes are based on the de/intercalation of lithium ions from/into the materials of electrodes. When the lithium ions intercalate into materials, the crystal structure is changed. The information of the structural changes and the location of lithium ions in the crystal structure lead to improvement of the present lithium-ion battery and the invention of an out-of-the-box battery.

In order to clarify at an atomic level the structures of cathode, anode and the interface between electrode and organic electrolyte, a new neutron powder diffractometer, SPICA, has been designed and constructed as one of the state-of-the-art measurement apparatuses. Compared to the X-ray, the neutrons are well known to be a powerful probe to get information about the location and movement of light elements such as hydrogen and lithium atoms. Therefore, the advantage of the neutron diffraction will allow us to expand our knowledge about the location and movement of lithium ions, as well as the changes of the atomic arrangement in the cathode, anode and the electrolyte solution.

2. Present Status

In a previous S-type project, a new special environment diffractometer, SPICA was designed and constructed on BL09 in J-PARC/MLF. In the new S-type project (2014S10), structure changes in variety of charge and discharge rates will be collected and analyzed to determine the reasons for the batteries' deterioration and find out the underlying issues.

Typical examples of in operando measurement for a commercialized Li-ion battery (LIB) in low rate of charge and discharge were carried out in the stage of the commissioning. Those data revealed that SPICA had a high potential of in operando measurement.

Figure 1 shows the discharge rate dependence of structure changes in anode materials. These diffraction patterns show 00l diffraction of the graphite. Stage 1, 2, 3, 4 are different stacking structures of lithium in the graphite layers respectively. Stage 1 and 2 coexisted in both discharge rates. However, the coexistence regions in the low-rate discharging were narrower than in the high-rate one. This discharge rate dependence might indicate the inhomogeneous reaction on the large area of anode sheet or/and slow conductivity of Li-ion in the graphite. Because the slurry of the anode material, which was made from graphite, PVDF (PolyVinylidene DiFluoride) and NMP (N-Methyl-2-Pyrrolidinone) coated by just putting over using scrapers on power collector film, the high and low reactive region might coexist on the electrode sheets.

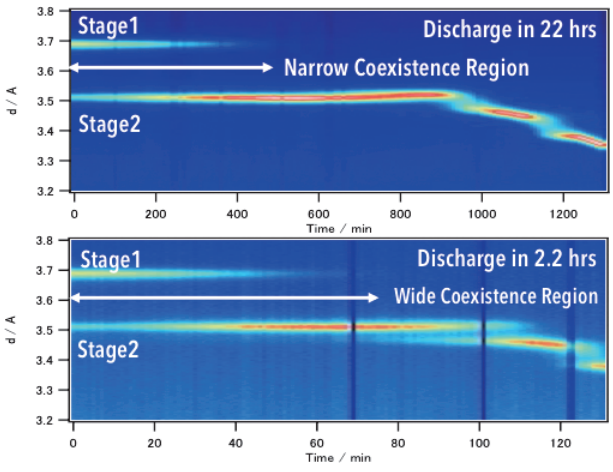

Figure 1. The discharging rate dependence of the structure changes of the anode material, graphite in discharge processes. Those diffraction patterns were obtained by *in operando* measurements on SPICA.

Figure 2 shows the structure change of graphite in higher discharge rate (2C). The white line indicates the border of stopping the discharge. After the discharging stopped, the structure still continued changing. Stage 1

and 2 also coexisted at the same low rate. Stage 3 also appeared from the early stage of the discharge process. The graphite phase appeared before Stage 4. After the discharging stopped, the graphite peak disappeared and Stage 4 appeared simultaneously. In discharge in 2 C rate, the lithium ions still remained in the anodes. Therefore, the relaxation behavior might be observed because some concentration distributions of lithium ions were formed in the high rate discharging.

3. Conclusion

The 18650-type lithium-ion batteries were measured using in operando technique. From those data, the dependence on the charge–discharge rate was determined. The relaxation reactions in the anodes were quite different by charge–discharge rate. To find out the issues causing degradation and unsafety, the relationship between reaction in batteries and structure changes of electrodes will be determined in a variety of charge-discharge conditions.

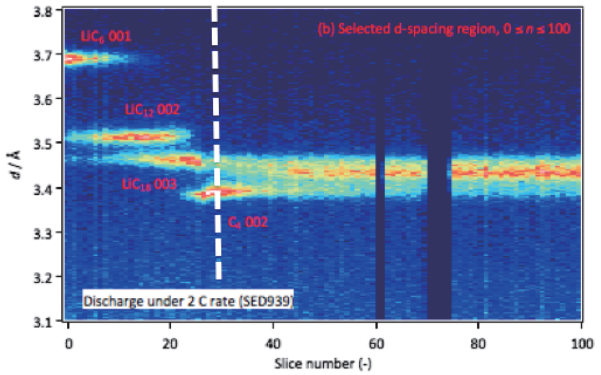

Figure 2. The structure changes of anode material, graphite in 2 C rate charge process.

Acknowledgements

We would like to appreciate Mr. K. Muroya and Mr. S. Sugai for their technical support in constructing the SPICA diffractometer. This work was supported by the Research and Development Initiative for Scientific Innovation of New Generation Batteries (RISING) project of the New Energy and Industrial Technology Development Organization (NEDO).

M. Yonemura[1,2], T. Kamiyama[1,2,3], K. Mori[4], T. Fukunaga[4], Y. ishikawa[1], S. Torii[1,2], R. Tomiyasu[1], K. Kino[5], T. Naka[6], M. Morishima[6], S. Shiotani[6], S. Taminato[7], M. Hirayama[7], R. Kanno[7], Y. Onodera[4], Y. Ukyo[6], H. Arai[6], Y. Uchimoto[8], and Z. Ogumi[6]

[1]Institute of Materials Structure Science, KEK; [2]Neutron Science Section, Materials and Life Science Division, J-PARC center; [3]Neutron Science Section, Materials and Life Science Division, J-PARC Center; [4]Research Reactor Institute, Kyoto University; [5]Hokkaido University; [6]Office of Society-Academia Collaboration for Innovation, Kyoto University; [7]Interdisciplinary Graduate School of Science and Engineering, Tokyo Institute of Technology; [8]Graduate School of Human and Environmental Studies, Kyoto University

BL10: NOBORU

In FY 2014, 23 general use proposals were carried out at NOBORU, but some of them have not been completed due to the fire in the MLF on January 16, 2015. This year, we measured the neutron flux with high-power proton beam study up to 0.53 MW. Figure 1 summarizes ratio of the neutron flux vs. proton beam power measured at BL10. Each neutron flux was integrated from 1 meV to 100 meV. The result indicated that the neutron intensity was almost proportional to the proton beam power but depended on the proton beam profile, because the proton beam profile differed in both measurement years. This study will continue up to the 1 MW proton beam operation.

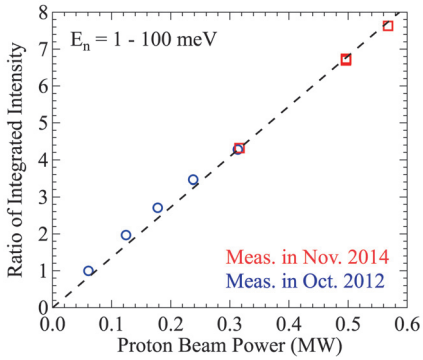

Figure 1. Ratio of intensity vs. proton beam power.

[Feasibility study on Bragg edge imaging and diffraction experiment using the same sample]

Energy resolved neutron imaging has been developed at BL10 since 2008. Now we have some characteristic 2D counting-type detectors. In particular, the micro-pixel chamber (μPIC) detector and the Gas Electron Multiplier (GEM) detector show good spatial resolution and high-count rate capability, respectively. This year we purchased 1D-PSDs for diffraction measurement to obtain complementary information of the sample used in the imaging experiment. Figure 2 shows a high-resolution transmission image of four pieces of cast duplex stainless steel using the μPIC detector and the fitting result of transmission data of a small part of sample no.1. The fitting result suggests the existence of a strong texture structure in the BCC phase. The same sample was measured by diffraction method at the BL10 using PSDs. Figure 3 shows the diffraction pattern and the textured Deby-Scheller ring on a PSD. The right figure shows a strong BCC (110) texture pattern as predicted by the Bragg edge analysis.

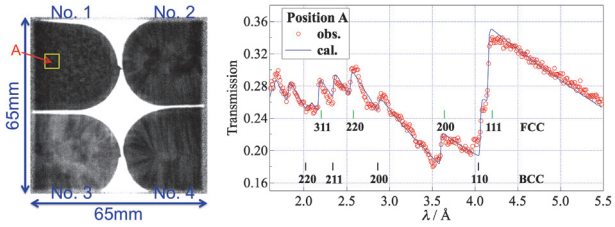

Figure 2. Transmission image of wavelengths of 3.3–3.6 Å collected using the μPIC detector (left); Fitting of the Bragg-edge spectra of the position A in specimen no. 1 using RITS code (right) [1].

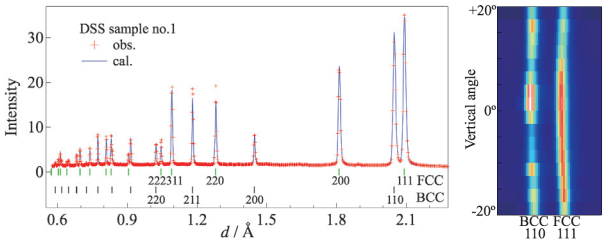

Figure 3. Pawley fitting pattern of the diffraction data of sample no.1 (left) and the textured Deby-Scheller ring on the PSD (right).

Reference

[1] Y. Su *et al.*, JPS Conf. Proc. 8 031015 (2015).

K. Oikawa and M. Harada
Neutron Science Section, Materials and Life Science Division, J-PARC center

BL11: Structure Analysis of Crystals and Amorphous Solids at 18 GPa with Paris-Edinburgh Press

1. Introduction

The compression of materials induces changes in their physical properties. To understand that mechanism, it is essential to explore their structure. Neutron diffraction is effective in revealing structures of materials including light elements, such as hydrogen and oxygen. In particular, the *in-situ* observation of structures under high pressures is important because the structure appeared at high pressures sometimes reverts to the original one after the release of pressure.

In past research in Japan, the routinely accessible pressure of in-situ observation has been limited to about 3 GPa, although it has reached up to 30 GPa at other research facilities around the world. This year we tried in-situ neutron diffraction at 18 GPa by using Paris-Edinburgh press (PE press) [1, 2].

Generally, the quality of the diffraction pattern taken at such pressures is not good due to the contamination of Bragg peaks from the high-pressure anvils. PLANET [3] is equipped with radial collimators which can eliminate them. By coupling the radial collimators and the PE press, we managed to obtain clear patterns and analyzing structures of crystals and amorphous solids precisely at 18 GPa. Here, we report the experimental details and share several examples.

2. Method

The diffraction geometry used in the experiments is shown in Fig. 1. The sample (typically 4 mm in diameter and 3.1 mm in height) is compressed by a couple of sintered diamond anvils. The press is placed at sample position with the compression axis parallel to the incident beam. Neutrons scattered by the sample are detected with two 90° banks. The incident collimator of boron nitride with a hole of 4 mm defines the neutron beam introduced into the sample and the radial collimator with a gauge length of 1.5 mm along the beam direction eliminates the scattering from the anvils. This setup enables us to obtain signals exclusively from the sample over scattering angles of 90°±3.7° horizontally and 0°±34.6° vertically.

3. Example

Application to crystalline materials

To investigate the pressure response of hydrogen bond in the hydrous mineral δ-AlOOH and its D/H isotope effect, we performed neutron diffraction experiments at pressures up to 18.2 GPa. The sample was loaded into a TiZr gasket together with pressure-transmitting medium of methanol-ethanol mixture and compressed with a PE press. The initial volume of the sample chamber was 26 mm^3. The booster focusing mirror was used to increase the beam flux. Above 10 GPa, a slight broadening of the diffraction peaks was observed, from 0.7% in $\Delta d/d$ at ambient condition to 1.08% at 17.4 GPa because of the non-hydrostatic stress caused by the solidification of the pressure transmitting medium.

Figure 2 shows the observed diffraction pattern of δ-AlOOD at 17.4 GPa and the results of Rietveld fitting. The exposure time of 4 hours at 17.4 GPa at the accelerator power of 290 kW was sufficient to refine the structure. The transition from the $P2_1nm$ phase to a $Pnnm$ one

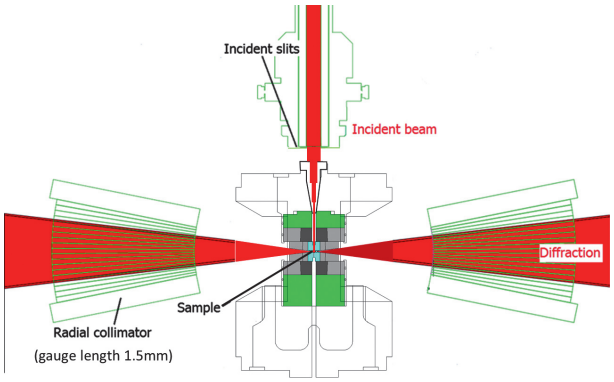

Figure 1. Diffraction geometry employed in the in-situ neutron diffraction experiments using Paris-Edinburgh press.

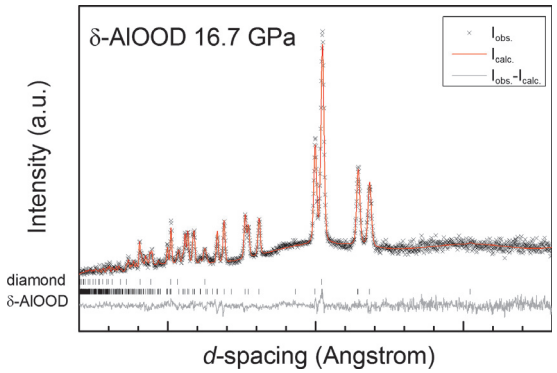

Figure 2. Observed and calculated patterns of δ-AlOOD at 17.4 GPa. Tickmarks show the calculated peak positions of δ-AlOOD and the diamond that was used as the anvil of the PE press.

was observed at 12.1 GPa in δ-AlOOD. This pressure was almost the same as the condition at which the change in compressibility was found previously. The result revealed that even small changes of the hydrogen position by compression affect the bulk compression behavior.

Structure analysis of amorphous materials

We have investigated the structure of SiO_2 glass at pressures up to about 17 GPa in order to reveal the contraction mechanism and the possible existence of first-order amorphous-amorphous transition under high-pressure condition.

The sample shaped into a form which fits into the dip on the anvil top (4 mm in diameter and 3.6 mm in height) was placed between the anvils and compressed to 17 GPa with no pressure transmitting medium. The generated pressure was estimated from the pressure-load curve checked prior to the experiments.

Figure 3 shows a set of raw data for three profiles (i.e. sample, vanadium and empty) taken with the PE press. The exposure time for each pattern was typically 24 hours. It is clear that the Bragg peaks from the anvils were hardly observed in any profile, thanks to the radial collimator.

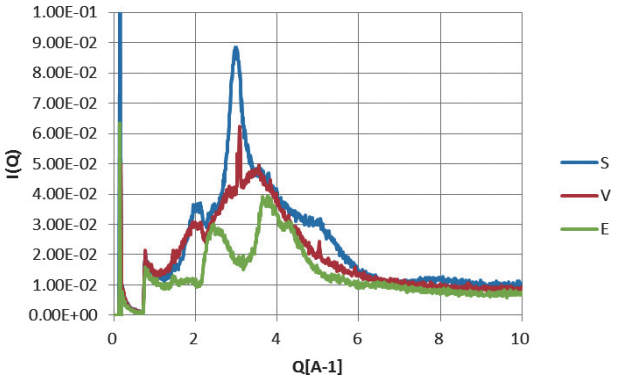

Figure 3. Raw data taken with the PE press (S; sample at 17 GPa, V: vanadium at 17 GPa, E: Empty: gasket only at ambient pressure).

The data were analyzed with the Python code "nvaSq" developed for structure analysis of disordered materials at BL21 NOVA. Figure 4 shows the S(Q) obtained in this study, together with that below 10 GPa in the previous study. The pressure dependence shows marked changes in the raw-Q region reflecting the structure of intermediate range order. On the other hand, no significant changes were observed in the long-range oscillation part reflecting the short-range order. These observations are consistent with the previous view on the contraction of the SiO_2 glass. The results of the detailed analysis will be published elsewhere.

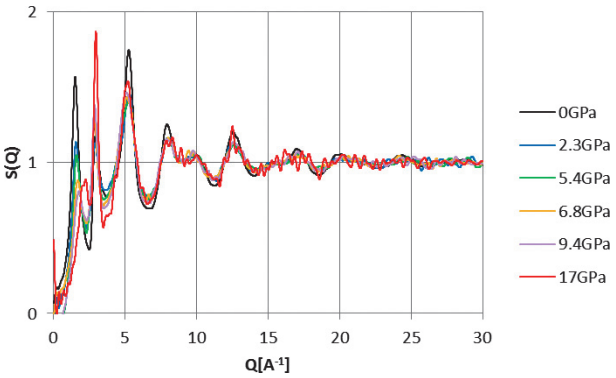

Figure 4. S(Q) of SiO_2 glass at pressures up to 17 GPa. S(Q) below 10 GPa was taken with six-axis press [4] and that at 17 GPa was taken with PE press.

References

[1] J. M. Besson *et al.*, Phyica B 180-181, 907 (1992).
[2] S. Klotz *et al.*, High Press. Res.24 219 (2004).
[3] T. Hattori *et al.*, Nuclear Inst. and Meth. Phys. Res., A780 55 (2015).
[4] A. Sano-Furukawa *et al.*, Review of Scientific Instruments, 85, 113905 (2014).

T. Hattori[1,2], A. Sano-Furukawa[1,2], K. Funakoshi[3], J. Abe[3], and S. Machida[3]
[1]Neutron Science Section, Materials and Life Science Division, J-PARC Center; [2]Quantum Beam Science Directorate, JAEA; [3]Neutron R&D Division CROSS-Tokai

High Resolution Chopper Spectrometer at BL12

1. Introduction

The High Resolution Chopper Spectrometer (HRC) is being operated at BL12 to study the dynamics in condensed matters with high resolutions using relatively high energy neutrons. A research project using the HRC is being conducted to observe a wide range of correlated electron systems. Based on the achievements in the 1st phase of our project (FY2009-2013), we will improve the performance of the HRC in the 2nd phase starting from FY2014, in the following areas: (1) low angle detecting system for high energy experiments, (2) Fermi choppers for higher resolution and lower background in the high energy region, (3) sample environment equipment, especially the superconducting magnet, (4) completion of installing detectors at high angles, and (5) computational environment for easy operation of experiments.

2. Instrumentation in FY2014

In the initial construction, 128 pieces of 2.8 m PSDs, which are mounted into two detector banks, covered ϕ = 3° - 42°. 64 pieces of 2.8 m PSDs are mounted on each detector bank panel of 1.5 × 3 m^2 with a vacuum flange on the vacuum scattering chamber. 128 more pieces of PSDs for another two detector banks were purchased and mounted. These detectors cover ϕ = −30° - 60° at present.

We have a variety of sample environments: three types of refrigerators – GM type, ^{3}He sorption pumping type, ^{3}He circulation type – and a superconducting magnet.

The GM-type refrigerator is conventionally used to cool the sample stably down to 4 K. This refrigerator shows a good cooling performance by improving the radiation shielding, which is made of thin Al foil and is in contact with the cold head. Sample temperature as low as to 2.5 K and heat-up rate of 26 μK/min on the sample have been confirmed, as shown in Fig. 1. A temperature sensor with fine calibration is used at the sample, and another one with rough calibration is at the cold head. This may cause higher than normal indication at the cold head for the best case indicated by "*ike*" and "*masu*".

The lowest temperatures of 0.3 K and 0.6 K were confirmed for the ^{3}He sorption pumping type refrigerator and the ^{3}He circulation type refrigerator, respectively. For the ^{3}He sorption pumping type refrigerator, an outer vacuum chamber (OVC) was attached in order to separate the vacuum surrounding the sample from the vacuum scattering chamber and keep the lowest temperature, and the goniometer was modified for the attachment. For the ^{3}He circulation type refrigerator, an OVC was mounted in the initial manufacture process. In order to reduce the background noise from the OVC for these refrigerators, an oscillating radial collimator was introduced.

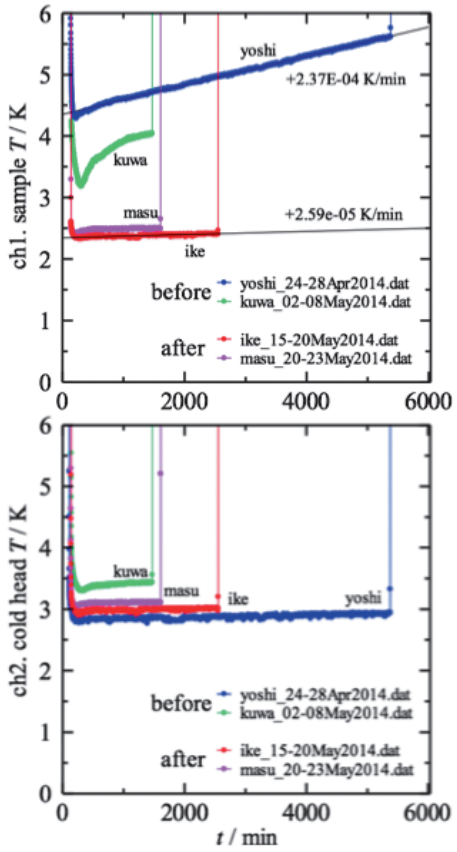

Figure 1. Temperature variations at the sample can (top) and the cold head of the refrigerator (bottom) before and after the improvement of the radiation shielding on the GM-type refrigerator.

On HRC we also installed a superconducting magnet with performance of maximum magnetic field of 14 T and the lowest temperature of 0.3 K. We performed the commissioning at the Guide Hall of JRR-3M, and confirmed that it was successfully operated with the maximum magnetic field of 14 T at the lowest temperature of 0.3 K. Then we moved the superconducting magnet to the HRC, and examined the maximum magnetic field in the actual setup of the experiments. We confirmed a maximum magnetic field of 10 T on the HRC without any damage to the devices around the sample area (Fig. 2).

Figure 2. Successful operation of the superconducting magnet with the application of magnetic field of 10 T at the sample position of the HRC.

In the control software, the graphical user interface (GUI) for the Fermi chopper was improved. Also, the software necessary to control the superconducting magnet, such as that for monitoring the magnetic field and the temperature and controlling the sample orientation, was installed.

In the analysis software, some algorithms were improved, such as for the alignment of the sample crystal, for plural runs, for extraction of event data at a specified time range, and for masking unused detectors or detector pixels.

In the computer hardware, the network attached storage (NAS) was increased from 44 TB to 76 TB, and a workstation (Dell Precision T7610) for the MSlice analysis was set up.

Because the phase control of the Fermi chopper is sometimes unstable, the stability in the phase control and the balancing of the magnetic bearing were investigated. However, we could not obtain conclusive results.

A regular maintenance was performed for some vacuum pumps such as two sets of scroll pumps and a mechanical booster pump for the vacuum scattering chamber, and two scroll pumps for the T0 chopper and the guide tube. The turbo molecular pump for the Fermi chopper was replaced.

3. Scientific Results

On the HRC, the following studies were conducted in this fiscal year: magnetic model in multiferroics $NdFe_3(BO_3)_4$ [1], crystal field excitations in breathing pyrochlore antiferromagnet $Ba_3Yb_2Zn_5O_{11}$ [2], high energy excitations in itinerant antiferromaget γ-FeMn [3], ferromagnetic order in $CePd_2P_2$ [4], investigation of stripe and over-doped checkerboard ordering in layered nickel oxide $Nd_{2-x}Sr_xNiO_4$ [5, 6], crystal electric field excitations in filled skutterudite $PrRu_4P_{12}$ [7], spin and hole dynamics in carrier doped quantum Haldane chain [8], intermultiplet transitions in filled skutterudite $SmFe_4P_{12}$ [9].

References

[1] S. Hayashida, M. Soda, S. Itoh, T. Yokoo, K. Ohgushi, D. Kawana, H. M. Rønnow and T. Masuda, Phys. Rev. B 92 (2015) 054402.
[2] T. Haku, M. Soda, M. Sera, K. Kimura, S. Itoh, T. Yokoo, T. Masuda, in preparation.
[3] S. Ibuka, S. Itoh, T. Yokoo, Y. Endoh, unpublished.
[4] Y. Ikeda, H. Yoshizawa, S. Konishi, S. Araki, T. C. Kobayashi, T. Yokoo, and S. Itoh, J. Phys.: Conf. Series 592 (2015) 012013.
[5] Y. Ikeda, S. Suzuki, T. Nakabayashi, H. Yoshizawa, T. Yokoo, and S. Itoh, J. Phys. Soc. Jpn. 84 (2015) 023706.
[6] Y. Ikeda, S. Suzuki, T. Nakabayashi, H. Yoshizawa, T. Yokoo, and S. Itoh, J. Phys. Soc. Jpn. in press.
[7] K. Iwasa, A. Yonemoto, S. Takagi, S. Itoh, T. Yokoo, S. Ibuka, C. Sekine, and H. Sugawara, Physics Procedia, in press.
[8] T. Yokoo, S. Itoh, S. Ibuka, H. Yoshizawa and J. Akimitsu, J. Phys.: Conf. Series 568 (2014) 042035.
[9] S. Konno, A. Ssuzuki, K. Nihei, K. Kuwahara, D. Kawana, T. Yokoo, S. Itoh, J. Phys.: Conf. Series 592 (2015) 012029.

S. Itoh[1,2], T. Yokoo[1,2], T. Masuda[3], H. Yoshizawa[3], M. Soda[3], Y. Ikeda[3], S. Ibuka[1,2], T. Asami[3], R. Sugiura[3], D. Kawana[3], Y. Kawamura[3], T. Shinozaki[3], and Y. Ihata[4]

[1]Institute of Materials Structure Science, KEK; [2]Neutron Science Section, J-PARC Center; [3]The Institute for Solid State Physics, The University of Tokyo; [4]Technology Development Section, J-PARC Center

BL14 AMATERAS

1. Introduction

2014 was the sixth year of operation of AMATERAS, a cold-neutron disk-chopper spectrometer (Fig. 1). We continued the user program steadily without any serious problems, as described below.

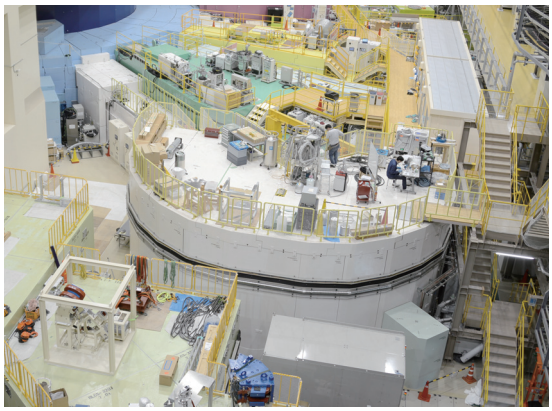

Figure 1. Photo of AMATERAS (May, 2014).

2. Instrumental activities

In JFY2014, we carried out the following main instrumental activities: installation of a top-loading-type cryostat and increase of the shielding.

Since the beginning of the user program, AMATERAS has been equipped with a bottom-loading-type closed-cycle refrigerator (CCR) as a standard sample environment, which realizes low background due to a minimal Al window. This cryostat does not have an outer vacuum chamber to share the adiabatic space with the scattering vacuum chamber of the instrument, so it takes half a day to change the sample. In order to reduce this time and perform experiments more effectively, this fiscal year a new top-loading-type CCR for users' experiments was installed on AMATERAS. In our commissioning, we measured the reduction of background from the CCR and performed off-bench and on-beam operation. This CCR enables us to change the sample within an hour.

AMATERAS has a stainless steel duct to receive the direct neutron beam, called get-lost tube. We had a problem with high radiation level around the beam dump due to the γ-ray yielded at the duct, then we needed to take some measures before increasing the beam power to 1 MW. In JFY2014, we covered the inside of the get-lost tube with 10-mm thick B_4C to prevent neutrons from hitting the stainless steel directly (Fig. 2). Furthermore, 100-mm thick iron shielding was added onto the beam dump (Fig. 3). After these measures, the radiation level around the beam dump was dramatically lowered.

Figure 2. B4C liners (10 mm in the thickness) were inserted in-side the get-lost tube of AMATERAS.

Figure 3. Additional shielding on the beam dump of AMATERAS.

3. User Program

The research fields of the proposals on AMATERAS had vary widely. In the 2014A and 2014B periods, 16 general use proposals were accepted, and six proposals were listed on the reserved subjects. We accepted two project use proposals as continuations from the 2013 period, which are 'Study of structure and electronic properties of functional materials at BL14' (PI: T. Masuda) and 'Project research on structure and dynamics of protonic, superionic and amorphous functional materials using AMATERAS' (PI: Y. Inamura). Also, two element strategy use proposals, 'In-situ Neutron Analysis of Advanced Structural Materials in Elements Strategy

Initiative for Structural Materials (ESISM)' (PI: N. Tsuji) and 'Neutron-scattering research on element-strategy project for electronic materials' (PI: Y. Murakami) were accepted. Unfortunately, due to problems with the neutron targets and the linac and the fire accident in MLF, we could not finish 5 proposals (general use: 3, element strategy use: 1, project use: 1) and it was decided to transfer them to the next year.

AMATERAS joined the MLF School for the first time in mid-December. Three students participated and studied QENS measurement and analysis for room temperature ionic liquids (Fig. 4). From a curve fitting with a jump diffusion model consisting of three Lorentzian dynamical modes at several temperatures, they reduced the diffusion constant of the energy width of each component and activation energy of slowest diffusion mode. We hope the neutron experiment will become one of the tools used in their research activity.

4. Other Topics

AMATERAS had interim assessment done by the MLF Neutron Instruments Review Committees. Achievements in hardware development, user programs and other activities for the last five years were reviewed through documents and interviews. We received very positive comments and recommendations to continue our activities in the way we had performed them before.

Dr. H. Nakagawa was awarded by the Japanese Society for Neutron Science (JSNS) for his work on the study of DNA dynamics done on AMATERAS. His work was also covered in a press release issued on August 29, 2104.

Figure 4. Students set sample in cryostat in MLF School.

K. Nakajima, S. Ohira-Kawamura, Y. Kawakita, and T. Kikuchi
Materials and Life Science Division, J-PARC Center

Upgrading of TAIKAN

1. Introduction

The small and wide angle neutron scattering instrument TAIKAN (BL15) has been developed and upgraded to analyze microstructures or hierarchical structures of substances in various scientific fields precisely and efficiently with a 1 MW spallation neutron source in J-PARC. In FY2014, further upgradings for low-*q* measurement and high-*q* measurement were done.

2. Upgrading of for low-*q* measurement

A focusing-geometry SANS method is adopted for the measurement in a *q* range of 0.0005 – 0.005 A^{-1}. For the method, beam focusing devices and an ultra-small-angle detector are used. Figure 1 shows the beam focusing devices installed in the beam line. The devices are a quadrupole magnet to polarize a neutron beam and two sextupole magnets to focus the neutron beam polarized by the quadrupole magnet on the ultra-small-angle detector. The detector is a high-resolution scintillation detector with an active size of 5 inch in diameter and spatial resolution of about 0.5 mm. Figure 2 shows the detector and neutron image data obtained by the detector with a mesh cadmium plate. From the data it was confirmed that the detector can give data with small distortion and is available for SANS measurement.

3. Upgrading of for high-*q* measurement

A backward detector has been installed in TAIKAN. The performance of the detector was evaluated with CeO_2 powder. Figure 3 shows diffraction data measured with the detector. The diffraction data can be analyzed well by the Rietveld method.

4. Future prospect

The evaluation of the focusing-geometry SANS system will be performed with the devices and the ultra-small-angle detector after installation of neutron spin flippers in FY2015. TAIKAN will be a small and wide neutron scattering instrument in name and in reality before long.

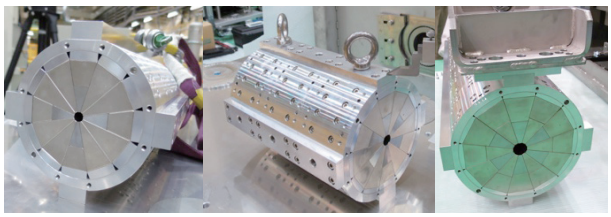

Figure 1. Magnets developed for focusing-geometry SANS measurement: (left) a quadrupole magnet, (middle) the first sextupole magnet, and (right) the second sextupole magnet.

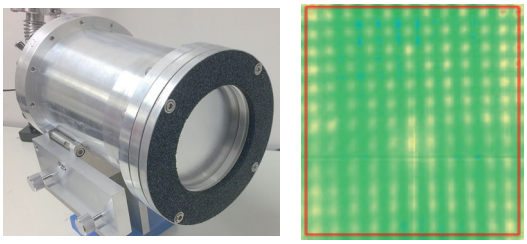

Figure 2. (Left) a high-resolution 2D detector and (right) neutron image data obtained by the detector.

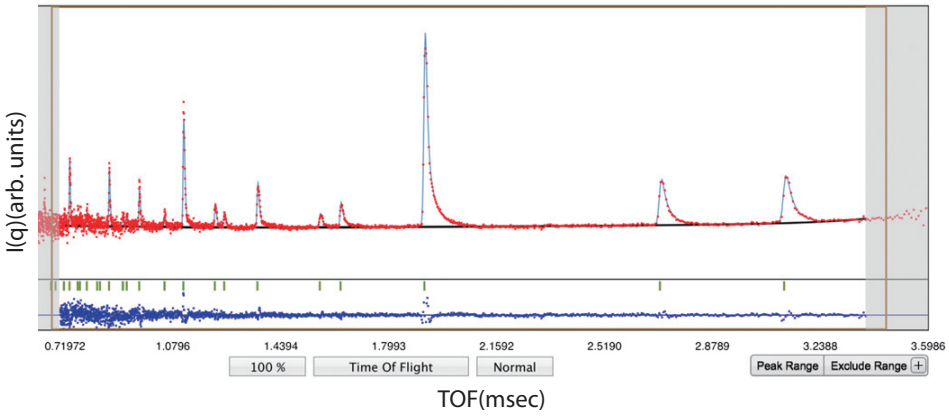

Figure 3. Diffraction data of CeO_2 powder measured with a backward detector.

J. Suzuki[1], S. Takata[2], K. Ohishi[1], H. Iwase[1], T. Morikawa[1], Y. Kawamura[1], M. Sahara[1], T. Hosoya[2], Y. Inamura[2], T. Ito[1], T. Nakatani[2], T. Shinohara[2], T. Oku[2], K. Suzuya[2], K. Aizawa[2], and M. Arai[2]

[1]Neutron R&D Division, CROSS-Tokai; [2]Neutron Science Section, Materials and Life Science Division, J-PARC Center

Development of Elliptic Focusing Mirror for Sample-focusing Neutron Reflectometry at BL16

1. Introduction

Neutron reflectometry (NR) is very useful for investigations of structures of surfaces and buried interfaces composed of soft materials. SOFIA is a horizontal-type neutron reflectometer constructed at Beamline 16 (BL16) of the Materials and Life Science Experimental Facility (MLF) of the Japan Proton Accelerator Research Complex (J-PARC) [1, 2]. Due to the high-flux beam of J-PARC, less than one hour is needed for taking a full *Q*-range data and only a few seconds for a limited *Q*-range data in the case of a sample with 3 inches (76 mm) in diameter; even though the beam power is still one-third of the planned value, 1 MW. However, several hours are still needed for a small sample such as 10 mm × 10 mm, which is a typical size of a sample for X-ray reflectometry.

In the near future we plan to install an elliptical focusing mirror as a further upgrade of the SOFIA reflectometer. The focusing mirror will enable us to illuminate a sample with a neutron beam with a large beam divergence. In the case of conventional double slit collimation, the optimal beam divergence decreases according to the sample size. Hence, the focusing optics with the mirror has an advantage on the beam flux especially for small samples. The planned specifications of the focusing mirror and detector are a beam size of 0.1 mm at a sample position with divergence of 2.5 mrad.

In this report we cover the development of a prototype of a focusing mirror with an elliptic shape and the result of a reflectivity measurement with the focusing mirror performed at BL16.

2. Manufacture and ray trace simulation

We employed an aluminum alloy as a base plate for the focusing mirror. First, the base plate was machined with a single diamond tool to produce a rough surface shape, in which the surface follows the center part of an ellipse with a long axis of 4300 mm and a short axis of 430 mm. Then, the plate was coated with nickel phosphorous by electroless plating process, and finished by an ultrahigh precision cutting (UPC) process. The surface was polished before coating the super mirror to create a smooth surface of less than 1 nm in root mean square (RMS) roughness. The super mirror with the m-value of 3 was deposited on the substrate using an ion beam sputtering instrument at the Kyoto University Research Reactor Institute [3]. Since the mirror size, 550 mm in length and 60 mm in width, was too large to coat the super mirror, the mirror was divided into two pieces and assembled into one unit after the processes above were completed.

Figure 1 shows a photo of the mirror and the shape and figure error measured by a contact type three-dimensional coordinate measurement machine (Mitsutoyo Bright Apex 1230). Although the surface follows an elliptic shape, there were slight figure deviations from the ideal shape. To evaluate the effect of the figure error, we performed a ray trace simulation with the shape measurement result. The size of the light source at a focal point was 50 μm; therefore, the beam focused on the other focal point, that is, the sample position, ideally should be the same size. However, the beam size at the sample position by the simulation was 0.3 to 0.4 mm because of the figure error. This means that the minimum beam size focused by the mirror is limited by the figure error.

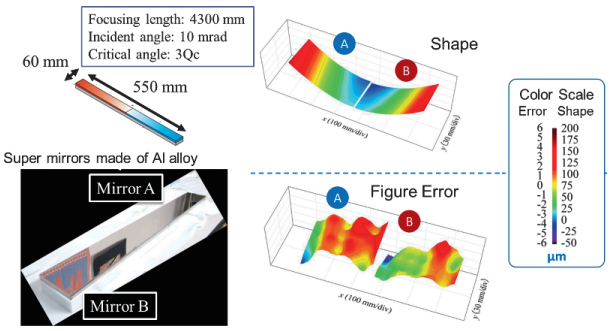

Figure 1. Photo and shape of the focusing mirror made of aluminum plates.

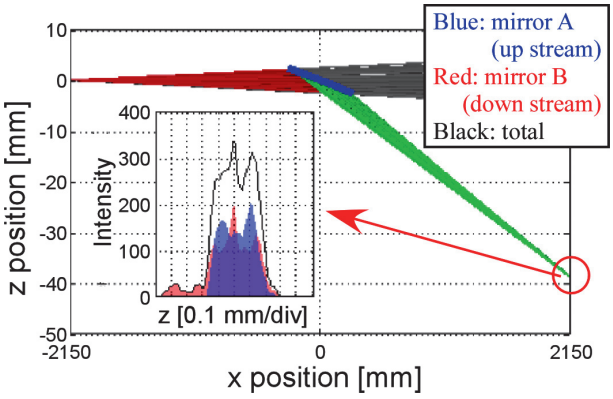

Figure 2. Ray trace simulation using a figure error measured with a three-dimensional coordinate measurement machine.

3. Results

With the focusing mirror, we performed the focusing experiment at BL16. Figure 3 presents the focal image at the sample position. The size of a neutron source, slit aperture, was 50 μm as the simulation above and the image of the simulation was well reproduced. The full width at half maximum (FWHM) of the image was evaluated to be 0.34 mm by the fitting with a Gaussian function.

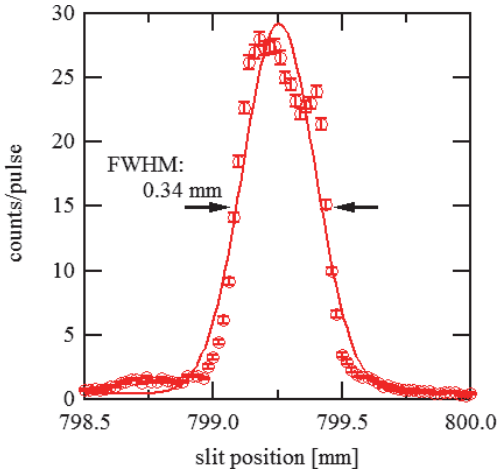

Figure 3. Focal image of neutrons at a focal point with a source size of 0.05 mm.

Furthermore, we attempted to measure the neutron reflectivity using an optics with the focusing mirror. The size of the neutron source and incident angle of neutrons were 0.4 mm and 1.2° degrees, respectively, in which the beam size in the traveling direction was 20 mm. The sample was a deuterated polystyrene thin film on a Si substrate with a diameter of 2 inches (50.8 mm). For comparison, we also performed the reflectivity measurement using a conventional optics with double slits. Figure 4 shows the reflectivity profiles with and without the focusing mirror, in which the profiles show good consistency. One thing we should emphasize here is that the count rate with the focusing mirror (6.40 counts/pulse) is approximately 3 times larger than that without the mirror (1.94 counts/pulse).

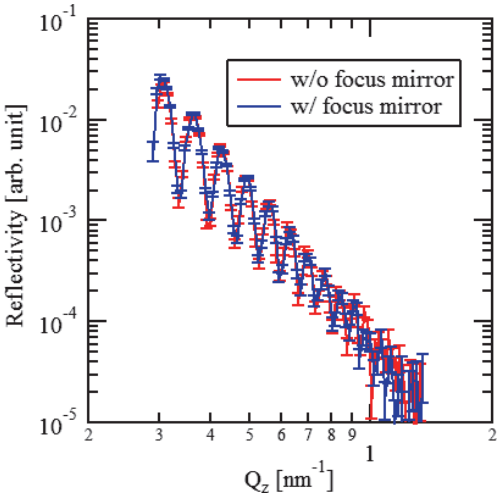

Figure 4. Reflectivity profiles taken with a double slit collimation and a focusing mirror.

4. Summary

Here, we reported the development of the focusing mirror for the neutron reflectometer SOFIA. The mirror is capable of focusing neutrons with a width of 0.34 mm in FWHM. With this mirror, a reflectivity measurement was carried out and the gain factor was approximately 3 in comparison with the conventional double slit collimation. We are now planning to fabricate a new focusing mirror, in which some critical processes we became aware of by using the prototype mirror are modified to decrease figure errors for 0.1 mm focusing. As the gain factor increases with the reduction of the beam size, this mirror will enable us to measure smaller samples more efficiently.

References

[1] N. L. Yamada *et al.*, *Euro. Phys. J. Plus*, **44** (2011) 9424.
[2] K. Mitamura *et al.*, *Polymer J.*, **45** (2013) 100.
[3] M. Hino *et al.*, *Nucl. Instr. and Meth. A*, **797** (2015) 265.

N. L. Yamada[1,2], T. Hosobata[3], M. Hino[4], S. Takeda[5], J. Guo[3], S. Morita[6], T. Oda[4], J. Kato[3], Y. Yamagata[3], and M. Furusaka[5]
[1]High Energy Accelerator Research Organization, Tokai, Japan; [2]Japan Proton Accelerator Research Complex, Tokai, Japan; [3]RIKEN Center for Advanced Photonics, Wako, Japan; [4]Kyoto University, Kumatori, Japan; [5]Hokkaido University, Sapporo, Japan; [6]Tokyo Denki University, Tokyo, Japan

BL17: Neutron Reflectometer SHARAKU

1. Introduction

Polarized neutron reflectometry is one of the powerful methods for studying the surface and interface structure of magnetic materials. The polarized neutron reflectometer SHARAKU [1], named after the famous Japanese ukiyo-e printer, was installed at BL17 as the second reflectometer of the MLF. SHARAKU was constructed in the beginning of 2012, and then we started the commissioning and a portion of the user program. Now SHARAKU is widely open to international users. In this article, we cover the progress achieved in this fiscal year.

2. Neutron polarization in weak magnetic field

Weak magnetic materials are widely used in electric and electronic devices, and are some of the most interesting targets for the polarized neutron reflectometer. Due to their low magnetic coercivity, the weak-magnetic-field polarization system should be generated for their polarized neutron reflectivity analysis. In SHARAKU, the polarization system in a strong magnetic field (10 kOe in a sample position) works well. However, the polarization system in a weak magnetic field is not enough to analyze weak magnetic materials. Therefore, we installed some guide coils to connect the guide magnetic field before and after a sample position, and optimized their current values.

Figure 1 shows the time-of-flight (TOF) spectra obtained with the polarized neutron analysis mode in weak magnetic field (50 Oe in a sample position). The spin states of incident and scattered neutrons were selected to produce the non-spin-flip cross sections (R^{++}(red) and R^{--}(green)) and the spin-flip cross sections (R^{+-}(yellow) and R^{-+}(blue)) as shown in Fig. 1. The flipping ratio (F) values were determined by the ratio of $F^{+} = R^{++}/R^{+-}$ or $F^{-} = R^{--}/R^{-+}$. It is clear that the neutron polarization was maintained in weak magnetic field, and its mean flipping ratio of 50 Oe condition within the wavelength of $2.4 < \lambda$ (Å) < 8.4 was 51.8.

Since the mean flipping ratio of 10 kOe was 54.5, it can be concluded that the magnetic field construction was sufficiently improved by this commissioning. Further improvement in the lower magnetic field (< 50 Oe) will be conducted in the future.

3. Development of the data analysis system

We have used the software Utsusemi [2] and BL17 original software to analyze the measured neutron TOF

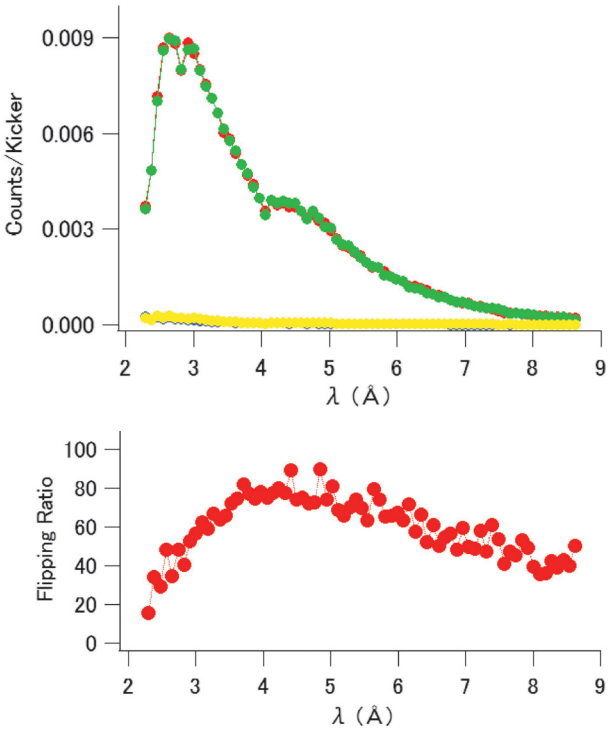

Figure 1. TOF spectra obtained with polarized neutron analysis mode (above) and theflipping ratios (below) in 50 Oe condition.

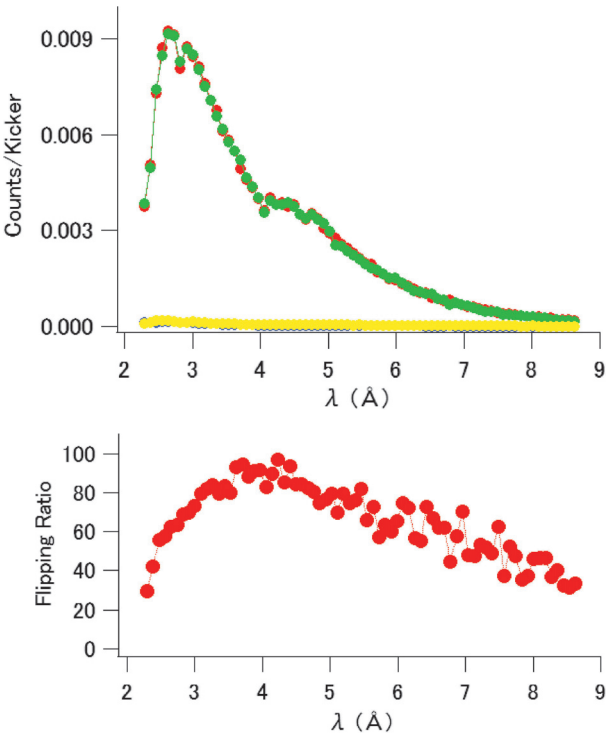

Figure 2. TOF spectra obtained with polarized neutron analysis mode (above) and the flipping ratios (below) in 10 kOe condition.

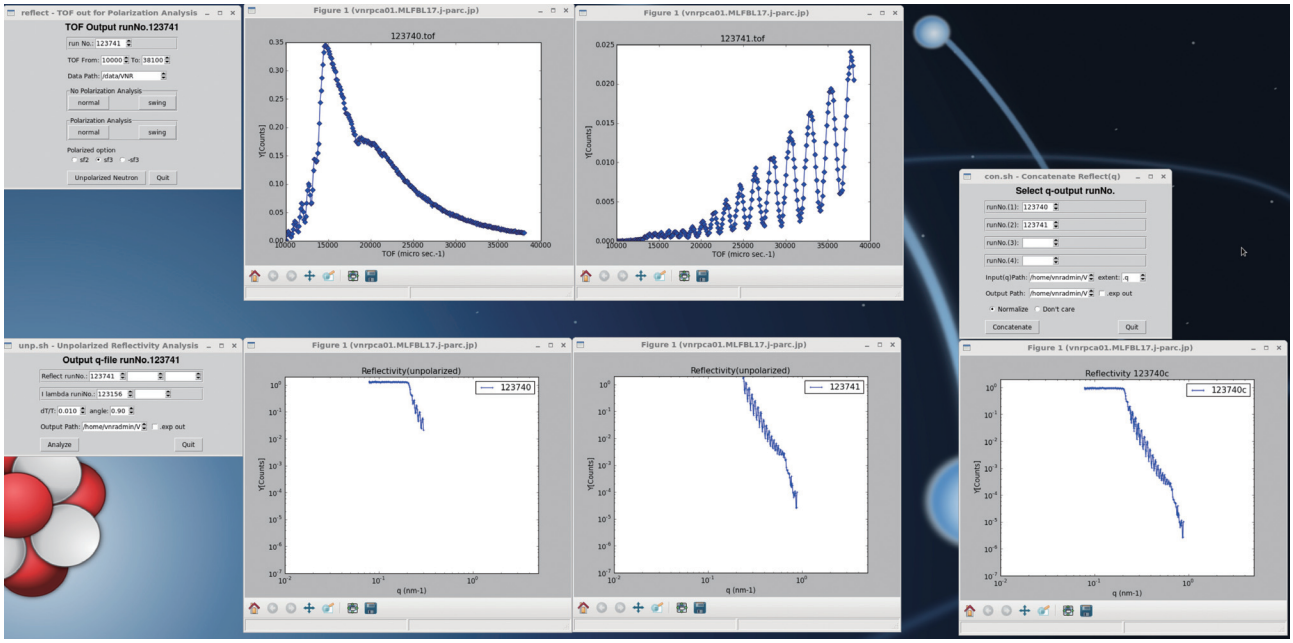

Figure 3. Operation panels of the data reduction program. Upper left is a TOF data output program, lower left is a reflectivity calculation program, and right is a reflectivity data connection program.

data and to convert the TOF data into neutron reflectivity profiles, respectively. However, these data reduction procedures are slightly complicated and it was difficult to obtain and check the reflectivity profiles during measurement. Therefore, we had to improve this situation by development of a new data analysis system.

In 2014, new data reduction, normalization, and subtraction programs were developed and installed in SHARAKU. Figure 3 shows the operation panels of the data reduction program. The TOF and reflectivity profiles can be obtained by input of a run number and experimental conditions, and these programs can show reflectivity profiles on display even during measurement. Now, the data analysis system has been utilized not only for data reduction but also for the on-time monitoring system of reflectivity measurement.

References

[1] M. Takeda *et al.*, *Chinese J. Phys.* **50** (2012) 161.

[2] Y. Inamura *et al.*, *Proc. 19th Meeting on Int. Collaboration of Advanced Neutron Sources* (2010) 10-01.

N. Miyata[1], S. Kasai[1], K. Akutsu[1], M. Takeda[2,3], D. Yamazaki[3,4], K. Soyama[4], J. Suzuki[1], Y. Inamura[3], and T. Nakatani[3]

[1]Neutron R&D Division, CROSS-Tokai; [2]Quantum Beam Science Center, JAEA; [3]Neutron Science Section, Materials and Life Science Division, J-PARC Center; [4]Neutron Instrumentation Section, Materials and Life Science Division, J-PARC Center

BL18: Current Status of SENJU

1. Introduction

SENJU is a TOF single-crystal neutron diffractometer designed for precise crystal and magnetic structure analyses under multiple extreme environments such as low-temperature, high-pressure and high-magnetic fields, and also capable of taking diffraction intensities of small single crystals with volumes of less than 1.0 mm^3 down to 0.1 mm^3.

In 2014, we developed a cryostat for photo crystallography to enable in-situ light-exposure neutron diffraction measurements, and upgraded the data visualization program to ease the development of a diffraction measurement strategy.

2. Development of a cryostat for photo crystallography

Photo-induced crystalline-state properties, such as light-emission and magnetism of organic molecular crystals, have been actively investigated because they can derive new photo-functional organic materials. In recent investigations of those molecular crystals, in-situ light-exposure X-ray diffraction is one of the most important techniques to determine the photo-induced chemical species. On the other hand, neutron diffraction is a powerful technique to observe hydrogen atoms, which are difficult to observe by X-rays. If visible light is induced in a closed-cycle cryostat and in-situ light-exposure neutron diffraction measurement of those crystals under low temperature becomes possible, we will be able to trap the photo-induced metastable species produced by the proton transfer and determine their structure including the transferred proton, which is hard to determine by X-rays. Consequently, the researchers of photo-functional materials will obtain a new powerful analysis technique.

In 2014, as shown in Figure 1, we developed a new closed-cycle cryostat with 2-axe goniometer in which visible white light can be induced to carry out an in-situ single crystal neutron structure analysis of a photo-induced species in a single crystal on SENJU. The cryostat is composed from a 4 K pulse-tube refrigerator, a fixed-χ type 2-axe goniometer using piezo-rotators and an optic fiber light guide. There are several service ports at the interface between the vacuum part and the atmospheric part and a vacuum connector, in which the light guide is embedded, is set on one of the service ports. The forefront of the light guide is covered with super-insulation film and fixed on an optical port of the 4 K radiation shield near the goniometer. Visible light is led into the vacuum part of the cryostat through this light guide and exposed to the sample crystal, as shown in Figure 2. The Xe light source for the cryostat, MAX-303 (ASAHI SPECTRA Co.), has some wavelength selecting filters and the optimum wavelength region for each experiment can be chosen. The lowest temperature at the sample position is 8 K without photo-irradiation, 11 K with a 400 nm band-path filter, 18 K with a 400 nm long-cut filter and 66 K with no filter.

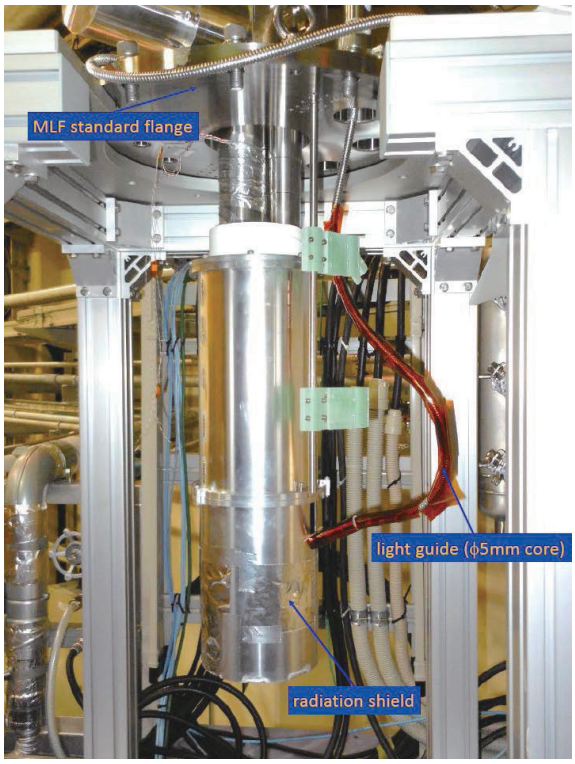

Figure 1. Side view of the cryostat for photo crystallography.

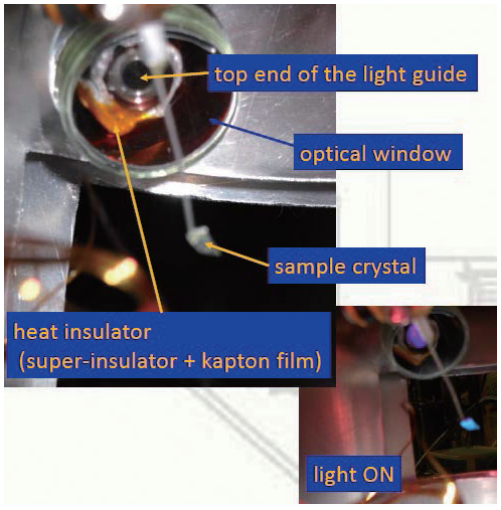

Figure 2. Sample position of the cryostat.

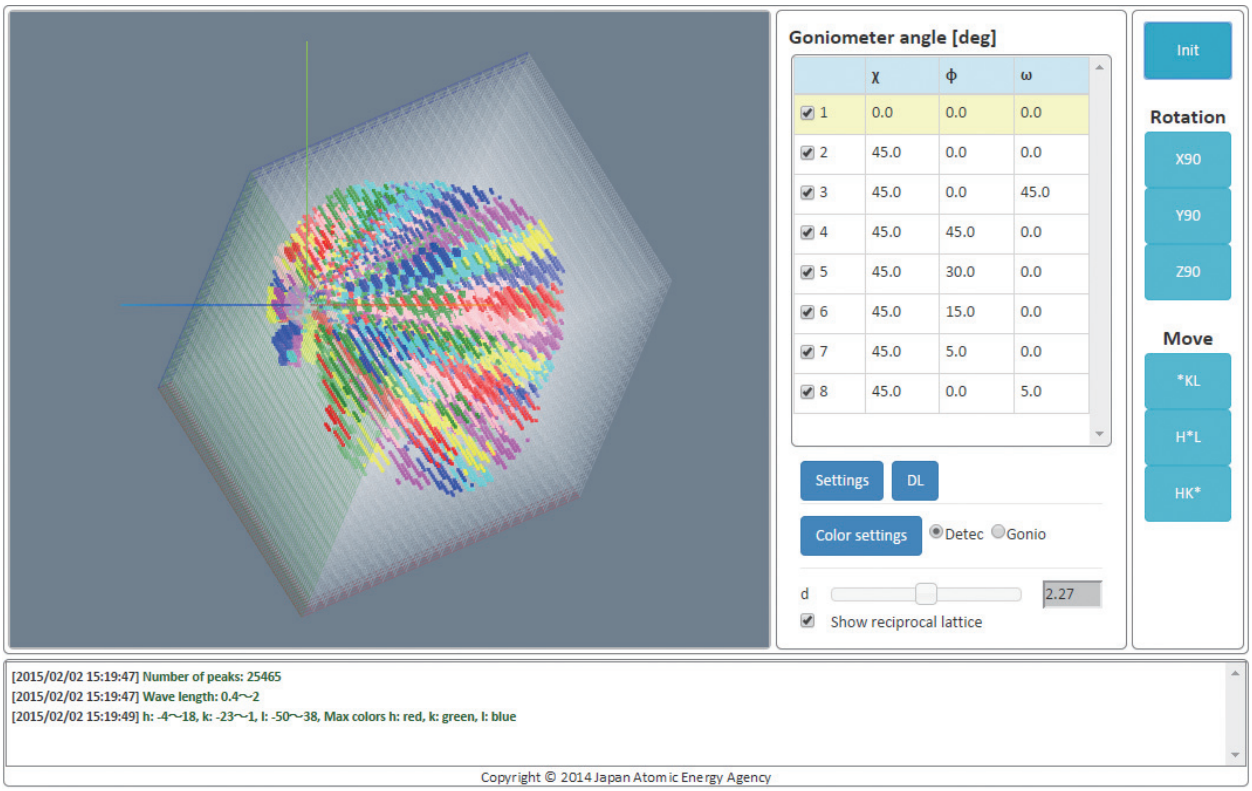

Figure 3. Screen of STARExplorer. The upper left window shows the reciprocal space and the colored dots indicate surveyed Bragg peaks. The upper right window displays the goniometer angles.

3. Development of a new reciprocal-space visualization program "STARExplorer"

In a usual experiment at SENJU, diffraction images of one sample crystal are measured with several orientations of the crystal. Thus, visualization of "surveyed" and "unsurveyed" reciprocal space is very important to optimize the orientation of the crystal. Therefore, in 2014, we developed a new reciprocal-space visualization program called "STARExplorer".

STARExplorer is a web-browser based program written in JavaScript (WebGL), which works on Windows, OSX and CentOS. It shows a 3D image of the surveyed reciprocal space as shown in Figure 3 from a UB-matrix and goniometer angles entered by a user. The 3D image of the reciprocal space can be rotated and enlarged by mouse action.

4. User program

Seven general proposals were conducted in 2014A, and five more in 2014B.

T. Ohhara[1], R. Kiyanagi[1], A. Nakao[2], T. Hanashima[2], K. Munakata[2], T. Moyoshi[2], and T. Kuroda[2]
[1]Neutron Science Section, Materials and Life Science Division, J-PARC Center; [2]Neutron R&D Division CROSS-Tokai

Status of TAKUMI (BL19)

1. Overview

The TAKUMI operation in JFY2014 was stable. The user, project and instrumental programs were performed successfully. Also, several enhancements in both the hardware and the software were performed, and their details are described below.

2. Enhancement of the neutron detection bank

There is a pair of neutron detector banks (north and south detector bank) in TAKUMI for simultaneous detections of two orthogonal strains. Each neutron detector bank was optimally designed to have seven 1-dimensional position-sensitive scintillator detectors, which are laid vertically. Five 1-dimensional scintillator detectors have been installed to each bank in the construction phase to reach a horizontal angular coverage of ±15° and an off-angle of 30°. There are ten detectors in total and four detectors have not yet been installed.

In this year, one detector was installed to the north detector bank to enhance the neutron detection. The commissioning and the utilization for the experiments, together with the installation of another one to the south bank will be carried out.

3. Installation of Thermec Master

The Thermec Master's purpose is to observe the forming process of steel, etc. by in-situ neutron diffraction; it was installed in TAKUMI by the Elements Strategy Initiative for Structural Materials, Kyoto University and the BL19 instrumental group. The main specifications are shown in Table 1. The commissioning was completed and the utilization started. Using a standard steel sample, it was confirmed that a 1 sec time-slice analysis was feasible during a forming process at 300 kW beam power.

Table 1. Specification of Thermec Master.

Item	Specification
Driving	Servo motor driving
Heating	High frequency heating
Cooling	Gas injection of N_2 or He
Maximum temperature	1473 K
Heating, cooling rate	≤ 30 K/s
Working rate	≤ 100 mm/s, 30 kN (compression)
Atmosphere	Vacuum or inert gas

4. Development peak profile analysis

One of the advantages of the neutron diffraction technique compared with other techniques used to determine material characterizations is its high penetrability into materials. Therefore, the neutron diffraction can evaluate averaged characteristics in bulk samples. As an advanced analysis technique, the convolutional multiple whole profile (CMWP) fitting method was introduced into TAKUMI to determine the crystallite size, the dislocation density, the dislocation arrangement parameters, and the dislocation character, which is related to the fraction of edge and screw dislocations from line profiles of the whole sample. The demonstration experiment was performed under tensile loading of as-quenched lath martensitic steel (22SiMn2TiB steel).

5. Development of stroboscopic measurement

The event recording technique was extended not only for data acquisition of neutron detection, but also for data acquisition of various conditions of external fields. By developing a 'condition filtering data reduction', we introduced successfully an *in-situ* stroboscopic measurement during the cyclic test. This technique was applied to a multilayer piezoelectric actuator (PSt150, Piezomechanik GmbH) to study the behavior of the lattice strain and the domain switching under cyclic electric field, and revealed that the microscopic deformation estimated from this technique agreed with the macroscopic behavior of the actuator.

6. Development of *in-situ* neutron diffraction with AE measurement under loading

The acoustic emission (AE) technique is sensitive to internal motion in the range from several tens of kHz to several hundred kHz of bulk material. On the other hand, the neutron diffraction can evaluate the strain precisely at atomic plane level. Therefore, the combination of the AE measurement and the *in-situ* neutron diffraction provide unique information about the deformation mechanism. A development of simultaneous measurements about the AE and the *in-situ* neutron diffraction at room temperature has advanced. Then, this technique was successfully applied to Mg alloys (AZ31, $Mg_{85}Zn_6Y_9$, etc.).

K. Aizawa[1], S. Harjo[2], and T. Kawasaki[2]

[1]Technology Development Section, Materials and Life Science Division J-PARC Center; [2]Neutron Science Section, Materials and Life Science Division, J-PARC Center

The Current Status of the Versatile Neutron Diffractometer, iMATERIA

1. Introduction

Ibaraki prefecture, the local government in Japan in the area where the J-PARC sites are located, has decided to build a versatile neutron diffractometer (IBARAKI Materials Design Diffractometer, iMATERIA [1]) to promote industrial applications for the neutron beam in J-PARC. iMATERIA is planned to be a high throughput diffractometer so that materials engineers and scientists could use it like the chemical analytical instruments in their materials development process.

The roles for neutron diffraction in materials science are (1) to do structural analyses of newly developed materials, (2) to clarify the correlation between structures and properties (functions), and (3) to clarify the relation between structural changes and improvements of functions, especially for the practical materials. To achieve those purposes, a diffractometer with super high resolution is not required. The matching among intermediate resolution around $\Delta d/d = 0.15\%$, high intensity and wide d coverage is more necessary.

This diffractometer is designed to look at a decoupled-poisoned liquid hydrogen moderator (36 mm, off-centered) (BL20), and to have the incident flight path (L1) of 26.5 m with three wavelength selection disk-choppers and straight neutron guides with a total length of 14.0 m. The instrumental parameters are listed in Table 1. There are four detector banks including a low angle and a small angle scattering detector bank. The angular coverage of each detector bank is also shown in Table 1. The rotation speeds for the disk-choppers are the same with a pulse repetition rate of 25 Hz for the most applications (SF mode). In this case, the diffractometer covers $0.18 < d\ (Å) < 2.5$ with $\Delta d/d = 0.16\%$ and covers $2.5 < d\ (Å) < 800$ at three detector banks of 90 degree, low angle and small angle with gradually changing resolution. When the speed for the wavelength selection disk-choppers is reduced to 12.5 Hz (DF mode), we can access a wider d-range, $0.18 < d\ (Å) < 5$ with $\Delta d/d = 0.16\%$, and $5 < d\ (Å) < 800$ with gradually changing resolution with doubled measurement time from SF mode.

Table 1. Instrumental parameters of iMATERIA. L2 is the scattered flight path. The d-range for each bank is the maximum value for 2-measurement mode.

L1	26.5m	
Guide length		Total 14m (3section)
Position of Disk choppers		7.5m(double) 11.25m(single) 18.75m(single)
High	2θ	$150^\circ \le 2\theta \le 175$
Resolution	L2	2.0 - 2.3m
Bank	d-range	$0.09 \le d(A^\circ) \le 5.0$
Special	2θ	$80^\circ \le 2\theta \le 100^\circ$
Environment	L2	1.5m
Bank	d-range	$0.127 \le d(A^\circ) \le 7.2$
Low	2θ	$10^\circ \le 2\theta \le 40^\circ$
Angle	L2	1.2 - 4.5 m
Bank	d-range	$0.37 \le d(A^\circ) \le 58$
Small	2q	$0.7^\circ \le 2q \le 5^\circ$
Angle	L2	4.5 m
Bank	d-range	$1.69 \le d(A^\circ) \le 800$

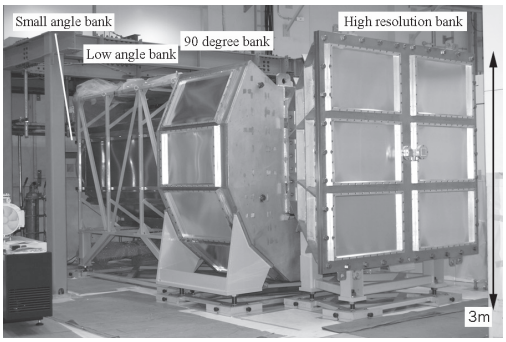

Figure 1. IBARAKI Materials Design Diffractometer, iMATERIA without detector for each bank and instrument shielding. The high-resolution bank, special environment bank (90 degree bank), low angle bank, can be seen from right to left. The small angle detector bank, which is not shown in picture, is situated in the low angle vacuum chamber (left hand of the picture).

2. Current status

The three banks, high resolution bank (BS bank), special environment bank (90 degree bank) and low angle bank, are operational and small angle bank is under commissioning. It takes about 5 minutes (DF mode) to obtain a 'Rietveld-quality' data in high resolution bank at 500 kW beam power for about 1 g of standard oxide samples.

Figure 2 is a typical Rietveld refinement pattern for $LiCoO_2$ sample, cathode material for LIB, at the high resolution (BS) bank by multi-bank analysis function of Z-Rietveld [2]. It takes 20 min at DF mode to collect Rietveld available data, due to high neutron absorption cross section for natural Li ($\sigma_s^{Nat} = 70$ barn).

Small angle detector bank is also start operation with limited d-range.

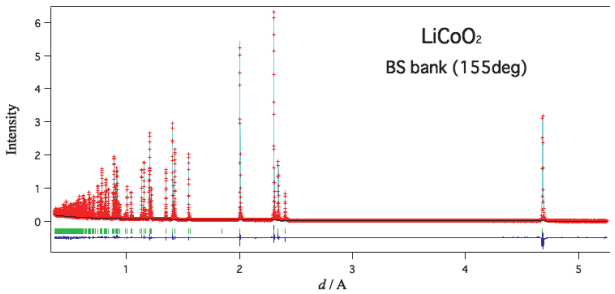

Figure 2. Rietveld refinement pattern for $LiCoO_2$ at high resolution bank of iMATERIA.

3. Sample Environments

The automatic sample changer is the most important sample environment for high throughput experiments. Our automatic sample changer [3] consisted of sample storage, two lines of elevating system, two sets of pre-vacuum chambers and a sample sorting system. We can handle more than 600 samples continuously at room temperature without breaking a vacuum of sample chamber.

The V-furnace (~900 C), the crio-furnace (4 K) and the 1 K crio are ready for experiment. The gas furnace (~900 C) is under modification.

4. Small sample measurements

Accordingly, the beam power became higher than before; it is possible to measure the mg samples for about one day. Small sample measurement is very important for the research for practically materials. We are making some trial neutron diffraction measurement for small quantities samples. For example, we have measured 25.4 mg YBa_2Cu_3Oy sample for 18.5 h at 300 kW beam power. The occupation parameters for deficient oxygen site are almost same with the result of measurement at 1 g samples. This result supported that the neutron diffraction experiment with mg sample can be performed.

In small sample measurement, the selection of sample holder is very important. We have tested $LiCoO_2$ sample using 0.5 mmφ quartz capillary for XRD. The sample weight is 7.3 mg for the beam size (2 cm). The measurement time is only 2 hours and half in 300 kW due to beam stopped, though 10 hours we expected. Figure 3 shows Rietveld analysis patterns for this measurement. Measurement time for this experiment is shorter than the time to get enough statistics. But, Rietveld refinement patterns and obtained parameters are not so bad. We were planning to longer measurement and measurements for another sample to show possibility for small sample measurements.

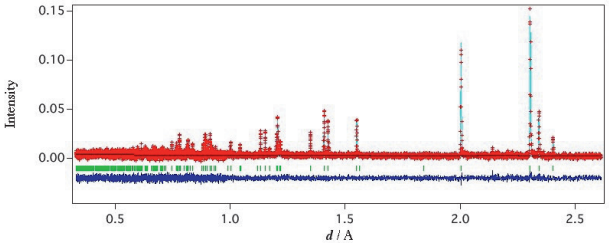

Figure 3. Rietveld refinement pattern for 7.3 mg for beam size $LiCoO_2$ using quartz capillary at high resolution bank of iMATERIA.

References

[1] T. Ishigaki *et al.*, Nucl. Instr. Meth. Phys. Res. A 600 (2009) 189-191.

[2] R. Oishi *et al.*, Nucl. Instr. Meth. Phys. Res. A 600 (2009) 94-96.

[3] A. Hoshikawa *et al.*, J. Phys.: Conf. Ser. 251 (2010) 012083.

T. Ishigaki, A. Hoshikwa, Y. Yoshida, T. Matsukawa, and Y. Onuki
Frontier Research Center for Applied Nuclear Sciences, Ibaraki University

Status of the High Intensity Total Diffractometer (BL21, NOVA)

1. Introduction

Total scattering is a technique to analyze non-crystalline structure in materials. NOVA was designed to perform total scattering and is the most intense powder diffractometer with reasonable resolution ($\Delta d/d$ ~ 0.5%) in J-PARC. To realize high statistical accuracy in the high-Q range, the neutron flight pass between the neutron source and the sample was set at short (15 m) and the wavelength band width of the incident neutron was widened (~ 8 Å). It is easy to adapt NOVA to a very wide field: liquids, glass, local disordered crystalline, magnetic structure of long lattice constant and so on. The observation of the hydrogen position in materials is one of the most important scientific themes of NOVA.

2. Sample environment

For effective measurements with intense neutron flux at the 1-MW operation, a faster and automatic sample exchange is important. A temperature-controlled auto sample exchanger (Fig. 1) was fabricated to realize such an experiment. It can load 12 samples and users can perform the experiment sequentially as an automatic measurement: timing of the exchange of sample on neutron beam and the sample temperature (10 K ~ 500 K). A top loading cryostat was also introduced for the measurement in the temperature range between 5 K ~ 700 K. An automatic sample exchanger with 40 samples for room temperature measurements will be ready in FY 2015.

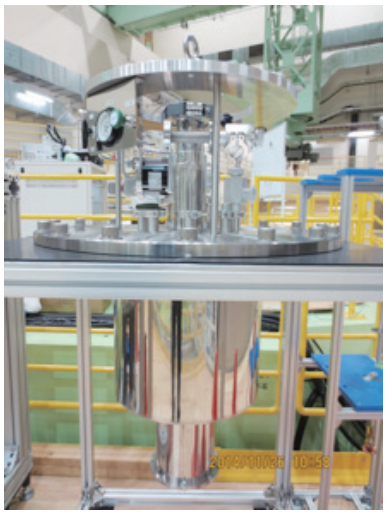

Figure 1. Temperature controlled auto sample exchanger of NOVA.

3. Data reduction software

The goal of the data reduction of total scattering is to obtain static structure factor, $S(Q)$,

$$S(Q) = \frac{1}{<b^2>}\left(\frac{d\sigma_{coh}}{d\Omega} - <b^2> + <b^2>\right) \quad (1)$$

where, b is scattering length, σ_{coh} is coherent cross section, Ω is solid angle, respectively. It is essential for total scattering to obtain an absolute coherent cross section from the observed intensity by the data reduction. Since pair correlation functions will be obtained from $S(Q)$ by Fourier transform, the reliability of pair correlation functions simply relies on the reliability of $S(Q)$.

However, it is not always trivial to get the absolute value and the users need to check whether the reduction is satisfactory. To help with this, the reduction software of NOVA outputs intermediate data as cross section value. Figure 2 shows typical outputs from the

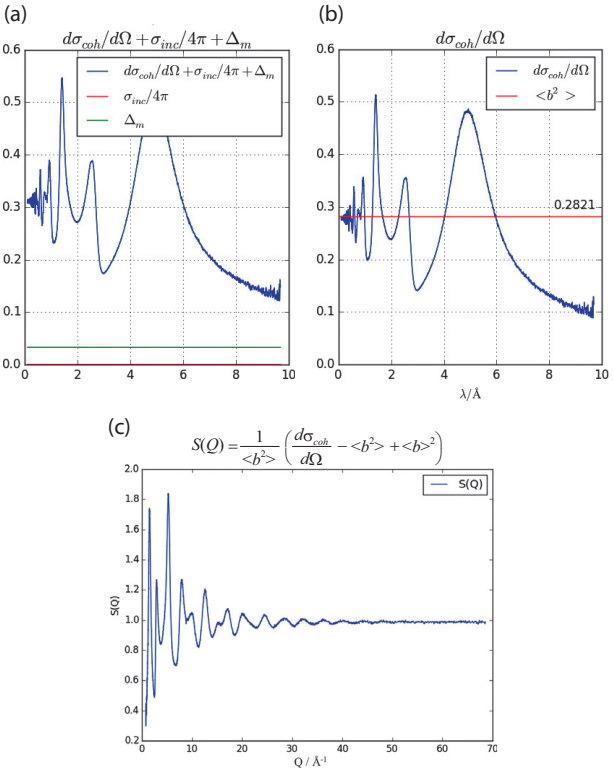

Figure 2. Typical three snap shots of the data reduction process of SiO_2 glass on NOVA. (a) multiple scattering and incoherent cross section, (b) obtained coherent cross section (blue) and (c) calculated cross section with table value and bottom: $S(Q)$ converted from coherent cross section with equation (1).

data reduction software of NOVA. Input parameters of sample information such as bulk density (no. of sample atoms in a beam) and concentration will be checked. If necessary, further corrections with inverse Fourier transform, fitting with polynomial function and self-term correction with Powles method [1] and null-H_2O method [2] will be performed.

References

[1] J. G. Powles, "The analysis of a time-of-flight neutron diffractometer for amorphous materials: the structure of a molecule in a liquid", Mol. Phys. **26**, 1325 (1973).

[2] Y. Kameda *et al.*, "Inelasticity Effect on Neutron Scattering Intensities of the Null-H_2O", Journal of Neutron Research, **11**, 153 - 163 (2003).

T. Otomo[1], K. Ikeda[1], H. Ohshita[1], N. Kaneko[1], T. Seya[1], and K. Suzuya[2]

[1]*Institute of Materials Structure Science, KEK;* [2]*Materials and Life Science Division, J-PARC Center*

Current Status of the Energy-Resolved Neutron Imaging System "RADEN"

1. Introduction

The Energy-Resolved Neutron Imaging System, RADEN, installed at beam line BL22 in MLF, is the first instrument in the world dedicated to pulsed neutron imaging [1]. The aim of this instrument is to carry out not only energy-resolved neutron imaging experiments but also state-of-the-art neutron radiography and tomography experiments using the pulsed neutron beam. The construction of RADEN started in 2013 and the neutron beam was transported for the first time in November 2014 (Fig. 1). After the first beam, we began on-beam commissioning of RADEN to clarify its performance and perform some demonstration experiments.

2. Commissioning of RADEN

To confirm the performance of RADEN, commissioning studies have been carried out. There were several items that had to be characterized. In terms of the basic neutron beam characteristics, the spectrum, the pulse width and the beam intensity were investigated. Also, for the image acquisition, the available field of views and L/D ratios were confirmed by changing the aperture sizes and positions and compared with the expectations. As a result, a maximum FOV of up to 300 × 300 mm^2 was achieved. To characterize the optical device performance, the T0 chopper and the double-disk low-speed chopper were tested. Using the T0 chopper, while the accessible shortest neutron wavelength was restricted to 0.43 Å, the high energy neutron intensity and the prompt burst were decreased to about 10^{-4} of that without the T0 chopper. The double-disk chopper, used to define the wavelength range by changing the opening angle of two disks, was confirmed to provide the neutron beam with well-defined wavelength range and remove properly the higher frame. Moreover, setting one disk in counter-rotation direction and at the smallest opening angle, we can obtain monochromatic beam with coarse wavelength resolution of about 10% by changing the phase of the rotating disks (Fig. 2). Hence, these choppers enable us to conduct neutron radiography experiments with a white or a monochromatic beam easily by just changing the condition of the choppers. As the polarized neutron imaging is planned in RADEN, the neutron polarization devices are installed in the beam

Figure 1. Left: Photograph taken at the time of the first beam. Center and right: first radiographs.

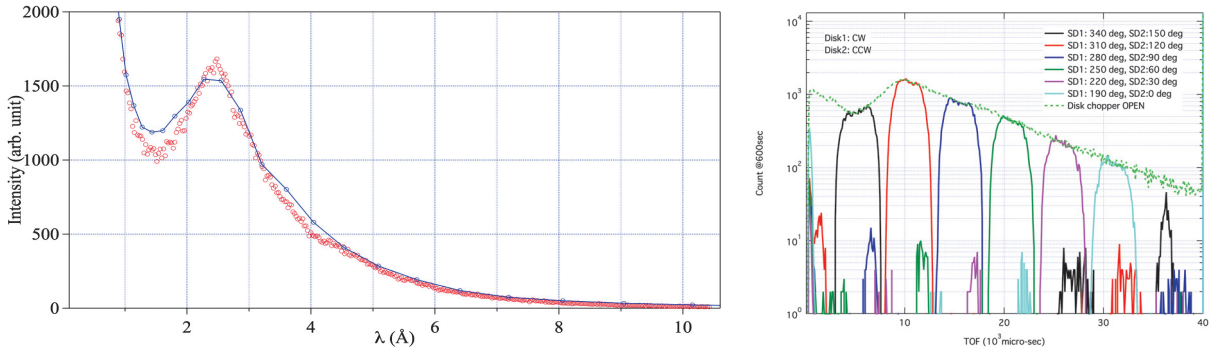

Figure 2. On-beam commissioning results. Left: neutron spectrum (red marker: experiment, blue line: simulation). Right: results of the double disk chopper test to obtain monochromatic beam with coarse wavelength resolution.

line as optional equipment. The polarizability of the device was studied, and the maximum polarization was confirmed to be 97% at a wavelength longer than 5 Å and the critical wavelength was found to be 1.5 Å. Those agreed well with the designed values. However, because small polarization oscillation against the neutron wavelength was observed, improvement in the magnetic field connection is necessary.

Several two-dimensional neutron detectors are prepared in RADEN. For the conventional neutron radiography and tomography, CCD-based camera systems are used, while to perform energy-resolved neutron imaging, which requires accurate measurements of neutron energy by means of time-of-flight technique, counting type neutron detectors, the μNID [2], the nGEM [3], and a pixelated Li-glass scintillator detector [4], are used. The fundamental performance of detectors, such as spatial resolution, linearity, counting rate, and efficiency, was studied in the commissioning. Fig. 3 shows typical result of a spatial resolution measurement using standard indicators. Using CCD-based detector, a spatial resolution of around 300 μm was reached, with the FOV of 300 mm and around 100 μm with selected FOV using a neutron image-intensifier system. We continue the improvement of the detector system to increase the homogeneity of the scintillator screen and obtain much finer spatial resolution.

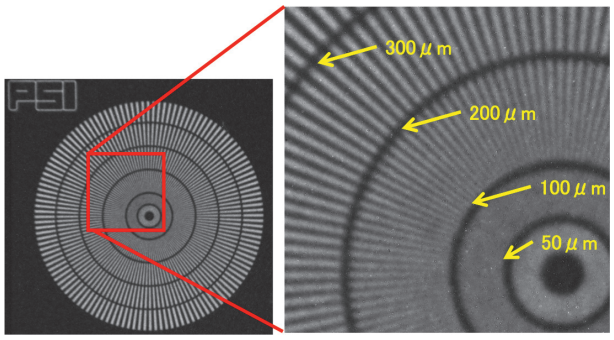

Figure 3. Image of the standard indicator. Left: overall image of the indicator (PSI Siemens star), right: enlarged image. Gaps with 100 μm width are visible.

3. Demonstration experiments

In addition to the commissioning, we have performed some demonstration experiments of the conventional neutron imaging and the energy-resolved neutron imaging, i.e., Bragg-edge, resonance absorption, and polarized neutron imaging. In RADEN, neutron CT experiments can be performed automatically by computer-controlled motorized sample stage and CCD camera system. Fig. 4 is an example of a CT reconstructed image of bearings. This is the first result of CT experiments using the pulsed neutron beam.

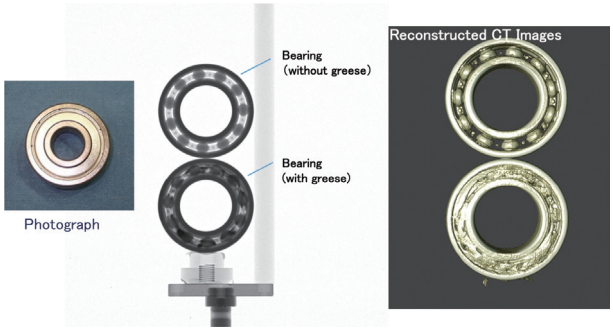

Figure 4. Example of a CT reconstruction image of bearings.

4. Summary

We have completed the construction of the energy-resolved neutron imaging system, RADEN, and began the commissioning study with the pulsed neutron beam. Together with the performance confirmation experiments, we conducted some demonstration experiments in both the conventional neutron radiography/tomography and the energy-resolved neutron imaging. We plan to start the user program from FY 2015.

References

[1] T. Shinohara, T. Kai, Neutron News, 26 11 (2015).
[2] J. D. Parker *et al.*, Nuclear Inst. and Meth. Phys. Res., A726 155 (2013).
[3] S. Uno *et al.*, Phys. Proc. 37 600 (2012).
[4] S. Satoh, JPSJ Conf. Proc. 8 051001 (2015).

T. Shinohara[1], T. Kai[1], K. Oikawa[1], T. Nakatani[1], M. Segawa[1], K. Hiroi[1], Y. Su[1], H. Hayashida[2], J. D. Parker[2], Y. Matsumoto[2], S. Zhang[2], and Y. Kiyanagi[3]

[1]Neutron Science Section, Materials and Life Science Division, J-PARC Center, JAEA; [2]Neutron R&D Division CROSS-Tokai; [3]Nagoya University

BL23 Polarized Neutron Scattering Spectrometer POLANO

1. Introduction

The success of the chopper spectrometer MARI applied to materials science at the ISIS neutron facility has highlighted the importance of the so-called chopper spectrometers to neutron beam line instruments. At the Japan Proton Accelerator Research Complex (J-PARC), the Materials and Life Science Experimental Facility (MLF) is a newly constructed world-leading pulse neutron experimental facility, where three chopper-type spectrometers are now part of the research program. One of the remaining technical issues that should be applied at MLF is the use of a polarization neutron technique with a pulsed neutron beam. Although the polarized neutron technique has been developed and used for many years, the application of the time-of-flight (TOF) method has been put into practice only in the recent years. In particular, with regard to the inelastic spectrometer, the polarized neutron technique finds limited practical use in wide scattering angle instruments. The use of the polarized neutron technique option has been planned for some of the elastic neutron instruments, such as a small angle scattering instrument, a reflectometer, a single crystal diffractometer and an imaging instrument, but not yet for the instruments dedicated to the inelastic scattering. In the light of recent discoveries in material science, many of the observed complex phenomena are predominantly due to the entangled physical degrees of freedom of spins, charges, orbitals, and even lattice vibration. In neutron scattering experiments, the varying dependence of momentum, energy, and temperature can be interpreted by these degrees of freedoms. However, a unique, effective, and direct way to observe these properties separately is via polarization analysis. Thus, the polarized neutron experiments are quite significant for material science particularly for research on magnetism, hydrogen materials, and strongly correlated electron systems with multiple physical degrees of freedom.

2. Construction of the spectrometer

The project was launched in 2009 starting as an S-type project with financial support from the KENS neutron facility. After the budget for the project was successfully sanctioned and obtained, the actual construction began in 2013. In 2014, many of the main beam line components have been designed, manufactured, tested and installed [1-3].

A vacuum chamber (VC) is one of the crucial components, where neutron detectors are positioned at its end. The dimensions of the chamber are approximately 4 × 3 × 3 m and its weight is 20,000 kg, as depicted in Fig. 1. This type of large VC is normaly made of steel, whereas stainless steel was used for POLANO VC to avoid magnetic interactions. Neutron detectors (position sensitive detectors (PSD)) are installed at the end of the chamber (called "detector banks"). The detector banks were designed to make the install and change of PSDs easy by opening and closing the bank hanging on the trolley. Inside the VC, a B_4C liner was fixed on the wall as a neutron absorber eliminating the unintended scattering from the wall and other materials inside.

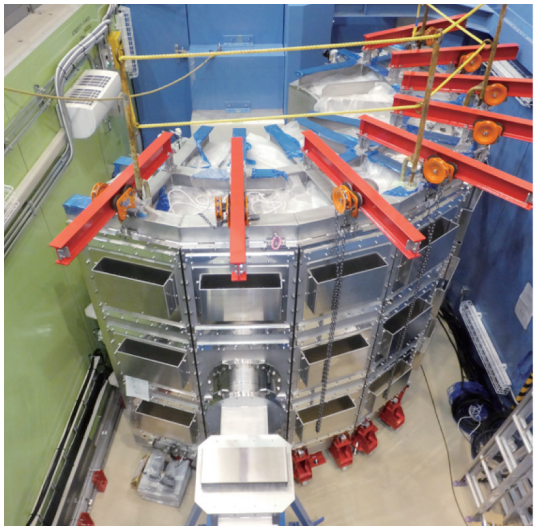

Figure 1. Newly installed large vacuum chamber.

Epoch-making in the design of the VC was the creation of one large chamber composed of three parts (sample chamber, scattering chamber and a part in-between the two (we call it "joint chamber")). Since the sample chamber and the scattering chambers can be evacuated separately, the joint chamber can be removed and put some devices in the position as spin flipper. Another remarkable feature is that in the scattering chamber a large trestle table for analyzer mirror has been set into the VC. The table can rotate in vacuum and even its rotational and tilting angles can be fine-tuned. As the analyzer mirror mounted on the table will weigh 80 kg, the frames of the trestle need to be robust and able to be accurately controlled in vacuum. A moving test has been performed in a factory as shown in Fig. 2, then the device was installed at the MLF beam line with the VC.

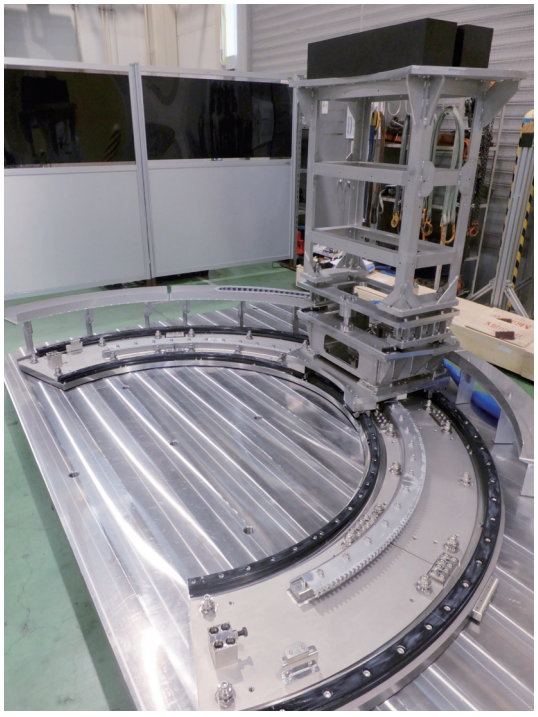

Figure 2. The trestle and moving system for analyzer mirror, testing at a factory with 80 kg dummy load.

After many designing reviews other devices were included in the manufacturing schedule. Choppers are some of the beam-line components, which are utilized for shaping the neutron pulse, eliminating the background, and monochromatizing the neutron energy. Four different types of choppers are used in POLANO, namely T0 chopper, disk choppers (25 Hz), Fermi chopper and fast rotating disk chopper. Fig. 3 depicts the newly designed Fermi chopper for POLANO. In the spinning test, the payload was nicely controlled and 600 Hz of the rotor rotation was achieved. The required phase accuracy at 600 Hz was 0.3 μs, the acquired phase accuracy 0.18 μs was satisfactorily achieved.

Figure 3. Newly assembled POLANO Fermi chopper rotor (a) and the display of the chopper rotational speed at the spinning test (b).

This year neutron guide tubes with 4 Qc super mirror are ready to be installed in the beam line. The use of an elliptical guide tube provides a flux that is 10 times higher than in a no-mirror guide tube (collimator) even for 100 meV neutrons. For the monochromatic beam, we also evaluated the neutron flux at the sample position and the resolution of the diffracted beam at the detector position by using McStas [4, 5]. Since POLANO is aimed at the incident neutron energy range up to Ei = 100 meV, the evaluated intensity and resolution below 100 meV were found reasonable for conducting polarization analysis experiments.

References

[1] T. Yokoo *et al.*, J. Phys. Conf. Series **502**, 012045 (2014).
[2] T. Yokoo *et al.*, J. Phys. Soc. Jpn. **82**, SA035 (2013).
[3] K. Ohoyama *et al.*, J. Phys. Conf. Series **502**, 012051 (2014).
[4] K. Lefmann and K. Nielsen, Neutron News **10**, 20 (1999).
[5] P. Willendrup, E. Farhi and K. Lefmann, Physica B **350**, 735 (2004).

T. Yokoo[1,2], K. Ohoyama[3], S. Itoh[1,2], M. Fujita[3], N. Kaneko[1,2], S. Sugai[1,2], M. Ohkawara[3], T. Ino[1,2], and M. Sakaguchi[1,2]
[1]Neutron Science Section, Materials and Life Science Division, J-PARC center; [2]Institute of Materials Structure Science, KEK; [3]Institute for Materials Research, Tohoku University

Status of the Common Technical Development

1. Overview

To achieve the 1-MW operation on neutron instruments in MLF, the common technical issues are selected and the work on their development is performed by individual teams which include JAEA, KEK and CROSS staffs.

The selected common technical issues are the realization of the polarized-neutron scattering technique, the utilization of a common sample environment, the establishment of advanced computational environment, and the fabrication of high performance neutron choppers. Specifically, these works have been carried out by the ^{3}He SEOP team, the sample environment team, the computational environment team and the chopper team, respectively.

(1) ^{3}He SEOP team

A prototype of an *in-situ* SEOP ^{3}He spin filter as an analyzer for BL17 was constructed, and good polarization performance was observed at the beam line. Also, a demonstrative SANS study of hydrogen-contained material was performed at the BL15, and the coherent and incoherent scattering components were successfully extracted by the polarization analysis by using an off-line SEOP ^{3}He spin filter.

(2) Sample environment team

Commissioning and improvements were performed by the sample environment team on the vertical-field superconducting magnet, the high temperature furnace and the ^{3}He cryostat, which are standard common sample-environments in MLF, while the devices were operating. The development of a pulsed magnet system for neutron diffraction, which is defined as an advanced sample environment in MLF, was carried out. The high-voltage unit for 30 T class high-magnetic field was assembled in JFY 2014. Test neutron scattering experiments will be performed the next year.

(3) Computational environment team

One of the user requests about computational environment is for a remote access to the MLF computational environment, including individual BL computers. Phase 1 is defined as a first stage in the development of the advanced computational environment in MLF. At phase 1, the users can login in the MLF computational environment, including individual BL computers, and observe the status of the experiment. The development of phase 1 was completed in JFY 2014 and several BLs started to use the remote access function. As a next step, phase 2 and phase 3 are planned. Users can perform advanced analysis by virtual environment at phase 2. Further analysis environment combined with various simulation tools will be provided in phase 3.

In JFY 2014 the MLF experimental database was redesigned to treat large data effectively. The main areas of development were data access function, web portal function, database link function and access control function and these functions were added successfully.

(4) Copper team

It is very important to fabricate highly reliable choppers, especially a T0 chopper, because their components, such as the hammer of the T0 chopper, will be highly activated due to the high dose at a 1-MW operation. Therefore, the requirements for new T0-chopper's performance include an expanded maintenance period, which should be as long as possible with a very low failure probability. The design of a new highly reliable T0-chopper was completed while taking into account the operational experience of the current machine. Its rotational speed specification is 100 Hz. Figure 1 shows the drawing of new T0 chopper. Its dimensions are 820 mm wide, 494 mm long, and 860 mm high. The designed maintenance period is 39,200 hours.

The assembling, operational test and evaluation of the test equipment will be performed the next year.

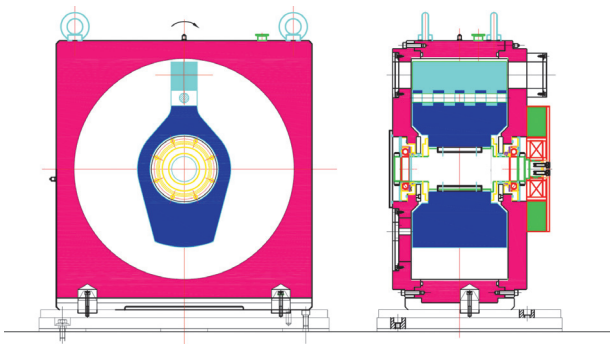

Figure 1. Drawing of the new high-performance T0- chopper. Its maximum rotational speed is 100 Hz.

K. Aizawa and T. Oku
Technology Development Section, Materials and Life Science Division, J-PARC Center

Development of an in-situ SEOP ^{3}He Neutron Spin Filter

1. Introduction

We have been developing an in-situ spin-exchange optical-pumping based polarized ^{3}He neutron spin filter (in-situ SEOP ^{3}He NSF) for efficient utilization of pulsed neutrons at J-PARC. In this study, i) we have developed a prototype of the in-situ SEOP ^{3}He NSF as the analyzer for the polarized neutron reflectometer SHARAKU (BL17) and evaluated its performance at the beamline, ii) we have developed the in-situ SEOP ^{3}He NSF as the polarizer for the polarization analysis neutron spectrometer POLANO which is under construction.

2. The in-situ SEOP ^{3}He NSF as the analyzer for the polarized neutron reflectometer SHARAKU (BL17)

Figure 1 shows the constructed ^{3}He NSF as a prototype for SHARAKU. All of its components were put in a laser shield box made of black anodized aluminum boards for laser safety. The dimensions of the laser shield box are 605 mm × 605 mm × 350 mm. The ^{3}He cell was installed in a solenoid coil with a double layered Permalloy magnetic shield. The size of the ^{3}He spin filter cell was 35 mm in diameter and 55 mm in length. The ^{3}He-gas pressure length product of the cell was 11 bar-cm. The magnetic shield was designed for the in-situ ^{3}He NSF with a cell size of 100 mm in diameter and 100 mm in length under a peripheral magnetic field of several tens Gauss.

We set up the ^{3}He NSF in a scattering chamber of SHARAKU and evaluated its performance in terms of the maximum ^{3}He polarization, the relaxation time constant of the ^{3}He polarization and the magnetic guide field for polarized neutron beam transportation. Figure 2 shows a schematic layout of the experimental setup at SHARAKU. We used a magnetic supermirror to polarize the incident neutron beam and a Drabkin spin flipper to change the polarization of the neutron beam. Those devices were installed in the shield upstream of the sample position. A guide field was applied along

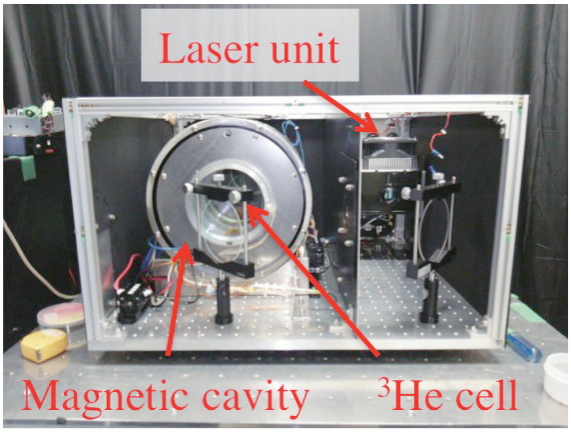

Figure 1. The prototype of the in-situ SEOP ^{3}He NSF for SHARAKU.

the neutron beam path to transfer neutrons while conserving the neutron spin state. The ^{3}He NSF was placed in the scattering chamber. The reflected neutrons were analyzed by using the ^{3}He NSF and ^{3}He detector (Fig. 2). We checked the magnetic guide field of SHARAKU for polarized neutron beam transportation (Fig. 2). Two solenoid coils were placed at the upstream of the sample stage and inside the scattering chamber. The strength of solenoid coil's magnetic field was >10 G, strong enough to keep the polarization of the neutron beam. The direction of solenoid coil's magnetic guide field was parallel to the neutron beam axis (z-axis) (Fig. 2). We applied a magnetic field of 20 G onto the ^{3}He cell along the neutron beam axis.

After the adjustment of the magnetic guide field, we started the optical pumping of the ^{3}He gas to polarize it. The time development of the ^{3}He polarization was monitored by using the AFP-NMR, as shown in Fig. 3. Here, the amplitude of the AFP-NMR signal is proportional to the ^{3}He polarization degree. Thus, we can estimate the ^{3}He polarization from the AFP-NMR signal by using the conversion parameter.

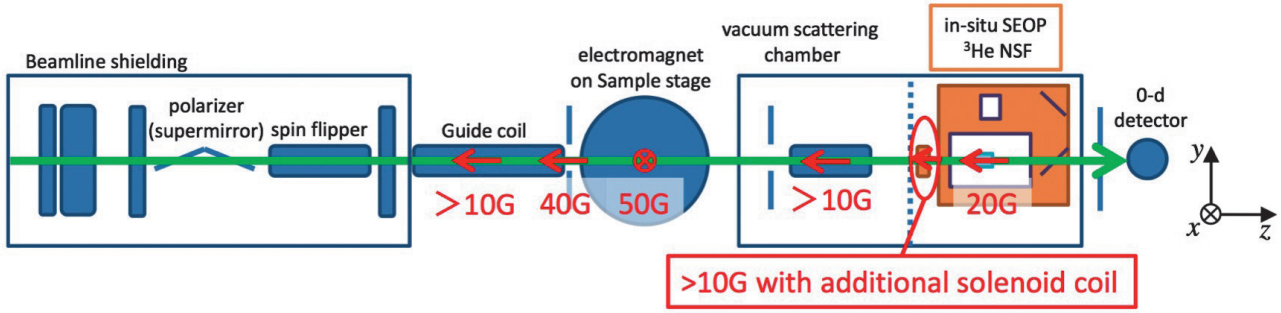

Figure 2. Schematic layout of the experimental setup at SHARAKU.

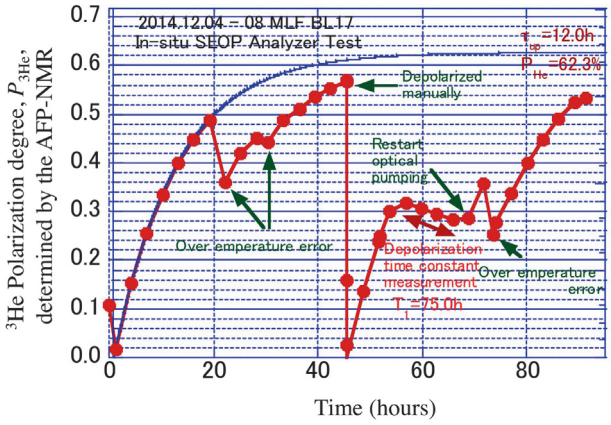

Figure 3. The time development of the ^{3}He polarization measured by the AFP-NMR.

The laser power supply for the optical pumping was stopped several times due to a temperature error with the laser diode. The SEOP box had a cooling fan to keep the temperature low inside the box. However, since the temperature within the scattering chamber, in which the SEOP box was located, rose with time, a temperature error occurred. We added the fan to lower the temperature of the scattering chamber. However, the system was stopped several times even after the improvement. So we had to reduce the laser power down to the moderated level to ensure a stable operation.

The maximum ^{3}He polarization P_{3He} was determined to be 56.9% by the AFP-NMR (Fig. 3). By analyzing the time development of the ^{3}He polarization during the optical pumping, it was estimated that the maximum ^{3}He polarization P_{3He} reached about 62% (Fig. 3). The relaxation property of the ^{3}He polarization was measured after the laser irradiation and the heater were stopped. The relaxation time constant was 75 hours.

Finally, we evaluated the ^{3}He polarization by using unpolarized neutrons. We measured the intensities of the neutrons transmitted through the ^{3}He NSF in polarized and unpolarized ^{3}He gas conditions. The obtained neutron intensities are shown in Fig. 4 (a). The ^{3}He polarization degree was calculated to be 56.9% based on the neutron transmission measurements (Fig. 4 (b)). The result was well consistent with the value determined by the AFP-NMR.

3. The in-situ SEOP ^{3}He NSF as the polarizer for the polarization analysis neutron spectrometer POLANO (BL23)

We have been developing a compact system of the in-situ SEOP ^{3}He NSF for the limited space of the POLANO. A schematic view of the ^{3}He NSF in POLANO is shown in Fig. 5.

We will prepare cylindrical cells made of GE180 aluminosilicate glass with diameter of 60 mm and length of 60 to 100 mm. The cells will be filled with ^{3}He at 2.0 to 3.5 atm, and the effective ^{3}He thickness would range from 12 to 35 atm-cm for various measurements.

A solenoid and compensation coils at both solenoid edges with Permalloy magnetic shield were designed, and a proto-type magnet has been constructed. The neutrons are polarized in the axial direction in the ^{3}He NSF, and the spins are rotated adiabatically in the transverse direction by the magnetic guide field. The compensation coils will be optimized according to the guide field.

A laser diode array with an output power of 100 W with a chirped volume Bragg (holographic) grating (VBG or VHG) emits a spectrally narrowed 795 nm (Rb D_1 line) for the optical pumping of Rb (Fig. 6). A quarter

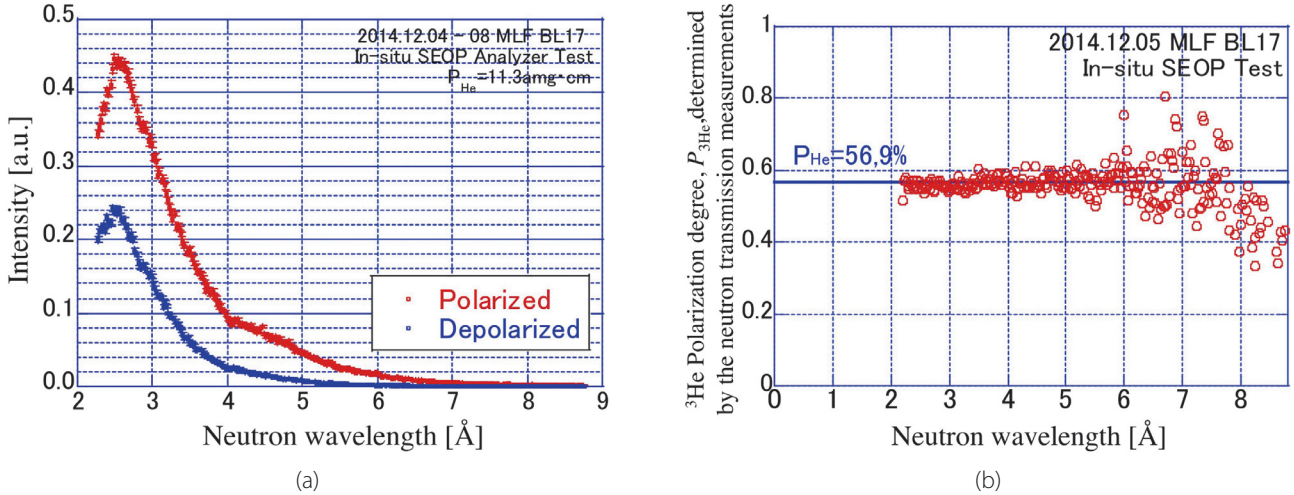

(a) (b)

Figure 4. (a) Intensities of the neutrons transmitted through the ^{3}He cell with the polarized and depolarized ^{3}He, and (b) ^{3}He polarization determined by the neutron transmission measurements.

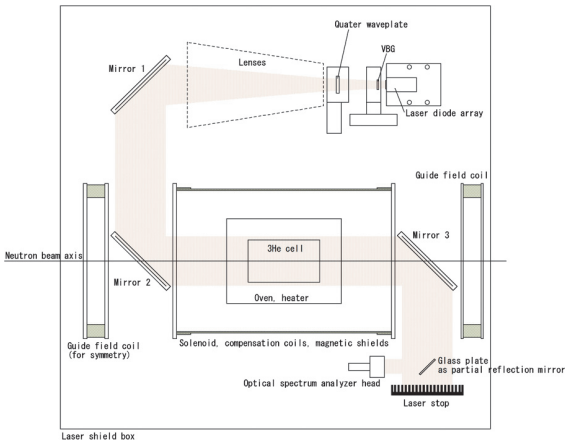

Figure 5. A schematic view of the ^{3}He NSF in POLANO. All essential elements are packed in a laser shield box with a size of 600 mm × 600 mm × 250 mm.

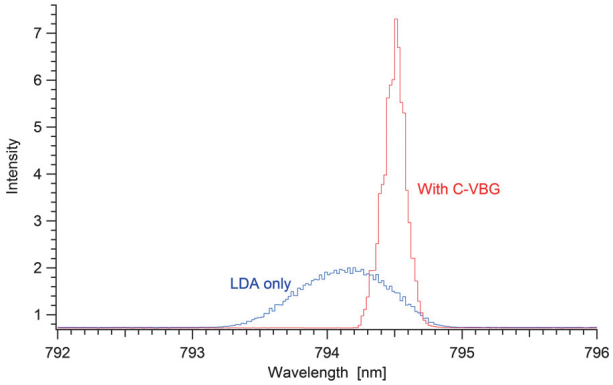

Figure 6. Laser spectra from the 100 W laser diode array (LDA) with and without the chirped volume Bragg grating (C-VBG). Not only is the spectrum narrowed but also the peak intensity is much higher with the use of the C-VBG.

waveplate converts linear polarization into circular polarization. The waveplate can be remotely rotated by +/−90 degrees to change the left and right states according to the AFP spin flipping of ^{3}He. The laser optical apparatus is shown in Fig. 7.

In SEOP, hot air blowers (compressed air blowers) are commonly used to keep ^{3}He cells at an elevated temperature because they do not interfere with the homogeneous magnetic field while conventional electric heaters produce unnecessary magnetic fields. However, a hot air blower occupies a fair amount of space and requires heat insulation around itself for safety. Due to the limited available space, we have decided not to use a hot air blower but a thin electric heater made of polyimide films and NiCr strips, which is attached to the outer surface of an aluminum oven for a ^{3}He cell. The NiCr strips will be designed specifically to minimize the magnetic field interference.

In almost all measurements with polarized neutrons, neutron spin flipping is a must for cancelling out any systematic uncertainties. We have successfully demonstrated a compact AFP spin flipper for polarized ^{3}He with an RF coil positioned inside an aluminum oven. The ^{3}He spins can be flipped within half a second, and the polarization loss was measured to be less than 4×10^{-4} in one spin flip. Such an AFP spin flipper will be redesigned to fit the ^{3}He cells described previously.

4. Conclusion

In conclusion, we are developing the in-situ SEOP NSF as the analyzer for SHARAKU and POLANO. The main components have been almost developed, and we are going to fix some problems and/or optimize the operation parameters for application at the beamlines.

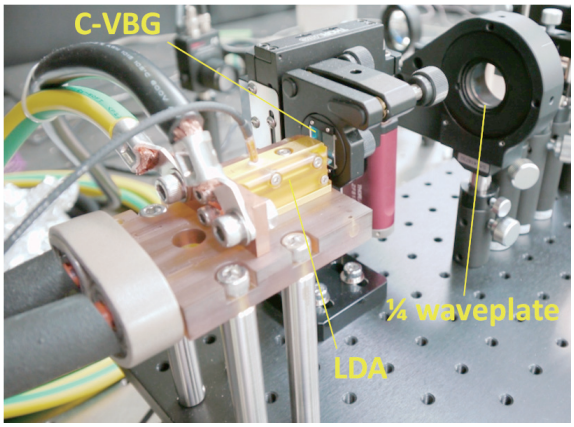

Figure 7. A picture showing the laser optical apparatus, a laser diode array (LDA), a chirped volume Bragg grating (C-VBG), and a quarter waveplate.

T. Oku[1], T. Ino[2], K. Sakai[1,3], K. Hiroi[4], T. Shinohara[4], K. Aizawa[1], M. Arai[5], M. Takeda[6], K. Kakurai[6], H. Kira[7], H. Hayashida[7], N. Miyata[7], K. Akutsu[7], J. Suzuki[7], M. Ohkawara[8], and K. Ohyama[8]

[1]Technology Development Science Section, Materials and Life Science Division, J-PARC Center; [2]Institute of Materials Structure Science, KEK; [3]Neutron Source Section, Materials and Life Science Division, J-PARC Center; [4]Neutron Science Section, Materials and Life Science Division, J-PARC Center; [5]Materials and Life Science Division, J-PARC Center; [6]Quantum Beam Science Directorate, JAEA; [7]CROSS-Tokai; [8]Institute for Material Research, Tohoku University

Sample Environment at MLF

1. Introduction

The SE team is working on adopting and operating the so-called beamline (BL)-common SE equipment, and on developing new SE equipment. We currently have a vertical-field superconducting magnet, a ^{3}He-^{4}He dilution refrigerator insert and a high-temperature furnace as the BL-common SE equipment. In JFY2014, three new members (JAEA: 1, CROSS: 2) were joined the SE team, and then a total of 13 members were divided into sub-teams, such as cryogenics and magnets, high temperature, high pressure, soft-matter, and development. The development items are a pulsed magnet system, a low-temperature and high-pressure environment equipment and a hydrogen environment equipment.

2. Operation of the BL-common SE equipment

In April, 2014, we operated the superconducting magnet at BL17 for its commissioning of polarized neutron reflectivity measurement. The applied magnetic field was from 1.00 T to 6.00 T at a base temperature of 4.2 K during the operation. Following the operation at BL17, we have performed the commissioning at the SE area, and then VTI (Variable Temperature Insert) reached 1.068 K, the lowest temperature ever registered by a single shot mode. In this period, three CROSS members in the SE team joined the operation from the setup of the superconducting magnet at the SE area (Fig. 1) for the first time since the current SE team was organized.

Figure 1. Setup of the 7T superconducting magnet at the SE area (liquid He transfer).

Along with our task of supporting the users of the experiment, we also work on improving the BL common SE equipment to make it easier to use. We modified a high temperature furnace with niobium heater to improve the convenience and safety in users experiment. In the last fiscal year, we installed a control panel for the vacuum pumping system and an electric distribution board, as well as equipped an argon gas inlet line for experiments under argon atmosphere. To make further improvements, we equipped the system with automatic vacuum evacuation and argon gas inlet (Fig. 2). In addition, we introduced a touch panel device, which made it possible to integrate various pieces of information, such as the settings parameters and an alarm list of all controllers, heating conditions and so on.

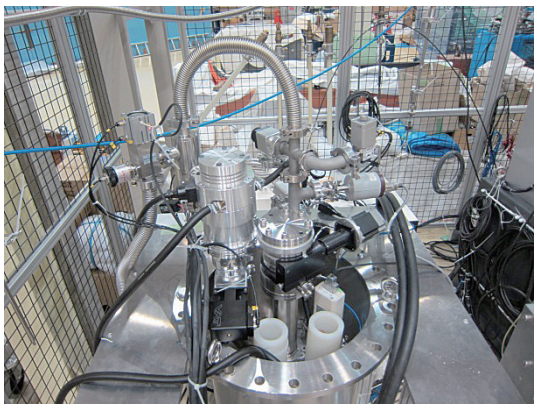

Figure 2. Improved vacuum pumping system of a high temperature furnace.

3. New equipment and development

In JFY2014, a new closed-cycle ^{3}He cryostat was introduced as part of the BL-common SE equipment. This cryostat is a one-shot ^{3}He system including a pulse tube refrigerator to precool ^{3}He. Its lowest temperature is 0.3 K, which can be maintained about 50 hours without sample. The system is automatically cooled down to the lowest temperature within 24 hours. The cryostat was designed to fit the goniometer. A rotation stage to fit it to the vacuum chamber will be fabricated in the next fiscal year.

With the magnet technologies we can perform diffraction experiments, small angle scattering, inelastic scattering and so on. Recently, measurements using neutron beams have been rapidly developed under high magnetic field. We developed a prototype of compact power supply in J-PARC MLF. Figure 3 shows the appearance of the power supply. The size is as follows: 760 mm in width, 1000 mm in depth, and 1400 mm in height. Maximum charged voltage and output current is 2 kV and 8 kA respectively. Repetition rate is one

pulse every several minutes. The pulse duration is a few milliseconds.

The operation examination of the power supply was performed using a solenoid coil (200 μH) as a load. The obtained peak current was approximately 7.7 kA when the charged voltage of the capacitor was 2 kV.

A new coil and a sample stick is being developed for the neutron scattering experiment.

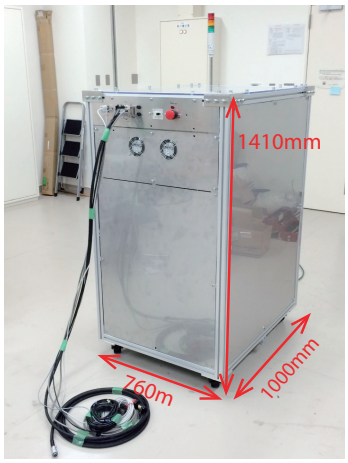

Figure 3. Photograph of the power supply.

The SE high-pressure sub-team started their substantial activities in JFY 2014. In the MLF, there is a beamline dedicated for high-pressure experiments (BL11). Furthermore, some groups have carried out their experiments under high-pressure with their own high-pressure apparatus. However, so far we did not have a high-pressure environment device as part of the BL-common equipment. Therefore, we held an opinion-exchange meeting with each BL staff in charge, and discussed the development of high-pressure environments. In JFY 2014, VX-6 type Paris-Edinburgh press (with capacity of 130 tons), widely used in neutron facilities, was introduced as the first BL-common high-pressure device. Expansion into low-temperature environment is also planned.

4. SE Workshop

The 8th International Workshop on Sample Environment at Neutron Scattering Facilities was held in Oxford, UK, October 12-16 2014. It included 70 participants from 16 facilities in 11 countries, including 4 members from J-PARC/MLF. T. Aso reported on the current status of SE at MLF, Y. Yamauchi introduced the activities in managing the SE equipment at MLF, and K. Munakata presented the development of high-pressure sample environment for single crystal neutron diffractometer SENJU at J-PARC MLF. During the workshop, there was a meeting of ISSE (International Society for SE), an organization for activate collaborations and information sharing among the facilities, S. Ohira-Kawamura attended the meeting. At the event it was decided that the next SE workshop will take place at near NIST, USA, in 2016.

Figure 4. Photograph of workshop members at Eynsham Hall, Oxford, UK.

T. Aso[1], Y. Yamauchi[2], M. Ishikado[3], S. Ohira-Kawamura[4], M. Watanabe[2], K. Munakata[3], S. Takata[4], Y. Sakaguchi[3], K. Ohuchi[3], M. Obinata[3], T. Yokoo[4,5], W. Kambara[2], and R. Takahashi[6]

[1]Neutron Source Section, Materials and Life Science Division, J-PARC Center; [2]Technology Development Section, Materials and Life Science Division; [3]Neutron R&D Division CROSS-Tokai; [4]Neutron Science Section, Materials and Life Science Division, J-PARC Center; [5]Institute of Materials Structure Science, KEK; [6]Nippon Advanced Technology co.

Present Status of the MLF Experimental Database

1. Introduction

The neutron instruments in MLF create a huge amount of experimental data. A typical volume of data produced in one experiment is from several tens MB to several hundreds GB. Since a lot of experiments under various experimental conditions are carried out in a short period of time using high-intensity beams, the total amount of data generated annually in a whole facility at full performance is in the order of PB. In those situations, it is required to safely and efficiently manage a huge amount of data over a long period of time. In particular, an appropriate protection and preservation of the experimental data produced at MLF as intellectual property is required. Furthermore, it is needed to provide the facility users with a data access service enabling the effective utilization of a lot of experimental data.

To meet these requirements, we are developing and operating the MLF experimental database (MLF EXP-DB) shown in Fig. 1. The main features of the MLF EXP-DB are as follows: [1]

- Data Management
  - Experimental data cataloging (online/offline)
  - Centralized raw data management (registration, archive, retrieve)
- Data Access
  - Browsing/Searching the meta-data catalog
  - Downloading raw data and meta-data
  - Executing simple data analysis
- Web portal
  - Web-based interface for data management and access
- Database Link
  - Collecting user, proposal and sample information from other databases
- Access Control
  - Authentication and Authorization

2. Recent update features

Recently, we have redesigned the MLF EXP-DB to enhance the availability and scalability, and improved a function of the experimental data retrieval in the web portal.

For the core system of the data management infrastructure, high availability is required. A service outage caused by system failure and maintenance applying patches should be avoided as much as possible. A redundancy of the system allows avoidance of such service outage, so that the availability is improved. We have turned the system into a redundant distributed system.

It is also necessary to consider scalability of the system especially in data cataloging. The data production rate in the facility is continuously rising. It depends on the beam intensity and the performance of the neutron instruments. In MLF, the beam intensity has been increasing in phases according to the development plan for the accelerators and the neutron sources. The scale of the experimental data catalog will be in the order of tens of millions of tags recorded in XML-format at full power operation in MLF. Also, the additional installation of detectors and improvement of various devices in the instruments have been increasing consistently. Considering this situation, we have improved the MLF EXP-DB into the system to be capable of scaling-out responding to the scale of data quantity produced in the facility.

Furthermore, an improvement of the experimental data retrieval can promote better data utilization. We have improved the experimental meta-data retrieval with a flexible search settings according to the experimental conditions.

High Availability

The improved redundant system is composed of two servers in a switch over relationship. When one of them is operated as an active server responsible for collecting experimental data from the instrument's local systems and data access, the other is operated as a hot-standby server. The database replication is regularly performed from the active server to the hot-standby server. In the case of system failure or maintenance, the active server is switched. The data access is provided via a front-end web server, so that the users need not to take account of the access destinations.

Scaling-out

The system has been scaled out to improve scalability for the data cataloging. It is composed of the two redundant system units mentioned in the previous subsection. There are two experimental halls in MLF. Currently, one system is allocated to the instruments in the 1st experimental hall and the other system is allocated to the instruments in the 2nd experimental hall. It is capable of performing further scaling out of a load distribution by adding the redundant systems responding to the data production rate.

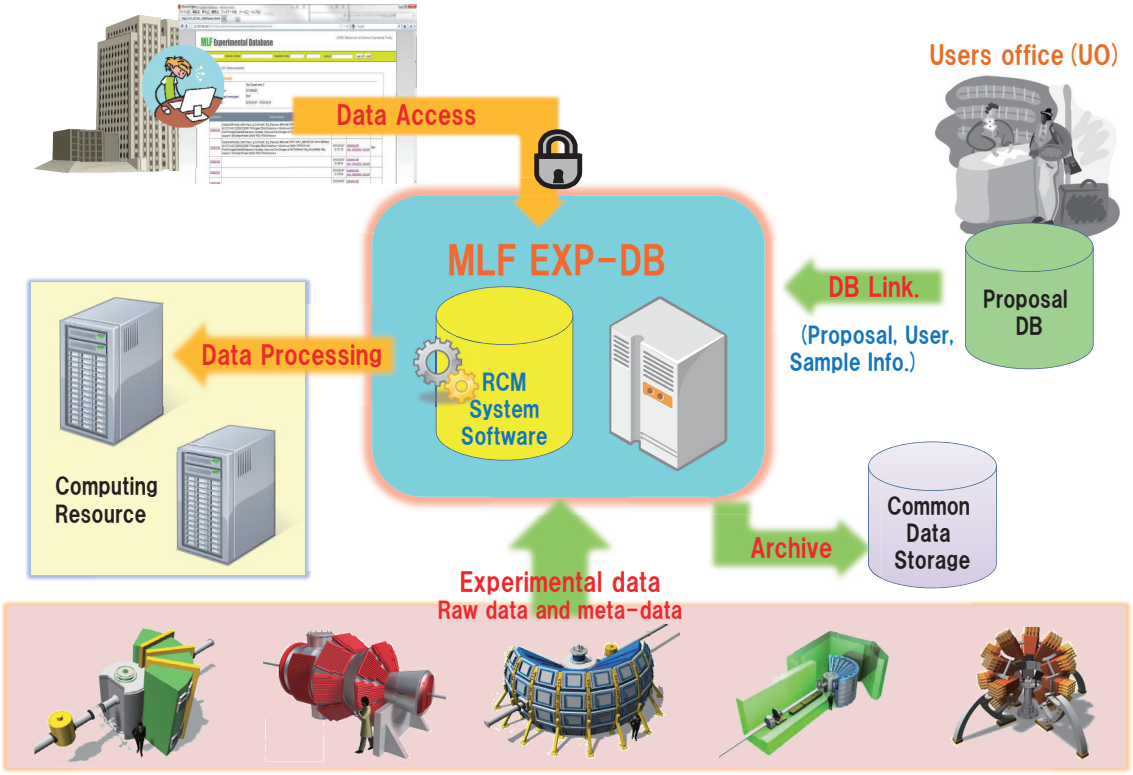

Figure 1. The schematic view of the MLF experimental database (MLF EXP-DB).

Flexible Data Retrieval

Since various sample environmental apparatuses in neutron instruments are used depending on the purpose of the experiment, the structure of the experimental meta-data can be changed with every experiment or instrument. Although every variety of information associated with the experimental conditions as experimental meta-data in XML-format is registered in the experimental data catalog, in the conventional retrieval function the options are limited to some basic information on the experiment such as run No., date and time, experimental title, and primary investigator. In the improved retrieval, it is possible to execute a flexible data search for more information by specifying the search conditions for each tag of experimental meta-data corresponding to the device condition.

3. Conclusion and future plans

We are operating and updating the data management infrastructure in J-PARC/MLF. The infrastructure is mainly composed of the MLF EXP-DB, which is responsible for data management and access, and the data repository for the central preservation of experimental raw data and meta-data. Currently, it manages the experimental data at four neutron instruments (DNA, PLANET, SHARAKU and SENJU) in MLF and it is planned to expand the management to other instruments soon. The MLF EXP-DB provides the web portal as the interface for data management and access. The web portal offering data access for facility users is under trial use. We will start the data access service with this web portal, including the flexible data retrieval, next year.

We have also improved the MLF EXP-DB by redesigning the redundant and scaling-out system. We have a plan for a performance evaluation in the near future.

Reference

[1] T. Nakatani, Y. Inamura, K. Moriyama, T. Ito, S. Muto, T. Otomo, "Event recording data acquisition system and experiment data management system for neutron experiments at MLF, J-PARC" JPS Conference Proceedings Volume 1, 014010, 2014 (Proceedings of the 12th Asia Pacific Physics Conference).

K. Moriyama and T. Nakatani
Technology Development Section, Materials and Life Science Division, J-PARC Center

Supermirror Coating for Special Figuring

1. Large-m supermirror coated on thin silicon substrate

For supermirror benders and polarizers, thinner silicon substrate is adequate to provide better transmission efficiency, because substrate materials have serious effect on the total cross-section.

We fabricated NiC/Ti supermirrors (m = 5) coated on Si substrates with 0.1 mm thickness. A total of 5,000 layers was coated on the both sides of the Si substrates. An ion beam sputtering instrument [1] with a coating area of 50 cm in diameter was used. Figure 1 shows a substrate holder on which 74 substrates with size 20 × 50 mm were set in the large-scale instrument.

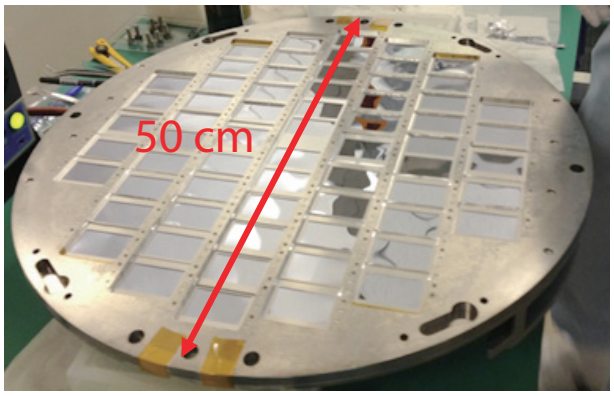

Figure 1. The substrate holder with 74 substrates of the ion beam sputtering instrument.

The neutron reflectivity of the m = 5 supermirror was 70% at the critical angle, and the profile gradually increased to the total reflection.

2. Supermirror coating on aspheric-cylinder substrate

The neutron focusing mirrors play an important role to enhance the neutron intensity at a sample position or to improve the q-resolution of small angle scattering experiments. For 3-dimensional focusing optics, Kirkpatrick-Baez (K-B) mirrors were developed for having intense neutron beam by using elliptic supermirrors (m = 4) [2].

We have been developing a Wolter type I supermirror, which consists of ellipsoid-hyperboloid of revolution. In order to fabricate the Wolter mirror, replica method is applied and NiC/Ti supermirror was coated on a mold with aspherical shape [3]. Figure 2 shows a mold holder which has spin rotating mechanism for coating around the mold and the whole substrate holder which rotates for spatially-homogeneous coating in the ion beam sputtering instrument.

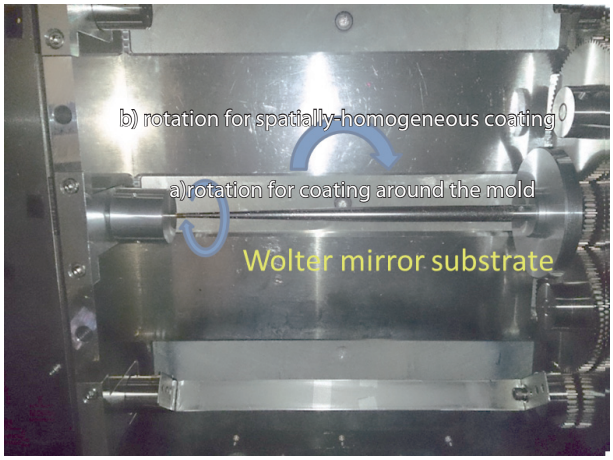

Figure 2. The substrate holder on the ion beam sputtering instrument; a) the mold holder which has spin rotating mechanism and b) the whole substrate holder which has rotating mechanism for spatially-homogeneous coating.

The NiC/Ti supermirror (m = 2) were coated on the mold of the Wolter mirror type I with a length of 20 cm, and the Wolter supermirror was fabricated by using replica method [4].

References

[1] R. Maruyama *et al.*, Physica B, Vol.385-86 1256-1258 (2006).
[2] D. Yamazaki *et al.*, JPS Conf. Proc. 8, 051009 (2015).
[3] H. Hayashida *et al.*, Journal of Physics: Conference Series 528 (2014) 012007.
[4] K. Soyama *et al.*, Proc. 4th International Workshop on Neutron Delivery Systems (2015).

D. Yamazaki[1], R. Maruyama[1], K. Soyama[1], T. Miyauchi[1], and H. Hayashida[2]
[1]Neutron Insrumentation Section, Materials and Life Science Division, J-PARC Center; [2]Neutron R&D Division, CROSS-Toka

Large Area One-dimensional Scintillator Neutron Detectors for TAKUMI at BL19

1. Introduction

The Engineering Materials Diffractometer, TAKUMI at BL19, is one of the neutron instruments installed at the MLF of J-PARC. TAKUMI is designed specifically for analysis of residual stress and crystallographic structure of industrial materials. The commissioning of TAKUMI was started in September, 2008, and completed in March, 2009. TAKUMI has been operated for more than 5 years with 10 detectors.

2. Neutron Detectors at TAKUMI

The neutron detectors installed at TAKUMI [1, 2] are large one-dimensional neutron detectors with a sensitive area of 1 m × 20 cm and a position resolution of 3 mm, as shown in Fig. 1, which have been developed under international collaboration with ISIS, Rutherford Appleton Laboratory. The detectors were designed based on those installed at the ENGIN-X instrument of ISIS. The TAKUMI detector has 360 pixels, each with a size of 3 mm × 20 mm, while the ENGIN-X detectors have 240 pixels with a neutron sensitive area of 750 mm × 20 cm.

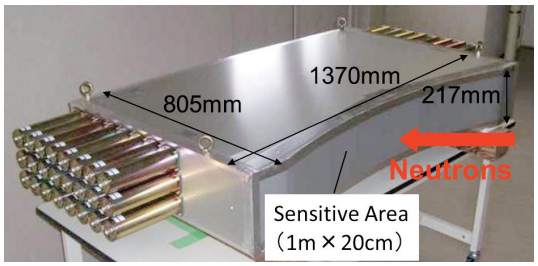

Figure 1. A Photograph of the neutron detector developed for TAKUMI.

The detector head consists mainly of ZnS/^{6}LiF scintillator, reflectors, and optical fibers. The scintillation light generated as a result of nuclear reaction of ^{6}Li with neutrons is efficiently collected into the optical fibers of the pixel, where the pixels are separated from each other with a reflector. This "venetian" type head [3], originally developed by the ISIS facility, was adopted to improve the efficiency of the light collection and neutron detection. The optical fibers are connected with photomultiplier tubes (PMTs) and the electric signals from the PMTs are sent to data acquisition electronics (DAE) and decoders. The position of the incident neutrons was determined by introducing $_{2}C_{n}$ coding or a pair-coded method in the arrangement of the fiber bundle to PMTs, and hence each of the 360 pixels can be specified by only 48 PMTs. The method also contributes significantly to the noise reduction because the neutron incident position is determined in the decoders by the coincidence of the DAE output of any two PMTs. Another feature of the detector is that the output count from each PMT has plateau characteristics, as shown in Fig. 2. This is very favorable for setting the applied voltage.

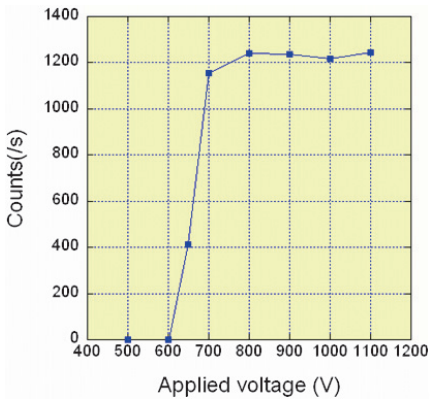

Figure 2. Plateau characteristics of the PMT output count.

Last year these two types of detectors were fabricated and delivered to BL19, and thus a total of 12 detectors will be in service at TAKUMI. These detectors have neutron sensitivity of more than 50% at 1 Å and gamma-ray sensitivity of less than 10^{-6} at a gamma-ray energy of 1.3 MeV. The performances sufficiently meet the requirements for residual stress analysis in the neutron scattering experiments at BL19.

References

[1] K. Sakasai *et al.*, Nucl. Instr. and Meth. A600 (2009) 157.
[2] K. Sakasai *et al.*, Proc. of ICANS-XIX, (2010) IP131.
[3] E. M. Schooneveld and N. J. Rhodes, Proc. ICANS-XVI (2003) 455.

K. Sakasai, T. Nakamura, K. Toh, K. Honda, and K. Soyama
Neutron Instrumentation Section, Materials and Life Science Division, J-PARC Center

Development of Alternatives to the ^{3}He Gas-based Neutron Detectors in Nuclear Security

1. Introduction

The recent shortage of Helium-3 stockpiles severely affected various fields such as neutron science and nuclear security. The US government established an initial strategy for further allocation of the existing ^{3}He supply. Consequently, in nuclear security, alternative technologies were encouraged and no further ^{3}He gas was allocated. Thus, it is quite urgent to develop a technology alternative to the conventional ^{3}He gas-based neutron detectors in this field. Therefore, we have started to develop alternative detectors with support from the Japanese government.

2. Developed Neutron Detector

The designed detector is shown in Fig.1. The detector has a simple design, comprising of a scintillator strip, light-reflecting case, and two photomultiplier tubes (PMTs) at both ends [1, 2]. We have selected ZnS/$^{10}B_2O_3$ ceramic scintillator as a neutron sensitive material, which has been successfully adopted in detectors of BL03, BL17, and BL18 at the MLF.

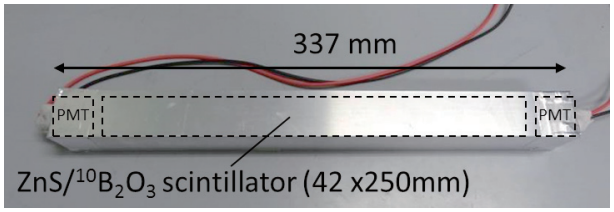

Figure 1. Photograph of the developed detector.

The scintillation light is generated in the scintillator as a result of the nuclear reaction of ^{10}B with neutrons propagates to both ends of the case and then it is collected by the PMTs. The electrical signals from the two PMTs are fed into inputs of the readout board which was developed separately. Figure 2 shows a schematic readout diagram of the detector. The electrical signals from two PMTs are summed up by fast amplifiers and the summed signal is again amplified and discriminated from background events in the board to obtain a logic signal as a neutron event.

In order to evaluate the detector performances objectively, demonstration experiments were conducted at the Facility of Radiation Standard, JAEA, in the presence of three evaluators from IAEA, LANL, and JRC (Joint Research Center). In the experiments, the neutron detection efficiency and gamma-ray sensitivity of our three detectors were precisely measured using a ^{252}Cf source and a ^{60}Co source, respectively. The results of the experiments showed that the neutron efficiency of the detectors was in the range between 74% and 80% and the gamma-ray sensitivity was less than 10^{-7} for all detectors. Here the neutron detection efficiency is represented in a relative way, depending on the unit length compared to that of a standard ^{3}He neutron counter (^{3}He pressure: 4 atm, diameter: 1 inch). Note that the gamma-ray sensitivity was measured under a high gamma-ray field of 100 mSv/hr. In such a high field, a ^{3}He-based neutron detector cannot be used because of pile-up of the gamma-ray pulses. These high performances of the detectors were confirmed by the three evaluators. The developed detector proved to be one of promising alternatives to the conventional ^{3}He detectors used in nuclear security by this experiment.

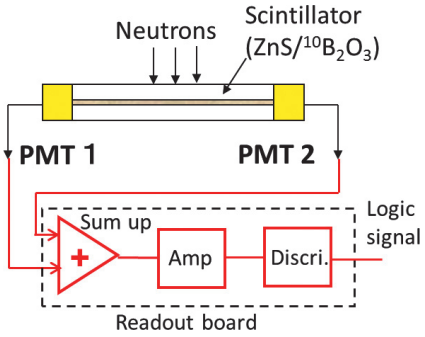

Figure 2. A schematic readout diagram of the detector.

This work was partially supported by the Ministry of Education, Culture, Sports, Science and Technology.

References

[1] T. Nakamura *et al.*, Proc. of 54th Annual Meeting of the Institute of Nuclear Material Management.
[2] T. Nakamura *et al.*, Nucl. Instr. and Meth. A763 (2014) 340.

K. Sakasai, T. Nakamura, K. Toh, H. Suzuki, K. Honda, and K. Soyama
Neutron Instrumentation Section, Materials and Life Science Division, J-PARC Center

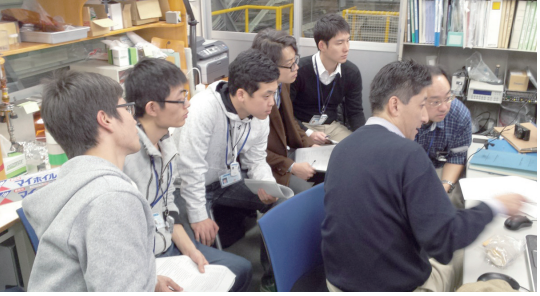
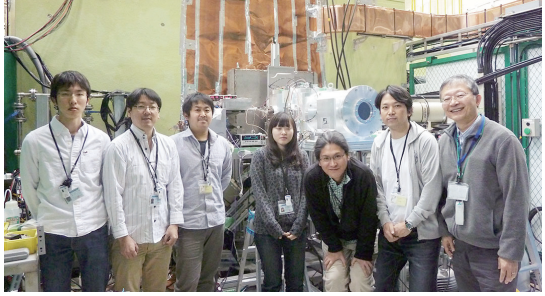



Muon Scinece

Status of J-PARC MUSE

Because of the fire caused by the power supply for the septum magnet at the muon D-line on January 16, 2015, we had to stop completely the operation of J-PARC for one and a half months. Thanks to the tremendous efforts of the members of the J-PARC task force, the neutrino and neutron operations were restarted in the end of February, 2015. Although we were about to restart the muon experiments in the end of April, we faced a second trouble, a water leakage from the neutron target. According to the beam time schedule, we will restart muon users' RUN in the end of October.

1. Fire at the muon D-line

The fire at the Second Experimental Hall of the Materials and Life Science Experimental Facility, J-PARC, occurred at 15:01 on January 16, 2015. It happened in the power supply for the septum magnet at the muon D-line. To improve the stability of the current for the septum magnet, an additional transformer was newly fabricated and was going to be installed into the existing power supply. The installation work started on January 7, 2015, and the electric power was energized for the first time on January 16. In a few minutes, after the circuit breaker was turned on, it was observed that the transformer was smoking and burning locally. Fortunately, the fire was put out by an extinguisher immediately, while calling 119 (emergency call). The cause of the fire was attributed to a miss-design of the circuit of the power supply, and specifically to the insufficient safety check of the circuit, skipping the inspection by the manufacturer under normal operation, as well as the under-evaluation of the risk in the electrical power test in the radiation control area by the J-PARC staff.

2. Installation of the rotating graphite target

Since September, 2008, we have been utilizing safely and stably an edge-cooled non-rotating graphite target for the muon and pion production at J-PARC MUSE. Considering the degradation of the thermal conductivity by the neutron irradiation, it was designed by inserting the buffer layer of the Ti interface between the graphite and copper frame in order to release stress. So far, proton beam intensity from the 3 GeV RCS has been less than 300 kW, but it is planned to be upgraded up to 1.0 MW in one and a half years. Therefore, we decided to replace the non-rotating target with a newly designed rotating graphite target, which can accept proton beam with much wider area, consequently reducing the radiation damage. Its thickness, outer and inner diameter are 20, 330 and 230 mm ϕ. It is designed to be operated at 15 r.p.m. (rotations per minute) using WS_2 solid lubricant for the bearings, and its lifetime is expected to be longer than 10 years, even in the 1 MW operation.

It has been operating stably without any trouble since the beginning of November against 300 kW proton beam. Figure 1 shows a picture at the installation of the muon rotating graphite target.

Figure 1. Installation of the muon rotating graphite target.

3. A new μSR spectrometer, KALLIOPE, at the D-Line

A new μSR spectrometer was installed at the D1 area. It consists of 1280 scintillators (640 telescopes) with their scintillation light detected by pixelled avalanched photo diodes (MPPCs), covering a total solid angle of 23.4%, which is 3.3 times larger than the conventional D1 spectrometer, D-OMEGA1. The spectrometer, named KALLIOPE, is equipped with a 4-kG Helmholtz coil with a gap of 135 mm, which can be rotated by 90°, making it possible to apply either transverse or longitudinal magnetic field. It is also designed to be connected with a fly path chamber with a diameter of 410 mm. During the commissioning, it was demonstrated that 200 M of coincidence positron events per hour were collected for a sample specimen of 15 × 15 mm with a 20-mm collimator. The event rate is 2-3 times higher than that in ISIS-RAL, thanks to the stronger muon beam intensity of J-PARC.

We also installed a new dilution refrigerator at the beginning of the users' beam time for 2014B. Its features can be summarized in three points: 1) The cooling period can be reduced to as low as 1.5 days without any manpower by adopting an automatic cooling system;

2) Sample exchange can be done quickly by adopting a top-loading configuration; 3) No liquid helium is required due to adopting a pulse-tube refrigerator. Figure 2 shows a picture of the new dilution refrigerator installed at the D1 spectrometer KALLIOPE.

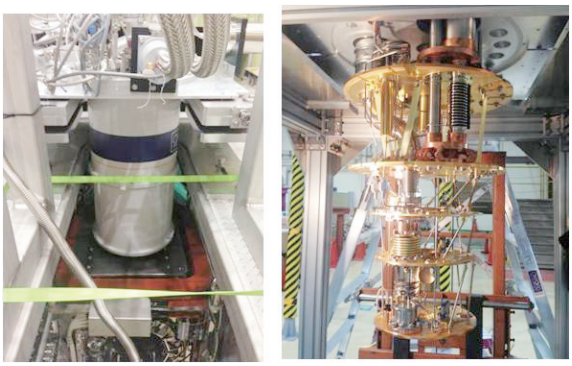

Figure 2. Installation of a new dilution refrigerator for the D1 spectrometer.

4. The S-Line

We are constructing a new surface muon beamline dedicated to materials sciences research, called the S-Line. Although eventually we are planning to construct four experimental areas, S1, S2, S3, and S4, during this fiscal year we have received funding for construction of a beamline up to the S1 area. It consists of large-acceptance quadrupole triplet magnets made of mineral insulation cables (MIC) as a front-end in the vicinity of the muon target, four sets of normal quadrupole triplet magnets and three sets of bending magnets and an electrical kicker system, associated with a set of ±250 kV DC separators.

Since we passed the facility inspection radiation test in November, 2014, we are ready to perform beam line commissioning. Figure 3 shows a picture of the S1 area.

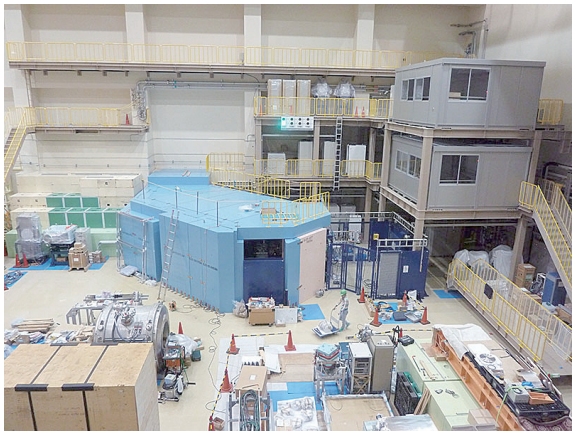

Figure 3. We passed the facility inspection radiation test in November, 2014.

5. U-LINE, the damaged window

At the U-Line, the front-end superconducting magnet in the superconducting curved solenoid, which transports intense surface muons efficiently from the proton beam line to the experimental area, had difficulties cooling down below the superconducting temperature. A fiber telescope, inserted into the superconducting curved solenoid, revealed that the thermal insulation window, designed to stop the heat radiation from the components at room temperature, was broken. In order to fix the damaged thermal insulation window, we removed the shields in the vicinity of the superconducting curved solenoid, prepared a temporal radiation control area to prevent radioactive materials from spilling out, and moved the curved solenoid from the primary tunnel to the experimental area in order to fix it. In August, 2014, all repair works were completed and we made sure that the device cooled down below the superconducting temperature. Figure 4 shows a picture of the fixed thermal insulation window of the superconducting curved solenoid.

Figure 4. The damaged thermal insulation window was fixed by removing all shields in the vicinity of the superconducting curved solenoid.

Y. Miyake[1,2], N. Kawamura[1,2], K. Shimomura[1,2], P. Strasser[1,2], A. Koda[1,2], H. Fujimori[1,2], S. Makimura[1,2], Y. Kobayashi[1,2], J. Nakamura[1,2], K. Nishiyama[1,2], Y. Ikedo[1,2], K. M. Kojima[1,2], R. Kadono[1,2], W. Higemoto[2,3], and T. U. Ito[2,3]

[1]Muon Science Laboratory, High Energy Accelerator Research Organization (KEK); [2]Muon Science Section, Materials and Life Science Division, J-PARC center; [3]Advanced Science Research Center, Japan Atomic Energy Agency (JAEA)

Installation and Operation of the Muon Rotating Target

1. Introduction

The muon production target is placed on the upstream of the neutron mercury target at J-PARC/MLF/MUSE. A pulsed muon beam will be generated on a muon target made of 20-mm thick isotropic graphite. The energy deposited by the 1-MW proton beam is estimated to be 3.9 kW on the muon target by PHITS. The first muon beam was successfully generated on September 26th, 2008. Gradually upgrading the beam intensity up to 300 kW, the muon target with a fixed target method has been used without replacement from the first muon beam generation until May, 2014. Proton irradiation causes radiation damage to the material properties of graphite. In particular, the effect on the graphite dimension is serious [1]. It is estimated that under the 1-MW proton irradiation on graphite simulation, the lifetime of the muon fixed target is 1 year. Because the muon target is highly activated by proton irradiation, its handling after use must be performed at a remote handling room, Hot cell. The remote controlled tasks require significant time, cost and manpower. Therefore, the lifetime extension is essential for the stable operation of our facility. To extend the lifetime, development of a muon rotating target, in which the radiation damage is distributed to a wider area, began in 2008 in parallel with the proton beam operation. While the lifetime of graphite becomes long enough, the lifetime of the bearing becomes a critical issue. The development of the muon rotating target has already been completed according to the results of analyses, detailed designs, and durability tests with a heating and rotating mock-up [2]. The muon rotating was installed in September, 2014. Figure 1 shows pictures of the rotating target assembly on the left and the rotating target on the lower-right. The schematic cutting section is shown on the upper-right. A horizontal shaft, which is a rotation axis of the rotating target, is parallel to the proton beam line. Because a motor device of the rotating target must be located 2.4 m above the beam line level due to high radiation, the rotating motion is transmitted into the horizontal shaft through a vertical long shaft and a pair of bevel gears. The rotating body is composed of a graphite wheel, wheel support, and horizontal shaft supported by two horizontal bearings. The two bearings are attached to a cooling jacket in which water piping is embedded. The outer and inner diameters of the graphite wheel are 336 mm and 230 mm, respectively. The temperature of the graphite wheel was estimated to be 940 K. The temperature of the hottest bearing was 390 K. The rotation speed of the rotating target could be determined from the evaluation of the maximum temperature gradients inside the graphite. Consequently, it was determined to be 15 rounds per minute (abbreviated as rpm afterwards). For the rotating target, bearings supplied by JTEKT CO., LTD [3] were selected.

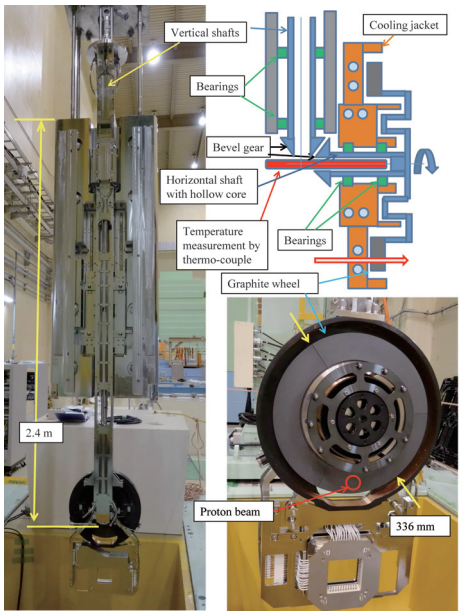

Figure 1. Pictures of the muon rotating target.

2. Bearing and solid lubricant

When the rotating target method is applied, the lifetime of the graphite will exceed 30 years. Then, the durability of the bearing will have a crucial impact on the lifetime of the muon target. The bearings of the rotating target are located in high vacuum of 10^{-4} Pa, at a high temperature of 390 K, and under a high radiation dose of 100 MGy/year. Though disulfide molybdenum or silver is generally used in these conditions, the sintered compact of disulfide tungsten is used for our target. Hereafter, disulfide molybdenum, silver, and disulfide tungsten are abbreviated as MoS2, Ag, and WS2 respectively. MoS2 or Ag is coated on the components of the bearing, such as balls, inner ring, outer ring, and retainers. On the other hand, the sintered compact of WS2 is inserted as separator of the balls. When WS2 is used, the quantity of the lubricants is expected to be much larger than in the case of MoS2 and Ag. Actually, according to the evaluation formula in the JTEKT catalogue, the lifetimes of our bearings when using MoS2, Ag, and WS2 are 1100 hours, 5800 hours, and 110000 hours, respectively. The proton beam has been actually operated for 5000 hours per

year. In the case of WS2, the lifetime of the bearings is estimated to be 22 years. However, it is not proven that the WS2 could be used as a solid lubricant under a high radiation dose. Therefore, an irradiation test of WS2 by an electron beam was performed. In the irradiation test, 80 [pieces of the sintered compacts of WS2 were irradiated by a 2-MV, 1-mA electron beam in Takasaki Advanced Radiation Research Institute, Japan Atomic Energy Agency [4]. The estimate of radiation damage caused to the pieces of WS2 was from 50 to 100 MGy. The irradiated pieces of WS2 were assembled into 8 bearings. Then durability tests under conditions similar to those at the beam line were performed in JTEKT. As a result, no irradiation effect was observed in the durability tests. Figure 2 shows the pictures of the disassembled bearing in the upper-left, the irradiation jig including only the compacts of the solid lubricant in the upper-right, and the electron-irradiation apparatus at the bottom.

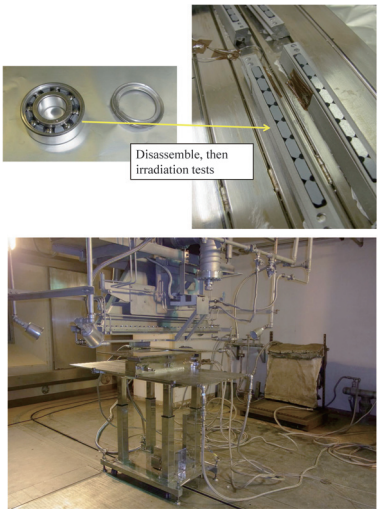

Figure 2. Pictures of the electron irradiation test of the solid lubricants.

3. Installation and operation of the muon rotating target

The muon fixed or rotating target is rigidly fabricated into the target rod. The target rod is integrated into the plug shield through four screws, which can be handled remotely. The assembled components are called target assembly. Because the muon target is highly activated by proton irradiation, the used muon target must be handled remotely. The used target assembly will be transported by the shielding vessel, named muon transfer cask, and stored in the tentative storage pod at the Large Apparatus Handling Room, which is located 10 m above floor level [10]. Since the muon target assembly must be kept in vacuum for corrosion control, suitable storage vessels have been prepared. The muon fixed target, used for five years, was successfully replaced with a new rotating target in September, 2014. Then, the used muon fixed target was activated at up to 400 mSv/hour with 20-cm distance. The observation through remote-controlled digital cameras did not register any cracks on the target. Figure 3 shows pictures of the muon fixed target utilized for five years in the upper-left, the storage vessels in the upper-right, and the replacement by the muon transfer cask at the bottom. Since then, the proton beam operation by the muon rotating target has been successfully performed without the increment of the rotation-motor current. So far, the 300-kW and 400-kW proton beam operation had been performed for three months. Furthermore, the 500-kW and the 600-kW operation had been performed for 2 weeks and for 1 hour, respectively.

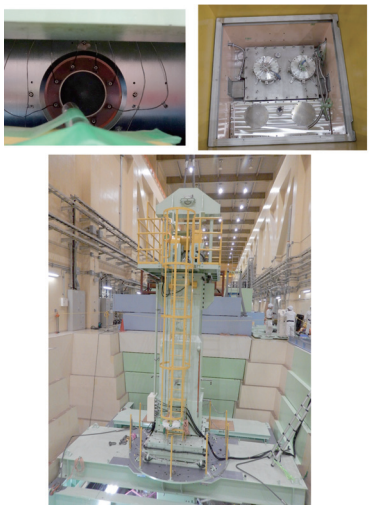

Figure 3. Pictures of the replacement of the muon target.

References

[1] H. Matsuo: Graphite 150 (1991) 290.
[2] S. Makimura *et al.*, J. Radioanal. Nucl. Chem., DOI: 10.1007/s10967-015-3949-0.
[3] http://www.jtekt.co.jp/e/index.html
[4] http://www.taka.jaea.go.jp/index_e.html

S. Makimura[1], N. Kawamura[1], S. Onizawa[2], Y. Matsuzawa[2], M. Tabe[3], Y Kobayashi[1], H. Fujimori[1], Y. Ikedo[1], A. Koda[1], K. Kojima[1], Y. Miyake[1], J. Nakamura[1], K. Shimomura[1], P. Strasser[1], Y. Taniguchi[1], and R. Kadono[1]
[1]*Muon Science Laboratory, J-PARC, High Energy Accelerator Research Organization (KEK);* [2]*Nippon Advanced Technology Co., LTD (NAT);* [3]*Seekel Co., LTD*

Present Status of the D-Line

1. Replacement of the superconducting solenoid magnet and the compressor

A conventional superconducting muon channel, which can extract surface (positive) muons and decay positive/negative muons up to 120 MeV/c, was operating successfully at the MLF experimental hall II before the devastating earthquake of March 11th 2011. The superconducting solenoid magnet of 6 m of length consists of twelve units of 0.5 m coil. The magnet coil was forced-indirectly cooled with supercritical helium gas (4.8 K at 0.80 MPaG) supplied by the on-line helium refrigeration system. The magnetic field was designed to reach a maximum of up to 5 T (current 730 A) at operational temperature of 6 K. The present magnetic field for normal operation for surface/decay muon extraction is 0.308 T (45 A)/2.33 T (340 A), respectively

On-line helium refrigeration system was employed to ensure the long-term stability of the operation. The cooling power of the latter was 35 W at 4.5 K and 200 W at 80 K, and it was also able to produce 8 l/h of liquid helium. The whole system was monitored and controlled by a VME controller, combined with a personal computer with dedicated software based on the LabVIEW System, and cooled down automatically. The typical cooling period from room temperature to operation temperature (~5 K) is about 3 days. Now the long-term (typically 1 month) operation functions under quite stable conditions.

In FY 2010 the solenoid and the on-line refrigeration system operated smoothly for more than 5000 hrs until the devastating earthquake on March 11th 2011. On that day the system was operating, however, it was stopped safely and no He gas was released. The damage caused by the ground sinkage was serious, especially in the on-line helium refrigeration system which became unstable and the superconducting magnets also displayedfrequent instability under high current operations. Therefore we decided to replace these devices.

In FY 2014, the compressor of the on-line refrigeration system was replaced from Kaser to Mycom. Thus, the cooling power of the on-line helium refrigeration system was increased to 275 W at 4.5 K and to 400 W at 80 K, a new superconducting solenoid was also fabricated. This time we adopted warm bore type solenoid, where no foils are needed to protect from thermal radiation. And the inner radius of the coils was increased from 12 cm to 20 cm. The changes are expected to improve drastically the low energy muon (~100 keV) intensity.

Figure 1. Photograph of the new compressor (above) and the solenoid (below).

2. Kicker system

The muon kicker system is used to separate the muon pulses and feed them simultaneously to two experimental areas (D1, D2). The beam operation with the kicker system started successfully in the winter of 2011. However, it was found that the ignition of the kicker power supply produced kicker noise. The noise mainly comprises a 10-MHz component that is dispersed into the air, AC lines and detector signal lines. The kicker noise level was drastically reduced by RF-shielding the transmission lines with copper sheets and by reinforcing both the ground lines of the kicker system and the detectors [1]. Employing bypass capacitors at the New D1-μSR spectrometer was also successful [2]. However, further improvements are required for negative muons and muonium experiments at the D2 area. Therefore, electrically insulating the kicker chamber from the beam ducts and its base, and reducing the ground impedance were tested in this fiscal year. A plan to utilize a saturable inductor for eliminating the noise is also described.

Copper plates were laid under the kicker oil tank to reduce the ground (GND) impedance. The vacuum ducts connecting to the kicker chamber at both ends were replaced with ceramic ducts in order to electrically insulate the kicker chamber from the beam ducts and its base.

An outline of the kicker ground is shown in Fig. 2. The kicker system was isolated from the beamline to prevent the noise through the ground line. The AC line was also isolated from the other power lines with isolation transformers. Wide copper plates were used as low impedance GND. However, these measures were not very effective and actually increased the radiation noise.

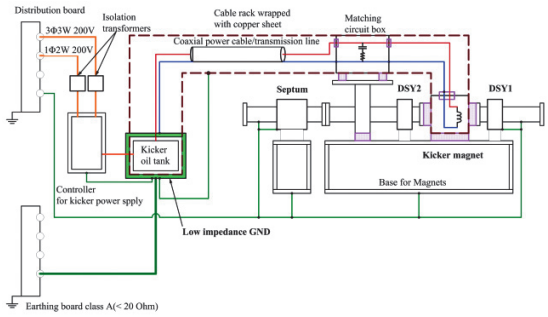

Figure 2. Outline of the kicker ground. Squares with pink line denote the ceramic insulations.

The kicker noise source is the surge voltage at about 10 MHz that occurs with the ignition of the charged Pulse Forming Network (PFN). So far we have taken measures to protect the experimental signals against the surge noise. A fundamental new measure, however, should be taken to remove the surge voltage at the output from PFN. Bypassing the surge noise with capacitors could be a possible solution. However, this method sacrifices the rise-time of the kicker field instead. Alternatively, a saturable inductor (SI) was considered to eliminate the surge without delaying the rise-time. The SI is made of saturable ferrite cores, and it functions as a large inductance at the onset of the surge voltage/current, then the inductance decreases sharply due to the saturation of ferrite as the current increases. In the circuit simulation code, SPICE, the SI can be modeled as

$$L_{sat}(I) = L_0\left(Ae^{-\alpha|I|} + 1\right)$$

where L_0 is the air-core inductance and I the current. Two kinds of ferrite will be tested and their characteristics are summarized in Table 1. The present parameters are optimized for the initial charging voltage of PFN at 20 kV.

The diagram of the kicker system with the SI is shown in Fig. 3.

Figure 4 shows the result of the SPICE calculations. It can clearly be seen that the surge current peaks at both ends of the transmission line are eliminated, while the rise-time of the kicker magnet current is kept unchanged.

Table 1. Parameter of the saturable inductors optimized for 20 kV operation.

Type	A	α	Bandwidth	Power loss
I	29.0	0.001171	>80 MHz	12.5 W
II	189.0	0.002263	12 MHz	2.6 W

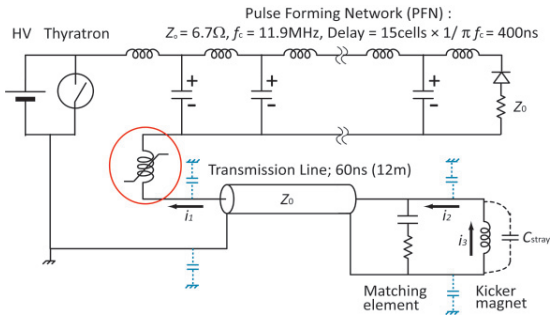

Figure 3. Kicker system with saturable inductor.

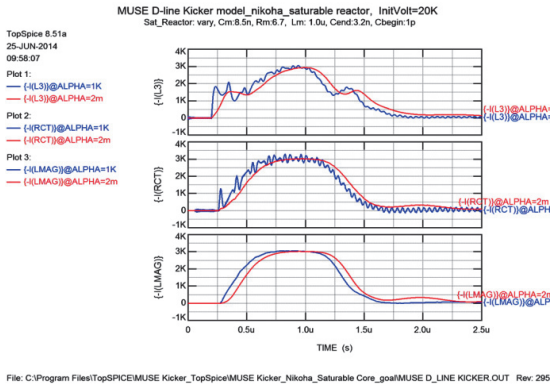

Figure 4. Result of SPICE analysis for the case with (red) and without (blue) the SI. From top are shown the currents I_1, I_2 and I_3 indicated in Fig. 3.

A kicker system directed single-pulsed muon beams to the two existing experimental areas D1 and D2 simultaneously in March 2012. Now experiments with the new spectrometer in the D1 area can be performed with kicker-on without any noise problems. However, the kicker noise level is still high for the experiments in the D2 area. The trial with the saturable inductor is scheduled for September, 2015, in order to eliminate the kicker noises at all relevant experimental areas.

References

[1] H. Fujimori *et al.*, KEK-MSL Report 2012 (2013) 16-17.
[2] H. Fujimori *et al.*, KEK-MSL Report 2013 (2014) 20-21.

K. Shimomura[1,2] and H. Fujimori[1,2]
[1]*Muon Science Laboratory, High Energy Accelerator Research Organization (KEK), Tsukuba;* [2]*J-PARC Center Cryogenics Section, Tokai*

U-Line; Lyman-α Laser Developments and Slow Muon Beamline Commissioning

As it was mentioned in the previous report, the U-line is one of the muon beamlines in the Material and Life Science Experimental Facility of J-PARC, which provides the world's highest intensity of pulsed surface muons. It was designed to produce ultra-slow muons through the thermal muonium laser resonant ionization method. The ultra-slow muon beam is expected to be a new research field in surface and interface physics. A new slow muon beamline to supply ultra-slow muons is now under commissioning. The layout of the beamline is shown in Fig. 1.

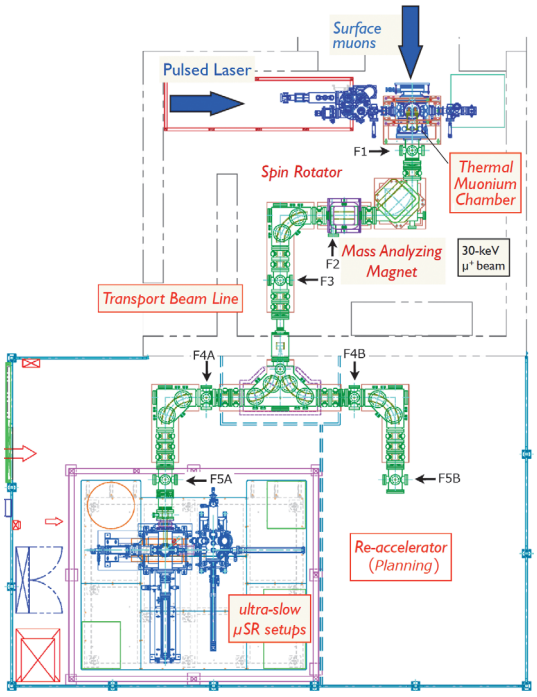

Figure 1. The layout of the Ultra-Slow Muon Transport System. F1~F5 show the focusing points of the beam line.

1. Developments of the laser system

Ultra-slow muons are generated in resonant ionization by the simultaneous irradiation of 122.089 nm, which is the muonium Lyman-α resonance line and corresponds to the 1S-2P transition of the muonium atom, and ultraviolet radiation at a wavelength of around 355 nm. Therefore, a high-energy coherent Lyman-α resonance radiation source is a critical element to efficiently produce ultra-slow muons.

Solid-state materials are not suitable for the generation of vacuum ultraviolet (VUV) radiation because they are not transparent for a wavelength below 160 nm. We chose two-photon resonance four-wave mixing in krypton to generate 122.089 nm pulses. A coherent 212.556 nm light source for two-photon excitation and a tunable near-infrared light source are required in the two-photon resonance four-wave mixing. The tunable near-infrared light source is tuned around 820.649 and 845.015 nm to generate VUV radiation at the muonium Lyman-α resonance line and the hydrogen Lyman-α resonance line. In this fiscal year, we focused specifically on the VUV generation at the hydrogen Lyman-α resonance line.

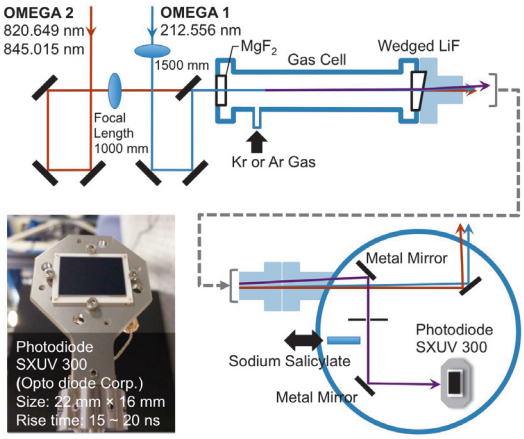

Figure 2. Optical system for two-photon resonance four-wave mixing [6]. Sodium salicylate and a photodiode, SXUV 300 were used for the observation of Lyman-α resonance radiation and the determination of output energy, respectively.

Coherent light sources are required for the two-photon resonance four-wave mixing. The output pulses at 212.556 and 845.015 nm were synchronized with the use of an optical delay system and coaxially input to a krypton-argon gas cell for two-photon resonance four-wave mixing, as shown in Fig. 2. Although we obtained 3.2 and 1.6 mJ at 212.556 and 845.015 nm, the input energies practically were restricted up to 0.8 and 1.5 mJ at 212.556 and 845.015 nm because of optical losses in the transmission system. Figure 3 shows the output energies at the hydrogen Lyman-α resonance line. While Kr exhibits negative dispersion at vacuum ultra violet wavelengths shorter than 124 nm, Ar exhibits positive dispersion. Therefore, we have to mix Ar with Kr and control the mixture ratio of Ar and Kr for phase matching in four-wave mixing. We adjusted the mixture ratio to $P_{Ar}/P_{Kr} \approx 5$ and changed the pressure from 0.02×10^3 to

3.20×10^3 Pa. When the pressure was approximately 2.20×10^3 Pa, the output energy at the hydrogen Lyman-α resonance line increased up to 8.4 μJ in the gas cell. The output energy corresponds to a conversion efficiency of 3.6×10^{-3} ($\approx 8.4 \times 10^{-6}$ J / [1.5×10^{-3} J + 0.8×10^{-3} J]).

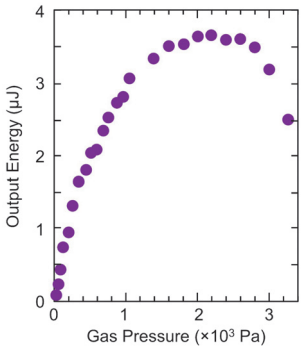

Figure 3. Output energy of coherent hydrogen Lyman-α resonance radiation (121.57 nm). 8.4 μJ in the gas cell and 3.7 μJ at its outer side were obtained.

The conversion efficiency is an order of magnitude higher than the one reported previously. The increase of conversion efficiency is probably attributed to longer interaction length and high-efficient mode matching in four-wave mixing caused by high beam qualities and the same temporal profile of pump pulses.

In conclusion, we have accomplished a high-conversion efficiency in two-photon resonance four-wave mixing to generate Lyman-α resonance radiation. Furthermore, we are currently developing Nd:$Y_3Ga_2Al_3O_{12}$ ceramic power amplifiers to efficiently increase the output energy up to 1 J at the fundamental wavelength of 212.556 and 820.649 nm toward the realization of 100 μJ at 122.089 nm

2. Slow muon beam line tuning

In the previous fiscal year, almost all components of the ultra-slow muon beam line were installed and the optimization of the beam transportation was started by using Li-ions.

In this fiscal year, we successfully transported Li-ions to μSR experimental port. Beam position and size are estimated by using slits and Micro Channel Plates (ROENDEC DLD40) at each focusing point. The results of the measurements are shown in Fig. 4 and Table 1.

Table 1. Li-ion beam width in sigma at each focusing point.

Position	Horizontal Width	Vertical Width
F1	1.2 mm	1.3 mm
F2	3.8 mm	4.1 mm
F3	1.0 mm	2.1 mm
F4A	3.8 mm	4.0 mm
F5A	2.9 mm	6.4 mm

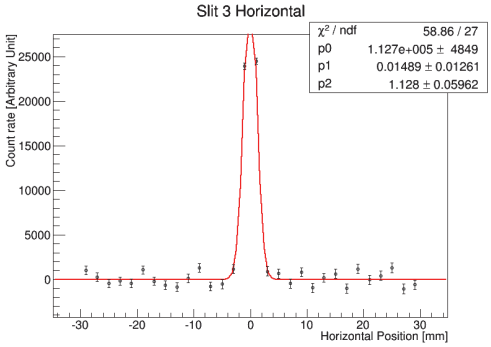

Figure 4. An example of measured beam distribution. A horizontal distribution of the Li-ions at F3. Dots show the measured particle late and red lines show the fitted gauss function.

For tests of the laser system and better tuning of the beamline, hydrogen atoms are ionized by laser and transported as a pilot beam. The laser ionized hydrogens are successfully transported to the μSR experimental port. The measured time of flights (TOF) between the laser injections and the particle detections agree with the calculated TOF of the hydrogen ion, as shown in Fig. 5.

The tuning of the beamline is currently underway for the first ultra-slow muon beam at J-PARC.

This work was supported by MEXT KAKENHI Grant Number 23108002.

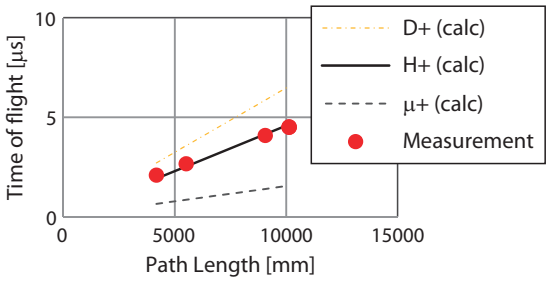

Figure 5. Time of flight of the beam. Dots show the results of the measurements. Lines show the calculated TOF of the deuterium-ion, hydrogen-ion and muon.

T. Adachi[1,2], Y. Ikedo[1,2], J. Nakamura[1,2], A. Yabuuchi[1,2], P. Strasser[1,2], Y. Oishi[3], N. Saito[4], K. Miyazaki[4], K. Okamura[4], S. Wada[4], T. U. Ito[2,5], W. Higemoto[2,5], K. M. Kojima[1,2], K. Shimomura[1,2], R. Kadono[1,2], Y. Miyake[1,2], M. Iwasaki[3], and E. Torikai[6]

[1]Muon Science Laboratory, High Energy Accelerator Research Organization (KEK); [2]Muon Section, Materials and Life Science Division, J-PARC centre; [3]Advanced Meson Science Laboratory, RIKEN Nishina Center for Accelerator-Based Science (RNC); [4]Photonics Control Technology Team, RIKEN Center for Advanced Photonics (RAP); [5]Advanced Science Research Centre, Japan Atomic Energy Agency (JAEA); [6]Interdisciplinary Graduate School of Medicine and Engineering, University of Yamanashi

Construction of the Muon S-Line and Installation of the General Purpose μSR Spectrometer

1. Introduction

The surface muon beamline (S-Line) in experimental hall No.1 of the Materials and Life science experimental Facility (MLF) building is designed to provide low-energy muon beam, which is mainly utilized by materials and life science experiments (Fig. 1). Following the construction of the power supply yard and the concrete shields completed in the previous fiscal year [1], the primary goal of the project in 2014 was the installation of the beamline components.

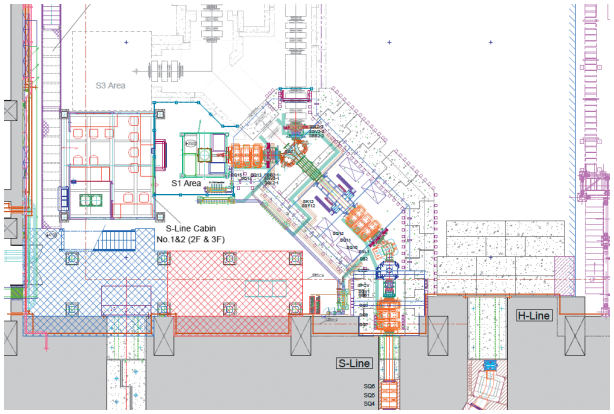

Figure 1. Beamline layout of the S-Line (phase1).

2. Cooling water

Soon after the MLF shutdown in July, the concrete shields were removed to install cooling water pipes along the beamline magnets. In order to reduce the number of the pipes passing through the piping duct of the concrete shield, one triplet quadrupole magnet, e.g. SQ7-8-9, uses a common water pipe to control the total flow rate. To cope with the change in the flow balance among quadrupole magnets, a small water manifold with three controlling valves to distribute cooling water is situated near the magnet. Besides, three power supplies connected to each of the triplet quadrupole magnets monitor a common flow switch activated in case of problems with the water supply. In addition to this, the status of each quadrupole magnet is monitored by two devices: a differential pressure switch and thermal switches attached to hollow conductors. The same monitoring devices are installed for SQ4-5-6, which is placed in the primary beam tunnel.

3. Beamline equipment assembly

The final assembling and testing of the beamline equipment continued along with the installation, because some of the assembled equipment included a few devices manufactured by independent companies. In the case of the electric kicker, for example, the vacuum chamber and electrodes were made by Irie Koken Co., Ltd., the switch-yard magnet and the magnetic end-guards were made by NEC Tokin Corp., and the high-voltage pulse transformer was made by Pulse Power Japan. Fig. 2 shows that the main components of the electric kicker situated at the beamline height, such as the vacuum chamber and the pulse transformers, can be integrally manipulated after being assembled, since they are carried on the upper stage of the kicker support. This part, which is detachable from the lower support frame, is installed in the beamline with sufficient reproducibility by using guiding pivots. The scheme mentioned above is also helpful to conduct some installation tasks simultaneously, such as anchoring supports on the floor, assembling devices, and alignment along the beamline axis.

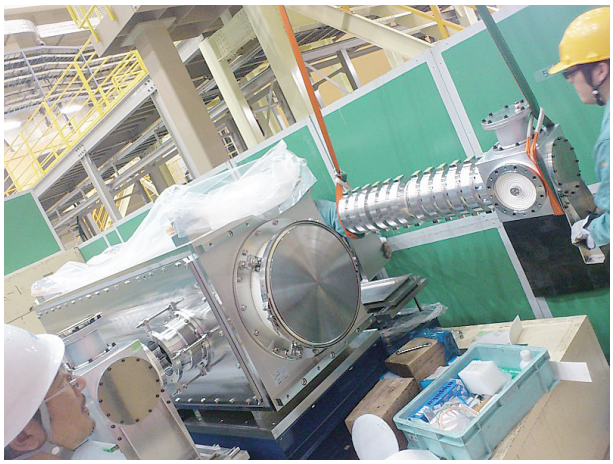

Figure 2. Assembling the electric kicker. One of the pulse transformers is about to be attached to the vacuum chamber.

4. Installation of the beamline components

In the beginning of September, 2014, most of the beamline components were successfully installed and the major task at this stage was to place cables. On the other hand, due to a technical problem during the pressure test of the cooling water pipe, the operation of the magnets and the power supplies for adjustment was suspended. After discussions among the task force organized by the MLF division members, the cooling

system was restarted in mid-October. Finally, the facility inspection on November 7, 2014, confirmed that the Muon S-Line was operating successfully.

5. General-purpose spectrometer

As reported elsewhere [2], we have designed and installed a general-purpose μSR spectrometer (0.4 Tesla longitudinal field coil with capability of accepting various sample environment inserts) at the D1 experimental area. In FY2014, we manufactured another general-purpose spectrometer with Element Strategy grant. Its design is identical to that of the D1 spectrometer, and is to be installed at the S1 experimental area (Fig. 3).

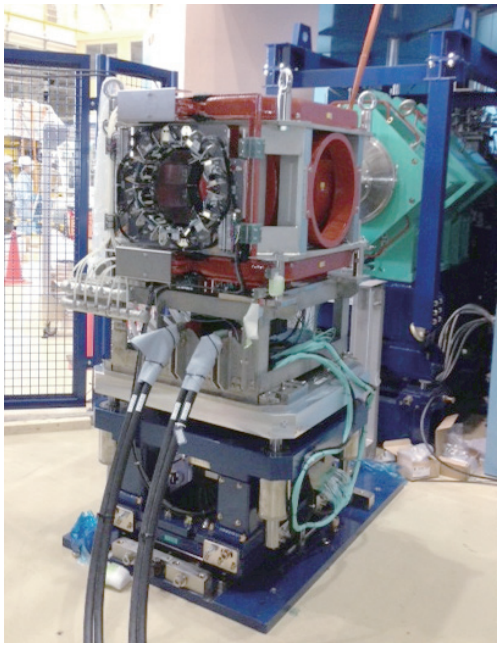

Figure 3. General-purpose μSR spectrometer installed at the S1 experimental area.

The specifications of the D1/S1 spectrometer are listed in Table I. It is equipped with a 0.4 Tesla longitudinal field (Bz) coil and a 14-m Tesla transverse-field coil (By), both of which are normal conducting magnets. The stability and the homogeneity of the magnetic fields are shown in Table I. The zero-field correction coils are driven by an active feedback system based on the magnetic field vectors measured at four points around the sample. The feedback system actively achieves < 0.4 μTesla stray field at the sample position.

Table I. specification of D1/S1 μSR spectrometer.

Magnets	
Longitudinal field Bz (//beam)	Maximum 0.4 Tesla (1000 amps, 100 V)
LF magnet bore and gap	ø400, 135 mm
LF homogeneity	0.1% ø20 mm, 1% ø50 mm
LF stability	Drift < 0.01% for 8 hours Ripple Vp-p < 0.01%
Transverse field By (⊥beam, vertical)	Maximum 14-m Tesla (100 amps, 40 V)
TF homogeneity	0.1% ø20 mm, 1% ø50 mm
TF stability	Drift < 0.05% Ripple Vp-p < 0.1%
Correction field coils for zero-field (CCBx, y, z)	Maximum 1-m Tesla (10 amps, 20 V)
CF homogeneity	0.5% ø20 mm, 10% ø50 mm
Positron Counters	
Number of channels	32ch × 40 Kalliope units = 1280 channels (640 pairs)
Detector solid angle	21.2% of 4π (2 × 8 array of 10 × 12 mm scintillator cubes: covers 1920 mm^2 area at 180 mm and 161 mm from sample)
Sample insert	
bore and the gap	ø254, 135 mm

The positron detectors are 40 Kalliope units each of which has 32 sets of 10 × 10 × 12 mm cubic scintillators [1]. The total number of the individual positron counters is thus 40 × 32 = 1280 channels (640 coincidenced pairs) covering 21.2% of the 4π solid angle.

The count rate and the spectrum features have to wait for the beam commissioning of the S1 experimental area, starting in FY2015.

References

[1] A.Koda *et al.,* KEK-MSL Annual report (2013).
[2] K. M. Kojima *et al.,* J. Phys: Conf. Ser., **551** (2014) 012063, (2014); K. M. Kojima *et al.,* KEK-MSL Annual report (2013).

A. Koda[1,2], P. Strasser[1,2], K. M. Kojima[1,2], N. Kawamura[1,2], H. Fujimori[1,2], K. Nishiyama[1,2], and J-PARC Muse staff
[1]Muon Science Laboratory, High Energy Accelerator Research Organization(KEK); [2]Muon Section, Materials and Life science Division, J-PARC Center

Present Status of the H-Line

The construction of a brand new 4th beam line, the H line, has been planned for MUSE. The new beam line is designed to have a large acceptance, momentum tunability, and the ability to use kicker magnet and Wien filter. This beam line will provide an intense beam for experiments which require high statistics and need to be conducted for relatively long periods in the experimental areas. Several experiments in the field of fundamental physics studies have been proposed for the H line [2-4].

From the existing muon production target at MUSE, it is possible to extract 4 muon beam lines. The H line is extracted to the south east direction in experimental hall #1.

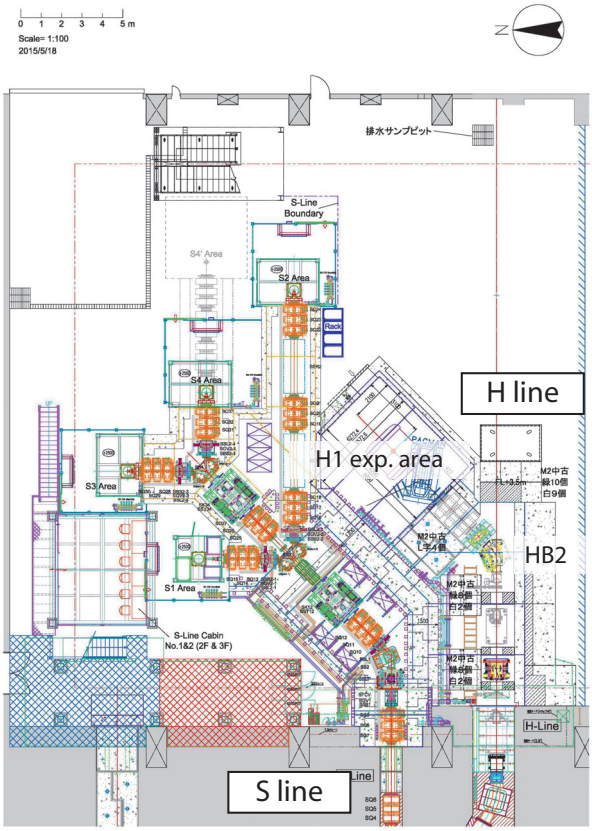

Figure 1. A layout plan of experimental hall #1 in the first phase.

In the initial stage of the MUSE construction, only the D line and the front-end magnets in the S line were installed, consequently the front-end magnets in the U line were installed in 2009. Temporary radiation-shield blocks were placed in the H line. J-PARC has been operating since 2008, so the activation around the muon production target becomes more serious with every passing year. According to the evaluation using a Monte-Carlo code [5], the dose rate beside the target chamber was estimated to be close to 1 Sv/h, and the summer shutdown in 2012 was the ultimate time limit to install the frontend magnets in the H line. Thus, the installation of the frontend devices was completed mainly in 2012 and partially in 2014, as shown in Fig. 2 and 3.

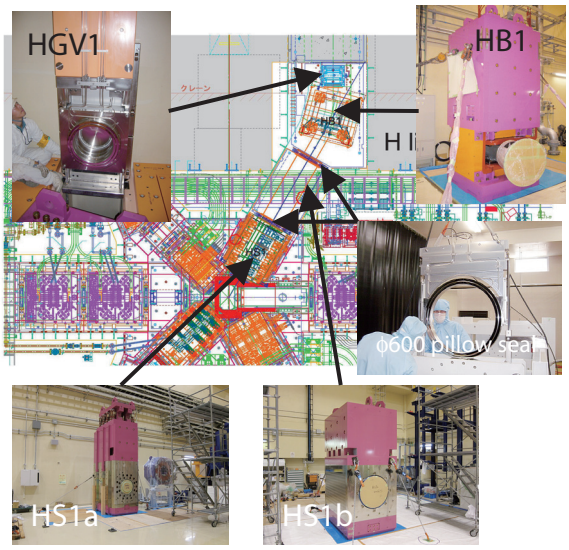

Figure 2. Installed frontend devices in the H line.

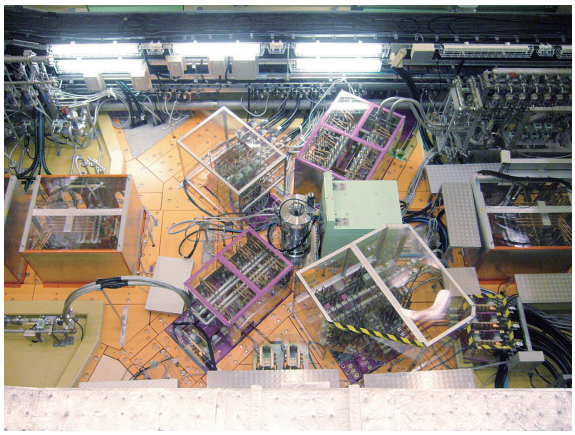

Figure 3. Picture taken after the installation of the frontend devices in the H line was completed.

In the other high intensity beam line in MUSE, the U line, we adopted only axial focusing magnets to obtain high transmission efficiency [6]. On the other hand, in the H line, the beam captured by an axial focusing large-aperture solenoid magnet is transmitted through bending magnets, although these non-axial focusing magnets increase the beam loss. To compensate for this

and improve the high transmission efficiency, large aperture magnets and other devices have been adopted in the H line. A typical size of the aperture is 600 mm in diameter.

The conceptual design work of the major components in the experimental hall, *i.e.* magnets, vacuum components and so on, is almost converged for the first phase of the H line in which the beam line is constructed to the first experimental area, as shown in Fig. 1. At present, the detailed mechanical design work is in progress. In order to provide sufficient muon beam to all planed experiments in the H line, the design work is performed with the participation of the collaborators in the proposed experiments. For instance, the g-2/EDM experiment [3], for which the beam line is extended straight through the bending magnet (HB2), needs to focus the surface muon beam on the muonium production target which will be placed several tens of centimeters apart from the exit of the last magnet. The beam spot size is required to be as small as possible. In addition, the magnetic field in the muonium production target is required to be smaller than 1 mT, and thus the leakage field of the beam line magnet generally is not negligible. To satisfy these requirements, after HB2 the surface muons are transported and semi-focused by a solenoid magnet (HS4), and then focused on the muonium target by quadrupole magnets [7].

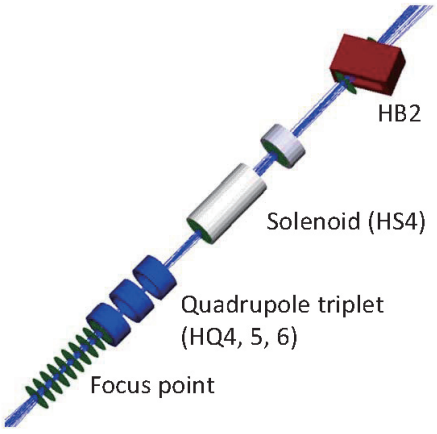

Figure 4. Final focusing part for the g-2/EDM branch.

The radiation shield design proceeds according to the method previously applied at the other beam lines [5]. Along the beam line, a few-meter thick concrete shield will be necessary to enclose the streaming neutrons and other radiation sources. Because the H line adopts large aperture devices, the effects of the streaming neutrons are more serious than in the case of other beam lines. The evaluation of the streaming neutrons is important not only for radiation safety but also to check their effect on the detectors and other devices in the experimental area. Figure 5 shows a typical result of the simulation. While the proton beam is on, the dose rate in the experimental area is expected to reach 100 μSv/h, and no one can enter into the area even if no beam is delivered. By inserting a beam blocker, which is a 40-cm thick copper block, the dose rate is reduced by a factor of ten. Both the beam blocker and the switching off of HB2 guarantee the personnel safety against radiation, and comprise the personal protection interlock system.

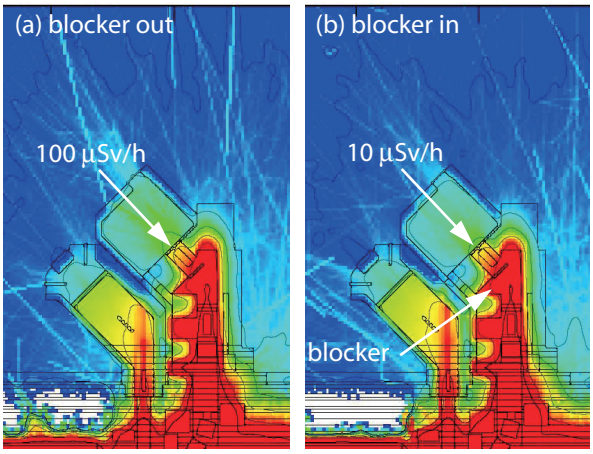

Figure 5. A typical simulated result of the radiation dose around the H line. To enter the experimental area, a beam blocker was inserted in the right while no blocker was used in the left.

References

[1] N. Kawamura *et al.*, *2013 Journal of Physics: Conference Series* **408** 012072.
[2] K. Shimomura *et al.*, *ibid.*
[3] N. Saito *et al.*, *ibid.*
[4] S. Mihara *et al.*, *ibid.*
[5] N. Kawamura *et al.*, 2009 *NIM A* **600** 114.
[6] K. Nakahara *et al.*, 2010 AIP Conf. Proc. **1222** 420.
[7] A. Yoyoda *et al.*, *2013 Journal of Physics: Conference Series* **408** 012073.

N. Kawamura[1,2], MuHFS collab., DeeMe collab., and g-2/EDM collab.
[1]*Muon Science Section, Materials and Life Science Division, J-PARC;* [2]*Muon Science Laboratory, High Energy Accelerator Research Organization (KEK)*

MLF Safety

Research Safety

1. Radiation safety

(Improvement of shielding estimation)

From the construction stage of MLF, shields of only each beamline (single-beamline-model) were considered as the shielding estimation. However, because the proton beam-power increases and many beamlines with their shields have been constructed, the shielding estimation with the single-beamline- model is not realistic and is over spec. Therefore, shields of all the beamlines (all-beamline model) were proposed as the new shielding estimation method and adopted in the new application of the radiological license. Figure 1 shows an example of the all-beamline-model for the shielding estimation [1].

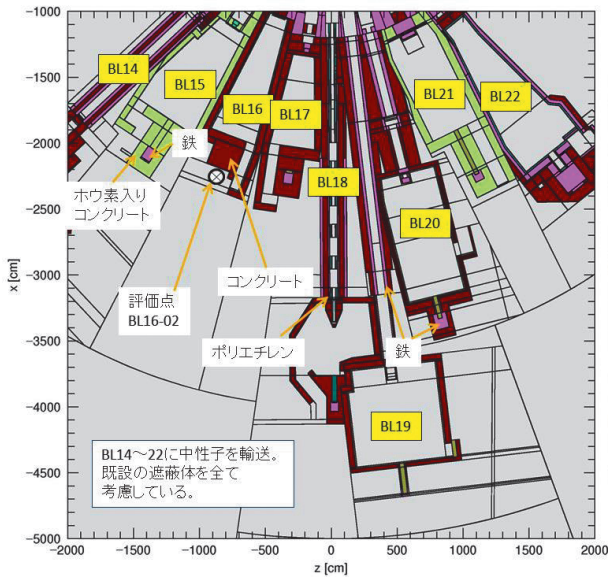

Figure 1. Example of the all-beamline-model for the shielding estimation at the 2nd experimental hall.

(Measurement of shielding performance of all neutron beamlines)

In order to apply the 1 MW operation in the radiological license, we measured dose rates at outside of the shields of the all neutron beamlines with the 300 kW proton beam operation.

As the results, it was confirmed that it was enough shielding performance at almost beamlines. However, it was found that there was not enough shielding performance at several beamlines with only a specific case. Therefore, shields of such the beam lines were estimated by the shielding calculation and several shields were added. Finally enough low dose rates could be confirmed by the measurement.

(Radiological license upgrade)

Normally, we have two chance of the application on radiological license upgrade in a year.

In the first application, the radiological license was permitted on Sep.9, 2014, and was updated for the following items:

(1) Installation of the neutron beam line BL22,
(2) Minor change to the shielding configuration for preparation of installation of the muon beam line (H line),
(3) Extension of controlled area and addition of one entrance to it at the BL09 building.

In the second application, the radiological license was permitted on Dec. 11, 2014, and was updated for the following items:

(4) Upgrade the maximum proton beam power induced to MLF from 2.6×10^{18} proton/h (350 kW) to 7.5×10^{18} proton/h (1 MW),
(5) Improvement of the shielding estimation method (The all-beamline-model was adopted.)
(6) Extension of controlled area for completion of the experiment preparation building.

By this permission, the 1 MW proton beam operation at MLF became available as the license.

The neutron beam line BL06 and the muon beam line S line are available because the two beam lines passed the facility inspection in 2014.

2. Chemical safety

For neutron and muon experiments, a lot of chemical substances have been brought into and used in MLF. The checking-in process, usage and storage of chemicals such as solid, gas and liquid are managed by the chemical safety group. Figure 2 shows an annual change on the number of experimental samples which were submitted for MLF proposals and safety-checked by using sample risk assessment sheets.

In particular, the chemical safety group makes assessments of the handling of highly toxic chemicals, and requires extra care which may cause serious injury. Chemicals are stored safely in cabinets and on shelves in an upright position. Chemical fume hoods are surveyed annually by the group. Chemical fume hood velocities for all hoods on MLF are evaluated on an annual basis by Facilities.

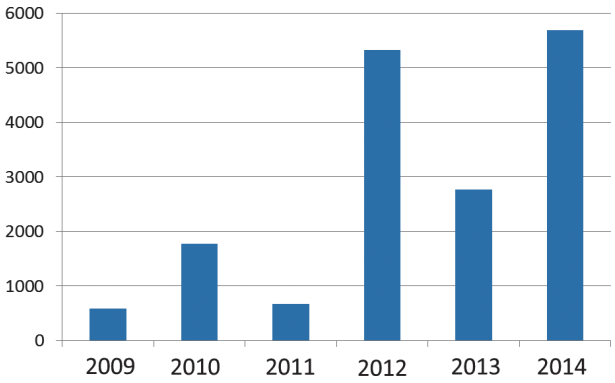

Figure 2. Annual change on the number of experimental samples which were safety-checked.

3. Electrical safety

For safety check of a lot of electrical equipment, internal regulations based on governmental regulations and appropriate standards are applied to prevent hazard and damages in MLF. The number of user's devices safety-checked by the electrical safety group was 289 on the 2014A and 334 on the 2014B proposal.

In particular, safety interlock system is required for experimental devices. For example, an overcurrent protective circuit is required for an electrical power supply and so on in order to prevent fire and injuries caused by electricity include electrical shock and burns.

Fuses and circuit breakers, which are safety devices that protect equipment from high currents or voltages and prevent overheating of electrical wires, are periodically safety-checked by the electrical safety group using meggers.

4. Machine Safety

In each experimental hall at MLF, 7.5 ton crane and 30 ton crane are under operation. These are operated, inspected, and maintained by the machine safety group. Pre-use, monthly, and annual inspection are conducted according to the J-PARC center safety instructions. Figure 3 shows a monthly change on the number of times of crane use.

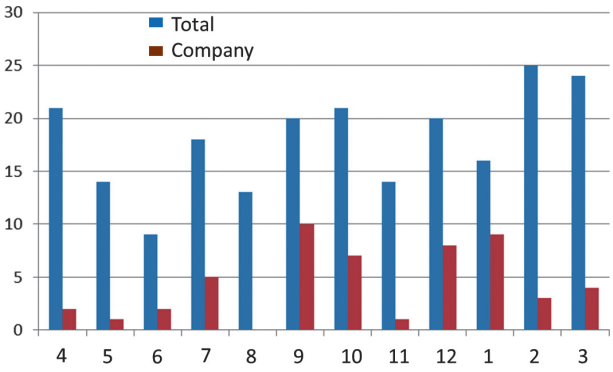

Figure 3. Monthly change on the number of times of crane use.

The total number of times of use of cranes in 2014 is 215. Those were mainly used by inside operators, but the 52 was used by outside company's operators. The machine safety group safety-checked how to use the cranes and slings about all of proposals.

For safety check of laser equipment used for neutron and muon experiments, internal regulations based on the Japanese Industrial Standards Committee (JIS) is applied. Technical reviews of 4 equipment were conducted in 2014A and 2014B at MLF by the special committee on laser.

Reference

[1] Application of the radiological license (attached reference material for MLF), permitted on Dec.11, 2014, (2014).

M. Harada[1], M. Ooi[1], M. Sekijima[1], T. Kai[2], Y. Kasugai[5], K. Aizawa[3], S. Ono[3], H. Tanaka[3], W. Kambara[3], Y. Ito[3], M. Nakamura[2], K. Suzuya[2], S. Makimura[4], Y. Sakaguchi[6], and T. Yamashita[6]

[1]Neutron Source Section; [2]Neutron Science Section; [3]Technology Development Section; [4]Muon Science Section, Materials and Life Science Division, J-PARC Center; [5]Radiation Safety Section, Safety Division, J-PARC Center; [6]Neutron R&D Division, CROSS-Tokai

MLF Operations in 2014

CROSS-Tokai 2014 Update

The Public Neutron Beam Facility at J-PARC

Consistent with its longstanding policy of promoting open access to major publicly-funded research facilities, the Japanese government established in July 2009 the Public Neutron Beam Facility at J-PARC. The Facility consists of the accelerators and target station used to generate pulsed neutron beams and a proportion of the beamlines that exploit the neutron beams for research purposes.

The legislative framework within which the Public Neutron Beam Facility was established requires that an independent third-party organization be responsible for the administration and support of the science program on the so-called 'Public Beamlines'. CROSS-Tokai was appointed to this role and began operations from its offices in the Ibaraki Quantum Beam Research Center adjacent to the J-PARC site in early 2011.

Although CROSS-Tokai is structurally independent of JAEA and KEK – the co-owners and operators of J-PARC – it maintains a high level of cooperation and collaboration with the two founding organizations and other stakeholders that is driven by shared scientific objectives.

The Role of CROSS-Tokai

CROSS-Tokai is entrusted with specific responsibilities relating to the Public Beamlines which, In practical terms, can be summarized as follows:

- *Manage proposal selection and beamtime allocation*
- *Provide user support and ancillary experimental facilities*
- *Provide assistance and expert advice to existing and potential users*
- *Initiate and undertake outreach and facility utilization promotion activities*
- *Manage the selection and assessment of Contract Beamlines*

The Public Beamlines at J-PARC MLF

The MLF has capacity to accommodate up to 23 neutron beamlines around the present target station. There are currently 18 neutron and 2 muon beam instruments in operation, 2 neutron instrument in commissioning and 2 new beamlines under construction. Of these, 6 beamlines have been designated as Public Beamlines as part of the Public Neutron Beam Facility and are supported by CROSS-Tokai.

Though not exhaustive in their experimental capabilities, the Public Beamlines cover a wide range of neutron scattering techniques and can be used in a variety of research fields. The Public Beamlines at J-PARC MLF are listed in Table 1 with examples of their research applications.

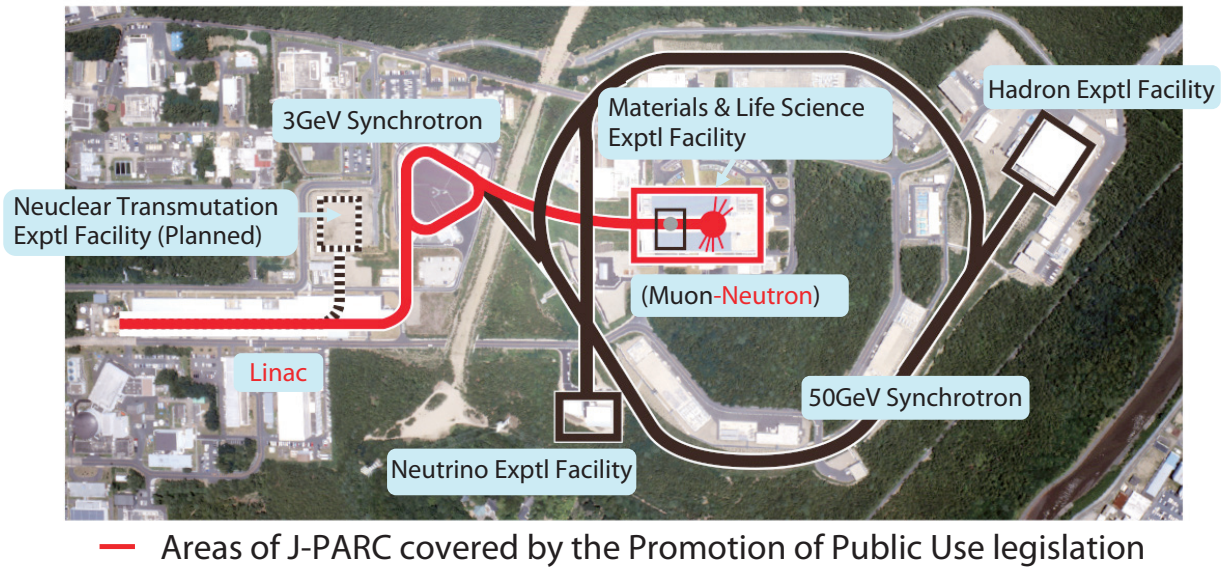

Figure 1. The Public Neutron Beam Facility at J-PARC (shown in red).

Table 1. The Public Beamlines at J-PARC MLF.

Number	Instrument	Applications
BL01	4SEASONS – 4D-Space Access Neutron Spectrometer	Lattice and spin dynamics in condensed matter over a wide range of 4D momentum-energy space
BL02	*DNA* – Biomolecular Dynamics Spectrometer	Atomic and spin dynamics of biological macromolecules soft matter and functional biomaterials
BL11	*PLANET* – High-Pressure Neutron Diffractometer	Structural analysis and radiography of materials under extreme pressure and temperature
BL15	*TAIKAN* – Small and Wide Angle Neutron Scattering Instrument	Nano and micro scale structural analysis of metals, magnetic materials, soft matter and bio-macromolecules
BL17	*SHARAKU* – Polarized Neutron Reflectometer	Structural analysis of functional and magnetic thin films, biological thin films and buried interfaces
BL18	*SENJU* – Extreme Environment Single Crystal Diffractometer	Microcrystalline and magnetic structural analysis of functional materials
BL22 in commissioning	*RADEN- Energy-Resolved Neutron Imaging System*	Visualization of the spatial distribution of crystal structures, nuclides and magnetic domains by neutron transmission imaging and 3D reconstruction

Distribution of Beamtime on the Public Beamlines

The Selection Committee of CROSS-Tokai regularly reviews and sets policies for the distribution of beamtime on the Public Beamlines at the MLF. In line with the prescribed role of the Public Beamlines and taking into account operational requirements, beamtime is currently distributed in approximately the following ratios:

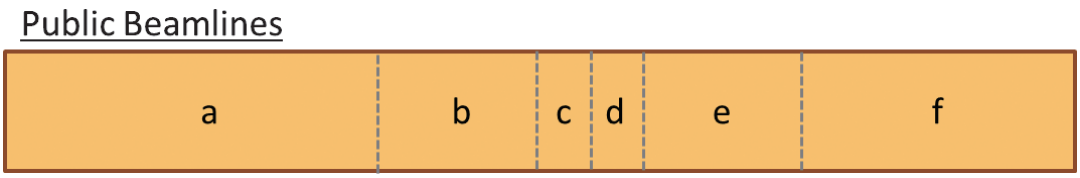

(a) General Use
(b) Elements Strategy Initiative (up to 15%)
(C) Trial Use (up to 5%)
(d) Director's Discretion (up to 5%)
(e) CROSS-Tokai Research (up to 15%)
(f) Facility Use (up to 25%)

Figure 2. Beamtime Distribution on the Public Beamlines.

CROSS-Tokai in 2014

Overview

After four years of operation, CROSS-Tokai is now fully engaged in the full range of its mandated activities: proposal selection via an open and transparent assessment process, provision of high-quality user support, and facility utilization promotion within both the academic and industrial research sectors.

At the start FY2014, CROSS-Tokai was supporting the user program on six fully-operational Public Beamlines: BL01 *4SEASONS*, BL02 *DNA*, BL11 PLANET BL15 *TAIKAN*, BL17 *SHARAKU* and BL18 *SENJU*. BL22 *RADEN* had been prepared as the 7th Public Beamline and will be available to users in 2015. For information on the current status and science programs on the Public Beamlines, please see the individual beamline updates in Chapter 3 of this Report.

As the number of Public Beamlines at the MLF continues to increase, and with strong growth in user demand for beamtime, CROSS-Tok0ai has continued to grow as an organization. During FY2014, the total number of CROSS-Tokai staff rose to 62 with five team members being employed: all of them in the Neutron R&D Division and working in direct support of the science program on the beamlines.

The Public Beamlines hosted during FY2014, experiments associated with over 250 research proposals and CROSS-Tokai continued to vigorously promote facility utilization both in Japan and internationally.

CROSS-Tokai 2014 Highlights

- **Dr. Yokomizo became the Director of CROSS-Tokai.**

On 1 June 2014, Dr. Hideaki Yokomizo became the second Director of CROSS-Tokai, succeeding Prof. Yasuhiko Fujii who so ably served in this role for more than three years since CROSS-Tokai began operations in support of the Public Neutron Beam Facility at J-PARC.

Figure 3. An acceptance speech by Director Yokomizo.

- ***Commissioning of RADEN to begin user operations as the 7th Public Beamline from 2015***

From April 1, 2015, BL22 *RADEN* will become the seventh Public Beamline at the MLF and will be made available for user operations for the first time in 2015A.

CROSS-Tokai is proceeding with preparatory work for starting user operations from April 2015 in cooperation with J-PARC.

With the addition of RADEN, the range of scientific fields that can be undertaken on the Public Beamlines has been extended to include the study of visualization of the spatial distribution of crystal structure, nuclides and magnetic domains by neutron transmission imaging and 3D reconstruction.

For more information about *RADEN* and its capabilities, please see the detailed beamline update in Chapter 3 of this report.

Figure 4. A flight tube (Front) and a detector (rear) in RADEN measuring room.

- **Trial Use**

An important part of CROSS-Tokai's work in promoting the utilization of the Public Beamlines is to grow the user community – particularly among industry-based researchers – through outreach and education activities. In addition, from 2012B, CROSS-Tokai has been operating the Trial Use Access Program that aims to assist novice users of neutron-based techniques gain experience and expertise that will allow them to become independent General Use applicants in the future.

The specific objectives of the Trial Use Access Program are:

- To grow the user community and,
- To promote the use and utility of pulsed neutrons through the development and demonstration of innovative new applications

Accordingly, up to a maximum of five percent (5%) of the total beamtime on each of the Public Beamlines at the MLF can be allocated for Trial Use experiments in each round.

Employing the specialist expertise and experience of the CROSS-Tokai Science Coordinators and other appropriate staff, the Trial Use system offers support to prospective users through the whole process of facility utilization including:

- Instrument selection and experiment feasibility assessment
- Proposal preparation
- Experiment design, planning and execution
- Data analysis and interpretation
- Publication of results

The Trial Use program continued to gather pace during Fy2014 with expressions of interest coming from organizations in the industrial and academic sectors. Ultimately, 11 projects were developed into full beamtime proposals and approved by the Selection Committee. A list of the Trial Use proposals approved in FY2014 is given in Table 2. It is particularly pleasing to note the diversity of science and the high degree of academia-industry collaboration that is being encouraged and supported by the Trial Use program.

We look forward to describing in future reports, scientific outcomes from the Trial use program as well as the return of Trial use applicants in future rounds as General Users.

Table 2. Trial Use proposals approved inFY2014.

Round	Beamline	Applicant organization	Industry	Research Area
2014A	BL01 *4SEASONS*	Toyota Motor Corporation	Automotive	Thermoelectric Materials
	BL02 *DNA*	IBARAKI University.	University	Cement
	BL15 *TAIKAN*	JSR Co.	Chemicals	Polymer
	BL15 *TAIKAN*	DNP FINE CHEMICALS Co., Ltd.	Chemicals	Pigment
2014B	BL01 *4SEASONS*	Tokyo Institute of Technology	University	Phase Transitions
	BL02 *DNA*	FC-Cubic	Battery	Fuel Cell
	BL11 *PLANET*	Shinshu University†	University	Carbon Fiber
	BL15 *TAIKAN*	Nagoya Institute of Technology	University	Gel
	BL15 *TAIKAN*	Toray Research Center, Inc.†	Analysis Service	Polymer
	BL17 *SHARAKU*	KONICA MINOLTA, Inc.†	Electric equipment	Film
	BL18 *SENJU*	Tokyo Metropolitan University†	University	Organic Material

† TU experiments approved by the Selection Committee but not carried out due to the Muon facility incident.

Other Key CROSS-Tokai activities FY2014

- **Proposal Selection**
  - Public Beamlines proposal selection for 2014B
    - Call for Proposals (Jun-Jul 2014) – 128 proposals submitted
    - Review by Expert Panels and Proposal Evaluation Committee (31 July-1 Aug, 2014)
    - Selection Committee (21 Aug 2014) – 74 proposals approved (incl. 7 Trial Use and 2 Proprietary Use)
  - Public Beamlines proposal selection for 2015A
    - Call for Proposals (Oct-Nov 2014) – 118 proposals submitted
    - Review by Expert Panels and Proposal Evaluation Committee (16, 19-20 Jan -2014)
    - Selection Committee (27 Jan 2015) – 75 proposals approved (incl. 6 Trial Use and 2 Proprietary Use)

Figure 5. Public beamlines proposal selection for 2014B (Selection Committee, 21 Aug 2014).

  - CROSS Development Proposal Evaluation Panel (25-26 Dec 2014) – 3 one-year proposals approved for FY2015.

- **User Support**

CROSS-Tokai is now supporting user operations and ongoing instrument development activities on the six Public Beamlines with a Neutron R&D team of 38 scientists, programmers, engineers and technicians. Table 2 shows by type and operation period, the number of research proposals supported on the Public Beamlines during FY2014.

In addition to our work at the beamlines, CROSS-Tokai continues to develop and maintain ancillary user facilities in the Ibaraki Quantum Beam Research Center including:

- User Experiment Preparation Laboratories I (Sample processing), II (Hard Matter) and III (Soft Matter & Biomaterials).
- User Data Analysis Room
- User Lounge and "Refresh Rooms"

- **Outreach and Facility Promotion**

Throughout FY2014, CROSS-Tokai has continued to engage in a wide variety of outreach and facility utilization promotion activities. Both independently and in collaboration with other stakeholders in the neutron science community, CROSS-Tokai convened or otherwise supported in more than 20 events designed to inform new potential users about the research possibilities of neutrons, disseminate the latest research results and experimental capabilities and build opportunities for collaboration with other large-scale research facilities.

Table 3. Research proposals supported on the Public Beamlines in FY2014.

		BL01	BL02	BL11	BL15	BL17	BL18	TOTAL
2014A	GU	13	9	11	16	14	7	**70**
	TU	1	1	0	2	0	0	**4**
2014B	GU	12	12	8	15	11	9	**67**
	TU	1	1	1	2	1	1	**7**
Full year	ESI	1	0	0	3	1	0	**5**
	DP	0	1	0	0	0	2	**3**
	PU	3	3	0	5	1	3	**15**
	Instrum.	1	1	1	1	1	1	**6**
TOTAL		**32**	**28**	**21**	**44**	**29**	**23**	**177**

GU: General Use **TU**: Trial Use **ESI**: Element Strategy Initiative
DP: CROSS Development Proposals **PU**: JAEA Project Use **Instrum:** Instrument Group Proposals

User Experiment Preparation Laboratory I | User Experiment Preparation Laboratory II | User Experiment Preparation Laboratory III

User Data Analysis Room | User Lounge | Refresh Rooms

Figure 6. User facilities in the Ibaraki Quantum Beam Research Center.

Highlights of these activities in 2014 included:

- Promotional booths at local and international conferences
- The CROSSroads Workshop Series
- Industrial Applications workshops and user meetings
- Complementary Use workshops
- Research presentations at local and international scientific meetings

For a comprehensive summary of workshops, symposiums, seminars, etc. hosted or supported by CROSS-Tokai in 2014, please see the full listing of events in Chapter 6 of this report.

Beam Operation Status at MLF

In Japanese Fiscal Year (JFY) 2014, the beam operation at the MLF started with a beam power of 300 kW. Figure 1 shows the trend of the beam power and the accumulation of beam power during JFY2014. For the accelerator study, a high power beam of up to 1 MW operated in January, 2015, for several shots of beam.

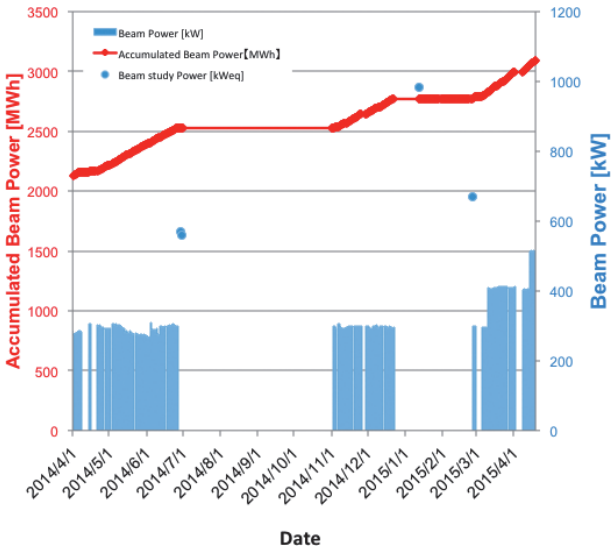

Figure 1. Beam power trend (shown in blue line) at MLF and cumulative beam power (shown in red line) in JFY2014.

Table 1 shows the scheduled time and availability. In JFY2015, we had a good start with relatively high availability in Run #53. During Run #54, a lower availability such as 52% was caused by trouble with the choke transformer of the RCS. Up to end of June, a relatively high availability with 300 kW beam operation was achieved. During the summer shutdown period, the front end of the LINAC such as the ion source and RFQ were replaced to produce 1 MW beam. After the exchange of the mercury target of the MLF, a relatively stable beam operation was performed with 300 kW beam until the end of December. In early January, several shots of beam with 1 MW equivalent beam power were successfully delivered to the mercury targets. On January 16th, a fire incident occurred at the power supply for the muon decay line and as a result the beam operation at Run #60 was completely canceled. After recovering from the incident, a beam operation has started with 400 kW beam power. Although the beam was stopped for 5 days from February 28 to March 4 because the cryogenic system had to be recovered, a relatively high beam availability was achieved. The overall record for JFY2014 shows that about 70% availability was achieved, and the down period was caused mainly by the beam loss during Run #60.

Table 1. Run cycle, scheduled time and availability.

Run #	Date	Scheduled Time (h)	Availability (%)
53	Apr 1 – 7	151	89.7
54	Apr 14 – May 1	382	52.2
55	May 2 – Jun 3	718	91.1
56	Jun 4 – Jun 26	488	87.4
57			nouse
58	Nov 1 – Nov 25	478	79.6
59	Nov 29 – Dec 22	466	96
60	Jan 17 – Feb 17	646	0
61	Feb 18 – Mar 31	790	76.1
Overall		4119	69.1

Users at the MLF

After a long shutdown of the accelerator operation due to an incident at the Hadron Facility, the operation was resumed in January, 2014. Therefore, the combined number of neutron and muon users at the MLF in fiscal year 2014 was the largest ever recorded. On the other hand, there were fewer foreign users of the muon instruments than in the previous fiscal year, which may have been a result of the shutdown of the muon-beam operation due to a fire of a power supply in the muon experimental hall, which occurred in January, 2015. The transition of the number of users at the MLF is summarized in Table and Figure for domestic and foreign users of neutron and muon experimental facilities.

Table 1. The number of Japanese and foreign users in the period of fiscal year.

	FY2008		FY2009		FY2010		FY2011		FY2012		FY2013		FY2014	
	Japanese	Foreigners	Japanese	Foreigners	Japanese	Foreigners	Japanese	Foreigners	Japanese	Foreigners	Japanese	Foreigners	Japanese	Foreigners
Neutron	182		378		529		222		735		520		824	
	161	21	353	25	485	44	198	24	650	85	452	68	755	69
Muon	12		57		55		30		72		77		91	
	12	0	55	2	48	7	28	2	62	10	62	15	88	3

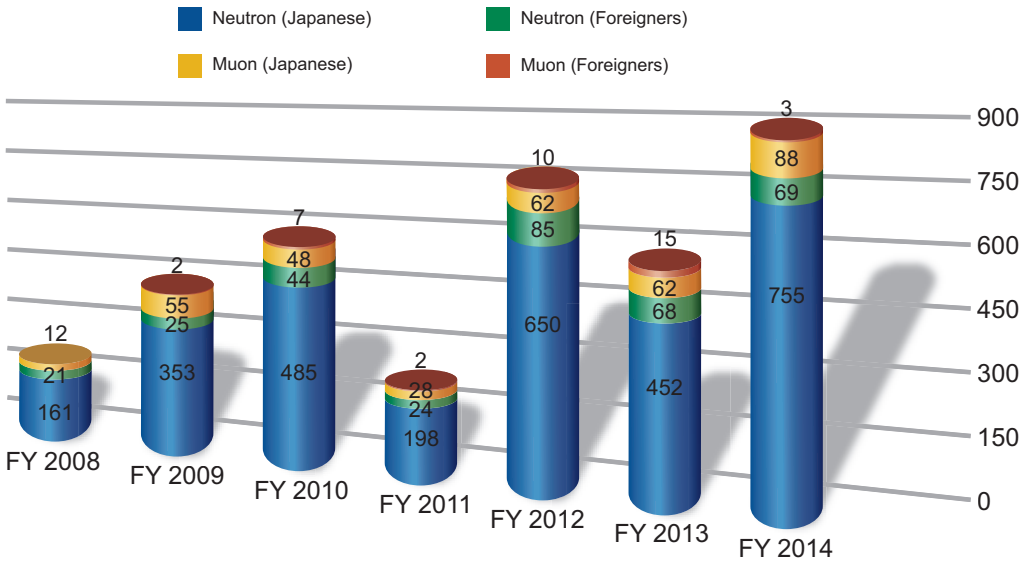

Figure 1. The number of Japanese and foreign users in the period of fiscal year.

MLF Proposals Summary – FY2014

Table 1. Breakdown of Proposals Numbers for the 2014A & 2014B Rounds.

Beam-line	Instrument		2014A		2014B		Full Year					
			Submitted	Approved	Submitted	Approved	Submitted			Approved		
			GU	GU	GU	GU	PU/S	IU	ES	PU/S	IU	ES
BL01	4D-Space Access Neutron Spectrometer - ***4SEASONS***		20 (1)	14 (1)	17 (1)	13 (1)	3	1	1	3	1	1
BL02	Biomolecular Dynamics Spectrometer - ***DNA***		18 (1)	10 (1)	23 (1)	13 (1)	3	2	0	3	2	0
BL03	Ibaraki Biological Crystal Diffractometer - ***iBIX***	(100-β)‡	6	2	8	2	0	0	0	0	0	0
		(β)†	0	0	0	0	15	0	0	9	0	0
BL04	Accurate Neutron-Nucleus Reaction Measurement Instrument - ***ANNRI***		6	6	12	10	1	1	0	1	1	0
BL05	Neutron Optics and Physics - ***NOP***		5	2	3	1	1	0	0	1	0	0
BL08	Super High Resolution Powder Diffractometer - ***S-HRPD***		15	8	14	10	1	0	1	1	0	1
BL09	Special Environment Neutron Power Diffractometer - ***SPICA***		0	0	0	0	1	0	0	1	0	0
BL10	Neutron Beamline for Observation and Research Use - ***NOBORU***		21	10	26	11	2	1	0	2	1	0
BL11	High-Pressure Neutron Diffractometer - ***PLANET***		14	11	9 (1)	9 (1)	0	1	0	0	1	0
BL12	High Resolution Chopper Spectrometer - ***HRC***		9	5	12 (2)	8 (2)	1	0	0	1	0	0
BL14	Cold-neutron Disk-chopper Spectrometer - ***AMATERAS***		21	7	29	9	2	1	2	2	1	2
BL15	Small and Wide Angle Neutron Scattering Instrument - ***TAIKAN***		37 (2)	18 (2)	40	15	5	1	3	5	1	3
BL16	High-Performance Neutron Reflectometer with a horizontal Sample Geometry - ***SOFIA***		11	10	7	7	1	0	0	1	0	0
BL17	Polarized Neutron Reflectometer - ***SHARAKU***		20	14	12 (1)	12 (1)	1	1	1	1	1	1
BL18	Extreme Environment Single Crystal Neutron Diffractometer - ***SENJU***		24	7	25 (1)	10 (1)	3	3	0	3	3	0
BL19	Engineering Diffractometer - ***TAKUMI***		25	15	28	13	3	1	2	3	1	2
BL20	Ibaraki Materials Design Diffractometer - ***iMATERIA***	(100-β)‡	16	7	9	9	0	0	0	0	0	0
		(β)‡	14	14	7	7	14	0	0	13	0	0
BL21	High Intensity Total Diffractometer - ***NOVA***		21	13	14	8	1	0	1	1	0	1
D1	Muon D1		21(1)	16 (1)	34 (2)	16 (2)	0	1	0	0	1	0
D2	Muon D2		11	10	13 (1)	9 (1)	0	1	0	0	1	0
U	Muon U		0	0	0	0	1	0	0	1	0	0
Total			**335**	**199**	**342**	**192**	**59**	**15**	**11**	**52**	**15**	**11**

GU : General Use **PU :** Project Use or Ibaraki Pref. Project Use **S :** S-type Proposals
IU : Instrument Group Use **ES :** Element Strategy
† : Ibaraki Pref. Exclusive Use Beamtime (β = 80% in FY2014)
‡ : J-PARC Center General Use Beamtime (100-β = 20% in FY2014)
( ) : Proposal Numbers under Trial Use Access System or P-type proposals (D1,D2) in GU

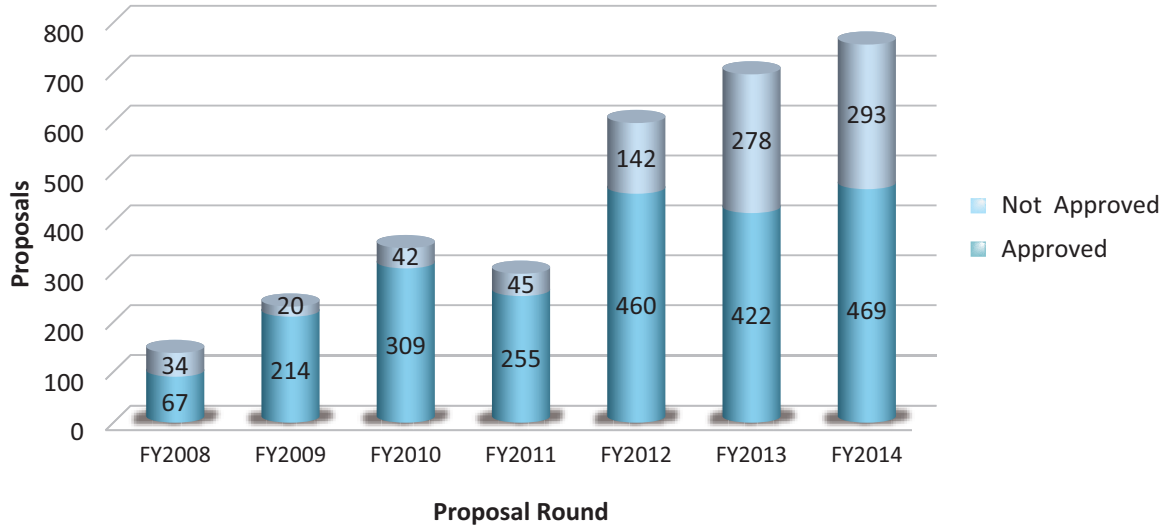

Figure 1. MLF Proposal Numbers over Time.

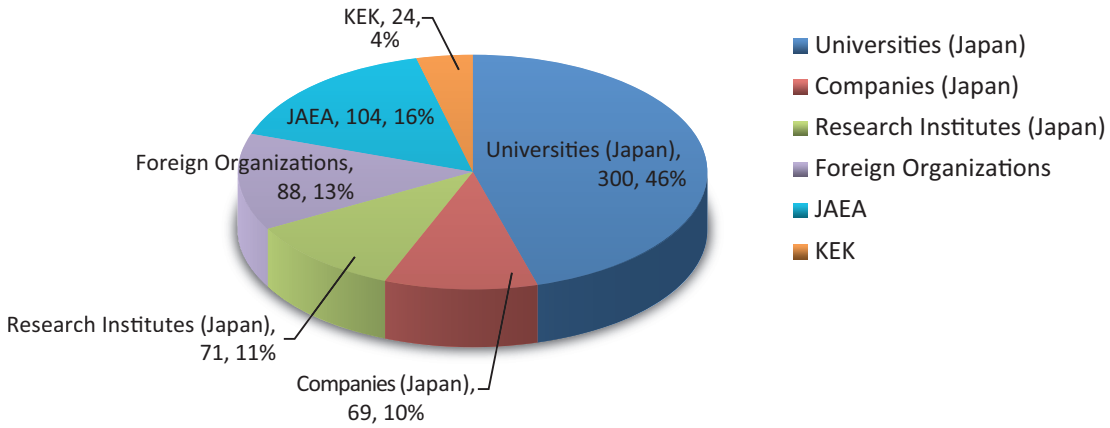

Figure 2. Origin of Submitted Proposals by affiliation - FY2014.

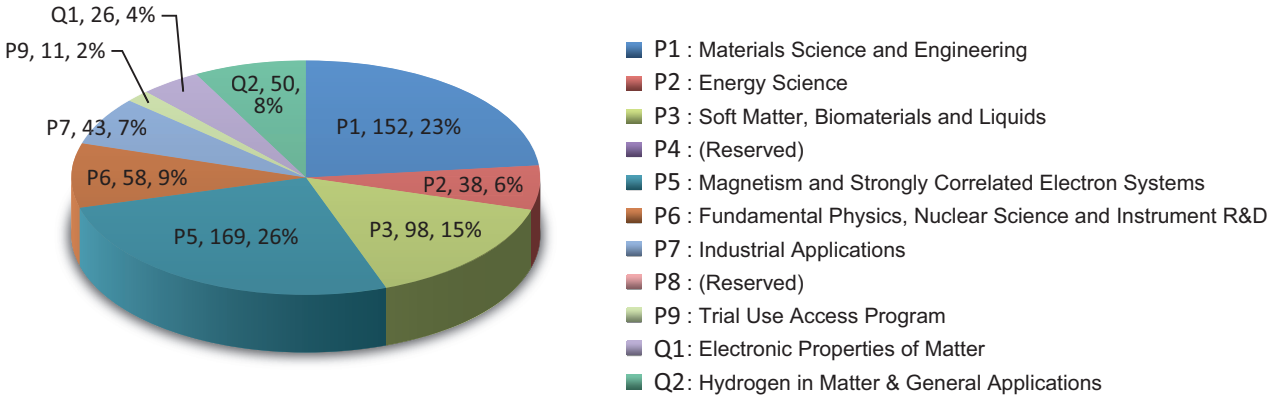

Figure 3. Origin of Submitted Proposals by Sub-committee/Expert Panel – FY2014.

MLF Division Staff 2014

2014 General Meeting of MLF (7 July, 2014)

Head	**Masatoshi Arai**
Deputy Head	**Hideki Seto**
	Masatoshi Futakawa

Neutron Source Section

*: additional duties

<JAEA>

Hiroshi Takada (Leader)
Yoshimi Kasugai (Sub-Leader)
Katsuhiro Haga (Sub-Leader)
Atsushi Akutsu
Katsuhiro Aoyagi
Tomokazu Aso*
Masahide Harada
Shoichi Hasegawa*
Mitsunori Hirane
Miyuki Hoshino
Masato Ida
Kenji Imahashi
Hideaki Ishii
Tetsuya Kai*
Yuuko Kato
Yoshihiko Kawakami
Tomoyuki Kawasakii
Ohtsu Kiichi
Hidetaka Kinoshita
Hiroyuki Kogawa
Shin-ichiro Meigo
Hideki Muto
Takashi Naoe
Norio Narui
Masaaki Nishikawa
Ken-ichi Oikawa*
Motoki Ooi
Kenji Sakai
Masakazu Seki
Hideki Tatsumoto
Makoto Teshigawara
Toshitsugu Uchida
Hideki Ueno
Takashi Wakui
Zhihong Xiong
Shizuka Yoshinari
Usamah Zaid Shahrul Bashah

Neutron Science Section

*: additional duties

<JAEA>

Kenji Nakajima (Leader)
Yukinobu Kawakita (Sub-Leader)
Kazuya Aizawa*
Kazuhiro Aoyama
Satoru Fujiwara*
Hideo Harada*
Masahide Harada*
Stefanus Harjo
Takanori Hattori
Kousuke Hiroi
Tomonori Hosoya
Hiroshi Iikura*
Yasuhiro Inamura
Takaaki Iwahashi
Nobuyuki Iwamoto*
Tetsuya Kai
Ryoichi Kajimoto
Wataru Kambara*
Kouji Kaneko*
Seiko Kawamura
Takuro Kawasaki
Naoko Kawase
Tatsuya Kikuchi
Atsushi Kimura*
Ryoji Kiyanagi
Satoshi Kunieda*
Kazuo Kurihara*
Futoshi Minato*
Hiroshi Nakagawa*
Mitsutaka Nakamura
Shoji Nakamura*
Takashi Ohhara
Ken-ichi Oikawa
Asami Sano*
Mariko Segawa*
Kaoru Shibata
Naoko Shimizu
Takenao Shinohara
Yuhua Su
Kentaro Suzuya
Shin-ichi Takata
Masayasu Takeda*
Tarou Tamada*
Itaru Tamura*
Chiho Tobe
Yousuke Tou*
Shuichi Wakimoto*
Masao Watanabe*

<KEK>

Shinichi Ito (Sub-Leader)
Hideki Seto
Hitoshi Endo
Haruhiro Hiraka
Soshi Ibuka
Kazutaka Ikeda
Takashi Ino
Takashi Kamiyama
Naokatsu Kaneko
Kenji Mishima
Hidetoshi Oshita
Toshiya Otomo
Kaoru Taketani
Shuki Torii
Norifumi Yamada
Tetsuya Yokoo
Masao Yonemura

Technology Development Section

*: additional duties

<JAEA>

Kazuya Aizawa (Leader)
Takayuki Oku (Sub-Leader)
Tomokazu Aso
Chikako Doda
Wu Gong
Katsuhiro Haga*
Yukihiro Ito
Tetsuya Kai*
Wataru Kambara
Yoshimi Kasugai*
Hiroyuki Kogawa*
Kentaro Moriyama
Mitsutaka Nakamura*
Tatsuya Nakamura*
Takeshi Nakatani
Motoki Ohi*
Shino Ono
Kenji Sakai*
Kaoru Sakasai*
Kentaro Suzuya*
Shin-ichi Takata*
Hiromichi Tanaka
Kazue Tanaka
Masao Watanabe
Yasuhiro Yamauchi

<KEK>

Tomohiro Seya
Hiroshi Fujimori*
Takashi Ino*
Naokatsu Kaneko*
Naritoshi Kawamura*
Kenji Kojima*
Shunsuke Makimura*
Masataka Sakaguchi
Setsuo Sato
Kaoru Taketani*
Shuki Torii*
Testuya Yokoo*

Neutron Instrumentation Section

*: additional duties

<JAEA>

Kazuhiko Soyama (Leader)	Katsunori Honda	Kaoru Sakasai
Noriko Amezawa	Ryuji Maruyama	Hiroyuki Suzuki
Kentaro Fuji	Tatsuya Nakamura	Dai Yamazaki
Hirotoshi Hayashida	Takurou Sakai*	Ryo Yasuda*

Muon Science Section

*: additional duties

<KEK>

Yasuhiro Miyake (Leader)	Yasuo Kobayashi	Hirotaka Okabe
Taihei Adachi	Akihiro Koda	Koichiro Shimomura
Hiroshi Fujimori	Kenji Kojima	Patrick Strasser
Koji Hamada	Shunsuke Makimura	Masato Tabe
Masatoshi Hiraishi	Masanori Miyazaki	Soshi Takeshita
Li Hua	Junpei Nakamura	Yutaka Taniguchi
Yutaka Ikedo	Yohei Nakatsugawa	Motonobu Tanpo
Ryosuke Kadono	Yasuhisa Nemoto	Atsushi Yabuuchi
Naritoshi Kawamura	Kusuo Nishiyama	Ichihiro Yamauchi

<JAEA>

Wataru Higemoto*	Takashi Ito*

CROSS-Tokai Staff 2014

Farewell party for Director Fujii (27 May, 2014)

Director **Yasuhiko Fujii (Until May, 2014)**
Hideaki Yokomizo (From June, 2014)

Science Coordinators

Masatoshi Sato
Yoshiaki Fukushima

Neutron R&D Division

Jun-ichi Suzuki (Head)
Kenichi Funakoshi (Head (Deputy))
Jun Abe
Kazuhiro Akutsu
Takayasu Hanashima
Hirotoshi Hayashida
Hideyuki Hiramatsu
Kazuki Iida
Kazuhiko Ikeuchi
Motoyuki Ishikado
Takayoshi Ito
Hiroki Iwase
Kazuya Kamazawa
Satoshi Kasai
Yukihiko Kawamura
Hiroshi Kira
Koji Kiriyama
Makoto Kobayashi
Tetsuya Kuroda
Shinichi Machida
Yoshihiro Matsumoto
Masato Matsuura
Noboru Miyata
Tazuko Mizusawa
Toshiaki Morikawa
Taketo Moyoshi
Koji Munakata
Akiko Nakao
Masashi Obinata
Kazuki Ohishi
Keiichi Ohuchi
Nobuo Okazaki
Joseph Don PARKER
Masae Sahara
Yoshifumi Sakaguchi
Taiki Tominaga
Takeshi Yamada
Shuoyuan Zhang

Health and Safety Division

*: additional duties

Toshiyuki Yamashita (Head)
Yukihiko Kawamura*
Rei Ohuchi*
Koji Kiriyama*

Utilization Promotion Division

Junichi Sato (Head)
Garry John FORAN (Head (Deputy))
Toshiki Asai
Yutaka Ebara
Asami Inoue
Ritsuka Ishikawa
Megumi Kawakami
Junko Ohta
Rei Ohuchi
Sayaka Suzuki
Emi Takaha
Hiroyuki Takasaki
Aya Yamada
Shinichi Yamaguchi

Admin and Finance Division

Yasuo Seishi (Head)
Masaru Yokoyama (Head (Deputy))
Mika Gunji
Takashi Hikita
Mutsumi Shiraishi
Tomoyuki Yabana

Proposals Review System, Committees and Meetings

Proposal Review System

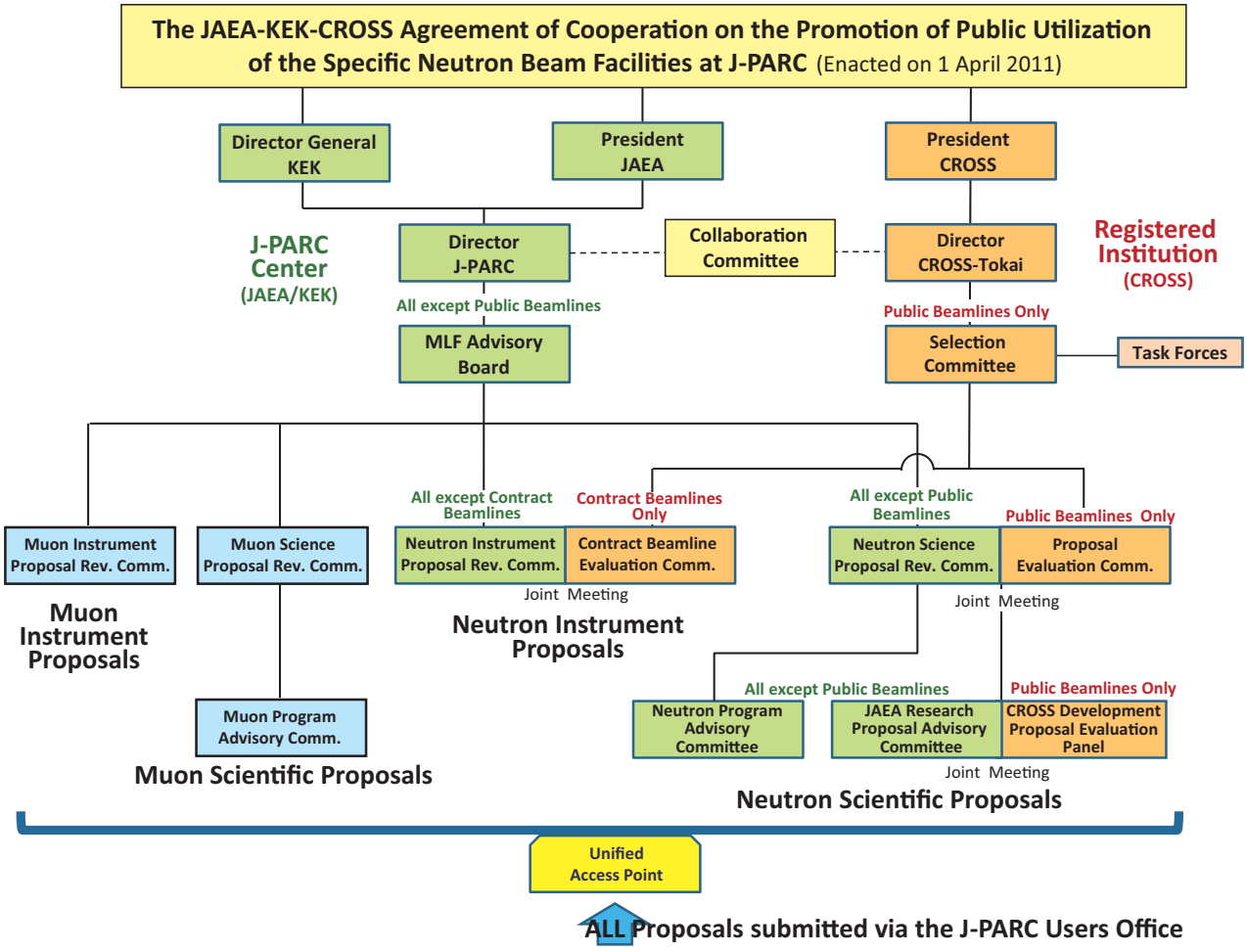

Figure 1. Proposals Review System Framework.

Materials and Life Science Facility Advisory Board

Jun Akimitsu	Aoyama Gakuin University, Japan
Koichiro Asahi	Tokyo Institute of Technology, Japan
Mikio Kataoka	Nara Institute of Science and Technology, Japan
Toshiji Kanaya	Kyoto University, Japan
Taku Sato	Tohoku University, Japan
Mitsuhiro Shibayama (Chair)	The University of Tokyo, Japan
Masaaki Sugiyama	Kyoto University, Japan
Makoto Hayashi	Ibaraki Prefectural Government, Japan
Toshio Yamaguchi (Deputy Chair)	Fukuoka University, Japan
Masahiko Iwasaki	RIKEN, Japan
Youji Koike	Tohoku University, Japan
Jun Sugiyama	Toyota Central R&D Labs., Inc., Japan
Yasuhiko Fujii	Comprehensive Research Organization for Science and Society, Japan
Masatoshi Arai	Japan Atomic Energy Agency, Japan
Takashi Kato	Japan Atomic Energy Agency, Japan
Masatoshi Futakawa	Japan Atomic Energy Agency, Japan
Kazuya Aizawa	Japan Atomic Energy Agency, Japan
Masayasu Takeda	Japan Atomic Energy Agency, Japan
Yukinobu Kawakita	Japan Atomic Energy Agency, Japan
Hideki Seto	High Energy Accelerator Research Organization, Japan
Takashi Kamiyama	High Energy Accelerator Research Organization, Japan
Toshiya Otomo	High Energy Accelerator Research Organization, Japan

Yasuhiro Miyake	High Energy Accelerator Research Organization, Japan
Ryosuke Kadono	High Energy Accelerator Research Organization, Japan
Shinichi Itoh	High Energy Accelerator Research Organization, Japan

Term: through March 31, 2015

Neutron Instrument Proposal Review Committee

Koichiro Asahi	Tokyo Institute of Technology, Japan
Muneyuki Imafuku	Tokyo City University, Japan
Kenji Ohoyama	Tohoku University, Japan
Hideaki Kitazawa	National Institute for Materials Science, Japan
Yoshiaki Kiyanagi	Nagoya University, Japan
Mamoru Sato	Yokohama City University, Japan
Jun-Ichi Suzuki	Comprehensive Research Organization for Science and Society, Japan
Naoya Torikai	Mie University, Japan
Yukio Morii	Radiation Application Development Association, Japan
Yukio Morimoto	Kyoto University, Japan
Hideki Yoshizawa	The University of Tokyo, Japan
Masatoshi Arai	Japan Atomic Energy Agency, Japan
Masatoshi Futakawa	Japan Atomic Energy Agency, Japan
Hideki Seto	High Energy Accelerator Research Organization, Japan
Kenji Nakajima	Japan Atomic Energy Agency, Japan
Takashi Kamiyama	High Energy Accelerator Research Organization, Japan
Toshiya Otomo	High Energy Accelerator Research Organization, Japan

Term: through March 31, 2015

Neutron Science Proposal Review Committee

Yoshiaki Akiniwa	Yokohama National University, Japan
Yukio Noda	Tohoku University, Japan
Jun-Ichi Suzuki	Comprehensive Research Organization for Science and Society, Japan
Masatoshi Futakawa	Japan Atomic Energy Agency, Japan
Hiroyuki Kagi	The University of Tokyo, Japan
Samrath Chaplot	Bhabha Atomic Research entre, India
Anna Paradowska	Australian Nuclear Science and Technology Organisation, Australia
Yasushi Idemoto	Tokyo University of Science, Japan
Takashi Kamiyama	High Energy Accelerator Research Organization, Japan
Yukinobu Kawakita	Japan Atomic Energy Agency, Japan
Toshiya Otomo	High Energy Accelerator Research Organization, Japan
Brendan Kennedy	The University of Sydney, Australia
Sergey Danilkin	Australian Nuclear Science and Technology Organisation, Australia
Masaaki Sugiyama	Kyoto University, Japan
Hideki Seto	High Energy Accelerator Research Organization, Japan
Toshio Yamaguchi	Fukuoka University, Japan
Mamoru Sato	Yokohama City University, Japan
Sung-Min Choi	Korea Advanced Institute of Science and Technology, Korea
Michael James	Australian Synchrotron, Australia
Paul Langan	Oak Ridge National Laboratory, U.S.A
Shinichi Shamoto	Japan Atomic Energy Agency, Japan
Masatoshi Arai	Japan Atomic Energy Agency, Japan
Takahisa Arima	The University of Tokyo, Japan
Shinichi Itoh	High Energy Accelerator Research Organization, Japan
Masaaki Matsuda	Oak Ridge National Laboratory, U.S.A
Je-Geun Park	Seoul National University, Korea
Seung-Hun Lee	University of Virginia, U.S.A
Hirohiko M. Shimizu	Nagoya University, Japan
Yuji Kawabata	Kyoto University, Japan
Yasuhiro Miyake	High Energy Accelerator Research Organization, Japan
Albert Young	North Carolina State University, U.S.A
Guinyun Kim	Kyongpook University, Korea
Koichi Akita	Japan Atomic Energy Agency , Japan
Yukio Morii	Radiation Application Development Association, Japan
Makoto Hayashi	Ibaraki Prefectural Government, Japan
Yoshiaki Fukushima	Comprehensive Research Organization for Science and Society, Japan

Term: through March 31, 2017

Neutron Program Advisory Committee

Koichiro Asahi	Tokyo Institute of Technology, Japan
Kazuaki Iwasa	Tohoku University, Japan
Masaki Azuma	Tokyo Institute of Technology, Japan
Mikio Kataoka	Nara Institute of Science and Technology, Japan
Toshiji Kanaya	Kyoto University, Japan
Michihiro Furusaka	Hokkaido University, Japan

Yasushi Idemoto	Tokyo University of Science, Japan
Hiroshi Kageyama	Kyoto University, Japan
Masaaki Sugiyama	Kyoto University, Japan
Yukinobu Kawakita	Japan Atomic Energy Agency, Japan
Moritomo Yutaka	University of Tsukuba, Japan
Mitsuhiro Shibayama	The University of Tokyo, Japan
Hirohiko M. Shimizu	Nagoya University, Japan
Hideki Seto	High Energy Accelerator Research Organization, Japan
Toshiya Otomo	High Energy Accelerator Research Organization, Japan
Ryosuke Kadono	High Energy Accelerator Research Organization, Japan
Reiji Kumai	High Energy Accelerator Research Organization, Japan
Noboru Yamamoto	High Energy Accelerator Research Organization, Japan
Youichi Murakami	High Energy Accelerator Research Organization, Japan
Takashi Kamiyama	High Energy Accelerator Research Organization, Japan
Shinichi Itoh	High Energy Accelerator Research Organization, Japan

Term: through March 31, 2015

JAEA Research Proposal Advisory Committee

Toshiya Otomo	High Energy Accelerator Research Organization, Japan
Hiroyuki Kagi	The University of Tokyo, Japan
Toshiji Kanaya	Kyoto University, Japan
Yuji Kawabata	Kyoto University, Japan
Hideaki Kitazawa	National Institute for Materials Science, Japan
Yoshiaki Kiyanagi	Nagoya University, Japan
Takashi Sakuma	Ibaraki University, Japan
Hirohiko M. Shimizu	Nagoya University, Japan
Jun-Ichi Suzuki	Comprehensive Research Organization for Science and Society, Japan
Hideki Seto	High Energy Accelerator Research Organization, Japan
Yo Tomota	Ibaraki University, Japan
Masaki Fujita	Tohoku University, Japan
Takatsugu Masuda	The University of Tokyo, Japan
Youichi Murakami	High Energy Accelerator Research Organization, Japan
Koichi Akita	Japan Atomic Energy Agency , Japan
Masatoshi Arai	Japan Atomic Energy Agency, Japan
Takashi Kato	Japan Atomic Energy Agency, Japan
Yukinobu Kawakita	Japan Atomic Energy Agency, Japan
Shinichi Shamoto	Japan Atomic Energy Agency, Japan
Kenji Nakajima	Japan Atomic Energy Agency, Japan

Term: through March 31, 2017

Muon Instrument Proposal Review Committee

Koichiro Asahi	Tokyo Institute of Technology, Japan
Nobuhiko Nishida	Tokyo Institute of Technology, Japan
Masahiko Iwasaki	RIKEN, Japan
Yoshitaka Kuno	Osaka University, Japan
Kenya Kubo	International Christian University, Japan
Hiroyuki Nojiri	Tohoku University, Japan
Yasunori Yamazaki	RIKEN, Japan
Masatoshi Arai	Japan Atomic Energy Agency, Japan
Takashi Kato	Japan Atomic Energy Agency, Japan
Masatoshi Futakawa	Japan Atomic Energy Agency, Japan
Toru Ogitsu	High Energy Accelerator Research Organization, Japan
Ryosuke Kadono	High Energy Accelerator Research Organization, Japan
Kenji Kojima	High Energy Accelerator Research Organization, Japan
Koichiro Shimomura	High Energy Accelerator Research Organization, Japan
Yasuhiro Miyake	High Energy Accelerator Research Organization, Japan
Wataru Higemoto	Japan Atomic Energy Agency, Japan

Term: through March 31, 2015

Muon Science Proposal Review Committee

Hiroshi Amitsuka (Chair)	Hokkaido University, Japan
Masatoshi Arai	Japan Atomic Energy Agency, Japan
Kazuyoshi Yoshimura	Kyoto University, Japan
Seiji Miyashita	The University of Tokyo , Japan
Ryosuke Kadono	High Energy Accelerator Research Organization, Japan
Reiji Kumai	High Energy Accelerator Research Organization, Japan
Yoji Koike	Tohoku University, Japan
Yoh Kohori	Chiba University, Japan
Yasuo Nozue	Osaka University, Japan
Wataru Higemoto	Japan Atomic Energy Agency, Japan
Kenji Kojima	High Energy Accelerator Research Organization, Japan
Takashi Kamiyama	High Energy Accelerator Research Organization, Japan
Alan Drew	University of London, U.K.
Koichiro Asahi (Chair)	Tokyo Institute of Technology, Japan

Hideki Seto	High Energy Accelerator Research Organization, Japan
Toshiji Kanaya	Kyoto University, Japan
Shinji Tsuneyuki	The University of Tokyo , Japan
Kenya Kubo	International Christian University, Japan
Yoko Sugawara	Kitazato University, Japan
Toshiya Otomo	High Energy Accelerator Research Organization, Japan
Tadashi Koseki	High Energy Accelerator Research Organization, Japan
Masaharu Aoki	Osaka University, Japan
Yasuyuki Matsuda	The University of Tokyo , Japan
Yuichiro Nagame	Japan Atomic Energy Agency, Japan
Koichiro Shimomura	High Energy Accelerator Research Organization, Japan
Roderick Macrae	Marian University, U.S.A, Japan
Yasuhiro Miyake	High Energy Accelerator Research Organization, Japan

Term: through March 31, 2015

Muon Program Advisory Committee

Masaharu Aoki	Osaka University, Japan
Koichiro Asahi	Tokyo Institute of Technology, Japan
Hiroshi Amitsuka	Hokkaido University, Japan
Masatoshi Arai	Japan Atomic Energy Agency, Japan
Toshiji Kanaya	Kyoto University, Japan
Kenya Kubo	International Christian University, Japan
Youji Koike	Tohoku University, Japan
Yoh Kohori	Chiba University, Japan
Yoko Sugawara	Kitazato University, Japan
Shinji Tsuneyuki	The University of Tokyo , Japan
Yasuo Nozue	Osaka University, Japan
Kazuyoshi Yoshimura	Kyoto University, Japan
Wataru Higemoto	Japan Atomic Energy Agency, Japan
Yasuyuki Matsuda	The University of Tokyo , Japan
Seiji Miyashita	The University of Tokyo , Japan
Hideki Seto	High Energy Accelerator Research Organization, Japan
Toshiya Otomo	High Energy Accelerator Research Organization, Japan
Ryosuke Kadono	High Energy Accelerator Research Organization, Japan
Reiji Kumai	High Energy Accelerator Research Organization, Japan
Tadashi Koseki	High Energy Accelerator Research Organization, Japan
Yasuhiro Miyake	High Energy Accelerator Research Organization, Japan
Kenji Kojima	High Energy Accelerator Research Organization, Japan
Koichiro Shimomura	High Energy Accelerator Research Organization, Japan

Term: through March 31, 2015

Selection Committee (CROSS)

Toshio Akai	Mitubishi Rayon co.,Ltd., Japan
Jun Akimitsu	Aoyama Gakuin University, Japan
Koichiro Asahi	Tokyo Institute of Technology, Japan
Mikio Kataoka	Nara Institute of Science and Technology, Japan
Toshiji Kanaya	Kyoto University, Japan
Shin-Ichi Kamei	Mitubishi Reserch Institute, Inc., Japan
Naoki Kishimoto	National Institute for Materials Science, Japan
Taku Sato	Tohoku University, Japan
Mitsuhiro Shibayama	The University of Tokyo, Japan
Masaaki Sugiyama	Kyoto University, Japan
Masaki Takada	RIKEN, Japan
Kiyoyuki Terakura	National Institute of Advanced Industrial Science and Technology, Japan
Kazumi Nishijima	Mochida Pharmaceutical co.,Ltd., Japan
Makoto Hayashi	Ibaraki Prefectural Government, Japan
Hidetoshi Fukuyama	Tokyo University of Science, Japan
Toshio Yamaguchi	Fukuoka University, Japan

Term: through March 31, 2015

Proposal Evaluation Committee (CROSS)

Yoshiaki Akiniwa	Yokohama National University, Japan
Yukio Noda	Tohoku University, Japan
Jun-ichi Suzuki	Comprehensive Research Organization for Science and Society, Japan
Hiroyuki Kagi	The University of Tokyo, Japan
Samrath Chaplot	Bhabha Atomic Research entre, India
Anna Paradowska	Australian Nuclear Science and Technology Organisation, Australia
Yasushi Idemoto	Tokyo University of Science, Japan
Brendan Kennedy	The University of Sydney, Australia
Sergey Danilkin	Australian Nuclear Science and Technology Organisation, Australia
Masaaki Sugiyama	Kyoto University, Japan
Toshio Yamaguchi	Fukuoka University, Japan
Mamoru Sato	Yokohama City University, Japan

Sung-Min Choi	Korea Advanced Institute of Science and Technology, Korea
Michael James	Australian Synchrotron, Australia
Paul Langan	Oak Ridge National Laboratory, U.S.A
Takahisa Arima	The University of Tokyo, Japan
Masaaki Matsuda	Oak Ridge National Laboratory, U.S.A
Je-Geun Park	Seoul National University, Korea
Seung-Hun Lee	University of Virginia, U.S.A
Hirohiko M. Shimizu	Nagoya University, Japan
Yuji Kawabata	Kyoto University, Japan
Albert Young	North Carolina State University, U.S.A
Guinyun Kim	Kyongpook University, Korea
Yukio Morii	Radiation Application Development Association, Japan
Makoto Hayashi	Ibaraki Prefectural Government, Japan
Yoshiaki Fukushima	Comprehensive Research Organization for Science and Society, Japan

Term: through March 31, 2017

CROSS Development Proposal Evaluation Panel

Hiroyuki Kagi	The University of Tokyo, Japan
Toshiji Kanaya	Kyoto University, Japan
Yuji Kawabata	Kyoto University, Japan
Hideaki Kitazawa	National Institute for Materials Science, Japan
Yoshiaki Kiyanagi	Nagoya University, Japan
Takashi Sakuma	Ibaraki University, Japan
Hirohiko M. Shimizu	Nagoya University, Japan
Jun-ichi Suzuki	Comprehensive Research Organization for Science and Society, Japan
Yo Tomota	Ibaraki University, Japan
Masaki Fujita	Tohoku University, Japan
Takatsugu Masuda	The University of Tokyo, Japan

Term: through March 31, 2017

Neutron Advisory Committee (NAC)

NAC-2015 convened 9-10 February, 2015 at the IBARAKI Quantum Beam Research Center, Tokai

Group photo of NAC-2015

Neutron Advisory Committee (9-10 Feb. 2015)

Robert McGreevy (chair)	Rutherford Appleton Laboratory
Dimitri Argyriou	European Spallation Source
Bertrand Blau	Paul Scherrer Institute
John D Galambos	Oak Ridge National Laboratory
Toshiji Kanaya	Kyoto University
Yoshiaki Kiyanagi	Nagoya University
Chang Hee Lee	Korea Atomic Energy Research Institute
Dan Alan Neumann	National Institute of Standards and Technology
Jamie Schulz	Australian Nuclear Science and Technology Organization
Mitsuhiro Shibayama	The University of Tokyo

Muon Advisory Committee (MAC)

MAC-2014 convened 11-12 February, 2015 at the KEK Tokai Campus, Tokai

Muon Advisory Committee (11-12 Feb. 2015)

Elvezio Morenzoni (Chair)	Paul Scherrer Institute
Toshiyuki Azuma	RIKEN
Klaus Jungmann	University of Groningen
Kenya Kubo	International Christian University
Yasuo Nozue	Osaka University
Francis Pratt	ISIS
Jeff Sonier	Simon Fraser University
Jun Sugiyama	Toyota Central R & D Labs. Inc.

Workshops, Conferences, Seminars and Schools in 2014

With the increasing level of science activity at the facility, the number and scope of research workshop held under the auspices of the MLF rapidly expanded in 2014.

International Symposiums held jointly by J-PARC MLF and CROSS-Tokai

The 2nd International Symposium on Science at J-PARC

12-15 Jul. 2014, Tsukuba International Congress Center, Ibaraki

Group Photo of The 2nd International Symposium on Science at J-PARC

New Opportunities for Better User Group Software 2014 (NOBUGS 2014)

24-26 Sep. 2014, KEK Tsukuba campus, Ibaraki

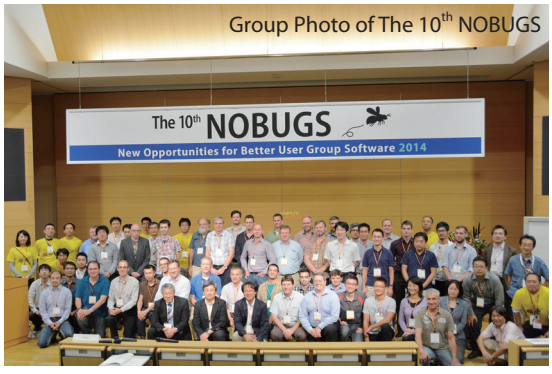

Group Photo of The 10th NOBUGS

International Collaboration on Advanced Neutron Sources XXI (ICANS XXI)

29 Sep. - 3 Oct. 2014, Ibaraki Prefectural Culture Center, Ibaraki

Group Photo of ICANS XXI

The 14th Korea-Japan Meeting on Neutron Science

7-9 Jan. 2015, IBARAKI Quantum Beam Research Center, Ibaraki

Group Photo of The 14th Korea-Japan Meeting on Neutron Science

Conferences held jointly by J-PARC MLF and CROSS-Tokai

The 3rd IMSS Science Festa, The 6th MLF symposium and The 32th PF symposium

17-18 Mar. 2015, Tsukuba International Congress Center, Ibaraki

Group Photo of The 3rd IMSS Science Festa

Workshops held by KEK

5th Progress report meeting of J-PARC MUSE

26 May 2014, KEK Tokai campus, Ibaraki

Workshop for neutron reflectometry

20 Oct. 2014, KCD Hall, Tokyo

Workshop for neutron reflectometry (BL16)

10-11 Nov. 2014, Research Center for Nuclear Physics, Osaka University, Osaka

Workshop for neutron total scattering (BL21)
26 Nov. 2014, KEK Tsukuba campus, Ibaraki

Workshop for neutron spin echo (BL06)
27 Nov. 2014, KEK Tokai campus, Ibaraki

Workshop for neutron inelastic scattering (BL12)
27 Nov. 2014, KEK Tokai campus, Ibaraki

Workshop for polarized neutron scattering (BL23)
18 Dec. 2014, KEK Tsukuba campus, Ibaraki

Workshop for neutron diffraction (BL08, 09)
5 Jan. 2015, KEK Tsukuba campus, Ibaraki

Workshops held by CROSS-Tokai

The 11th CROSSroads of Users and J-PARC "Functional Interfaces and Reactive Surfaces II"
18-19 Aug. 2014, IBARAKI Quantum Beam Research Center, Ibaraki


Group Photo of The 11th CROSSroads of Users and J-PARC

The 12th CROSSroads of Users and J-PARC "Characterizing the structure and functionality of inhomogeneous materials using quantum beams"
16-17 Sep. 2014, IBARAKI Quantum Beam Research Center, Ibaraki


Photo of The 12nd CROSSroads of Users and J-PARC

The 13th CROSSroads of Users and J-PARC "Physics of the strongly correlated electron systems"
2-3 Dec. 2014, IBARAKI Quantum Beam Research Center, Ibaraki

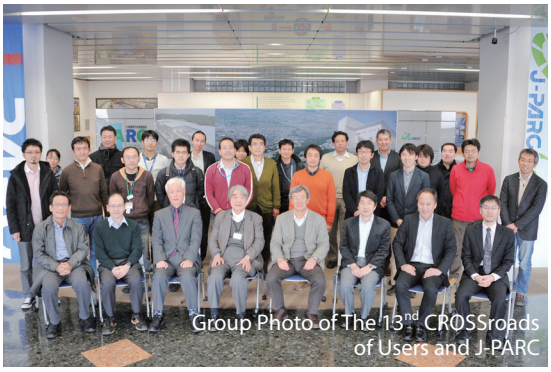
Group Photo of The 13nd CROSSroads of Users and J-PARC

The 14th CROSSroads of Users and J-PARC "Spin liquids and frustration"
3-4 Feb. 2015, IBARAKI Quantum Beam Research Center, Ibaraki


Photo of The 14th CROSSroads of Users and J-PARC

Workshops and Seminars held by CROSS-Tokai and other organizations

2014 Workshop on Materials Science
29 Jul. 2014 Essam Kanda Hall, Tokyo

1st 2014 Workshop on Structural Biology
3 Oct. 2014, Essam Kanda Hall, Tokyo

2014 Workshop on Metallographic Structure
8 Oct. 2014, KENKYUSHA EIGO Center, Tokyo

2013 The CROSS Trial Use and Ibaraki Beam Line Users Meeting
22 Oct. 2014, Kagaku-kaikan Hall, Tokyo

Ibaraki Society for Promotion of Use of Neutrons 2014 Meeting of Magnetic Materials
23 Oct. 2014 Essam Kanda Hall, Tokyo

1st 2014 Workshop on Residual Stress and Strain
28 Oct. 2014, KENKYUSHA EIGO Center, Tokyo

2014 Workshop on Surfaces and Interfaces
6 Nov. 2014, KENKYUSHA EIGO Center, Tokyo

2014 Workshop on Non-destructive Visualization and Analysis Methods
25 Nov. 2014, Osaka Science & Technology Center, Osaka

2013 Workshop on Battery Materials
2 Dec. 2014, Essam Kanda Hall, Tokyo

2013 Workshop on Neutron Science 2014
3 Dec. 2014, KENKYUSHA EIGO Center, Tokyo

Japanese Society for Neutron Science 2014
11-12 Dec. 2014, HOKKAIDO Citizens Actives Center, Hokkaido

2014 Workshop on Magnetic Materials
25 Dec. 2014, KENKYUSHA EIGO Center, Tokyo

2013 Workshop on Organic and Polymeric Materials Neutron Structure Elucidation
5 Feb. 2015, KENKYUSHA EIGO Center, Tokyo

Seminar about the Industrial Application by the Complementarity Use of Synchrotron Radiation and the Neutron in Hakata
20 Feb. 2015, TKP Conference City, Hakata

Workshop on Computational Science
21 Feb. 2015, Osaka University Nakanoshima Center, Osaka

6th Workshop on Analytical Methods in Small Angle Scattering
2 Mar. 2015, Tokyo Office of Kyoto University, Tokyo

2nd 2014 Workshop on Residual Stress and Strain
5 Mar. 2015, Essam Kanda Hall, Tokyo

2014 Workshop on Soft Matter Neutron Scattering
12 Mar. 2015, KENKYUSHA EIGO Center, Tokyo

2nd 2014 Workshop on Structural Biology
26 Mar. 2015, KENKYUSHA EIGO Center, Tokyo

Z-Code Training Course
30-31 Mar. 2015, LMJ Tokyo, Tokyo

Schools in 2014

MLF School 2014
16-19 Dec. 2014, IBARAKI Quantum Beam Research Center, Ibaraki

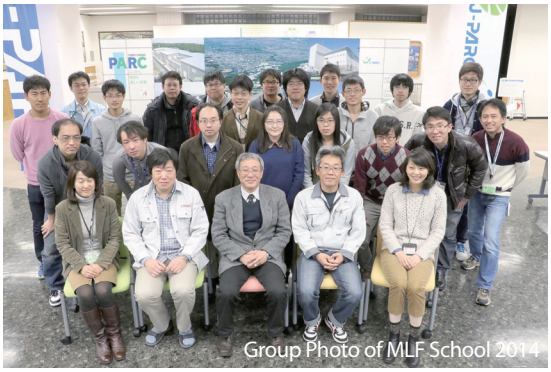

Group Photo of MLF School 2014

The 8th KEK Summer Challenge
19-27 Aug. 2014, KEK Tsukuba Campus, Ibaraki

Group Photo of the 8th KEK Summer Challenge
Credit : KEK

Award List

The Commendation for Science and Technology by the Minister of Education, Culture, Sports, Science and Technology (MEXT), The Young Scientists' Prize
Research on Hydrogen Bonds and the Isotope Effect in Minerals in the Earth's Deep Interior
Asami Sano (JAEA), April 2014

13th International Conference on Muon Spin Rotation, Relaxation and Resonance, Best Poster Award
Anomalous ^{63}Cu Knight shift in thiospinel $CuIr_2S_4$
Ichihiro Yamauchi(JAEA), June 2014

63rd Annual Denver X-ray Conference, Best XRF Poster Award
X-ray Fluorescence Imaging of Growing Chemical Patterns
Kenji Sakurai (NIMS) and Tazuko Mizusawa (CROSS), July 2014

NOBUGS Poster Award
Visualization and Data Processing Software for SENJU - Time-of-Flight Single Crystal Neutron Diffractometer at J-PARC
Takayasu Hanashima (CROSS), September 2014

JAEA President's Awards 2014
Developments of Pressure Wave Mitigation and In-situ Damage Diagnostic Techniques for the World Most Powerful Pulsed Spallation Neutron Source
Masatoshi Futagawa, Katsuhiro Haga, Hiroyuki Kogawa, Takashi Wakui, Takashi Naoe, Makoto Teshigawara, Hidetaka Kinoshita, Masahide Harada, Shin-ichiro Meigo, Motoki Ooi, Shinichi Sakamoto(JAEA) and Hiroshi Fujimori(KEK), October 2014

JAEA President's Awards 2014
Inelastic Scattering Study of Material by Complementary Use of Quantum Beams
Kenji Ishii (JAEA) and Ryoichi Kajimoto (JAEA), October 2014

The JSNS Encouragement Prizes
Development of Horizontal Type Neutron Reflectometer SOFIA in J-PARC
Norifumi Yamada (KEK), December 2014

The JSNS Encouragement Prizes
Dynamics and Hydration of Bio-molecules Studied by Neutron Incoherent Scattering and Molecular Simulation
Hiroshi Nakagawa (JAEA), December 2014

JSME Medal for New Technology
Development of Techniques Using Microbubbles to Curb Pressure Waves in Liquid Metal in order to Realize a High-Intensity Pulsed Neutron Source
Futagawa Masatoshi, Katsuhiro Haga, Hiroyuki Kogawa, Takashi Wakui and Takashi Naoe (JAEA), March 2015

MLF Publication 2014

1 R. Kiyanagi, Y. Matsuo, Y. Ishikawa, Y. Noda, T. Ohhara, T. Kawasaki, K. Oikawa, K. Kaneko, I. Tamura, T. Hanashima, K. Munakata, A. Nakao, and Y. Kawakita
Proton conduction mechanism and phase transition of $(Rb,K)_3H(SeO_4)_2$
Acta Crystallographica **A70** C1359 (2014)

2 K. Munakata, A. Nakao, T. Osakabe, R. Kiyanagi, K. Kaneko, T. Ohhara, T. Hanashima, K. Oikawa, I. Tamura, T. Kawasaki, K. Komatsu, and Y. Uwatoko
High-pressure environments of single crystal neutron diffractometer SENJU/J-PARC
Acta Crystallographica **A70** C273 (2014)

3 A. Nakao, R. Kumai, S. Horiuchi, Y. Tokura, T. Ohhara, T. Hanashima, K. Munakata, R. Kiyanagi, T. Kawasaki, K. Oikawa, K. Kaneko, and I. Mamura
Structural Study of Ferroelectric Phase in Acid-Base Supramolecule
Acta Crystallographica **A70** C553 (2014)

4 Y. Noda, R. Kiyanagi, T. Ohhara, T. Kawasaki, K. Oikawa, K. Kaneko, I. Tamura, T. Hanashima, T. Moyoshi, A. Nakao, K. Munakata, and T. Kuroda
Precision of the single crystal neutron diffractometer SENJU at J-PARC
Acta Crystallographica **A70** C400 (2014)

5 T. Ohhara, R. Kiyanagi, K. Kaneko, T. Kawasaki, K. Oikawa, I. Tamura, A. Nakao, T. Hanashima, K. Munakata, T. Moyoshi, T. Kuroda, Y. Yamauchi, and S. Kawamura
SENJU, Extreme Environment Single Crystal Neutron Diffractometer at J-PARC
Acta Crystallographica **A70** C163 (2014)

6 S. Ohisa, G. Matsuba, N. L. Yamada, Y.-J. Pu, H. Sasabe, and J. Kido
Precise Evaluation of Angstrom-Ordered Mixed Interfaces in Solution-Processed OLEDs by Neutron Reflectometry
Advanced Materials Interfaces **1** 9 1400097 (2014)

7 Z. H. Xiong, M. Futakawa, T. Naoe, and K. Maekawa
Very High Cycle Fatigue in Pulsed High Power Spallation Neutron Source
Advanced Materials Research **891** 536-541 (2014)

8 H. Tatsumoto, Y. Shirai, M. Shiotsu, K. Hata, Y. Naruo, H. Kobayasi, and Y. Inatani
Forced convection heat transfer of saturated liquid hydrogen in vertically-mounted heated pipes
AIP Conference Proceedings **1573** 44-51 (2014)

9 H. Tatsumoto, K. Ohtsu, T. Aso, Y. Kawakami, and M. Teshigawara
Operational characteristics of the J-PARC cryogenic hydrogen system for a spallation neutron source
AIP Conference Proceedings **1573** 66-73 (2014)

10 T. Ishii, H. Kojitani, S. Tsukamoto, K. Fujino, D. Mori, Y. Inaguma, N. Tsujino, T. Yoshino, D. Yamazaki, Y. Higo, K. Funakoshi, and M. Akaogi
High-Pressure Phase Transitions in $FeCr_2O_4$ and Structure Analysis of New Post-Spinel $FeCr_2O_4$ and $Fe_2Cr_2O_5$ Phases with Meteoritical and Petrological Implications
American Mineralogist **99** 1788-1797 (2014)

11 Y. Toh, M. Ebihara, A. Kimura, S. Nakamura, H. Harada, K. Y. Hara, M. Koizumi, F. Kitatani, and K. Furutaka
Synergistic Effect of Combining Two Nondestructive Analytical Methods for Multielemental Analysis
Analytical Chemistry **86** 24 12030-12036 (2014)

12 M. Futakawa
Proton Bombardment in Mercury Target for Neutron Production - Impact dynamics on interface between liquid and solid metals -
Applied Mechanics and Materials **566** 26-33 (2014)

13 T. Naoe, and M. Futakawa
Dynamic Behavior of Liquid Mercury Droplets Colliding with a Solid Surface
Applied Mechanics and Materials **566** 391-396 (2014)

14 T. Wan, T. Naoe, T. Wakui, M. Futakawa, and K. Maekawa
Damage Evaluation by Impulsive Response in Structure Filled with Liquid
Applied Mechanics and Materials **566** 629-636 (2014)

15 T. Yamaguchi, T. Fukuda, T. Kakeshita, S. Harjo, and T. Nakamoto
Neutron diffraction study on very high elastic strain of 6% in an Fe_3Pt under compressive stress
Applied Physics Letters **104** 23 231908 (2014)

16 Y. Fujii
An Overview of the Neutron Facilities and the Neutron Scattering Community in the Asia-Oceania Region
Association of Asia Pacific Physical Societies **24** 2 3-6 (2014)

17 K. Akutsu and T. Ohhara
Application and outlook of the pulsed neutron beam at J-PARC, 1; Introduction of neutron beam and neutron crystallography at J-PARC
BUNSEKI **2014** 11 617-621 (2014)

18 Y. Sakaguchi, H. Asaoka, Y. Uozumi, Y. Kawakita, T. Ito, M. Kubota, D. Yamazaki, K. Soyama, M. Ailavajhala, M. R. Latif, and M. Mitkova
Studies of Silver Photodiffusion Dynamics in Ag/Ge_xS_{1-x} (x = 0.2 and 0.4) Films Using Neutron Reflectometry
Canadian Journal of Physics **92** 654-658 (2014)

19 J. Yoshida, A. Ueda, A. Nakao, R. Kumai, H. Nakao, Y. Murakami, and H. Mori
Solid-Solid Phase Interconversion in an Organic Conductor Crystal: Hydrogen-Bond-Mediated Dynamic Changes in P-Stacked Molecular Arrangement and Physical Properties
Chemical Communications **50** 15557-15560 (2014)

20 S. C. Lee, A. Ueda, A. Nakao, R. Kumai, H. Nakao, Y. Murakami, and H. Mori
Protonation of Pyridyl-Substituted TTF Derivatives: Substituent Effects in Solution and in the Proton–Electron Correlated Charge-Transfer Complexes
Chemistry - A European Journal **20** 7 1909-1917 (2014)

21 K. Fujii, Y. Esaki, K. Omoto, M. Yashima, A. Hoshikawa, T. Ishigaki, and J. R. Hester
New Perovskite-Related Structure Family of Oxide-Ion Conducting Materials $NdBaInO_4$
Chemistry of Materials **26** 8 2488-2491 (2014)

22 I. Qasim, P. E. R. Blanchard, B. J. Kennedy, C. D. Ling, L.-Y. Jang, T. Kamiyama, P. Miao, and S. Torii
Soft ferromagnetism in mixed valence $Sr_{1-x}La_xTi_{0.5}Mn_{0.5}O_3$ perovskites
Dalton Transactions **43** 18 6909-6918 (2014)

23 M. Futakawa, T. Naoe, H. Kogawa, K. Haga, and K. Okita

Cavitation erosion induced by proton beam bombarding mercury target for high-power spallation neutron sources
Experimental Thermal and Fluid Science **57** 365-370 (2014)

24 A. M. Dymshits, K. D. Litasov, I. S. Sharygin, A. Shatskiy, E. Ohtani, A. Suzuki, and K. Funakoshi
Thermal Equation of State of Majoritic Knorringite and Its Significance for Continental Upper Mantle
Featured in Journal of Geophysical Research: Solid Earth **119** 8034-8046 (2014)

25 N. Purevjav, T. Okuchi, N. Tomioka, J. Abe, and S. Harjo
Hydrogen site analysis of hydrous ringwoodite in mantle transition zone by pulsed neutron diffraction
Geophysical Research Letters **41** 19 6718-6724 (2014)

26 Y. Fujii and T. Kamiyama
Evolution of Neutron Crystallography in Japan
Hamon **24** 2 132-140 (2014)

27 S. Iimura
Switching of Intra-orbital Spin Excitations in Electron-doped Iron Pnictide Superconductors
Hamon **24** 2 121-125 (2014)

28 T. Kume, S. Yamada, and M. Onoo
Structural Change of Human Stratum Corneum by the Treatment of Surfactant Solutions Studied using Neutron Scattering
Hamon **24** 1 15-19 (2014)

29 K. Nakajima, S. Kawamura, and M. Nakamura
Development of ^{3}He Neutron Spin Filter for the Application at an Intense Pulsed Neutron Source Facility
Hamon **24** 2 115-120 (2014)

30 H. Nozaki
Ion Conducting Behavior in Secondary Battery Materials Detected by Quasi-elastic Neutron Scattering Measurements
Hamon **24** 1 1 6-10 (2014)

31 T. Oku, H. Kira, H. Hayashida, K. Sakai, K. Hiroi, T. Shinohara, T. Ino, M. Ohkawara, K. Ohoyama, S. Takata, K. Ohishi, H. Iwase, N. Miyata, K. Akutsu, Y. Sakaguchi, M. Takeda, J. Suzuki, K. Aizawa, M. Arai, and K. Kakurai
Development of ^{3}He Neutron Spin Filter for the Application at an Intense Pulsed Neutron Source Facility
Hamon **24** 4 250-257 (2014)

32 Y. Sakaguchi
SKIN2014 Studying Kinetics with Neutrons (SANS and Reflectometry)
Hamon **24** 3 215 (2014)

33 T. Shinohara
Development of the Magnetic Field Imaging using Polarized Pulsed Neutrons
Hamon **24** 2 100-105 (2014)

34 H. Sueyoshi, N. Ishikawa, K. Yamada, K. Sato, T. Nakagaito, H. Matsuda, Y. Arakaki, and Y. Tomota
Steel Research using Neutron Beam Techniques / ~In-situ Neutron Diffraction, Small-angle Neutron Scattering and Residual Stress Analysis~
Hamon **24** 1 34-39 (2014)

35 S.-i. Takata, J.-i. Suzuki, K. Ohishi, H. Iwase, T. Shinohara, T. Oku, T. Tominaga, Y. Inamura, T. Ito, T. Nakatani, K. Suzuya, K. Aizawa, T. Otomo, M. Sugiyama, and M. Arai
The Small and Wide Angle Neutron Scattering Instrument TAIKAN at J-PARC
Hamon **24** 4 281-287 (2014)

36 Y. Tomota
Study on Thermo-mechanically Controlled Processing of Steel using Neutron Diffraction
Hamon **24** 1 40-44 (2014)

37 N. Yamada, M. Takeda, and D. Yamazaki
Neutron Reflectometers in J-PARC
Hamon **24** 4 288-295 (2014)

38 W. Yun
A Study on Phase Stress of Centrifugally Cast Duplex Stainless Steel by Neutron Diffraction
Hamon **24** 1 28-33 (2014)

39 K. Komatsu, S. Klotz, A. Shinozaki, R. Iizuka, L. E. Bove, and H. Kagi
Performance of ceramic anvils for high pressure neutron scattering
High Pressure Research **34** 4 494-499 (2014)

40 T. Okuchi, N. Tomioka, N. Purevjav, J. Abe, S. Harjo, and W. Gong
Structure refinement of sub-cubic-mm volume sample at high pressures by pulsed neutron powder diffraction: application to brucite in an opposed anvil cell
High Pressure Research **34** 2 273-280 (2014)

41 Y. Su, Y. Tomota, S. Harjo, J. Suzuki, and Y. Adachi
In Situ Observations of Microstructural Evolution During Annealing or Deformation in an Electro-Deposited Fine-Grained Iron
In-situ Studies with Photons, Neutrons and Electrons Scattering **II** 131-153 (2014)

42 J. Kim, A. Fujiwara, T. Sawada, Y. Kim, K. Sugimoto, K. Kato, H. Tanaka, M. Ishikado, S. Shamoto, and M. Takata
Evidence of Electronic Polarization of the As Ion in the Superconducting Phase of F-Doped LaFeAsO
International Union of Crystallography Journal **1** 155-159 (2014)

43 M. Futakawa
Material issues relating to high power spallation neutron sources
IOP Conf. Series: Materials Science and Engineering **74** 012011 (2015)

44 H. Terasaki, Y. Shibazaki, K. Nishida, R. Tateyama, S. Takahashi, M. Ishii, Y. Shimoyama, E. Ohtani, K. Funakoshi, and Y. Higo
Repulsive Nature for Hydrogen Incorporation to Fe_3C up to 14 GPa
ISIJ International **54** 2637-2642 (2014)

45 K. Ishii and M. Fujita
Observation of electron dynamics by use of three kinds of quantum beams
Isotope News **728** 10-13 (2014)

46 T. Kai
Recent progress of resonance neutron imaging
Isotope News **727** 16-19 (2014)

47 T. Hemmi
Investigation of Strain Using Neutron Diffraction —A Foundation for Improvement of ITER Conductor Performance
JAEA R&D Review 2014 111 (2014)

48 T. Sato, K. Tomiyasu, K. Ikeda, T. Otomo, M. Feygenson, J. Neuefeind, K. Yamada, and S.-i. Orimo
Local atomic structural investigations of precursory phenomenon of the hydrogen release from $LiAlD_4$
Journal of Alloys and Compounds **586** 244-247 (2014)

49 K. Ono, N. Inami, K. Saito, Y. Takeichi, M. Yano, T. Shoji, A. Manabe, A. Kato, Y. Kaneko, D. Kawana, T. Yokoo, and S. Itoh
Observation of spin-wave dispersion in Nd-Fe-B magnets using neutron Brillouin scattering
Journal of Applied Physics **115** 17 17A714(3) (2014)

50 Y. Yasui, Y. Kawamura, Y. Kobayashi, and M. Sato

Magnetic and dielectric properties of one-dimensional array of S = 1/2 linear trimer system $Na_2Cu_3Ge_4O_{12}$
Journal of Applied Physics **115** 17 E125 (2014)

51 W. Chuajiw, K. Takatori, T. Igarashi, H. Hara, and Y. Fukushima
The influence of aliphatic amines, diamines, and amino acids on the polymorph of calcium carbonate precipitated by the introduction of carbon dioxide gas into calcium hydroxide aqueous suspensions
Journal of Crystal Growth **386** 119-127 (2014)

52 T. Naoe, M. Futakawa, R. G. Kenny, and M. Otsuki
Experimental and numerical investigations of liquid mercury droplet impacts
Journal of Fluid Science and Technology **9** 1 JFST0002-1-12 (2014)

53 T. Mizumoto, D. Tomono, A. Takada, T. Tanimori, S. Komura, H. Kubo, Y. Matsuoka, Y. Mizumura, K. Nakamura, S. Nakamura, M. Oda, J. D. Parker, T. Sawano, N. Bando, and A. Nabetani
A Performance Study of an Electron-Tracking Compton Camera with a Compact System for Environmental Gamma-ray Observation
Journal of Instrumentation **10** C06003 (2014)

54 Y. Mizumura, T. Tanimori, H. Kubo, A. Takada, J. D. Parker, T. Mizumoto, S. Sonoda, D. Tomono, T. Sawano, K. Nakamura, Y. Matsuoka, S. Komura, S. Nakamura, M. Oda, K. Miuchi, S. Kabuki, Y. Kishimoto, S. Kurosawa, and S. Iwaki
Development of a 30 cm-cube Electron-Tracking Compton Camera for the SMILE-II Experiment
Journal of Instrumentation **8** C05045 (2014)

55 T. Nakamura, K. Toh, K. Honda, K. Sakasai, K. Soyama, and M. Katagiri
An empirical formula for calculating the spatial resolution of a wavelength-shifting fibre detector coupled with a ZnS/^{6}LiF scintillator for detecting thermal neutrons
Journal of Instrumentation **9** 11 C11020 (2014)

56 K. Toh, T. Nakamura, K. Sakasai, K. Soyama, and H. Yamagishi
Evaluation of two-dimensional multiwire neutron detector with individual line readout under pulsed neutron irradiation
Journal of Instrumentation **9** 11 C11019 (2014)

57 S. Makimura, N. Kawamura, K. M. Kojima, A. Koda, N. Kurosawa, R. Shimizu, P. Strasser, J. Nakamura, and Y. Miyake
Remote-controlled non-destructive measurement for thermal conductivity of highly radioactive isotropic graphite used as the muon production target at J-PARC/MUSE
Journal of Nuclear Materials **450** 1–3 110-116 (2014)

58 S.-i. Meigo
Conceptual design of proton beam transport system for ADS facilities at J-PARC
Journal of Nuclear Materials **450** 1–3 8-15 (2014)

59 S.-i. Meigo, M. Ooi, M. Harada, H. Kinoshita, and A. Akutsu
Radiation damage and lifetime estimation of the proton beam window at the Japan Spallation Neutron Source
Journal of Nuclear Materials **450** 1–3 141-146 (2014)

60 T. Naoe, M. Teshigawara, T. Wakui, H. Kinoshita, H. Kogawa, K. Haga, and M. Futakawa
Damage inspection of the first mercury target vessel of JSNS
Journal of Nuclear Materials **450** 1–3 123-129 (2014)

61 M. Ooi, M. Teshigawara, M. Harada, T. Naoe, F. Maekawa, and Y. Kasugai
Development of Au–In–Cd decoupler by a hot isostatic pressing (HIP) technique for short pulsed spallation neutron source
Journal of Nuclear Materials **450** 1–3 117-122 (2014)

62 B. W. Riemer, M. W. Wendel, D. K. Felde, R. L. Sangrey, A. Abdou, D. L. West, T. J. Shea, S. Hasegawa, H. Kogawa, T. Naoe, C. H. Farny, and A. L. Kaminsky
Small gas bubble experiment for mitigation of cavitation damage and pressure waves in short-pulse mercury spallation targets
Journal of Nuclear Materials **450** 1–3 192-203 (2014)

63 J. D. Parker, M. Harada, K. Hattori, S. Iwaki, S. Kabuki, Y. Kishimoto, H. Kubo, S. Kurosawa, Y. Matsuoka, K. Miuchi, T. Mizumoto, H. Nishimura, T. Oku, T. Sawano, T. Shinohara, J. Suzuki, A. Takada, T. Tanimori, K. Ueno, M. Ikeno, M. Tanaka, and T. Uchida
Applications of a Micro-Pixel Chamber (μPIC) Based, Time-Resolved Neutron Imaging Detector at Pulsed Neutron Beams
Journal of Physics: Conference Series **502** 012048 (2014)

64 H. Hayashida, K. Soyama, D. Yamazaki, R. Maruyama, and K. Yamamura
Development and demonstration of a multi-channel spheroidal focusing device for neutron beams
Journal of Physics: Conference Series **528** 1 12007 (2014)

65 H. Hayashida, T. Oku, H. Kira, K. Sakai, M. Takeda, Y. Sakaguchi, T. Ino, T. Shinohara, K. Ohoyama, J. Suzuki, K. Kakurai, M. Mizusawa, N. Miyata, D. Yamazaki, R. Maruyama, K. Soyama, and M. Arai
Development and Demonstration of In-situ SEOP ^{3}He Spin Filter System for Neutron Spin Analyzer on the SHARAKU Polarized Neutron Reflectometer at J-PARC
Journal of Physics: Conference Series **528** 1 012020 (2014)

66 S. Hosokawa, J. F. Bérar, N. Boudet, S. Kohara, J. Stellhorn, W. C. Pilgrim, A. Zeidler, H. Kato, Y. Kawakita, and T. Otomo
A combination of anomalous x-ray scattering and neutron diffraction for structural characterizations of Zr_{63} Ni_{25} Al_{12} metallic glass
Journal of Physics: Conference Series **502** 1 12023 (2014)

67 T. Ino, H. Otono, K. Mishima, and T. Yamada
Precision neutron flux measurement with a neutron beam monitor
Journal of Physics: Conference Series **528** 1 12039 (2014)

68 S. Itoh, T. Yokoo, D. Kawana, Y. Kaneko, Y. Tokura, M. Fujita, K. Yoshida, K. Saito, N. Inami, Y. Takeichi, K. Ono, and Y. Endoh
Neutron Brillouin Scattering Experiments with Pulsed Neutrons on High Resolution Chopper Spectrometer HRC
Journal of Physics: Conference Series **502** 1 12043 (2014)

69 S. Itoh, S. Yano, T. Yokoo, S. Satoh, D. Kawana, Y. Kousaka, J. Akimitsu, and Y. Endoh
Spin Waves in Ferromagnetic Phase of MnP
Journal of Physics: Conference Series **502** 1 12044 (2014)

70 R. Kajimoto, M. Fujita, K. Nakajima, K. Ikeuchi, Y. Inamura, M. Nakamura, and T. Imasato
Inelastic neutron scattering study of phonon anomalies in $La_{1.5}Sr_{0.5}NiO_4$
Journal of Physics: Conference Series **502** 1 12056 (2014)

71 N. Kawamura, A. Toyoda, M. Aoki, K. Shimomura, T. Mibe, Y. Nakatsugawa, M. Otani, N. Saito, and Y. Miyake
H line; a beam line for fundamental physics study
Journal of Physics: Conference Series **551** 1 012062 (1-6) (2014)

72 Y. Kobayashi, S. Kototani, M. Itoh, and M. Sato
Emergence of Superconducting and/or Magnetic Ordering Tuned by Fe-Vacancy Order in Alkali Metal Intercalated Fe Chalcogenides
Journal of Physics: Conference Series **568** 022024 (2014)

73 K. M. Kojima, T. Murakami, Y. Takahashi, H. Lee, S. Y. Suzuki, A. Koda, I. Yamauchi, M. Miyazaki, M. Hiraishi, H. Okabe, S. Takeshita, R. Kadono, T. U. Ito, W. Higemoto, S. Kanda, Y. Fukao, N. Saito, M. Saito, M. Ikeno, T. Uchida, and M. M. Tanaka
New μSR spectrometer at J-PARC MUSE based on Kalliope detectors
Journal of Physics: Conference Series **551** 1 012063 (1-6) (2014)

74 R. M. Macrae, C. Upchurch, D. K. Rose, Y. Miyake, A. Koda, J. S. Lord, and P. S. Shuttleworth
Paramagnetic muon states in mesoporous carbon materials
Journal of Physics: Conference Series **551** 1 012040 (1-7) (2014)

75 T. Masui, H. Kishimoto, T. Kikuchi, S. Ohira-Kawamura, Y. Inamura, T. Koga, and K. Nakajima
Quasielastic Neutron Scattering Study on Polymer Nanocomposites
Journal of Physics: Conference Series **502** 1 12057 (2014)

76 P. Miao, S. Torii, M. Yonemura, Y. Ishikawa, J. Zhang, and T. Kamiyama
Structure analysis on small molecular crystal by high resolution neutron powder diffraction
Journal of Physics: Conference Series **502** 1 12055 (2014)

77 K. Mishima, S. Imajo, M. Hino, T. Ino, Y. Iwashita, R. Katayama, M. Kitaguchi, T. Oda, H. M. Shimizu, M. Utsuro, S. Yamashita, and T. Yoshioka
Production of ultra cold neutrons by a doppler shifter with pulsed neutrons at J-PARC
Journal of Physics: Conference Series **528** 1 12030 (2014)

78 Y. Miyake, K. Shimomura, N. Kawamura, P. Strasser, A. Koda, H. Fujimori, Y. Ikedo, S. Makimura, Y. Kobayashi, J. Nakamura, K. M. Kojima, T. Adachi, R. Kadono, S. Takeshita, K. Nishiyama, W. Higemoto, T. Ito, K. Nagamine, H. Ohata, Y. Makida, M. Yoshida, T. Okamura, R. Okada, and T. Ogitsu
Current status of the J-PARC muon facility, MUSE
Journal of Physics: Conference Series **551** 1 012061 (1-7) (2014)

79 M. Miyazaki, R. Kadono, M. Hiraishi, I. Yamauchi, A. Koda, K. M. Kojima, I. Kawasaki, I. Watanabe, Y. Okamoto, and Z. Hiroi
Spin dynamics of Mn pyrochlore lattice in $YMn_2Zn_{20-x}In_x$
cJournal of Physics: Conference Series **551** 1 012019 (1-6) (2014)

80 T. Nakamura, K. Toh, K. Honda, A. Birumachi, M. Ebine, K. Sakasai, K. Soyama, and M. Katagiri
Development of a wavelength-shifting-fibre-based scintillator neutron detector as an alternative to ^{3}He at J-PARC/MLF
Journal of Physics: Conference Series **528** 1 12042 (2014)

81 T. Nakamura, M. Katagiri, N. Tsutsui, K. Toh, N. J. Rhodes, E. M. Schooneveld, H. Ooguri, Y. Noguchi, K. Sakasai, and K. Soyama
Development of a ZnS/$^{10}B_2O_3$scintillator with low-afterglow phosphor
Journal of Physics: Conference Series **528** 1 12043 (2014)

82 J. Nakamura, Y. Oishi, N. Saito, K. Miyazaki, K. Okamura, W. Higemoto, Y. Ikedo, K. M. Kojima, P. Strasser, T. Nagatomo, S. Makimura, Y. Miyake, N. Kawamura, K. Yokoyama, D. Tomono, K. Shimomura, S. Wada, A. Koda, Y. Kobayashi, H. Fujimori, R. Kadono, and K. Nishiyama
Optimal crossed overlap of coherent vacuum ultraviolet radiation and thermal muonium emission for μSR with the Ultra Slow Muon
Journal of Physics: Conference Series **551** 1 012066 (1-6) (2014)

83 J. Nakamura, T. Nagatomo, Y. Oishi, Y. Ikedo, P. Strasser, N. Saito, K. Miyazaki, K. Yokoyama, K. Okamura, Y. Miyake, S. Makimura, K. Nishiyama, K. Shimomura, N. Kawamura, A. Koda, W. Higemoto, S. Wada, M. Iwasaki, and E. Torikai
Ultra Slow Muon Microscope at MUSE / J-PARC
Journal of Physics: Conference Series **502** 1 012042 (1-4) (2014)

84 K. Ohoyama, T. Yokoo, S. Itoh, T. Ino, M. Ohkawara, T. Oku, S. Tasaki, K. Iwasa, T. J. Sato, S. Ishimoto, K. Taketani, H. Kira, Y. Sakaguch, M. Nanbu, H. Hiraka, H. M. Shimizu, M. Takeda, M. Hino, K. Hayashi, M. Kenzelmann, U. Fliges, and P. Hautle
Concepts of Neutron Polarisation Analysis Devices for a New Neutron Chopper Spectrometer, POLANO, in J-PARC
Journal of Physics: Conference Series **502** 1 12051 (2014)

85 T. Okuda, H. Hata, T. Eto, K. Nishina, H. Kuwahara, M. Nakamura, and R. Kajimoto
Effects of Mn Substitution on the Thermoelectric Properties of the Electron-Doped Perovskite $Sr_{1-x}La_xTiO_3$
Journal of Physics: Conference Series **568** 022035 (2014)

86 A. D. Pant, K. Nagamine, I. Shiraki, E. Torikai, K. Shimomura, F. L. Pratt, H. Ariga, K. Ishida, and J. S. Schultz
Muonium response to oxygen content in biological aqueous solutions for cancer research
Journal of Physics: Conference Series **551** 1 012043 (1-6) (2014)

87 K. Sakai, T. Oku, H. Hayashida, H. Kira, T. Shinohara, K. Oikawa, M. Harada, K. Kakurai, K. Aizawa, M. Arai, Y. Sakaguchi, J. Suzuki, T. Ino, and K. Ohoyama
Development of Portable Polarized ^{3}He Spin Flipper for Polarized Neutron Experiment at J-PARC
Journal of Physics: Conference Series **528** 012016 (2014)

88 D. Sakurai, J. Chiba, T. Ino, N. Kakusho, N. Kaneko, R. Katayama, M. Kitaguchi, K. Mishima, S. Muto, K. Ozeki, Y. Seki, H. M. Shimizu, S. Yamashita, T. Yoshioka, and D. Nishimura
Development of a new neutron mirror made of deuterated Diamond-like carbon
Journal of Physics: Conference Series **528** 1 12010 (2014)

89 S. Satoh, N. L. Yamada, and S. Muto
Detector development for a high-flux neutron reflectometer
Journal of Physics: Conference Series **502** 1 12050 (2014)

90 Y. Shirai, K. Hikawa, M. Shiotsu, H. Tatsumoto, Y. Naruo, H. Kobayashi, and Y. Inagaki
Cooling Stability Test of MgB_2 Wire Immersed in Liquid Hydrogen under External Magnetic Field
Journal of Physics: Conference Series **507** 2 22031 (2014)

91 P. Strasser, Y. Ikedo, S. Makimura, J. Nakamura, K. Nishiyama, K. Shimomura, H. Fujimori, T. Adachi, A. Koda, N. Kawamura, Y. Kobayashi, W. Higemoto, T. U. Ito, T. Nagatomo, E. Torikai, R. Kadono, and Y. Miyake
Design and construction of the ultra-slow muon beamline at J-PARC/MUSE
Journal of Physics: Conference Series **551** 1 012065 (1-7) (2014)

92 J. Sugiyama, H. Nozaki, I. Umegaki, M. Harada, Y. Higuchi, E. J. Ansaldo, J. H. Brewer, Y. Miyake, G. Kobayashi, and R. Kanno
Structural, magnetic, and diffusive nature of olivine-type Na_xFePO_4
Journal of Physics: Conference Series **551** 1 012012 (1-7) (2014)

93 T. Suzuki, I. Watanabe, F. Yamada, Y. Ishii, K. Ohishi, T. Goto, and H. Tanaka
Gradual Evolution in Spin Dynamics of $TlCu_{1-x}Mg_xCl_3$ Probed by Muon-Spin Relaxation (μSR) Technique
Journal of Physics: Conference Series **502** 012041 (2014)

94 H. Tatsumoto, Y. Shirai, M. Shiotsu, Y. Naruo, H. Kobayashi, and Y. Inatani
Development of an experimental system for characterization of high-temperature superconductors cooled by liquid hydrogen under the external magnetic field
Journal of Physics: Conference Series **507** 2 22042 (2014)

95 H. Tatsumoto, Y. Shirai, M. Shiotsu, Y. Naruo, H. Kobayashi, and Y. Inatani
Forced convection heat transfer from a wire inserted into a vertically-mounted pipe to liquid hydrogen flowing upward
Journal of Physics: Conference Series **568** 3 32017 (2014)

96 K. Toh, T. Nakamura, K. Sakasai, K. Soyama, and H. Yamagishi
Performance evaluation of high-pressure MWPC with individual line readout under Cf-252 neutron irradiation
Journal of Physics: Conference Series **528** 1 12045 (2014)

97 T. Tominaga, S. Takata, J. Suzuki, K. Aizawa, H. Seto, and M. Arai
Adsorption of Water to Double-Network Polymers Having a Hierarchical Structure
Journal of Physics: Conference Series **502** 012058 (2014)

98 S. Torii, M. Yonemura, Y. Ishikawa, P. Miao, R. Tomiyasu, S. Satoh, Y. Noda, and T. Kamiyama
Improvement of Instrument Devices for Super High Resolution Powder Diffractometer at J-PARC
Journal of Physics: Conference Series **502** 1 12052 (2014)

99 M. Toyoda, Y. Kobayashi, M. Itoh, and M. Sato
Lower Symmetrical Behaviour of Electronic State in the FeAs Plane of $Ba(Fe_{1-x}Co_x)_2As_2$ - ^{75}As NMR Study-
Journal of Physics: Conference Series **568** 022029 (2014)

100 I. Umegaki , H. Nozaki, M. Harada, Y. Higuchi, T. Noritake, M. Matsumoto, S-i. Towata, E. J. Ansaldo, J. H. Brewer, A. Koda, Y. Miyake, and J. Sugiyama
In situ μ^+SR measurements on the hydrogen desorption reaction of magnesium hydride
Journal of Physics: Conference Series **551** 1 012036 (1-6) (2014)

101 I. Yamauchi, M. Miyazaki, M. Hiraishi, A. Koda, K. M. Kojima, R. Kadono, and H. Nakamura
Muon Knight shift in d-electron heavy fermion compound $Y_{0.95}Sc_{0.05}Mn_2$
Journal of Physics: Conference Series **551** 1 012002 (1-6) (2014)

102 T. Yokoo, K. Ohoyama, S. Itoh, J. Suzuki, M. Nanbu, N. Kaneko, K. Iwasa, T. J. Sato, H. Kimura, and M. Ohkawara
Construction of Polarized Inelastic Neutron Spectrometer in J-PARC
Journal of Physics: Conference Series **502** 1 12046 (2014)

103 T. Yokoo, S. Itoh, D. Kawana, H. Yoshizawa, and J. Akimitsu
Dynamical properties of spins and holes in carrier doped quantum Haldane chain
Journal of Physics: Conference Series **502** 1 12045 (2014)

104 T. Yokoo, S. Itoh, S. Ibuka, H. Yoshizawa, and J. Akimitsu
Spin and Hole Dynamics in Carrier-Doped Quantum Haldane Chain
Journal of Physics: Conference Series **568** 4 42035 (2014)

105 M. Yonemura, M. Hirayama, K. Suzuki, R. Kanno, N. Torikai, and N. L. Yamada
Development of Spectroelectrochemical Cells for in situ Neutron Reflectometry
Journal of Physics: Conference Series **502** 1 12054 (2014)

106 M. Yonemura, K. Mori, T. Kamiyama, T. Fukunaga, S. Torii, M. Nagao, Y. Ishikawa, Y. Onodera, D. S. Adipranoto, H. Arai, Y. Uchimoto, and Z. Ogumi
Development of SPICA, New Dedicated Neutron Powder Diffractometer for Battery Studies
Journal of Physics: Conference Series **502** 1 12053 (2014)

107 R. Iizuka, K. Komatsu, H. Kagi, T. Nagai, A. Sano-Furukawa, T. Hattori, H. Gotou, and T. Yagi
Phase transitions and hydrogen bonding in deuterated calcium hydroxide: High-pressure and high-temperature neutron diffraction measurements
Journal of Solid State Chemistry **218** 95-102 (2014)

108 L. Kuo, H. Yufei, W. Yingxia, K. Takashi, W. Bingwu, L. Zhaofei, and L. Jianhua
Syntheses and properties of a family of new compounds $RE_3Sb_3Co_2O_{14}$(RE=La, Pr, Nd, Sm–Ho) with an ordered pyrochlore structure
Journal of Solid State Chemistry **217** 80-86 (2014)

109 I. Qasim, P. E. R. Blanchard, B. J. Kennedy, T. Kamiyama, P. Miao, and S. Torii
Structural and electronic properties of $Sr_{1-x}Ca_xTi_{0.5}Mn_{0.5}O_3$
Journal of Solid State Chemistry **213** 293-300 (2014)

110 Y. Kameda, T. Miyazaki, T. Otomo, Y. Amo, and T. Usuki
Neutron Diffraction Study on the Structure of Aqueous $LiNO_3$ Solutions
Journal of Solution Chemistry **43** 9-10 1588-1600 (2014)

111 J. Bang, S. Matsuishi, H. Hiraka, F. Fujisaki, T. Otomo, S. Maki, J.-i. Yamaura, R. Kumai, Y. Murakami, and H. Hosono
Hydrogen Ordering and New Polymorph of Layered Perovskite Oxyhydrides: $Sr_2VO_{4-x}H_x$
Journal of the American Chemical Society **136** 20 7221-7224 (2014)

112 A. Ueda, S. Yamada, T. Isono, H. Kamo, A. Nakao, R. Kumai, H. Nakao, Y. Murakami, K. Yamamoto, Y. Nishio, and H. Mori
Hydrogen-Bond-Dynamics-Based Switching of Conductivity and Magnetism: A Phase Transition Caused by Deuterium and Electron Transfer in a Hydrogen-Bonded Purely Organic Conductor Crystal
Journal of the American Chemical Society **136** 34 12184-12192 (2014)

113 Y. Fujii
原子炉中性子の利用
Journal of the Crystallographic Society of Japan (2014)

114 T. Ohhara
Recent Advance of the Neutron Crystal Chemistry by using High Intensity Neutron Beam at J-PARC
Journal of the Crystallographic Society of Japan **56** 5 301-306 (2014)

115 M. Hiraishi, R. Kadono, M. Miyazaki, I. Yamauchi, A. Koda, K. M. Kojima, M. Ishikado, S. Wakimoto, and S. Shamoto
Cooperative Order in the Weakly Magnetic Domain of $LaFeAsO_{1-x}F_x$ near the Doping Phase Boundary
Journal of the Physical Society of Japan **83** 103707 (1-5) (2014)

116 K. Kamazawa, M. Harada, T. Araki, Y. Matsuo, M. Tyagi, and J. Sugiyama
Interrelationship between the Number of Mobile Proton, Diffusion Coefficient and AC Conductivity in Superprotonic Conductors, $CsHSO_4$ and $Rb_3H(SeO_4)_2$
Journal of the Physical Society of Japan **83** 074604 (2014)

117 Y. Kobayashi, T. Iida, K. Suzuki, T. Kawamata, M. Itoh, and M. Sato
^{75}As NQR and NMR Studies on the Superconducting State of $Ca_{10}Pt_4As_8(Fe_{1-x}Pt_xAs)_{10}$
Journal of the Physical Society of Japan **83** 014712 (2014)

118 K. Motoya, T. Moyoshi, and M. Matsuda
Long-Time Variation in Magnetic Structure of $Ce_{0.98}La_{0.02}Ir_3Si_2$: Effect of Randomness on Time Variation
Journal of the Physical Society of Japan **83** 2 24708 (2014)

119 H. Shigematsu, K. Nishiyama, Y. Kawamura, and H. Mashiyama
Neutron and X-ray Scattering Studies of Rb_2CoCl_4 and Successive Phase Transition in A_2BX_4-Type Crystals
Journal of the Physical Society of Japan **83** 124601 (2014)

120 T. Yamamoto, Y. Nakazawa, M. Tamura, A. Nakao, A. Fukaya, R. Kato, and K. Yakushi
Property of the Valence-Bond Ordering in Molecular Superconductor with a Quasi-Triangular Lattice
Journal of the Physical Society of Japan **83** 053703 (2014)

121 T. Yamazaki, Y. Tabata, T. Waki, T. J. Sato, M. Matsuura, K. Ohoyama, M. Yokoyama, and H. Nakamura
Novel Magnetic Chiral Structures and Peculiar Temperature Hysteresis in the Metallic Helimagnet MnP
Journal of the Physical Society of Japan **83** 054711 (2014)

122 K. T. Lai, A. Takemori, S. Miyasaka, S. Tajima, A. Nakao, H. Nakao, R. Kumai, and Y. Murakami
Suppression of Superconductivity around x = 0.5–0.7 in $LaFeP_{1-x}As_xO_{0.95}F_{0.05}$
JPS Conference Proceedings **1** 012104 (2014)

123 H. Ariga, K. Shimomura, K. Ishida, F. Pratt, K. Yoshizawa, W. Higemoto, E. Torikai, and K. Asakura
Detection of Oxygen Vacancy in Rutile TiO_2 Single Crystal by μSR Measurement
JPS Conference Proceedings **2** 010307 (1-4) (2014)

124 M. Futakawa
Targetry overview - Various target concepts and expectable next generation targets in power frontier applications -
JPS Conference Proceedings **8** 001002 (1-12) (2015)

125 L. Hao, K. Iwasa, H. Kobayashi, K. Nakajima, S. Ohira-Kawamura, T. Kikuchi, D. Chen, Y. Liu, Z. Liu, S. Li, and D. Hu
Effects of Co Substitution on the Magnetic Excitation in Heavy Fermion Compound $PrFe_4P_{12}$
JPS Conference Proceedings **3** 11088 (2014)

126 M. Harada, K. Oikawa, M. Ooi, T. Kai, T. Shinohara, K. Sakai, and F. Maekawa
Performance of Optical Devices for Energy-Selective Neutron Imaging in NOBORU at J-PARC
JPS Conference Proceedings **1** 1 14015 (2014)

127 S. Harjo, J. Abe, K. Aizawa, W. Gong, and T. Iwahashi
Deformation Behavior of An Austenitic Steel by Neutron Diffraction
JPS Conference Proceedings **1** 14017 (2014)

128 W. Higemoto, A. Koda, R. Kadono, Y. Yoshida, and Y. Ōnuki
Investigation of Spontaneous Magnetic Field in Spin-Triplet Superconductor Sr_2RuO_4
JPS Conference Proceedings **2** 010202 (1-5) (2014)

129 K. Iida, K. Ikeuchi, M. Ishikado, J. Suzuki, R. Kajimoto, M. Nakamura, Y. Inamura, and M. Arai
Energy- and Q-Resolution Investigations of a Chopper Spectrometer 4SEASONS at J-PARC
JPS Conference Proceedings **1** 014016 (2014)

130 Y. Ikedo, Y. Miyake, K. Shimomura, P. Strasser, N. Kawamura, K. Nishiyama, S. Makimura, H. Fujimori, A. Koda, J. Nakamura, T. Nagatomo, Y. Kobayashi, T. Adachi, A. D. Pant, T. Ogitsu, T. Nakamoto, K. Sasaki, H. Ohhata, R. Okada, A. Yamamoto, Y. Makida, M. Yoshida, T. Okamura, R. Ohkubo, W. Higemoto, T. U. Ito, K. Nakahara, and K. Ishida
U-Line at MLF/J-PARC for Ultra Slow Muon Microscopy
JPS Conference Proceedings **2** 010103 (1-4) (2014)

131 K. Ikeuchi, M. Sato, R. Kajimoto, Y. Kobayashi, K. Suzuki, M. Itoh, P. Bourges, A. D. Christianson, H. Nakamura, and M. Machida
Phonons and Spin Excitations in Fe-Based Superconductor $Ca_{10}Pt_4As_8(Fe_{1-x}Pt_xAs)_{10}$ ($x^{\sim}0.2$)
JPS Conference Proceedings **3** 015043 (2014)

132 R. Kajimoto, K. Nakajima, S. Ohira-Kawamura, Y. Inamura, T. Okuda, and K. Tomiyasu
Low-Energy Spin Fluctuations in $CuCrO_2$ and $Cu_{0.85}Ag_{0.15}CrO_2$ Studied by Inelastic Neutron Scattering
JPS Conference Proceedings **3** 14018 (2014)

133 S. Kanda, H. Fujimori, Y. Fukao, Y. Ikedo, K. Ishida, M. Iwasaki, N. Kawamura, K. M. Kojima, M. Lee, S. Makimura, T. Mibe, Y. Miyake, J. Nakamura, Y. Nagashima, T. Nagatomo, K. Nagumo, S. Nishimura, S. Okada, N. Saito, K. Shimomura, T. Suzuki, P. Strasser, K. Ueno, and E. Won
Development of High-Rate Positron Tracker for the Muonium Production Experiment at J-PARC
JPS Conference Proceedings **2** 010404 (1-7) (2014)

134 N. Kawamura, A. Toyoda, T. Mibe, N. Saito, M. Aoki, K. Shimomura, and Y. Miyake
H Line; A Beamline for Fundamental Physics in J-PARC
JPS Conference Proceedings **2** 010112 (1-6) (2014)

135 T. Kawasaki, K. Kaneko, N. Aso, A. Nakamura, M. Hedo, T. Nakama, Y. Onuki, T. Ohhara, R. Kiyanagi, K. Oikawa, I. Tamura, A. Nakao, K. Munakata, and T. Hanashima
Single Crystal Neutron Diffraction Study of High Neutron Absorbing Compound $EuGa_4$
JPS Conference Proceedings **1** 014009 (2014)

136 R. Kiyanagi, Y. Ishikawa, and Y. Noda
Proton Conduction Path in $Rb_3H(SeO_4)_2$ Studied by High Temperature Neutron Single Crystal Diffraction
JPS Conference Proceedings **1** 12034 (2014)

137 Y. Kousaka, N. Ikeda, T. Ogura, T. Yoshii, J. Akimitsu, K. Ohishi, J. Suzuki, H. Hiraka, M. Miyagawa, S. Nishihara, K. Inoue, and J. Kishine
Chiral Magnetic Soliton Lattice in MnSi
JPS Conference Proceedings **2** 010205 (2014)

138 S. Makimura, M. Onoi, M. Wakasugi, T. Nagatomo, Y. Ikedo, P. Strasser, K. Shimomura, J. Nakamura, K. Nishiyama, and Y. Miyake
Development of Manufacturing Method of Highly Pure Tungsten Foil for Thermal Muonium Generation
JPS Conference Proceedings **2** 010104 (1-6) (2014)

139 Y. Miyake, Y. Ikedo, K. Shimomura, P. Strasser, N. Takashi, J. Nakamura, S. Makimura, N. Kawamura, H. Fujimori, A. Koda, Y. Kobayashi, K. Nishiyama, R. Kadono, W. Higemoto, T. U. Ito, T. Ogitsu, Y. Makida, K. Sasaki, T. Adachi, and E. Torikai
Ultra Slow Muon Project at J-PARC MUSE
JPS Conference Proceedings **2** 010101 (1-6) (2014)

140 K. Nagamine
Past, Present and Future of Ultra-Slow Muons
JPS Conference Proceedings **2** 010001 (-8) (2014)

141 T. Nagatomo, Y. Ikedo, P. Strasser, S. Makimura, J. Nakamura, K. Nishiyama, K. Shimomura, N. Kawamura, A. Koda, H. Fujimori, Y. Kobayashi, T. U. Ito, W. Higemoto, A. D. Pant, R. Kadono, E. Torikai, and Y. Miyake
Construction of Ultra Slow Muon Beam Line at J-PARC
JPS Conference Proceedings **2** 010102 (1-5) (2014)

142 M. Nakamura and R. Kajimoto
General Formulae for the Optimized Design of Fermi Chopper Spectrometer
JPS Conference Proceedings **1** 014018 (2014)

143 J. Nakamura, Y. Oishi, N. Saito, K. Miyazaki, K. Yokoyama, K. Okamura, S. Makimura, Y. Miyake, T. Nagatomo, P. Strasser, Y. Ikedo, D. Tomono, K. Shimomura, S. Wada, N. Kawamura, A. Koda, and K. Nishiyama
Transport of Coherent VUV Radiation to Muon U-Line for Ultra Slow Muon Microscope
JPS Conference Proceedings **2** 010108 (1-7) (2014)

144 T. Nakatani, Y. Inamura, K Moriyama, T. Ito, S. Muto, and T. Otomo
Event Recording Data Acquisition System and Experiment Data Management System for Neutron Experiments at MLF, J-PARC
JPS Conference Proceedings **1** 014010 (2014)

145 H. Nozaki, S. Ohta, M. Harada, M. Måsson, D. Sheptyakov, V. Pomjakushin, I. Watanabe, Y. Ikedo, Y. Miyake, and J. Sugiyama
Li-Ion Dynamics in $Li_{5+x}La_3Zr_xNb_{2-x}O_{12}$
JPS Conference Proceedings **2** 010303 (1-6) (2014)

146 K. Oikawa, T. Kawasaki, T. Ohhara, R. Kiyanagi, K. Kaneko, I. Tamura, T. Nakamura, M. Harada, A. Nakao, T. Hanashima, K. Munakata, H. Kimura, Y. Noda, M. Takahashi, and T. Kiyotani
Instrument Design and Performance Evaluation of a New Single Crystal Neutron Diffractometer SENJU at J-PARC
JPS Conference Proceedings **1** 014013 (2014)

147 K. Oikawa, M. Harada, and F. Maekawa
Study on the Pulse Shape of Thermal and Cold Neutrons Provided by the Decoupled Moderator of JSNS
JPS Conference Proceedings **1** 1 14012 (2014)

148 M. Sato, K. Ikeuchi, R. Kajimoto, Y. Kobayashi, Y. Yasui, K. Suzuki, M. Itoh, M. Nakamura, Y. Inamura, M. Arai, P. Bourges, A. D. Christianson, H. Nakamura, and M. Machida
On the Superconducting Symmetry of Fe-Based Systems -Impurity Effects and Microscopic Magnetic Behavior-
JPS Conference Proceedings **1** 014007 (2014)

149 K. Sato, M. Matsuura, M. Fujita, R. Kajimoto, S. Ji, K. Ikeuchi, M. Nakamura, Y. Inamura, M. Arai, M. Enoki, and K. Yamada
Temperature Dependence of Spin Fluctuations in Underdoped $La_{1.90}Sr_{0.10}CuO_4$
JPS Conference Proceedings **3** 017010 (2014)

150 K. Shimomura, R. Kadono, A. Koda, K. Nishiyama, W. Higemoto, and T. U. Ito
μSR Study on Isolated Hydrogen and Oxygen Vacancy in $SrTiO_3$
JPS Conference Proceedings **2** 010308 (1-4) (2014)

151 Y. Sugawara, A. D. Pant, W. Higemoto, K. Shimomura, E. Torikai, and K. Nagamine
Hydration Effects on Electron Transfer in Biological Systems Studied by μSR
JPS Conference Proceedings **2** 010310(1-5) (2014)

152 K. S. Tanaka, M. Aoki, H. Iinuma, Y. Ikedo, K. Ishida, M. Iwasaki, Y. Ueno, R. Ohkubo, T. Ogitsu, R. Kadono, O. Kamigaito, N. Kawamura, D. Kawall, S. Kanda, K. Kubo, T. Kume, A. Koda, K. Kojima, N. Saito, N. Sakamoto, K. Sasaki, K. Shimomura, M. Sugano, D. Tomono, A. Toyoda, H. A. Torii, E. Torikai, K. Nagamine, K. Nishiyama, P. Strasser, Y. Fukao, Y. Fujiwara, Y. Matsuda, T. Mibe, Y. Miyake, and M. Yoshida
Measurement of Muonium Hyperfine Splitting at J-PARC
JPS Conference Proceedings **2** 010405 (1-6) (2014)

153 T. Tominaga, S.-i. Takata, J.-i. Suzuki, K. Aizawa, H. Seto, and M. Arai
SANS Study of Static Structure of The Double Network Polymers
JPS Conference Proceedings **1** 14014 (2014)

154 T. Tominaga, S. Takata, J. Suzuki, T. Shinohara, T. Oku, K. Ohishi, T. Nakatani, Y. Inamura, H. Iwase, T. Ito, H. Kira, K. Suzuya, K. Aizawa, and M. Arai
SANS Study on Double-Network Polymers
JPS Conference Proceedings **1** 014014 (2014)

155 K. Tsutsumi, M. Fujita, K. Sato, M. Miyazaki, R. Kadono, and K. Yamada
Effects of Oxygen Reduction and Ce-Doping on Magnetic Order in T'*-*$Pr_{1.40-x}La_{0.60}Ce_xCuO_{4+\delta-\alpha}$ *Studied by μSR Measurement*
Key Engineering Materials **616** 297-301 (2014)

156 A. J. Clulow, C. Tao, K. H. Lee, M. Velusamy, J. A. McEwan, P. E. Shaw, N. L. Yamada, M. James, P. L. Burn, I. R. Gentle, and P. Meredith
Time-Resolved Neutron Reflectometry and Photovoltaic Device Studies on Sequentially Deposited PCDTBT-Fullerene Layers
Langmuir **30** 38 11474-11484 (2014)

157 A. Horinouchi, N. L. Yamada, and K. Tanaka
Aggregation States of Polystyrene at Nonsolvent Interfaces
Langmuir **30** 22 6565-6570 (2014)

158 C. M. Phan, C. V. Nguyen, S.-i. Yusa, and N. L. Yamada
Synergistic Adsorption of MIBC/CTAB Mixture at the Air/Water Interface and Applicability of Gibbs Adsorption Equation
Langmuir **30** 20 5790-5796 (2014)

159 H. Komiyama, R. Sakai, S. Hadano, S. Asaoka, K. Kamata, T. Iyoda, M. Komura, T. Yamada, and H. Yoshida
Enormously Wide Range Cylinder Phase of Liquid Crystalline PEObPMA(Az) Block Copolymer
Macromolecules **47** 5 1777–1782 (2014)

160 J. Abe, K. Sekine, S. Harjo, W. Gong, and K. Aizawa
Strain Analysis in Geological Materials Using Neutron Diffraction and AE Signal Measurement at J-PARC/BL19" TAKUMI"
Materials Science Forum **777** 219-224 (2014)

161 S. Harjo, K. Aizawa, J. Abe, W. Gong, T. Ito, T. Kawasaki, and T. Iwahashi
Engineering & Related Studies at J-PARC
Materials Science Forum **777** 12-18 (2014)

162 S. Harjo, T. Hemmi, J. Abe, W. Gong, Y. Nunoya, K. Aizawa, T. Ito, N. Koizumi, S. Machiya, and K. Osamura
Residual Strains in ITER Conductors by Neutron Diffraction
Materials Science Forum **777** 84-91 (2014)

163 T. Hirano, K. Hidaka, D. Takamatsu, N. Takahashi, K. Shishido, M. Sasaki, and Y. Kawashima
Analysis of Residual Stresses in Pistons of Motor Vehicle Engines Using Neutron Diffraction at J-PARC
Materials Science Forum **772** 27-32 (2014)

164 T. Ito, S. Harjo, Y. Inamura, T. Nakatani, T. Kawasaki, J. Abe, and K. Aizawa
Utilization of an event-recording system for neutron diffraction experiments
Materials Science Forum **783-786** 2071-2074 (2014)

165 X. Z. Jin, T. Nakamoto, K. Tsuchiya, A. Yamamoto, T. Ogitsu, M. Sugano, S. Harjo, J. Abe, W. Gong, T. Iwahashi, A. Kikuchi, T. Takeuchi, Y. Yanagisawa, M. Takahashi, and H. Maeda
Recent R&D on Superconducting Wires for High-Field Magnet
Materials Science Forum **783-786** 2081-2090 (2014)

166 H. Suzuki, S. Harjo, J. Abe, and K. Akita
Influence of Beam Divergence on Pseudo-Strain Induced in Time-of-Flight Neutron Diffraction
Materials Science Forum **777** 105-111 (2014)

167 K. Ikeda, T. Otomo, H. Ohshita, N. Kaneko, M. Tsubota, K. Suzuya, F. Fujisaki, T. Ono, T. Yamanaka, K. Shimoda, T. Ichikawa, and Y. Kojima
Local Structural Analysis on Decomposition Process of $LiAl(ND_2)_4$
MATERIALS TRANSACTIONS **55** 8 1129-1133 (2014)

168 T. Wan, T. Naoe, T. Wakui, M. Futakawa, and K. Maekawa
Cavitation Damage Evaluation Using Laser Impacts
MATERIALS TRANSACTIONS **55** 7 1024-1029 (2014)

169 W. Gong, K. Aizawa, S. Harjo, J. Abe, T. Iwahashi, and T. Kamiyama
Neutron Diffraction on LPSO Structure in Mg-Zn-Y Alloys
Materials Transactions **54** 974-976 (2014)

170 H. Suzuki, K. Kusunoki, Y. Hatanaka, T. Mukai, A. Tasai, M. Kanematsu, K. Kabayama, and S. Harjo
Measuring strain and stress distributions along rebar embedded in concrete using time-of-flight neutron diffraction
Measurement Science and Technology **25** 2 25602 (2014)

171 Y. Su, Y. Tomota, and S. Harjo

Microstructural Changes by Annealing in Ultrafine-Grained Electrodeposited Pure Iron
Metallurgical and Materials Transactions A **45** 2 990-1000 (2014)

172 Y. Tomota, S. Daikuhara, S. Nagayama, M. Sugawara, N. Ozawa, Y. Adachi, S. Harjo, and S. Hattori
Stress Corrosion Cracking Behavior at Inconel and Low Alloy Steel Weld Interfaces
Metallurgical and Materials Transactions A **45** 13 6103-6117 (2014)

173 Y. Tomota
量子ビーム解析を活用した複相組織制御と力学特性発現の解明
Microstructural analysis and computational material science for materials design: applications and future perspectives 87-110 (2014)

174 A. Takenaka and Y. Fujii
Elementry Scattering Theory
Morikita Publishing Co. , Ltd. (2014)

175 K. S.-. Ishii, M. Fujita, T. Sasaki, M. Minola, G. Dellea, C. Mazzoli, K. Kummer, G. Ghiringhelli, L. Braicovich, T. Tohyama, K. Tsutsumi, K. Sato, R. Kajimoto, K. Ikeuchi, K. Yamada, M. Yoshida, M. Kurooka, and J. Mizuki
High-energy spin and charge excitations in electron-doped copper oxide superconductors
Nature Communications **5** 3714 (2014)

176 I. Klich, S.-H. Lee, and K. Iida
Glassiness and Exotic Entropy Scaling Induced by Quantum Fluctuations in a Disorder-Free Frustrated Magnet
Nature Communications **5** 3498 (2014)

177 A. Machida, H. Saitoh, H. Sugimoto, T. Hattori, A. Sano-Furukawa, N. Endo, Y. Katayama, R. Iizuka, T. Sato, M. Matsuo, S.-i. Orimo, and K. Aoki
Site occupancy of interstitial deuterium atoms in face-centred cubic iron
Nature Communications **5** 5063_1 - 5063_6 (2014)

178 J. Zhu, S. Du, X. Yu, J. Zhang, H. Xu, S. C. Vogel, T. C. Germann, J. S. Francisco, F. Izumi, K. Momma, Y. Kawamura, C. Jin, and Y. Zhao
Encapsulation Kinetics and Dynamics of Carbon Monoxide in Clathrate Hydrate
Nature Communications **5** 4128 (2014)

179 M. Hashimoto, E. Nowadnick, R.-H. He, I. Vishik, B. Moritz, Y. He, K. Tanaka, R. Moore, D. Lu, Y. Yoshida, M. Ishikado, T. Sasagawa, K. Fujita, S. Ishida, S. Uchida, H. Eisaki, Z. Hussain, T. Devereaux, and Z.-X. Shen
Direct Spectroscopic Evidence for Phase Competition between the Pseudogap and Superconductivity in $Bi_2Sr_2CaCu_2O_{8+\delta}$
Nature Materials **14** 37-42 (2014)

180 M. Hiraishi, S. Iimura, K. M. Kojima, J. Yamaura, H. Hiraka, K. Ikeda, P. Miao, Y. Ishikawa, S. Torii, M. Miyazaki, I. Yamauchi, A. Koda, K. Ishii, M. Yoshida, J. Mizuki, R. Kadono, R. Kumai, T. Kamiyama, T. Otomo, Y. Murakami, S. Matsuishi, and H. Hosono
Bipartite magnetic parent phases in the iron oxypnictide superconductor
Nature Physics **10** 4 300-303 (2014)

181 M. Igashira, T. Katabuchi, H. Harada, S. Nakamura, A. Kimura, N. Iwamoto, J. Hori, and Y. Kiyanagi
A Nuclear Data Project on Neutron Capture Cross Sections of Long-Lived Fission Products and Minor Actinides
Nuclear Data Sheets **118** 72-77 (2014)

182 H. Harada, M. Ohta, A. Kimura, K. Furutaka, K. Hirose, K. Y. Hara, T. Kin, F. Kitatani, M. Koizumi, S. Nakamura, M. Oshima, Y. Toh, M. Igashira, T. Katabuchi, M. Mizumoto, K. Kino, Y. Kiyanagi, T. Fujii, S. Fukutani, J. Hori, and K. Takamiya
Capture Cross-section Measurement of ^{241}Am(n,γ) at J-PARC/MLF/ANNRI
Nuclear Data Sheets **119** 61-64 (2014)

183 K. Hirose, K. Furutaka, K. Y. Hara, H. Harada, J. Hori, M. Igashira, T. Kamiyama, T. Katabuchi, A. Kimura, T. Kin, K. Kino, F. Kitatani, Y. Kiyanagi, M. Koizumi, M. Mizumoto, S. Nakamura, M. Oshima, and Y. Toh
Cross Section Measurement of ^{237}Np(n,γ) at J-PARC/MLF/ANNRI
Nuclear Data Sheets **119** 48-51 (2014)

184 J. Hori, H. Yashima, S. Nakamura, K. Furutaka, K. Y. Hara, H. Harada, K. Hirose, A. Kimura, F. Kitatani, M. Koizumi, M. Oshima, Y. Toh, M. Igashira, T. Katabuchi, M. Mizumoto, T. Kamiyama, K. Kino, and Y. Kiyanagi
Measurements of Capture Gamma Rays from the Neutron Resonances of ^{74}Se and ^{77}Se at the J-PARC/MLF/ANNRI
Nuclear Data Sheets **119** 128-131 (2014)

185 T. Katabuchi, T. Matsuhashi, K. Terada, M. Mizumoto, K. Hirose, A. Kimura, K. Furutaka, K. Y. Hara, H. Harada, J. Hori, M. Igashira, T. Kamiyama, F. Kitatani, K. Kino, Y. Kiyanagi, M. Koizumi, S. Nakamura, M. Oshima, and Y. Toh
A New Signal Processing Technique for Neutron Capture Cross Section Measurement Based on Pulse Width Analysis
Nuclear Data Sheets **119** 398-400 (2014)

186 A. Kimura, K. Hirose, S. Nakamura, H. Harada, K. Y. Hara, J. Hori, M. Igashira, T. Kamiyama, T. Katabuchi, K. Kino, F. Kitatani, Y. Kiyanagi, M. Koizumi, M. Mizumoto, and Y. Toh
Measurements of Neutron Capture Cross Sections of ^{112}Sn and ^{118}Sn with J-PARC/MLF/ANNRI
Nuclear Data Sheets **119** 150-153 (2014)

187 K. Kino, F. Hiraga, T. Kamiyama, Y. Kiyanagi, H. Harada, K. Y. Hara, K. Hirose, A. Kimura, F. Kitatani, S. Nakamura, M. Igashira, T. Katabuchi, M. Mizumoto, and J. Hori
Measurement of Capture Gamma Rays from ^{99}Tc Neutron Resonances at the J-PARC/ANNRI
Nuclear Data Sheets **119** 140-142 (2014)

188 S. Nakamura, A. Kimura, F. Kitatani, M. Ohta, K. Furutaka, S. Goko, K. Y. Hara, H. Harada, K. Hirose, T. Kin, M. Koizumi, M. Oshima, Y. Toh, K. Kino, F. Hiraga, T. Kamiyama, Y. Kiyanagi, T. Katabuchi, M. Mizumoto, M. Igashira, J. Hori, T. Fujii, S. Fukutani, and K. Takamiya
Cross Section Measurements of the Radioactive ^{10}7Pd and Stable ^{105,108}Pd Nuclei at J-PARC/MLF/ANNRI
Nuclear Data Sheets **119** 143-146 (2014)

189 T. U. Ito, A. Toyoda, W. Higemoto, M. Tajima, Y. Matsuda, and K. Shimomura
Online full two-dimensional imaging of pulsed muon beams at J-PARC MUSE using a gated image intensifier
Nuclear Instruments and Methods in Physics Research Section A **754** 1-9 (2014)

190 T. Katabuchi, T. Matsuhashi, K. Terada, T. Arai, K. Furutaka, K. Y. Hara, H. Harada, K. Hirose, J.-i. Hori, M. Igashira, T. Kamiyama, A. Kimura, K. Kino, F. Kitatani, Y. Kiyanagi, M. Koizumi, M. Mizumoto, S. Nakamura, M. Oshima, and Y. Toh
Pulse-width analysis for neutron capture cross-section measurement using an NaI(Tl) detector
Nuclear Instruments and Methods in Physics Research Section A **764** 369-377 (2014)

191 N. Kawamura, Y. Irie, H. Fujimori, and Y. Miyake
Development of an ultra low field-ripple electromagnet
Nuclear Instruments and Methods in Physics Research Section A **741** 33-36 (2014)

192 T. Kawasaki, T. Nakamura, K. Toh, T. Hosoya, K. Oikawa, T. Ohhara, R. Kiyanagi, M. Ebine, A. Birumachi, K. Sakasai, K. Soyama, and M. Katagiri
Detector system of the SENJU single-crystal time-of-flight neutron diffractometer at J-PARC/MLF
Nuclear Instruments and Methods in Physics Research Section A **735** 444-451 (2014)

193 K. Kino, M. Furusaka, F. Hiraga, T. Kamiyama, Y. Kiyanagi, K. Furutaka, S. Goko, K. Y. Hara, H. Harada, M. Harada, K. Hirose, T. Kai, A. Kimura, T. Kin, F. Kitatani, M. Koizumi, F. Maekawa, S. Meigo, S. Nakamura, M. Ooi, M. Ohta, M. Oshima, Y. Toh, M. Igashira, T. Katabuchi, M. Mizumoto, and J. Hori
Energy resolution of pulsed neutron beam provided by the ANNRI beamline at the J-PARC/MLF
Nuclear Instruments and Methods in Physics Research Section A **736** 66-74 (2014)

194 T. Nakamura, M. Katagiri, K. Toh, K. Honda, H. Suzuki, M. Ebine, A. Birumachi, K. Sakasai, and K. Soyama
A position-sensitive tubular scintillator-based detector as an alternative to a ^{3}He-gas-based detector for neutron-scattering instruments
Nuclear Instruments and Methods in Physics Research Section A **741** 42-46 (2014)

195 T. Nakamura, K. Toh, T. Kawasaki, K. Honda, H. Suzuki, M. Ebine, A. Birumachi, K. Sakasai, K. Soyama, and M. Katagiri
A scintillator-based detector with sub-100-μm spatial resolution comprising a fibre-optic taper with wavelength-shifting fibre readout for time-of-flight neutron imaging
Nuclear Instruments and Methods in Physics Research Section A **737** 176-183 (2014)

196 M. Nakamura, W. Kambara, Th. Krist, T. Shinohara, K. Ikeuchi, M. Arai, R. Kajimoto, K. Nakajima, H. Tanaka, J. Suzuki, M. Harada, K. Oikawa, and F. Maekawa
Feasibility Demonstration of a New Fermi Chopper with Supermirror-Coated Slit Package
Nuclear Instruments and Methods in Physics Research Section A **737** 142-147 (2014)

197 T. Nakamura, A. Ohzu, K. Toh, K. Sakasai, H. Suzuki, K. Honda, A. Birumachi, M. Ebine, H. Yamagishi, M. Takase, M. Haruyama, M. Kureta, K. Soyama, H. Nakamura, and M. Seya
Neutron-sensitive ZnS/$^{10}B_2O_3$ ceramic scintillator detector as an alternative to a ^{3}He-gas-based detector for a plutonium canister assay system
Nuclear Instruments and Methods in Physics Research Section A **763** 340-346 (2014)

198 A. S. Tremsin, T. Shinohara, T. Kai, M. Ooi, T. Kamiyama, Y. Kiyanagi, Y. Shiota, J. B. McPhate, J. V. Vallerga, O. H. W. Siegmund, and W. B. Feller
Neutron resonance transmission spectroscopy with high spatial and energy resolution at the J-PARC pulsed neutron source
Nuclear Instruments and Methods in Physics Research Section A **746** 47-58 (2014)

199 S. K. Callear, T. Ramirez-Cuesta, K. Kamazawa, S. Towata, T. Noritake, S. Parker, M. O. Jones, J. Sugiyama, M. Ishikiriyama, and W. I. F. David
Understanding Composition-Property Relationships in Ti-Cr-V-Mo Alloys for Optimisation of Hydrogen Storage in Pressurised Tanks
Physical Chemistry Chemical Physics **21** 16563 (2014)

200 S. Miyatsu, M. Kofu, A. Nagoe, T. Yamada, M. Sadakiyo, T. Yamada, H. Kitagawa, M. Tyagi, V. G. Sakai, and O. Yamamuro
Proton Dynamics of Two-Dimensional Oxalate-Bridged Coordination Polymers
Physical Chemistry Chemical Physics **16** 32 17295-17304 (2014)

201 K. Amemiya, M. Sakamaki, M. Mizusawa, and M. Takeda
Twisted Magnetic Structure in Ferromagnetic Ultrathin Ni Films Induced by Magnetic Anisotropy Interaction with Antiferromagnetic FeMn
Physical Review B **89** 054404 (2014)

202 F. Hammerath, P. Bonf`a, S. Sanna, G. Prand, R. De Renzi, Y. Kobayashi, M. Sato, and P. Carretta
The Poisoning Effect of Mn in $LaFe_{1-x}Mn_xAsO_{0.89}F_{0.11}$: Unveiling a Quantum Critical Point in the Phase Diagram of Iron-Based Superconductors
Physical Review B **89** 134503 (2014)

203 M. Hase, M. Soda, T. Masuda, D. Kawana, T. Yokoo, S. Itoh, A. Matsuo, K. Kindo, and M. Kohno
Experimental confirmation of spin gap in antiferromagnetic alternating spin-3/2 chain substances $RCrGeO_5$ (R = Y or ^{154}Sm) by inelastic neutron scattering
Physical Review B **90** 24416 (2014)

204 K. Kodama, M. Ishikado, S. Wakimoto, K. Kihou, C. H. Lee, A. Iyo, H. Eisaki, and S. Shamoto
Anisotropic Magnetic Form Factor in a Detwinned Single Crystal of $BaFe_2As_2$
Physical Review B **90** 144510 (2014)

205 K. M. Kojima, Y. Krockenberger, I. Yamauchi, M. Miyazaki, M. Hiraishi, A. Koda, R. Kadono, R. Kumai, H. Yamamoto, A. Ikeda, and M. Naito
Bulk superconductivity in undoped T'-$La^{1.9}Y_{0.1}CuO_4$ probed by muon spin rotation
Physical Review B **89** 180508(1-5) (2014)

206 J. Lee, S. Demura, M. B. Stone, K. Iida, G. Ehlers, C. R. dela Cruz, M. Matsuda, K. Deguchi, Y. Takano, Y. Mizuguchi, O. Miura, D. Louca, and S.-H. Lee
Coexistence of Ferromagnetism and Superconductivity in $CeO_{0.3}F_{0.7}BiS_2$
Physical Review B **90** 224410 (2014)

207 H. Sim, D. C. Peets, S. Lee, T. Kamiyama, K. Ikeda, T. Otomo, S. W. Cheong, and J.-G. Park
High-resolution structure studies and magnetoelectric coupling of relaxor multiferroic $Pb(Fe_{0.5}Nb_{0.5})O_3$
Physical Review B **90** 21 214438 (2014)

208 H. Nakagawa, Y. Yonetani, K. Nakajima, S. Ohira-Kawamura, T. Kikuchi, Y. Inamura, M. Kataoka, and H. Kono
Local dynamics coupled to hydration water determines DNA-sequence-dependent deformability
Physical Review E **90** 2 22723 (2014)

209 K. Iida, S.-H. Lee, and S.-W. Cheong
Erratum: Coexisting Order and Disorder Hidden in a Quasi-Two-Dimensional Frustrated Magnet
Physical Review Letters **113** 079901 (2014)

210 K. M. Kojima, R. Kadono, M. Miyazaki, M. Hiraishi, I. Yamauchi, A. Koda, Y. Tsuchiya, H. S. Suzuki, and H. Kitazawa
Magnetic Frustration in Iridium Spinel Compound $CuIr_2S_4$
Physical Review Letters **112** 087203(1-5) (2014)

211 M. Soda, M. Matsumoto, M. Mansson, S. Ohira-Kawamura, K. Nakajima, R. Shiina, and T. Masuda
Spin nematic interaction in multiferroic compound $Ba_2CoGe_2O_7$
Physical Review Letters **112** 127205 (2014)

212 K. Tomiyasu, K. Iwasa, H. Ueda, S. Niitaka, H. Takagi, S. Ohira-Kawamura, T. Kikuchi, Y. Inamura, K. Nakajima, and K. Yamada
Spin-Orbit Fluctuations in Frustrated Heavy-Fermion Metal LiV_2O_4
Physical Review Letters **113** 23 236402 (2014)

213 A. M. Dymshits, K. D. Litasov, A. Shatskiy, I. S. Sharygin, E. Ohtani, A. Suzuki, N. P. Pokhilenko, and K. Funakoshi
P-V-T Equation of State of Na-Majorite to 21 GPa and 1673 K
Physics of the Earth and Planetary Interiors **227** 68-75 (2014)

214 E. Ito, D. Yamazaki, T. Yoshino, S. Shan, X. Guo, N. Tsujimo, T. Kunimoto, Y. Higo, and K. Funakoshi
High Pressure Study of Transition Metal Monoxides MnO and CoO: Structure and Electrical Resistance
Physics of the Earth and Planetary Interiors **228** 170-175 (2014)

215 Y. Shibazaki, H. Terasaki, E. Ohtani, R. Tateyama, K. Nishida, K. Funakoshi, and Y. Higo
High-Pressure and High-Temperature Phase Diagram for $Fe_{0.9}Ni_{0.1}$-H Alloy
Physics of the Earth and Planetary Interiors **228** 192-201 (2014)

216 D. Yamazaki, E. Ito, T. Yoshino, N. Tsujino, A. Yoneda, X. Guo, F. Xu, Y. Higo, and K. Funakoshi
Over 1 Mbar Generation in the Kawai-Type Multianvil Apparatus and Its Application to Compression of $(Mg_{0.92}Fe_{0.08})SiO_3$ Perovskite and Stishovite
Physics of the Earth and Planetary Interiors **228** 262-267 (2014)

217 W. Chuajiw, K. Takatori, and Y. Fukushima
Polymerization Properties of Polyamide in Bottom-Up Prepared Polyamide-Calcium Carbonate Composite
Polymer Composites **35** 1132–1139 (2014)

218 N. L. YAMADA
Structure Analysis of Polymer Thin Film Using Neutron Reflectometry
POLYMERS **63** 2 110-111 (2014)

219 T. Wakui, H. Ishii, T. Naoe, T. Wan, X. Zhihong, K. Haga, H. Takada, and M. Futakawa
Investigation on HIP diffusion bonding of invar alloy and stainless steel
Proceedings of International Conference on Hot Isostatic Pressing'14 210-219 (2014)

220 T. Kai, Y. Kasugai, M. Ooi, H. Kogawa, K. Haga, H. Kinoshita, M. Seki, and M. Harada
Experiences on radioactivity handling for mercury target system in MLF/J-PARC
Progress in Nuclear Science and Technology **4** 380-383 (2014)

221 M. Kawai, M. Yonemura, S. Torii, T. Muroya, K. Mori, T. Fukunaga, K. Okuno, K. Takeda, K. Niita, and T. Kamiyama
Novel monolayer shields of a neutron powder diffractometer SPICA at BL09 of J-PARC
Progress in nuclear science and technology **4** 156-159 (2014)

222 K. Okuno, M. Kawai, H. Yamada, T. Shinohara, S. Takata, J. Suzuki, K. Suzuya, and K. Aizawa
Application of neutron shield concrete to neutron scattering instrument TAIKAN in J-PARC
Progress in nuclear science and technology **4** 619-622 (2014)

223 K. Sakai, T. Kai, M. Ooi, A. Watanabe, T. Nakatani, W. Higemoto, S. Meigo, S. Sakamoto, H. Takada, and M. Futakawa
Operation status of interlock system of Materials and Life Science Experimental Facility (MLF) in J-PARC
Progress in nuclear science and technology **4** 264-267 (2014)

224 G. A. Beer, Y. Fujiwara, S. Hirota, K. Ishida, M. Iwasaki, S. Kanda, H. Kawai, N. Kawamura, R. Kitamura, S. Lee, W. Lee, G. M. Marshall, T. Mibe, Y. Miyake, S. Okada, K. Olchanski, A. Olin, H. Ohnishi, Y. Oishi, M. Otani, N. Saito, K. Shimomura, P. Strasser, M. Tabata, D. Tomono, K. Ueno, E. Won, and K. Yokoyama
Enhancement of muonium emission rate from silica aerogel with a laser-ablated surface
Progress of Theoretical and Experimental Physics 091C01(1-7) (2014)

225 Y. Fukushima and S. Fujita
Dynamics of Confined Water: Proton Dynamics
Radioisotopes **63** 381-387 (2014)

226 A. Sano-Furukawa, T. Hattori, H. Arima, A. Yamada, S. Tabata, M. Kondo, A. Nakamura, H. Kagi, and T. Yagi
Six-axis multi-anvil press for high-pressure, high-temperature neutron diffraction experiments
Review of Scientific Instruments **85** 11 113905 (2014)

227 K. Terada, K. Ninomiya, T. Osawa, S. Tachibana, Y. Miyake, M. K. Kubo, N. Kawamura, W. Higemoto, A. Tsuchiyama, M. Ebihara, and M. Uesugi
A new X-ray fluorescence spectroscopy for extraterrestrial materials using a muon beam
Scientific Reports **4** 5072(1-6) (2014)

228 M. Hambsch, H. Jin, A. J. Clulow, A. Nelson, N. L. Yamada, M. Velusamy, Q. Yang, F. Zhu, P. L. Burn, I. R. Gentle, and P. Meredith
Improved stability of non-ITO stacked electrodes for large area flexible organic solar cells
Solar Energy Materials and Solar Cells **130** 182-190 (2014)

229 D. S. Adipranoto, T. Ishigaki, A. Hoshikawa, K. Iwase, M. Yonemura, K. Mori, T. Kamiyama, Y. Morii, and M. Hayashi
Neutron diffraction studies on structural effect for Ni-doping in $LiCo_{1-x}Ni_xO_2$
Solid State Ionics **262** 92-97 (2014)

230 T. Hagiwara, K. Nomura, and H. Yamamura
Relationship between crystal structure and oxide-ion conduction in $Nd_2Zr_2O_7$ and $La_2Zr_2O_7$ deduced by high-temperature neutron diffraction
Solid State Ionics **262** 551-554 (2014)

231 Y. Ishikawa, T. Sakuma, H. Takahashi, and S. A. Danilkin
Pressure dependence of crystal structure of Cu_2O by TOF powder neutron diffraction
Solid State Ionics **262** 622-624 (2014)

232 E. Kartini, M. Nakamura, M. Arai, Y. Inamura, K. Nakajima, T. Maksum, W. Honggowiranto, and T. Putra
Structure and dynamics of solid electrolyte $(LiI)_{0.3}(LiPO_3)_{0.7}$
Solid State Ionics **262** 833-836 (2014)

233 H. Nozaki, M. Harada, S. Ohta, I. Watanabe, Y. Miyake, Y. Ikedo, N. H. Jalarvo, E. Mamontov, and J. Sugiyama
Li diffusive behavior of garnet-type oxides studied by muon-spin relaxation and QENS
Solid State Ionics **262** 585-588 (2014)

234 N. Tsuchida, S. Harjo, T. Ohnuki, and Y. Tomota
Stress-Strain Curves of Steels
Tetsu-to-Hagane **100** 10 1191-1206 (2014)

235 C. A. Tulk, S. Machida, D. D. Klug, H. Lu, M. Guthrie, and J. J. Molaison
The Structure of CO_2 Hydrate between 0.7 and 1.0 GPa
The Journal of Chemical Physics **141** 174503 (2014)

236 Y. Kameda, H. Deguchi, H. Furukawa, Y. Kubota, Y. Yagi, Y. Imai, N. Yamazaki, N. Watari, T. Hirata, and N. Matubayasi
Hydration Structure of CO_2-Absorbed 2-Aminoethanol Studied by Neutron Diffraction with the $^{14}N/^{15}N$ Isotopic Substitution Method
The Journal of Physical Chemistry B **118** 5 1403-1410 (2014)

237 H. Abe, T. Takekiyo, M. Shigemi, Y. Yoshimura, S. Tsuge, T. Hanasaki, K. Ohishi, S. Takata, and J.-i. Suzuki
Direct Evidence of Confined Water in Room-Temperature Ionic Liquids by Complementary Use of Small-Angle X-ray and Neutron

Scattering
The Journal of Physical Chemistry Letters **5** 7 1175-1180 (2014)

238 T. Naoe and M. Futakawa
Pressure wave-induced cavitation erosion in narrow channel of stagnant mercury
Transactions of the JSME **80** 810 FE0025 (2014)

239 K. Akutsu and T. Ohhara
Application and Outlook of the Pulsed Neutron Beam at J-PARC(1) Introduction of Neutron Beam and Neutron Crystallography at J-PARC
BUNSEKI **2014** 11 617-621 (2014)

Editorial Board - MLF Annual Report 2014

J-PARC

JAPAN PROTON ACCELERATOR RESEARCH COMPLEX

High Energy Accelerator Research Organization (KEK)
Japan Atomic Energy Agency (JAEA)

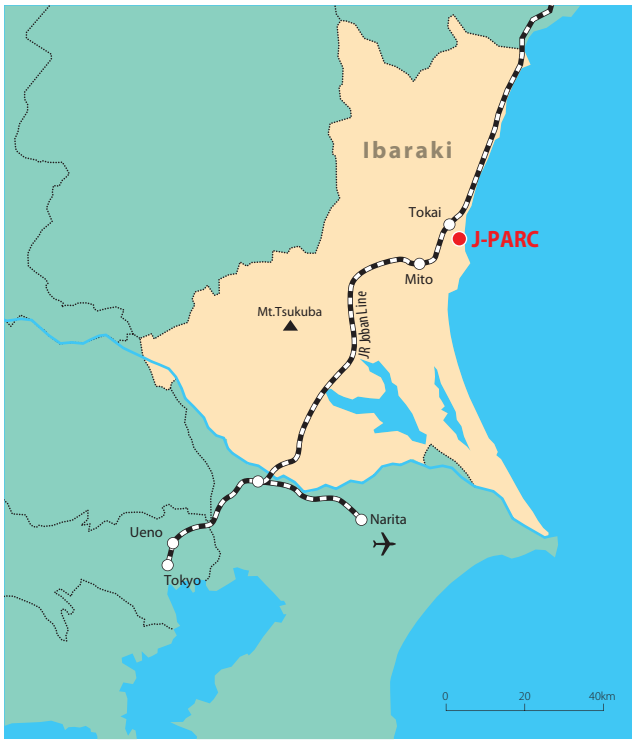

2-4 Shirakata , Tokai-mura, Naka-gun, Ibaraki 319-1195, Japan

http://j-parc.jp/

Materials and Life Science Division
J-PARC Center

http://j-parc.jp/MatLife/en/

CROSS
Comprehensive Research Organization for Science and Society

http://www.cross-tokai.jp/

J-PARC 16-01
KEK Progress Report 2015-5